Electrochemical Society

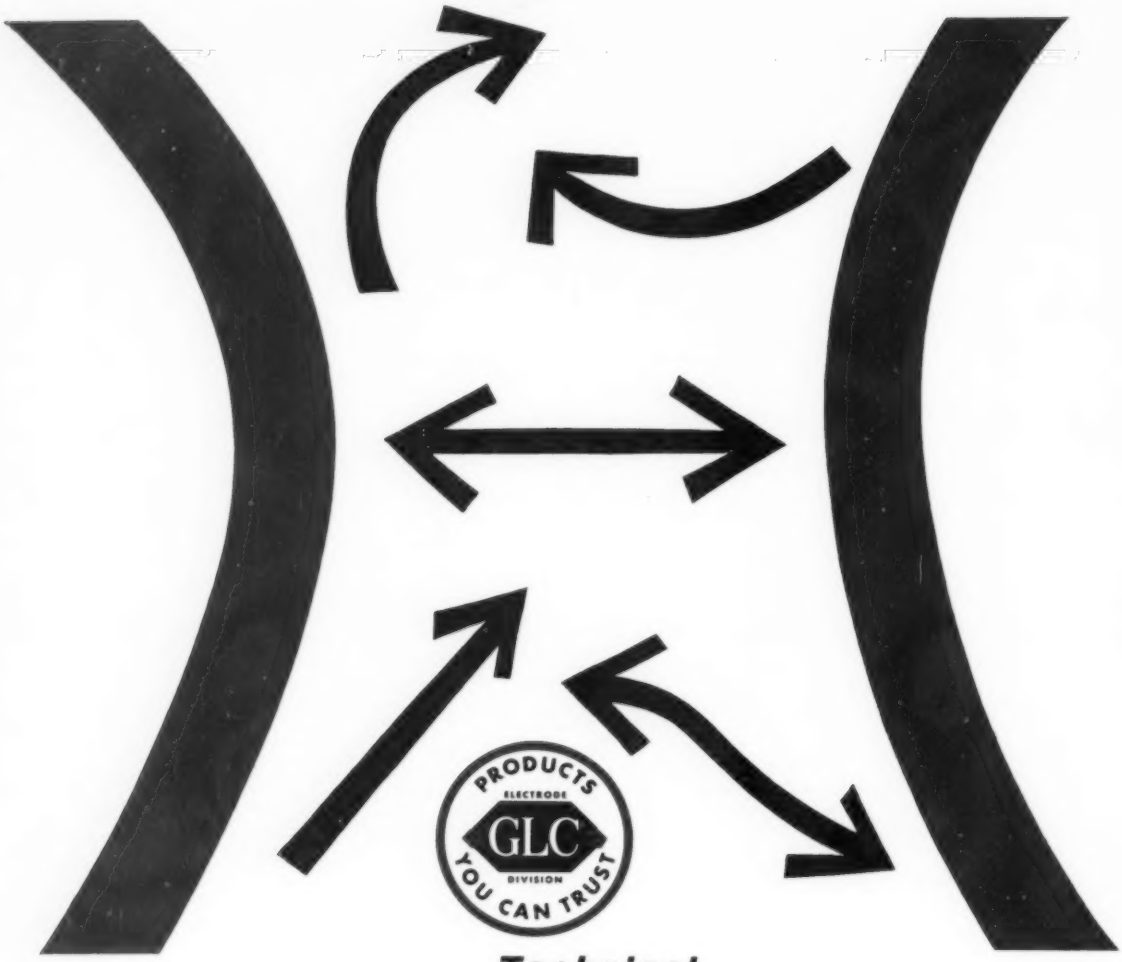

Technical

Exchanges

with

Customers . . . now provide conclusive proof that custom-made anodes materially lower electrolytic cell operating costs. May we show you the evidence?

GREAT LAKES CARBON CORPORATION

18 EAST 48TH STREET, NEW YORK 17, N. Y. OFFICES IN PRINCIPAL CITIES

EDITORIAL STAFF

H. H. Uhlig, Chairman, Publication Committee

Cecil V. King, Editor

Norman Hackerman, Technical Editor

Ruth G. Sterns, Managing Editor

U. B. Thomas, News Editor

H. W. Salzberg, Book Review Editor

Natalie Michalski, Assistant Editor

DIVISIONAL EDITORS

W. C. Vosburgh, Battery

Milton Stern, Corrosion, I

R. T. Foley, Corrosion, II

T. D. Callinan, Electric Insulation

Seymour Senderoff, Electrodeposition

H. C. Froelich, Electronics

Ernest Paskell, Electronics—Semiconductors

Sherlock Swann, Jr., Electro-Organic, I

Stanley Wawzonek, Electro-Organic, II

John M. Blocher, Jr., Electrothermics and Metallurgy, I

A. U. Seybolt, Electrothermics and Metallurgy, II

N. J. Johnson, Industrial Electrolytic

C. W. Tobias, Theoretical Electrochemistry, I

A. J. deBethune, Theoretical Electrochemistry, II

ADVERTISING OFFICE

ECS
1860 Broadway, New York 23, N. Y.

ECS OFFICERS

W. C. Gardiner, President
Olin Mathieson Chemical Corp., Niagara Falls, N. Y.

R. A. Schaefer, Vice-President
The Bunting Brass and Bronze Co., Toledo, Ohio

Henry B. Linford, Vice-President
Columbia University, New York, N. Y.

F. L. LaQue, Vice-President
International Nickel Co., Inc., New York, N. Y.

Lyle I. Gilbertson, Treasurer
Air Reduction Co., Murray Hill, N. J.

I. E. Campbell, Secretary
National Steel Corp., Weirton, W. Va.

Robert K. Shannon, Executive Secretary
National Headquarters, The ECS, 1860 Broadway, New York 23, N. Y.

Manuscripts submitted to the Journal should be sent, in triplicate, to the Editorial Office at 1860 Broadway, New York 23, N. Y. They should conform to the Instructions to Authors, last published in the August 1959 issue, pp. 232C-233C. Manuscripts so submitted become the property of The Electrochemical Society and may not be published elsewhere, in whole or in part, unless permission is requested and granted by the Editor.

Inquiries re positive microfilm copies of volumes should be addressed to University Microfilms, Inc., 313 N. First St., Ann Arbor, Mich.

Journal of the

Electrochemical Society

NOVEMBER 1959 **VOL. 106 • NO. 11**

CONTENTS

Editorial

Science in the Newspapers 282C

Technical Papers

The Anodic Oxidation of Cadmium, II. Electrical Properties of the Film. *P. E. Lake and E. J. Casey* 913

The Oxidation of the Silver Electrode in Alkaline Solutions. *T. P. Dirkse* 920

Effect of Sodium Pyrophosphate on Polarization and Corrosion of Tin. *I. A. Ammar and S. Riad* 926

Thin Film Formation on Zirconium. *R. E. Meyer* 930

The Oxidation of Iron-Nickel Alloys, III. Kinetics of Oxidation of Three Commercial Alloys. *R. T. Foley and C. J. Guare* 936

Oxidation Studies on the Nickel-Chromium and Nickel-Chromium-Aluminum Heater Alloys. *E. A. Gulbransen and K. F. Andrew* 941

The Action of Nickel and Cobalt in Electroluminescent Zinc Sulfide Phosphors. *P. Goldberg* 948

Optical Properties of Tin- and Lead-Activated Calcium Metasilicate Phosphors. *R. W. Mooney* 955

Phase Equilibria and Manganese-Activated Fluorescence in the System $Zn_3(PO_4)_2$-$Mg_3(PO_4)_2$. *J. F. Sarver, F. L. Katnack, and F. A. Hummel* 960

Cadmium Sulfide Photoconductive Sintered Layers. *M. J. B. Thomas and E. J. Zdanuk* 964

The Nature of Alumina in Quenched Cyrolite-Alumina Melts. *P. A. Foster, Jr.* 971

A Study of the Iodide Niobium Process. *R. F. Rolsten* 975

Reactions in the Niobium-Hydrogen System. *W. M. Albrecht, W. D. Goode, and M. W. Mallett* 981

Some Investigations of the Ag/AgCl in LiCl-KCl Eutectic Reference Electrode. *L. Yang and R. G. Hudson* 986

The Oxygen-Evolution Reaction at Gold Anodes, II. Overpotential Measurements and Reaction Mechanism in Sulfuric Acid Solutions. *S. Barnartt* 991

Technical Note

The Formation of Carbides at the Interface of Liquid Germanium and Graphite. *A. Epstein and I. G. Geib* 995

Current Affairs **287C-297C**

Published monthly by The Electrochemical Society, Inc., from Manchester, N. H., **Executive Offices, Editorial Office** and **Circulation Dept.**, and **Advertising Office** at 1860 Broadway, New York 23, N. Y., combining the JOURNAL and TRANSACTIONS OF THE ELECTROCHEMICAL SOCIETY. Statements and opinions given in articles and papers in the JOURNAL OF THE ELECTROCHEMICAL SOCIETY are those of the contributors, and The Electrochemical Society assumes no responsibility for them. Nondeductible subscription to members $5.00; subscription to nonmembers $18.00. Single copies $1.25 to members, $1.75 to nonmembers.

Copyright 1959 by The Electrochemical Society, Inc.

Entered as second-class matter at the Post Office at Manchester, N. H., under the act of **August 24, 1912.**

Operator making a routine quality control test of type and resistivity on silicon characterization crystal.

Round-the-clock operations at new Du Pont plant assure you of ample supplies of Hyperpure Silicon

Du Pont's new Brevard, N. C., HYPERPURE Silicon plant—with a 70,000 lbs./yr. capacity—is now operating at high production rate to assure you of a prompt supply of high-purity silicon in the form, grade and quantity you need. Du Pont is uniquely qualified to serve you because of its experience as pioneer producer of semiconductor grades of silicon. This experience includes installing the first full-scale commercial silicon plant in the world and frequent expansion of productive facilities since then.

Single crystals of Du Pont HYPERPURE Silicon are now available in a wide range of resistivities, thanks to Du Pont's new research and manufacturing techniques. Each has a specially prepared "spec. sheet."

Here's more news: Du Pont recently completed a $3,000,000 Technical Service Laboratory specifically designed, equipped and staffed to handle customer problems. Here, highly trained Du Pont Technical Specialists are available to discuss any difficulties in crystal growing or manufacture you may encounter.

Du Pont HYPERPURE Silicon is also available in densified cut rods . . . and rods specially designed for float-zone refining in Grades 1, 2 and 3, with carefully controlled purity levels. As an additional service, Du Pont offers doping material at no additional cost.

Free booklet is available upon request. It describes the manufacture, properties and uses of HYPERPURE Silicon. E. I. du Pont de Nemours & Co. (Inc.), Pigments Dept., Silicon Development Group, Wilmington 98, Delaware.

HYPERPURE SILICON

DU PONT

REG. U.S. PAT. OFF.

BETTER THINGS FOR BETTER LIVING
. . . THROUGH CHEMISTRY

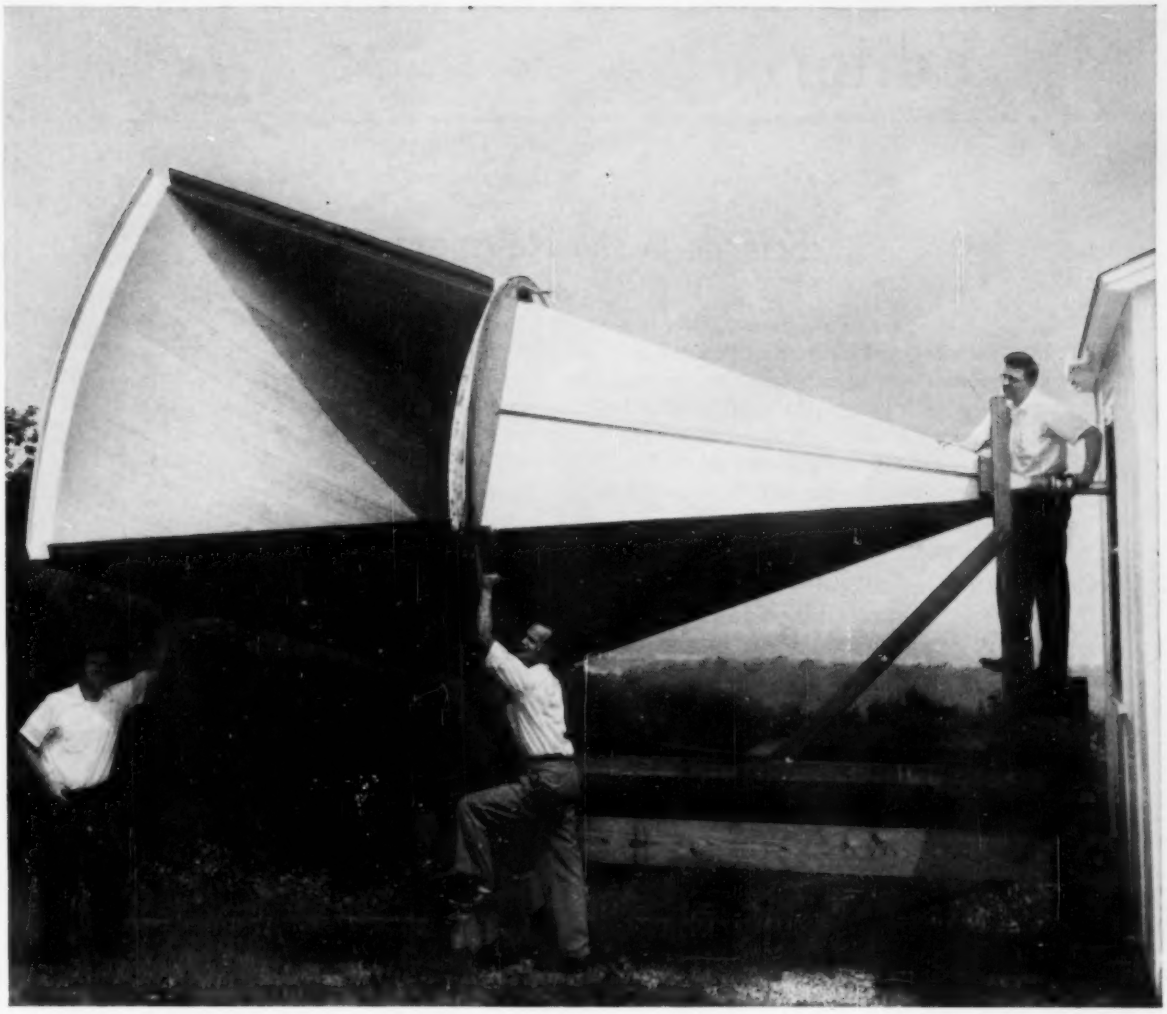

At Bell Laboratories, Holmdel, N. J., a horn reflector antenna is beamed skyward by scientists Edward Ohm, David Hogg and Robert DeGrasse. The maser amplifier, which employs a ruby cooled in liquid helium, is inside building at right. Over-all "noise" temperature of antenna, amplifier and sky is only 18°K at 5600 megacycles.

ANOTHER STEP TOWARD SPACE COMMUNICATIONS

The above antenna is part of a new ultra-sensitive radio receiving system under development at Bell Telephone Laboratories. It has extraordinary directivity. Beamed skyward, it ignores radio "noise" from the earth, yet picks up extremely weak signals from outer space.

The signals are amplified by the latest Bell Laboratories "maser" amplifier. The maser principle was first demonstrated, using gas, by Prof. C. H. Townes and his collaborators at Columbia University. Bell Laboratories scientists applied it to the solid state guided by a theoretical proposal of Prof. N. Bloembergen of Harvard University. Their latest traveling wave maser amplifier employs a ruby mounted in a waveguide. The ruby is excited to store energy. As signals pass through, they absorb this energy and are thus amplified. The device uniquely combines the characteristics needed for practical space communication: extremely low inherent noise and the ability to amplify a broad frequency band.

At present the receiving system is being used to pick up and measure minute radio noise generated by the atmosphere. It also foreshadows important advances in long distance communications. For example, it could extend the range of space-probe telemetering systems, could help make possible the transatlantic transmission of telephone and TV signals by bouncing them off balloon satellites—and has numerous applications in radio astronomy and radar.

This pioneer development in radio reception is one more example of the role Bell Laboratories plays in the pursuit of better communications technology.

BELL TELEPHONE LABORATORIES

WORLD CENTER OF COMMUNICATIONS RESEARCH AND DEVELOPMENT

Editorial

Science in the Newspapers

LAST January, this page carried a brief review of a report issued by the National Association of Science Writers, which indicated that the public would like more news about scientific findings, more fully and accurately written. NASW has tried to improve the quality of science news coverage in the press, by insisting that it should be handled by properly trained reporters who are given adequate time to do each assignment well. The Association must have been startled to see two newspaper stories which were given prominent display last August.

The first was the story of a fuel cell, and was distributed by Associated Press. It featured a picture of the inventor with a model cell capable of powering a two-ton fork-lift truck, with the caption: "NEW WAY TO MAKE ELECTRICITY — Francis T. Bacon in London yesterday with his invention which makes electricity by reversing the chemical process of storage batteries." The text explained further: "The cell produces electricity by combining gaseous hydrogen and oxygen. It yields water as an exhaust product. In batteries, power is obtained by splitting water into hydrogen and oxygen."

The rest of the story was scientifically plausible and, in fact, gave the impression of being written by a reporter with some training in science, who perhaps thought it unimportant to check in a reference book. What is incredible is that a garbled report should go through the editorial offices of AP and many prominent newspapers without adequate surveillance. Should the Press Associations be forced from outside to improve their methods, and, if so, by whom? One learns to take all newspaper stories with considerable skepticism, but it is disconcerting to find fundamental errors in an article which does not need to be rushed to the presses, and which will be read by students and others to whom it is confusing and misleading.

The second story was not primarily a science item, but does have a certain amount of scientific interest. It concerned a tragedy in a New Jersey jail, in which one prisoner was burned to death, seven others died of smoke suffocation, while other prisoners and several firemen were injured. The explanation offered for the origin of the fire was truly a novel one. A prisoner who was arrested on a drunk and disorderly charge on Friday became quite violent and apparently remained seriously disturbed. On Sunday he was given a cup of "highly flammable liquid tranquilizer" to "calm him down." At the same time, a "trusty" (also being held on a drunk and disorderly charge) gave the prisoner a lighted cigarette (strictly against the rules). The story adds that a detective soaked a rag in some of the tranquilizer solution to show that a match could ignite it.

We can think of only one flammable liquid tranquilizer, and that must be near 100-proof to burn easily. Waiter, some soda with the tranquilizer, or mix it with vermouth and shake it with ice. Seriously, shouldn't certain New Jersey reporters and editors become really inquisitive about what goes on in the jails, and pass their findings on to the public?

—CVK

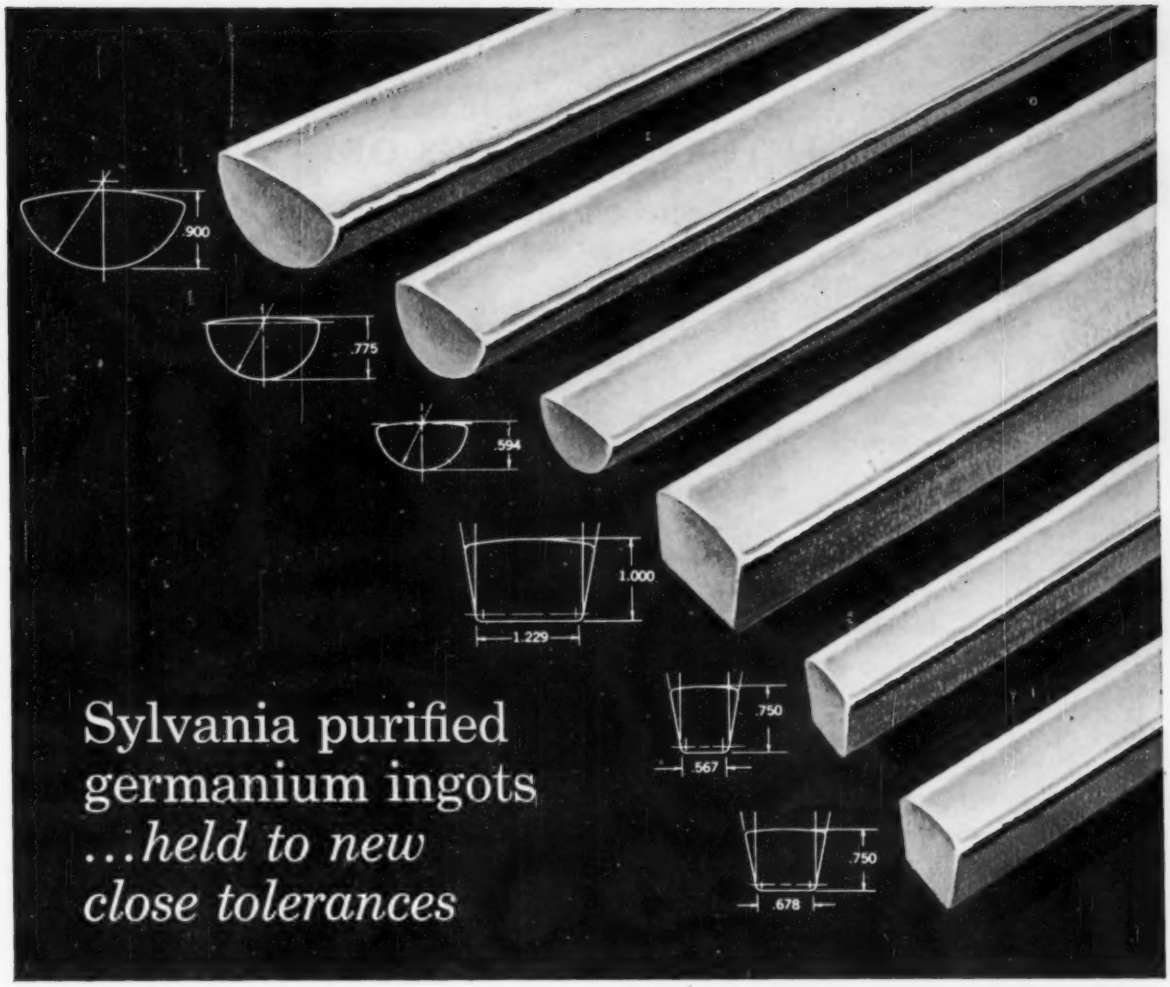

...new dimensions for precise crystal growing

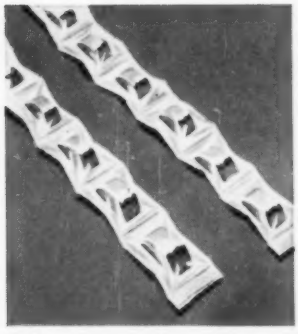

Sylvania germanium pieces, cut to specific size and weight for vertical crystal growing.

THROUGH THE YEARS, from early experimental projects to the place Sylvania now occupies as prime suppliers of as-reduced and purified germanium . . . Sylvania has constantly worked to provide ingots with the maximum yield potentials in single crystals.

Sylvania is now equipped to supply germanium ingots to the closest dimension-tolerances ever achieved. Shown here are the six standard shapes which fill practically every requirement. In each case, the dimensions are held to a new order of precision.

These new precise dimensions result in even melting, less shrinkage and almost negligible surface drop . . . all important factors in preventing waste through polycrystalline formation. You'll find that the unit cost of doped single crystals is lower too.

Special shapes of ingots can of course be supplied to your order if required, and users of the vertical growing method will like Sylvania germanium cut to specific size and weight. These pieces can be used as received, without processing.

Since Sylvania controls germanium purity from ore to ingot, you can't obtain better material. We'll be glad to send you a new technical bulletin on Sylvania germanium ingot dimensions, showing the new sizes, shapes and tolerances.

SYLVANIA GENERAL SYSTEM

Subsidiary of
GENERAL TELEPHONE & ELECTRONICS

Sylvania Electric Products Inc.
Chemical & Metallurgical Div.
Towanda, Penna.

FUTURE MEETINGS OF
The Electrochemical Society

Chicago, Ill., May 1, 2, 3, 4, and 5, 1960

Headquarters at the Lasalle Hotel

Sessions probably will be scheduled on

Electric Insulation (including a symposium on "Electrolytic Capacitors"),

Electronics (including Luminescence and Semiconductors),

Electrothermics and Metallurgy (including a symposium on "High-Purity Vanadium" and a round table on "Methods of Reducing Iron Ores"), Industrial Electrolytics, and Theoretical Electrochemistry

★ ★ ★

Houston, Texas, October 9, 10, 11, 12, and 13, 1960

Headquarters at the Shamrock Hotel

★ ★ ★

Indianapolis, Ind., April 30, May 1, 2, 3, and 4, 1961

Headquarters at the Claypool Hotel

★ ★ ★

Detroit, Mich., October 1, 2, 3, 4, and 5, 1961

Headquarters at the Statler Hotel

Papers are now being solicited for the meeting to be held in Chicago, Ill., May 1-5, 1960. Triplicate copies of each abstract (*not exceeding 75 words in length*) are due at Society Headquarters, 1860 Broadway, New York 23, N. Y., *not later than January 4, 1960* in order to be included in the program. *Please indicate on abstract for which Division's symposium the paper is to be scheduled, and underline the name of the author who will present the paper.* Complete manuscripts should be sent in triplicate to the Managing Editor of the JOURNAL at 1860 Broadway, New York 23, N.Y.

Germanium *and other semiconductors from* **EAGLE-PICHER**

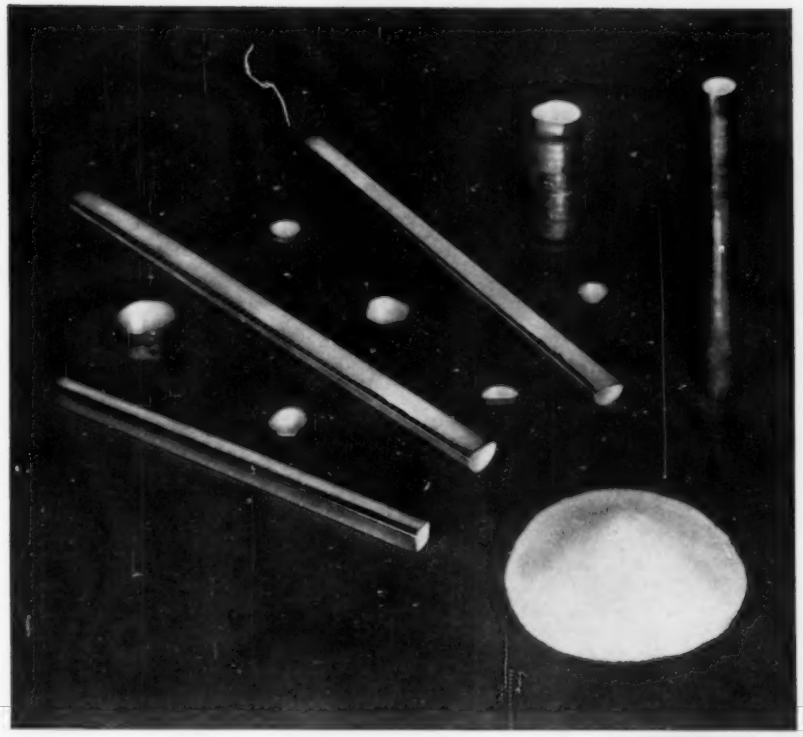

Eagle-Picher Rare Metals and Semiconductors

GERMANIUM DIOXIDE, minimum purity 99.999%.

FIRST REDUCTION GERMANIUM METAL, minimum resistivity 5 ohm-cm.

INTRINSIC GERMANIUM METAL, minimum resistivity 40 ohm-cm.

SINGLE CRYSTAL GERMANIUM [undoped] minimum resistivity 30 ohm-cm.

SINGLE CRYSTAL GERMANIUM [doped] to customers' specified resistivity.

SPECIAL SHAPES, INTRINSIC GERMANIUM METAL, for horizontal or vertical crystal growing. Wide variety in stock, other shapes furnished to customers' specifications.

SCRAP GERMANIUM PLAN, scrap Germanium may be returned for economical reprocessing under a toll arrangement.

— also immediately available

CADMIUM SULFIDE

GALLIUM, ultra pure.
Metallic crystals, minimum purity 99.9999%.
Metallic crystals, minimum purity 99.999%.

GALLIUM SESQUIOXIDE

Eagle-Picher, pioneer in Germanium, is an acknowledged leader in dependable production to meet the precise demands of the semiconductor industry. We offer a complete line of Germanium products and in addition, reprocess customers' *scrap Germanium* under our new low-cost toll arrangement.

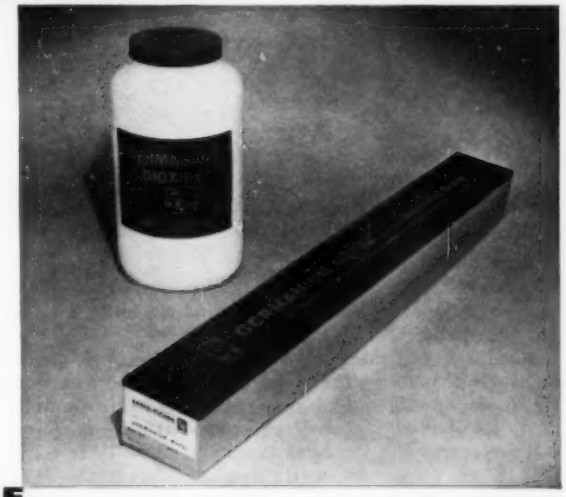

FREE! An interesting, new brochure, "EAGLE - PICHER GERMANIUM" is now available. Write for your copy today.

EAGLE EP PICHER

Since 1843

THE EAGLE-PICHER COMPANY

Chemical Division, Dept. JES 11

GENERAL OFFICES: CINCINNATI 1, OHIO

Conn produces the "heart" of good tone quality by electrodeposition, with "Plus-4" Copper Anodes

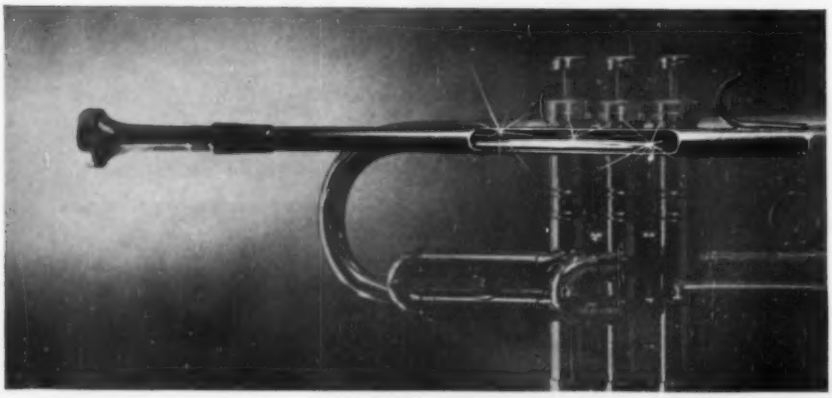

CONN ELECTRO-D TONE CHAMBER (mouthpipe) cut away to illustrate the "micro finish" interior surface. Chamber and mouthpiece receptacle are formed in one piece by electrodeposition; previously the two pieces were soldered together. (Patent pending.)

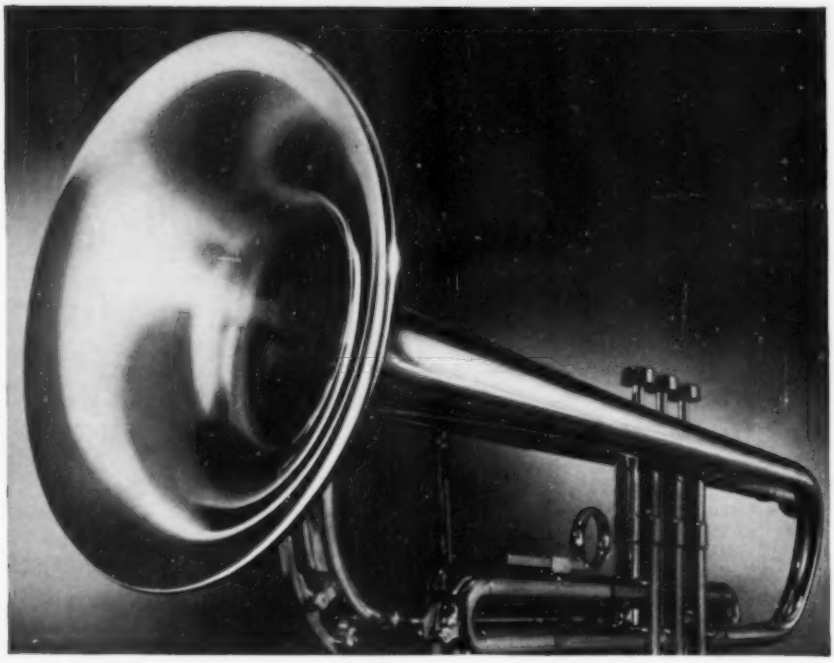

ELECTRO-D BELL, also formed by electrodeposition.

In a cornet or trumpet, good tone and easy playing depend largely on the inside shape and finish of the tone chamber (mouthpipe).

Aiming at perfection, C. G. Conn, Ltd., famous maker of band instruments, turned to forming these critical parts by electrodeposition of copper on stainless-steel mandrels. The deposited copper conforms perfectly to the precision mandrel—providing the exact taper and dimensions every time. It also gives the smooth mirrorlike inside surface that prevents acoustical losses. Even minor irregularities caused by forming sheet metal or tube can muffle, distort, or rattle the tone.

Using "Plus-4" Phosphorized Copper Anodes in its acid-copper electroplating tanks, Conn has found it gets the smooth, dense deposit it needs. The build-up of metal is fast and uniform, as "Plus-4" Anodes' extra "throwing power" is of particular value with the tubular shapes. There are few nodules, which minimizes finishing of the outside surface. And tank maintenance is simplified.

Conn also forms the bells used in cornets, trumpets, and trombones electrolytically. This gives still further control in the precision of the entire inside tone columns of its instruments—for increased resonance and live, powerful tone.

WRITE FOR INFORMATION on how you can obtain a test quantity of "Plus-4" Anodes to supply one tank. Address: The American Brass Company, Waterbury 20, Conn. In Canada: Anaconda American Brass Ltd., New Toronto, Toronto 14, Ontario.

59108

ANACONDA®

"PLUS-4"® ANODES Phosphorized Copper

Made by The American Brass Company

The Anodic Oxidation of Cadmium

II. Electrical Properties of the Film

Phyllis E. Lake and E. J. Casey

Defence Research Chemical Laboratory, Defence Research Board, Ottawa, Ontario, Canada

ABSTRACT

Cadmium electrodes under anodic oxidation in hydroxide and carbonate electrolytes have been examined by analysis of the decay of overpotential after current interruption.

After passivation while oxygen is being evolved, except for a small instantaneous (<1 msec) ohmic drop, the potential decays logarithmically with time in the manner usually found for the decay of activation overpotential of a gas electrode. Before passivation while the metal is actively being oxidized, however, except for the small ohmic drop, the potential decays exponentially with time in two steps. This behavior is not described by activation theory.

Determinations were made of the capacitance of both the oxidizing and the passivated cadmium, both from potential decay curves and from superimposed a.c. All the a-c values correspond to those of a normal double layer, as do those obtained from decay measurements after passivation has occurred. However, the values obtained from decay curves before passivation are two orders of magnitude higher early in the oxidation but drop rapidly toward the a-c values as oxidation proceeds.

It is proposed that next to the Helmholtz double-layer at the CdO-electrolyte interface, there exists a highly polarized inner double-layer in which the reaction $OH^- \rightarrow O^= + H^+$ takes place. When the field strength across the inner double layer becomes high enough for the reaction $OH^- \rightarrow OH + e^-$ to take place instead, oxygen is evolved and the electrode passivates.

The roles of adsorption of OH^- to form the Helmholtz layer and of interference by $CO_3^=$ are discussed in terms of the results.

In a previous paper (1) experimental observation of the anodic oxidation of cadmium in basic solutions was described, and on the basis of the results a general mechanism for the formation of the anodic film was proposed. Two important features of the reaction were recognized: first, conduction of ions must occur through the solid layer of primary reaction product;[1] and second, there exists a rather critical reaction in which the primary reaction product (essentially CdO) is converted to a secondary product [$Cd(OH)_2$ in pure KOH] at a rate which is strongly dependent on electrolyte composition and other experimental conditions. The conversion takes place through the liquid phase. The nature of the cadmium in this phase has since been shown (14) to be $Cd(OH)_4^=$. The purpose of the present work was to investigate the electrical properties of the underlying layer of primary reaction product, and to determine which electrical property is in fact responsible for anodic passivation.

Experimental Method

The samples of cadmium for oxidation were prepared as described previously (1). The test cell was a rectangular lucite box (5 cm long x 3 cm wide x 5 cm high) of which the cadmium anode and nickel cathode formed the ends.

[1] Since the preparation of the present paper, the definitive work of Dr. Croft has appeared (17), in which he found strong evidence (from an entirely different experimental approach involving verification of the laws of film growth) to support the existence of solid-state conduction of ions through reaction product.

Part of the cadmium metal area was covered with stop-off lacquer, which left a square working area of 2.54 cm on a side. The electrode was cleaned in nitric acid and pre-reduced, as described in the earlier work (1).

The potential of the working electrode was measured against a cadmium reference electrode, a piece of charged negative plate from a sintered-plate nickel-cadmium battery chosen because of its large surface area as well as its good voltage stability. Decay curves were recorded on an instrument with an input resistance of at least 10^8 ohms. The open-circuit potential of the electrolytically reduced cadmium test electrode was 0 ± 5 mv. No junction potentials existed in any of the experiments with this arrangement.

Several times during each oxidation experiment the current was interrupted and the decay of the total overpotential η recorded. Two methods were used: (A) Decays of up to 100 msec were displayed on a Tektronix 535 Oscilloscope equipped with type 53/54C preamplifier (input resistance 10^6 ohms), and photographed. Reference voltages were displayed on each trace. (B) Decays up to 5 sec were recorded on a Brush Recording Oscillograph No. BL902, with auxiliary amplifiers (input resistance 1.5×10^8 ohms). Typical voltage traces are shown in Fig. 1(a). Voltages and times were conveniently read off the oscilloscope photographs after enlargement to 8 x 8 in. through a microfilm reader whose

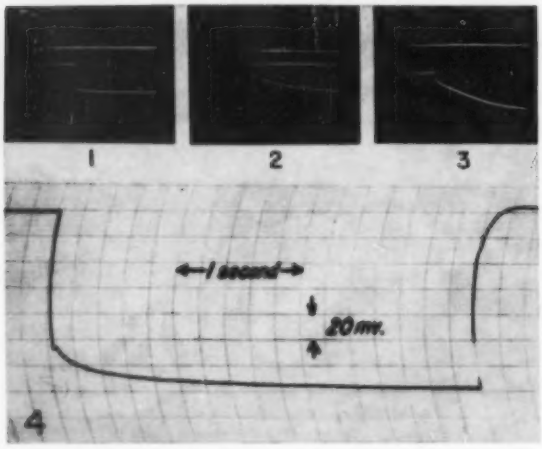

Fig. 1a. Photographs of decay curves, overvoltage vs. time: 1, 2 and 3—oscilloscope traces of curves of type (i), (ii), and (iii). Total sweep 100 msec. (Different vertical scales). 4—oscillograph trace of curve of type (ii). Total decay time 3.4 sec; 200 mv full scale.

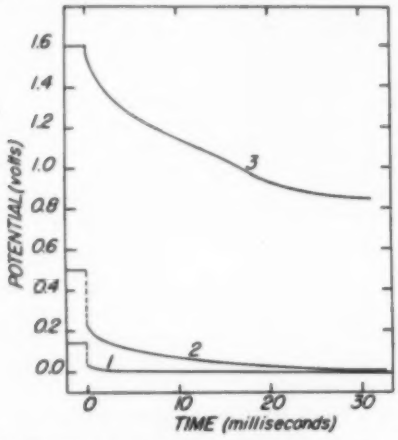

Fig. 1b. Decay curves after transposition (see text): 7.2N-KOH, 0°C, 3.83 ma/cm². For 1, 2, and 3, t/t_p = 0.1, 0.7, and 1.1 respectively.

face plate was equipped with a 2 mm grid; and off the Brush charts through a small hand lens. Figure 1(b) shows the transposed traces.

In addition to measurements of the decay of total overpotential, during several of the oxidation experiments a-c impedance measurements were made using an ESI Model 250 Impedance Bridge. Because of the very high capacitances per unit area of the electrodes, it was necessary to reduce the electrode area to ~1 mm² for these experiments. The error in area thus is appreciable, and this is taken into account in the discussion.

Experiments were done mostly at 25°C, but some were done at O° and −20°C. KOH concentrations ranged from 0.72-14.4*N*; and K_2CO_3 concentrations from 0.72-7.2*N*. Oxidation current densities were from 1-15 ma/cm².

Analysis of Decay Curves

The decay curves recorded fell into one of three general types (i) and (ii) before passivation, and (iii) after passivation:

(i) *Resistive decay.*—In all cases during the early stages of the oxidation, and also for longer periods, either in highly concentrated solutions or at low temperatures, the decay consisted principally of an instantaneous (<1 msec) drop plus a very small further decay to a value assymptotic to the open-circuit potential. Other than the determination of the magnitude of the initial drop, no analysis was attempted.

(ii) *Compound decay.*—Throughout most of the oxidation when $t < t_p$, [t_p is time at which passivation occurs (1)], the decay curve after current interruption consisted of an instantaneous drop, followed by a smooth exponential (log E vs. t) decay, which finally went over into a small and slow activation overpotential-like decay toward the open-circuit potential. The form of the tail end of the curve is discussed more fully later.

A plot of the experimental values of η and t, obtained from the oscilloscope trace, as log E vs. t ($E = \eta - E_\infty$, where E_∞ is the voltage to which the E has dropped after "infinite" time), it was possible to extrapolate the straight line back to zero time and obtain the value of E just at the instant of current interruption (henceforth called E°_{DL}). Thus it was possible to separate the rapid condenser-like decay from the resistive decay. From the slope of the log E vs. t curve, the value of E°_{DL} and the value of the current density before interruption, an apparent capacitance was calculated.

Inertia of the oscillograph pen rendered unreliable the voltages observed in the first 100 msec after current interruption. Values at $t > 100$ msec were quite reliable, but since voltages were small, and the reading error significant, no firm conclusions could be drawn from these results. It was apparent, however, that the curve changed form in the region of 200 msec and that the initial part of the curve was indeed a continuation of the log E vs. t decay observed on the oscilloscope. The latter part of the curve could be accounted for quite well as either a second slower log E vs. t decay, or as an E vs. log $(t + \theta)$ decay. The voltage obtained by extrapolation of the straight line to zero time (henceforth called E°_{act}), and the calculated capacitances were of the same order for both methods.

(iii) *Activation overpotential decay.*—After passivation, the decay curve was of a different form: a very small instantaneous drop was followed by a long activation overpotential-like decay [i.e. $\eta \propto \log (t + \theta)$; see ref. (4) and (8)], with no evidence of the condenser-like decay. In this respect the decay was normal for that following gas discharge at an electrode. Thus, a plot of the experimental values as η vs. log $(t + \theta)$ permitted graphical separation of the resistive drop from the activation overpotential ($E_{act(O_2)}$) decay. From the slope of the latter decay ($-b$), the value used for θ, and the current density before current interruption, the associated double-layer capacitance was obtained.

Results and Discussion

Components of η°

Concentration overpotential was not considered to be a significant factor determining the course of

the oxidation reaction partly because a log η vs. t relationship for the decay of a concentration polarization would demand that the concentration change as log log c vs. t, which seems most unlikely (10); and partly because values for concentration polarization estimated by Glasstone's method [see ref. (9)] were found to be <1% of η° at 20°C in the highly conducting alkaline solutions under study.

The activation overpotential-like decay at the tail of the decay curves (i.e., between 200 msec and 5 sec) obtained before passivation was small, not very reproducible, and difficult to analyze. An extrapolation of E_{act} to zero time gave the value of E°_{act}, which was between 5 and 20 mv over all the conditions studied. Theta (θ) values and Tafel b values varied considerably from run to run, but with no systematic variation: $0.01 < \theta < 0.6$ sec; $0.005 < b < 0.013$ v per decade of time. Capacitances calculated were always high, the values ranging from 10^4 to 10^5 μfd/cm^2, not unlike those observed on the nickel hydroxide electrode (5) and on some dry, compound oxides (7). Since E°_{act} consistently provided only a small fraction of the total η°, the values obtained need not be discussed further. As mentioned already, a plot of log E_{act} vs. t, actually favored on theoretical grounds for $\eta < 20$ mv, was also linear, and the capacitances obtained were of the same order of magnitude as those obtained from the E vs. log $(t + \theta)$ plot. Similar high values of capacitance at the tail end of decays of cathodic overpotential have been observed and attributed to "the last stages of desorption" (13).

Thus the major portion of the total overvoltage before passivation is made up of a resistive component which decays instantaneously and a capacitive component which decays rapidly and exponentially. Since current must be carried through the underlying CdO film by ions, the resistive part of the decay is assumed to be due to ionic resistance and is referred to as IR_i. Because: (a) Grahame's (4) theory of the capacitance of the electrical double layer predicts a linear log E vs. t plot during decay if forward and backward reactions are of nearly equal magnitude; and (b) in any case, a leaky condenser of fixed dimensions has this type of voltage

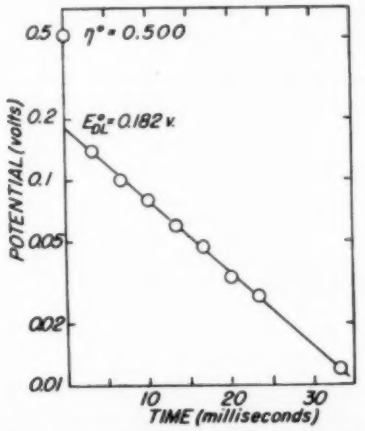

Fig. 2. Analysis of exponential part of decay curve; log $(\eta - E_e)$ vs. t.

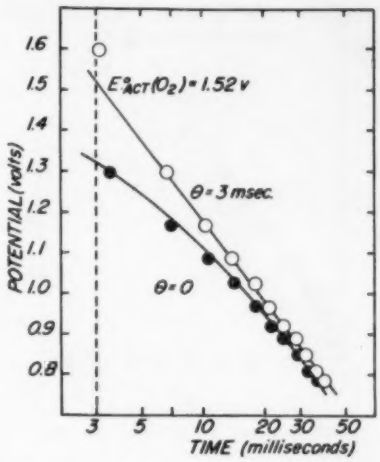

Fig. 3. Analysis of activation overpotential decay after passivation; η vs. log $(t + \theta)$.

decay and later in the paper is considered to be associated with the double-layer in a particular manner: the capacitive part is referred to as E_{DL} during decay or E°_{DL} just at current interruption. Figure 2 illustrates the method used to determine IR_i and E°_{DL} from a particular decay curve.

After passivation the resistive drop was small, there was no evidence of a condenser-like decay, and most of η° was made up of activation overpotential $E^\circ_{act(O_2)}$ associated with oxygen evolution. The small resistive component is thought to be due to only fair electronic conduction across the CdO film and is referred to as IR_e. Figure 3 illustrates the separation of these two components. Since the decay curves of type (iii) follow the theoretical plot for the decay of activation overpotential so rigorously, E°_{DL} after passivation must either (a) be very small compared to $E^\circ_{act(O_2)}$, or (b) refer to the same process and therefore be inseparable from $E^\circ_{act(O_2)}$.

Table I contains the results of determinations of the various components of η° at various times during two experiments, one in KOH and the other in K_2CO_3, both at 7.2N.

Table I. η° and its components during oxidation

Relative time, t/t_p	IR_i, v	E°_{DL}, v	C, μfd/cm^2	IR_e, v	$E^\circ_{act(O_2)}$, v	η°, v
7.2N-KOH, 0°C, 3.83 ma/cm^2; t_p = 26 min						
0.1	0.1	0.015	2850	—	—	0.12
0.7	0.3	0.047	1500	—	—	0.36
0.9	0.32	0.18	245	—	—	0.51
1.1	—	—	54*	0.1	1.7	1.9
* θ = 4 msec; b = 0.65 v/decade of time.						
7.2N-K_2CO_3, 0°C, 3.83 ma/cm^2; t_p = 22 min						
0.3	0.06	0.04	3600	—	—	0.13
0.6	0.16	0.09	2300	—	—	0.25
0.8	0.38	0.62	333	—	—	1.1
0.9	0.50	0.84	300	—	—	1.4
1.1	—	—	126*	0.17	2.0	2.2
* θ = 5 msec; b = 0.35 v/decade of time.						

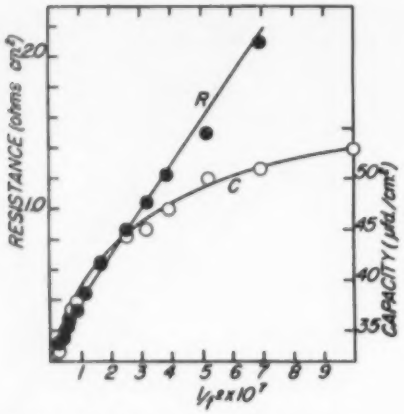

Fig. 4. Variation of series resistance and capacitance with $1/f^2$ for electrode passivated in 7.2N K_2CO_3 at room temperature at 1 ma/cm².

From the results, which are typical of analyses of current interruptions of oxidations at three temperatures, four concentrations, three current densities, and for both KOH and K_2CO_3, it is apparent that the approximate description of the total overpotentials of active (η°_A) and passive (η°_P) cadmium are given by:

$$\eta^\circ_A = IR_i + E^\circ_{DL}$$

$$\eta^\circ_P = IR_e + E^\circ_{act(O_2)}$$

At the moment of passivation then

$$IR_i + E^\circ_{DL} = IR_e + E^\circ_{act(O_2)}$$

and the problem reduces to interpreting E_{DL} and formulating a self-consistent mechanism which permits the transition from cadmium oxidation to oxygen evolution when passivation sets in. Consideration must first be given to capacitance measurements.

Capacitance Measurements

After Passivation: The passivated surface ($t/t_p > 1.0$) is the simplest and will be considered first. The a-c measurements made at 1000 cps during flow of oxidizing current gave values 36-180 μfd/cm²; the values were generally larger the larger the current density used to passivate the electrode. Capacitances determined from the decay of activation overpotential $E_{act(O_2)}$ from $C = 2.3\ i\theta/b$ were about the same, 50-500 μfd/cm². Since Grahame (6) found that double layer capacitances on clean mercury surfaces range up to 40 μfd/cm², a surface roughness factor of 1-5 is suggested for CdO underlayers after the electrodes have been passivated.

Frequency dependence of the series capacitance C_s and resistance R_s associated with the passivated surface also was measured from 1000-6000 cps while current was flowing. Since $R_P^2C_P^2\omega^2 >> 1$, both R_s and C_s should be linear functions of $1/f^2$ if the equivalent circuit for the electrode can be expressed as a pure R and C in parallel. The R vs. $1/f^2$ plot (Fig. 4) was linear, but the C vs. $1/f^2$ plot seems to approach a limiting value at the lower frequencies. Thus abnormally high capacitances at low frequencies are not indicated. Randles (15) found an inverse 0.5 power dependence of double layer capacitance on frequency from 60-1100 cps on clean amalgam electrodes. However, the frequency dependence of C_s on passivated cadmium surfaces studied here follows more closely an inverse 0.28 power dependence (determined from a plot of log C_s vs. log f from 1000-6000 cps) and is not interpretable at present. This property needs further study.

Before Passivation: At times before passivation, the a-c bridge capacitance C_s of the actively oxidizing metal was essentially constant throughout the oxidation, and on any one specimen the capacitance was the same before passivation as after (Table II). Hence there seems to be no essential difference in the composition and dimensions of the Helmholtz double layer before and after passivation.

In contrast, the capacitances obtained from the decay of E_{DL} were two orders of magnitude higher than the a-c values early in the oxidation, but dropped rapidly during the oxidation until at 0.9 t_p they were within a factor of two or three of the a-c values (Table II). [It is recalled that these values result from the experimental fact that the early part of the decay follows a log E vs. t plot, a decay which is far too rapid and with too much curvature to be accountable in terms of concentration polarization in the outer film (10).] The high initial values and the rapid fall of C as oxidation proceeds, the concurrent rapid rise in parallel resistance, and the results of a-c capacitance measurements suggest that the system is one which contains an inner or "crystal" (16) double layer structure in series with the normal Helmholtz double layer: and further that the inner double layer has relatively fixed dimensions and is capable of severe polarization [high dielectric

Table II. Capacitance of cadmium electrode during oxidation. 7.2N K_2CO_3, 25°C.

	From decay curves				a-c Impedance bridge							
					1000 cps				3000 cps			
t/t_p	1 ma/cm²		5 ma/cm²		1 ma/cm²		5 ma/cm²		1 ma/cm²		5 ma/cm²	
	C	R	C	R	C_s	R_s	C_s	R_s	C_s	R_s	C_s	R_s
0	—	—	—	—	51	2.6	—	—	—	—	56	0.17
0.01	5400	6.7	—	—	—	—	—	—	—	—	—	—
0.1	—	—	2700	9.7	50	3.3	74	1.7	26	0.83	60	0.45
0.3	—	—	1200	97	50	3.3	—	—	—	—	—	—
0.5	500	45	500	227	49	2.9	—	—	—	—	—	—
0.9	200	240	—	—	49	2.6	71.2	2.0	28	0.76	—	—
1.1	37	—	46	—	50	2.5	84	1.7	27	0.70	56	0.38

constant (12)] early in the oxidation. Since the inner structure is in series with, and has a capacitance larger than, the outer, it is the latter only which is detected in the a-c measurements. The model which has been most useful in describing qualitatively the experimental results is shown in Fig. 5, and a brief description of a possible mechanism of oxidation, based on this model, follows:

Following reduction prior to the oxidation experiment, the cadmium metal has a double layer due to adsorbed OH^- ions. With the first passage of current, OH^- is activated by removal of H^+ (i.e., $OH^- \rightarrow O^= + H^+$) and a cadmium ion in an active site loses its electrons and forms a CdO "molecule" attached to the surface. This process continues until a monolayer is built up, after which cadmium ions penetrate through the CdO layer to the oxide-electrolyte interface where the film-formation reaction takes place. The Helmholtz double layer then exists at the oxide-electrolyte interface. As the film thickens, after activation oxide ions are in the oxide film, i.e., chemisorbed, forming with the adsorbed OH^- an inner or crystal double layer. When the film is thin, capacitance is high because polarization of $O^=$ is high. As the film grows thicker, and $O^=$ ions diffuse into the film, the field strength (v/cm) across the crystal double layer drops, the dielectric constant decreases, and the capacitance drops. The model suggests that early in the oxidation the slowest step is activation; as film thickens, transport of ions across the film becomes equally slow.[8] Meanwhile the conversion reaction of CdO through soluble complex to $Cd(OH)_2$ or $CdCO_3$ proceeds at the oxide electrolyte interface, gradually building up an outer film, loosely adherent and porous. The activity of OH^- is high enough that the rate of conversion is never transport controlled by ions in solution.

This model accounts for the fact that the impedance bridge methods measure the smaller of the two capacitances in series, in this case the outer double layer. Interruption of the oxidizing current gives a decay of overpotential of which the chief component is the voltage across the inner double layer, whose charge leaks away exponentially with time because of the fixed dimensions.

[8] This point now seems to have been proven by Croft (17).

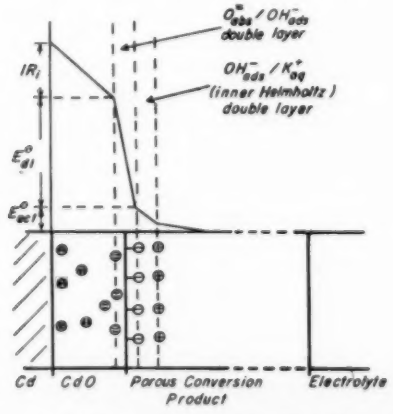

Fig. 5. Model of oxidizing electrode.

Table III. Rate of change of η° and its components with experimental variables

	d/dI	d/dc	d/dT	d/dt, $t < t_p$	d/dt, $t > t_p$
η°	+	−	−	+	+ small
R_i	+	−	−	+	−
R_e	U	U	−	NM	− small
E°_{DL}	0	−	−	+	NM
C°_{DL}	0	0	−	−	0
E°_{act}	0	NM	U	U	NM
$E^\circ_{act(O_2)}$	+	−	+	NM	+ small
E°_{CP}*	+	−	−	0	0

I, current density; T, temperature; c, concentration of KOH or K_2CO_3; t, time; U, unknown; NM, not measurable; +, positive; −, negative; and 0, nil.
* Rates of change assumed, not measured.

Toward t_p the surface charge of OH^-, which is current dependent, drops off because the film of conversion product closes over near the CdO surface, slows down the escape of complex through the inner Helmholtz double layer, and thus introduces a barrier to OH^- adsorption. The charge separation across the inner double layer increases rapidly until the field strength becomes high enough to remove electrons from OH^- to produce OH and ultimately O_2.

The model suggests further that before passivation E_{DL} decays by $Cd^{++} + O^= \rightarrow CdO$, or by $H^+ + O^= \rightarrow OH^-$ at the $O^=$ site (i.e., without change of dimensions) at a rate which depends on the first power of the concentration of $O^=$; this leads directly to the log E vs. t behavior observed during decay. After passivation, the decay is essentially that of adsorbed OH and/or O, similar to oxygen overpotential decay on a noble metal surface, where complicating films are absent.

Results of Changing Experimental Conditions

Before passivation: Table III is a summary of trends observed from the results of determination of the components of overpotential as a function of current density, electrolyte concentration, temperature, and oxidation time. Detailed examination of this table will reveal that the qualitative facts contained are consistent with the model proposed. Although the details of the results need not be discussed here, it is useful to examine the changes with experimental conditions of the major components involved in the passivation, viz., E°_{DL}, IR_i, and $E^\circ_{act(O_2)}$. Thus Fig. 6a and 6b show how E°_{DL} and IR_i build up as oxidation proceeds toward t_p in KOH and K_2CO_3. Figure 7 shows how E°_{DL} varies with time with increasing concentration of KOH. The value of E°_{DL} remains low until t approaches t_p and then climbs rapidly. It is thus this component which is responsible for the increased potential which ultimately liberates oxygen. At high KOH concentrations the rate of the conversion reaction is higher, and the surface charge density of OH^- remains high longer; hence E°_{DL} has a lower value in the higher KOH concentrations for the same number of coulombs passed. The fact that dE°_{DL}/dI is zero is further support that E°_{DL} is not a common polarization.

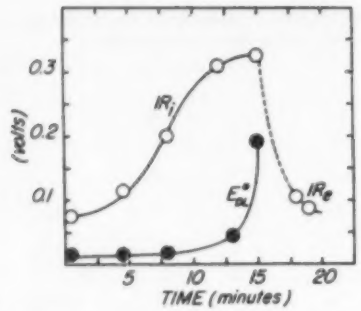

Fig. 6a. Variation of IR_i and $E°_{DL}$ with time, 7.2N KOH, 0°C, 3.83 ma/cm².

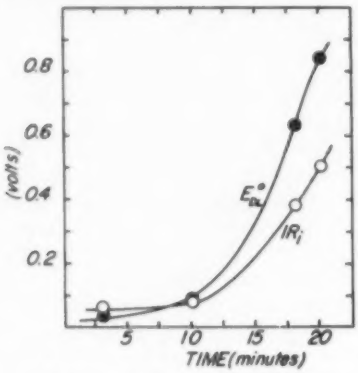

Fig. 6b. Variation of IR_i and $E°_{DL}$ with time, 7.2N K_2CO_3, 0°C, 3.83 ma/cm².

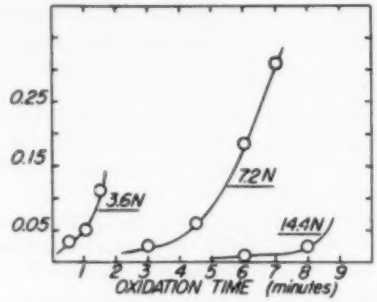

Fig. 7. $E°_{DL}$ vs. time for three concentrations of KOH, 25°C, 7.66 ma/cm².

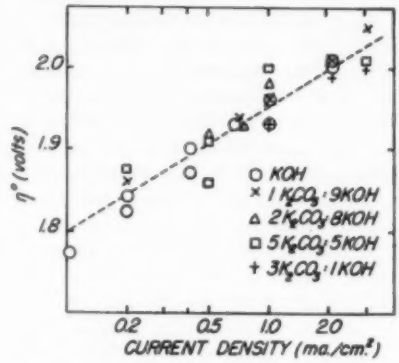

Fig. 8. $\eta°$ vs. log I for electrodes passivated and evolving oxygen in KOH and K_2CO_3-KOH mixtures at various current densities, 25°C. Each point represents a separate oxidation experiment; $\eta° \approx E°_{act(O_2)}$.

After Passivation: After the electrodes have passivated, it is possible to study properties of the oxide film in a steady-state condition and to compare films formed under different circumstances. A plot of $E°_{act(O_2)}$ vs. log I for an electrode passivated at 0.5 ma/cm² in 7.2*N*-KOH at 25°C was linear, with a slope $b = 0.15 \pm 0.01$ v. This value is close to the value of 0.12 expected (11) for a reaction in which discharge of hydroxyl ions to radicals is rate determining. In Fig. 8 are shown the results of measurements of $E°_{act(O_2)}$ all the points having been determined independently: i.e., on different electrodes, on films which were formed at different current densities, and in both KOH and mixed KOH-K_2CO_3 electrolytes. In terms of the different surface roughness factors of the underlying CdO films formed under such a wide range of conditions, the grouping around the line of slope 0.15 is remarkable.

The b values obtained indirectly from the slopes of the decay curves, however, were 2-3 times larger (Table IV) than the values obtained directly by current density variation; that is, the decay was 2-3 times more rapid than was expected. It is suggested that the reason for this is that, in contrast with current variation experiments in which the underlying film of CdO is in a steady-state condition, during voltage decay experiments (following current interruption) the conversion reaction proceeds unchecked at an appreciable rate [~0.3 ma/cm² initially, see Fig. 5 of Ref. (1)]. Thus the CdO layer is being etched away during the decay and carries with it the inner double layer. This chemical attack supplements the normal overpotential decay and increases the b value observed. Further, since the complexing reaction is in competition for OH^- with the oxygen discharge reaction, the greater the stability of the complex the greater its ability to decrease the surface activity of OH^- and hence to increase the potential drop across the inner double layer. The facts that the b's from decays in carbonate generally are larger than in caustic and are larger at lower temperature support this view, and support the further

Table IV. "b" values determined* from decay curves after passivation

	Conc. (*N*)	T, °C	Current density, ma/cm²	*b*
KOH	14.4	25	7.66 ma	0.34
	7.2	25	7.66	0.44
	7.2	25	3.83	0.28, 0.27
	3.6	25	7.66	0.29
	3.6	25	3.83	0.44
	7.2	0	7.66	0.36
	7.2	0	1.53	0.31
	7.2	−20	1.53	0.58
K_2CO_3	7.2	25	3.83	0.35, 0.27
	7.2	25	1.53	0.34
	7.2	0	7.66	0.54
	7.2	0	3.83	0.55, 0.50
	7.2	0	1.53	0.52, 0.50

* $\dfrac{\partial E°_{act(O_2)}}{\partial \log i} = -b$ [Ref. (8)].

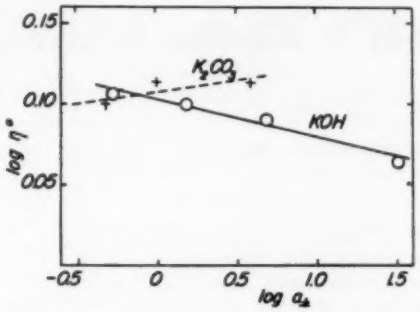

Fig. 9. Freundlich isotherm plot of log η° vs. log activity, adsorption of OH^- being assumed to be rate controlling; $\eta \approx E^\circ_{act(O_2)}$.

notion that E°_{DL} rises rapidly at passivation for the simple reason that the rate of absorption of OH^- through the double layer is reduced by the presence of the complex; in other words, the CdO surface becomes poisoned by reaction product which competes for active sites with reactant OH^-. The effect of poisoning should be less the higher the activity of OH^-, and greater the higher the activity of carbonate ion. Figure 9 shows values of $E^\circ_{act(O_2)}$ measured as function of concentration of OH^- and $CO_3^=$, and plotted as a Freundlich adsorption isotherm. The trends are as suggested and support the proposed mechanism. The large (500 mv/factor of ten change in concentration) negative value of $d\eta/d \log a_{OH^-}$ is very difficult to explain on the basis of activation theory, which predicts a value of zero (11).

Further, the fact that the b value of 0.15 is 25% higher than that predicted for a one-electron discharge reaction supports the suggestion of inhibition by reaction products. The higher the current density at which the passivated electrode is being anodized, the greater the surface concentration of still-sorbed complex. The role of adsorption indicated by the electrochemical behavior observed needs further examination.

Summary

The two equations $\eta^\circ_A = IR_i + E^\circ_{DL}$ and $\eta^\circ_P = IR_e + E^\circ_{act(O_2)}$ adequately describe the composition of overpotential when the electrode is active and passivated respectively. In the term E°_{DL} are included the voltage across the normal Helmholtz double layer, as well as that across a second inner or crystal double layer at the outer edge of the film, a charge separation which can build up to high voltages and decay rapidly in the manner of a condenser.

The relative sizes of the components making up the total overpotential are controlled by experimental conditions. It is ultimately the "inner" double layer and the field strength across it which determine when $\eta^\circ_A = \eta^\circ_P$ and the electrode goes from the active to the passivated state.

A mechanism which accounts qualitatively for the experimental results is proposed and discussed.

Acknowledgments

The authors gratefully acknowledge discussions on this work and correspondence with two laboratories: with Professor F. E. W. Wetmore, University of Toronto; and with Mr. U. B. Thomas and his very capable associates, Drs. Baker, Dewald, and Milner, Bell Telephone Laboratories.

Manuscript received May 4, 1959. This paper was prepared for delivery before the Ottawa Meeting, Sept. 28-Oct. 2, 1958. It is a contribution from the Defence Research Chemical Laboratories, Ottawa, Ontario, Canada. Issued as DRCL Report No. 303.

Any discussion of this paper will appear in a Discussion Section to be published in the June 1960 JOURNAL.

REFERENCES

1. P. E. Lake and E. J. Casey, *This Journal*, **105**, 52 (1958).
2. K. Huber, *This Journal*, **100**, 376 (1953); *Z. f. Elektrochem.*, **62**, 675 (1958).
3. D. Grahame, *J. Phys. Chem.*, **57**, 257 (1953).
4. H. B. Morely and F. E. W. Wetmore, *Can. J. Chem.*, **34**, 359 (1956).
5. B. E. Conway and P. L. Bourgault, *ibid.*, **37**, 292 (1959).
6. D. Grahame, *J. Amer. Chem. Soc.*, **68**, 301 (1946).
7. E. J. W. Verwey, "Semiconductor Materials," p. 158, H. K. Henisch, Editor, Butterworths Sci. Pub., Ltd., London (1951).
8. G. Armstrong and J. A. V. Butler, *Trans. Faraday Soc.*, **29**, 1261 (1933); J. O. Bockris, and E. C. Potter, *This Journal*, **99**, 169 (1952).
9. See e.g., J. O. Bockris, "Modern Aspects of Electrochemistry," p. 185, Butterworths Sci. Pubs., London (1954).
10. W. Jost, "Diffusion in Solids, Liquids and Gases," p. 47, Academic Press Inc., New York (1952).
11. J. O. Bockris, *J. Chem. Phys.*, **24**, 817 (1956).
12. C. J. F. Böttcher, "Theory of Electric Polarizations," pp. 201, 422, Elsevier Publishing Co., New York (1952).
13. P. Lukotsev and S. Lewina, *J. Phys. Chem., U.S.S.R.*, **21**, 599 (1947).
14. P. E. Lake and J. M. Goodings, *Can. J. Chem.*, **36**, 1089 (1958).
15. J. E. B. Randles, *Disc. Faraday Soc.*, No. 1, 11 (1947).
16. T. B. Grimley, *Proc. Royal Soc. A*, **201**, 40 (1950); T. B. Grimley and N. F. Mott, *Disc. Faraday Soc.* No. 1, 3 (1947).
17. G. T. Croft, *This Journal*, **106**, 278 (1959).

SYMBOLS

1. η — total overpotential at any time, measured against $Cd/Cd(OH)_2$ reference.
2. η° — total overpotential just at current interruption.
3. η°_A, η°_P — total overpotential while current is flowing: electrode active (A), passivated (P).
4. E_e — voltage to which exponential part of overpotential has dropped after "infinite" time (~100 msec).
5. E_{act} — value of logarithmic part of overpotential when $t < t_p$ (metal being oxidized).
   E°_{act} — value of E_{act} just at current interruption.
6. $E_{act(O_2)}$ — value of logarithmic part of overpotential when $t > t_p$ (oxygen being evolved).
   $E^\circ_{act(O_2)}$ — oxygen activation overpotential value of $\eta^\circ_P - IR_e$.
7. E_{DL} — $(\eta - E_e) - E_{act}$.
   E°_{DL} — value of E_{DL} just at current interruption.
8. IR_i — ionic resistance drop $\eta^\circ_A - E^\circ_{DL}$.
9. IR_e — electronic resistance drop $\eta^\circ_P - E^\circ_{act(O_2)}$.
10. E°_{CP} — concentration polarization.

The Oxidation of the Silver Electrode in Alkaline Solutions

Thedford P. Dirkse

Department of Chemistry, Calvin College, Grand Rapids, Michigan

ABSTRACT

The formation of Ag_2O and AgO was studied by means of constant current and constant potential processes. The efficiency of these oxide formations was determined by measuring the gain in weight of Ag electrodes under various conditions of charge, and the extent of the polarization of these processes was measured by using an interrupted current technique.

The electrolytic behavior of silver in alkaline solutions has been studied, but diverse opinions have been expressed as to the reactions taking place. Luther and Pokorny (1) plated silver on platinized platinum and observed its behavior in 1*N* NaOH solutions. They obtained the typical anodic (Fig. 1) and cathodic curves. They considered the first step of the anodic curve to correspond to the quantitative and reversible change of Ag to Ag_2O, and the second to correspond to the quantitative and reversible change of Ag_2O to AgO. Although they had evidence that a higher oxide, perhaps Ag_2O_3, was stable in alkaline solution, they could not produce it by oxidation of AgO in the NaOH solution. Instead, a third stage of the anodic curve corresponded to the evolution of oxygen.

Denison (2) worked with a system more nearly resembling a battery. His electrodes were made by pasting Ag_2O on a platinum gauze and reducing it to Ag. The electrolyte was a 25% KOH solution. He measured changes in weight of the electrode during anodic and cathodic processes. His results showed that by decreasing the current density a greater amount of weight was gained by the electrode, but he never quite obtained complete conversion to AgO. The anodic potential-time curves occasionally showed peaks but these were not interpreted. These curves also showed that the second stage was longer than the first. Furthermore, his final product always showed the presence of silver, indicating that the anodic process was not completely efficient.

Hickling and Taylor (3) studied an electrode made by plating silver on a platinum wire. The electrolyte was 1*N* NaOH and the results were recorded oscillographically. They found the second stage to be relatively short and interpreted it as due to the formation of Ag_2O_3 which then, being unstable, decomposed to form AgO.

More recently Jones, *et al.* (4) made a similar study of silver wire electrodes in 1*N* KOH solutions. They considered the second stage to be an inefficient one in which both oxidation of Ag_2O and evolution of oxygen occurred. Further, they gave evidence for the formation of Ag_2O_3 but only in small amounts and after completion of the second stage.

The work reported here is an attempt to resolve these differences with respect to the oxidation processes and to suggest a mechanism for them.

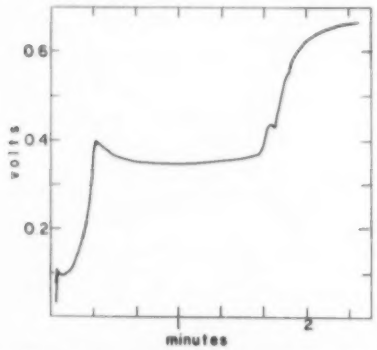

Fig. 1. Charging curve for silver in 15% KOH at room temperature, with a current density of 5 ma/cm².

Experimental

The electrodes were subjected to three kinds of treatment. In the first of these, the electrodes were charged at constant potential. The charging circuit is shown in Fig. 2. C is a 1.5-v source, F is a 100-ohm Helipot resistor from which a controlled voltage can be applied to the electrodes. In this way electrode B, the working electrode, can be kept at a definite potential above electrodes A. These latter electrodes were comparatively large electrodes made by pasting Ag_2O on silver screen. E has a resistance of 25,000 ohms so that the loss through this resistor is not large. D is a precision resistor of about 1 ohm which was used in recording the current passed through the system. Although this work was actually carried out at constant cell potential, yet, because of the low current density and relatively large amount

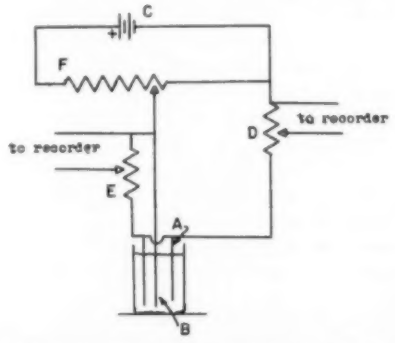

Fig. 2. Schematic diagram for constant-potential charging.

of material on electrodes A, the process in effect was a constant electrode potential one.

The electrodes were also subjected to a constant current oxidation. This circuit consisted of a high voltage source fed through a variable resistor and controlled by means of a Weston Model 534 d-c current relay. In carrying out these runs three currents were used: 1, 5, and 10 ma. The real current densities are unknown since the actual surface area of the silver electrodes was not measured. Four different electrolyte concentrations were used: 8, 21, 28, and 42% KOH.

The third type of treatment involved the use of interrupted current with silver wire electrodes. This technique and procedure have already been described (5).

For the first two methods of oxidation, the working electrodes were made by pasting a small amount of Ag_2O on a platinum screen. The area of the screen covered by the Ag_2O was about 2 cm^2 so that the total area exposed to the solution was about 4 cm^2. The Ag_2O was then reduced to Ag by heating at about 500°C for 15-30 sec. This electrode was placed between the two larger (2.5 cm^2) electrodes A. The 3 electrodes were placed in a polystyrene cell case which held about 35 ml of electrolyte. Unless otherwise indicated, all runs were made at room temperature.

After an electrode had been charged, it was soaked in distilled water for at least 8 hr, then it was dried in a stream of purified nitrogen at room temperature, and finally placed in a desiccator for at least 24 hr. All these operations were carried out in the absence of light. After this the electrode was weighed and the gain in weight was considered to be due to oxygen which had combined with the silver.

In the constant-current process the charging was continued until the voltage reached a certain predetermined value. In the constant-potential process the charging was continued until the current dropped to nearly zero or until 48 hr had elapsed, whichever occurred first.

All voltages are expressed with reference to the Ag-Ag_2O potential in alkaline solution.

Results

Ag to Ag_2O.—In the constant current processes the silver electrodes were oxidized until the voltage was 0.2 v. The electrode was then removed, dried, and weighed. Under all the conditions studied, the transformation of Ag to Ag_2O took place at a potential of about 50 to 100 mv. At the highest current densities very little of this transformation took place in the lower electrolyte concentrations. In no case was the Ag completely converted to Ag_2O, even though the current efficiencies (number of Faradays needed to produce the oxygen/number of Faradays actually used) were in the vicinity of 100%. The per cent conversion was usually less than 60%. The actual values will depend to some extent on such factors as the density of the silver.

In general, Ag_2O was produced on the surface of the working electrode. Its presence was verified by x-ray analysis and by emf measurements between the working electrode and the Ag-Ag_2O electrodes. It appears then that the Ag at the electrode-electrolyte interface is converted to Ag_2O, and when this has been completed the voltage increases abruptly and another process takes place—oxidation to AgO. The layer of Ag_2O produced on the Ag undoubtedly increases the electrical resistance of the electrode (5).

There is evidence that this electrical resistance of Ag_2O does limit the electrode process. An electrode similar to those used in this work was prepared using a grid of silver screen rather than of platinum. When this electrode was treated anodically in 20% KOH for some time at the lowest current density used in this work, the voltage rose to the higher level (about 0.35 v) after several days of treatment. Yet when this electrode was removed the surface appeared to be unattacked. It still had the appearance of reduced silver. However, on this material it was found that the active material next to the grid had been oxidized and that formation of Ag_2O seemed to proceed from the grid outward. This, of course, offered resistance to the flow of current from the grid to the surface of the active material and, although there was plenty of unoxidized Ag at the electrode-solution interface, the voltage rose to the level corresponding to the transformation of Ag_2O to AgO.

Another electrode was prepared by pasting a platinum screen with Ag_2O. When this was oxidized (without being reduced first) AgO was formed and, again, it was formed at the grid rather than at the electrode-solution interface. Thus the resistance of the Ag_2O seemed to make it easier for AgO to form at the grid where the amount of electrolyte was small rather than at the electrode surface where there was plenty of electrolyte.

In the constant potential processes Ag_2O was the

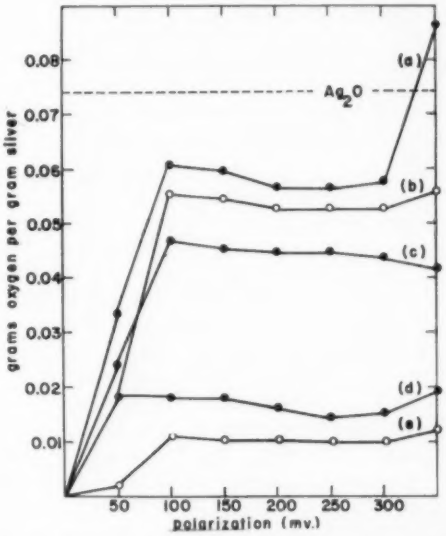

Fig. 3. Weight change for Ag electrode during constant-potential charge for 24 hr in KOH solutions at room temperature: (a) 23% KOH; (b) 20% KOH; (c) 42% KOH; (d) 8% KOH; (e) 23% KOH. Ag grid for (e), Pt grid for others.

product at potentials below 0.3 v. In general, the conversion of Ag to Ag_2O took place with a current efficiency of about 100%. The process appears to be a quantitative one but again, as with the constant current method, the Ag was not completely converted to Ag_2O. The maximum conversion, about 80%, took place in 28% KOH.

In carrying out this constant potential work it was found that on occasion an electrode lost rather than gained weight (6). To investigate this further, a series of experiments was carried out in which several electrodes were charged at constant potential for 24 hr, then dried and weighed. Each electrode was then charged further, without being reduced, at a potential 50 mv higher for 24 hr, and again weighed. This was repeated for several such increments of voltage increase. The results of the weight changes are shown on Fig. 3. It is noted that at potentials under 0.30 v the Ag was not completely converted to Ag_2O. Furthermore, at potentials above 0.10 v there appears to be a loss in weight. This, however, can be traced to a loss of Ag from the electrode. Such a loss was observed in each case and was of the proper magnitude to account for the decrease noted in oxygen content of the Ag_2O. As the electrode is held at a given potential some of the Ag_2O apparently is dissolved from the electrode. However, the results show also that once the initial film of Ag_2O is formed, raising the potential produces no further oxidation until the oxidation of Ag_2O to AgO takes place at potentials above 0.30 v. This is also noted on Fig. 4 where the current accepted by the electrode is practically zero at potentials above 0.10 v. In Fig. 4 each curve represents the current during the series of constant potential charges referred to above and on Fig. 3. The platinum grid is not responsible for this loss in weight. An electrode having a silver grid shows the same behavior, Fig. 3, curve e.

The results heretofore obtained show that the electrochemical oxidation of Ag to Ag_2O is an efficient one. It is the only one taking place under the conditions outlined above. However, the above results were obtained by using Ag pasted on a platinum screen grid. It is possible that the presence of the platinum may modify this process. To check on this, some commercial Ag electrodes were treated anodically under various conditions. These electrodes were about 4 cm square and contained on an average about 6.2 g of Ag. These were treated at 40 and 200 ma. Typical voltage-time curves were obtained. To change all the Ag in these electrodes to Ag_2O would require about 1.5 amp-hr. Using the current rates mentioned above, and KOH concentrations ranging from 8 to 40%, only 0.24 to 0.64 amp-hr were used to oxidize the Ag to Ag_2O. After this the voltage increased and the transformation to AgO took place. Here again the formation of Ag_2O was incomplete, only about 20 to 40% of the Ag being converted to the oxide. However, when this charging was continued at the higher voltage level, the conversion to AgO was above 80%.

Treatment of silver wire electrodes with interrupted current shows that the anodic overvoltage is relatively small while appreciable amounts of unoxidized Ag remain, but the *IR* drop increases as the surface coating of Ag_2O increases, Fig. 5. When a high current density at a temperature of −20°C was used, however, very little oxidation took place and the voltage rose rapidly. Under these conditions the low mobility of the OH^- ion was not sufficient to sustain the reaction.

Ag_2O *to* AgO.—After the oxidation of Ag to Ag_2O no longer takes place, the voltage rises to a higher level where AgO is formed. This is preceded by a peak shown on Fig. 1. The significance of this peak has been discussed earlier (5).

In the constant current processes the electrode containing Ag and Ag_2O was treated until the potential rose to about 0.5 v. The electrode was then removed, dried, and weighed to determine the oxygen gained while the potential ranged from 0.2 to 0.5 v. The amount of oxygen added to the electrode in this voltage range was practically always greater than that added in the range 0 to 0.2 v. The surface material in each case was AgO. This was determined by x-ray analysis. In no case, however, was Ag com-

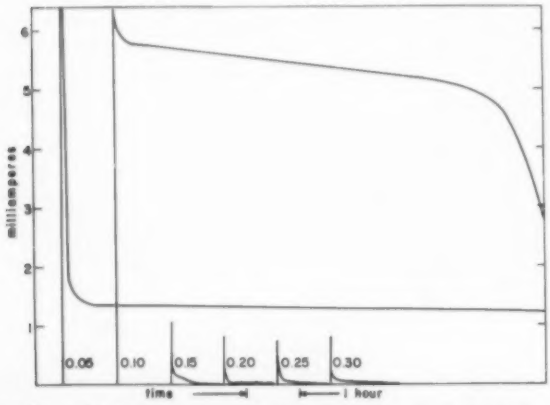

Fig. 4. Variation of current with change in extent of polarization for an Ag electrode in 23% KOH at room temperature. The numbers give the extent of polarization in volts.

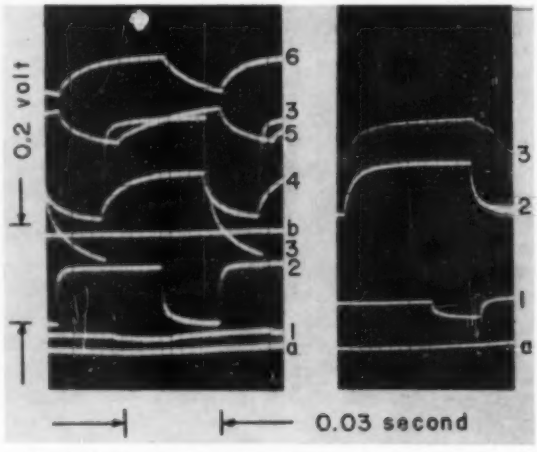

Fig. 5. Variation of voltage with time for Ag electrode at 3 ma/cm²; room temperature. Left picture, 10% KOH; right picture, 5% KOH. (a) Ag-Ag_2O potential; (b) Ag_2O-AgO potential. The numbers give the order in which these curves appeared during the charging process.

pletely changed to AgO. The current efficiencies varied with the current rate. They were about 100% when the process required about 8 hr. They were less at higher and at lower current densities.

With constant potential treatment, no AgO was formed at less than 0.3 to 0.35 v. When the overvoltage was high enough to bring about formation of AgO, the current efficiencies were close to 100% in all KOH concentrations studied. The current was high at the outset, then fell to a low value, then again increased, Fig. 6. The voltage also rose to a peak at the outset and then decreased, Fig. 7.

Furthermore, large amounts of oxygen could be introduced into the electrode by this constant potential process. When the electrode was kept at an overvoltage of 0.40 to 0.45 v for weeks or even months, increasing amounts of oxygen were added to the electrode. In one case, analysis showed a composition corresponding to $AgO_{1.6}$. This is approximately the composition of Ag_2O_3. Yet in preparing this material the electrode was kept at a potential less than that generally considered to be that of the AgO-Ag_2O_3 couple (1, 3). Moreover, the emf of this electrode was the same as that of AgO and the x-ray pattern, although less distinct, showed only lines of AgO, Fig. 8. This preparation was rather stable. A sample kept dry and in the dark showed practically no loss in weight over a period of several months.

The results obtained when a silver wire coated with Ag_2O was subjected to interrupted current showed a difference between this process and the formation of Ag_2O. The shape of the voltage curve was different, Fig. 5, the polarization was greater, and the voltage rise was slower than that for the Ag to Ag_2O transformation. The polarization for this process is 100-150 mv. This was determined over a KOH concentration range of 5-43% and with a variety of current densities. Measurements were also made at 0° and −20°C. At this lowest temperature the polarization was greater and the rate of voltage decay was much slower. This can be attributed to the increased viscosity of these solutions at this low temperature.

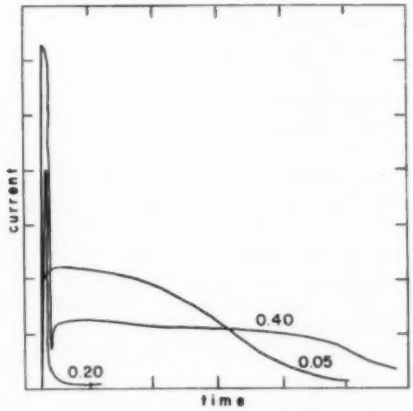

Fig. 6. Variation of current with time during constant-potential charge of an Ag electrode in 30% KOH at room temperature. The numbers give the polarization in volts above the Ag-Ag_2O potential. The scale is not the same for each curve.

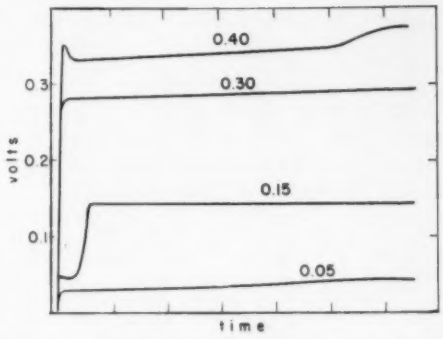

Fig. 7. Variation of potential of Ag electrode during constant-potential charge in 30% KOH at room temperature. The numbers give the polarization in volts above the Ag-Ag_2O potential.

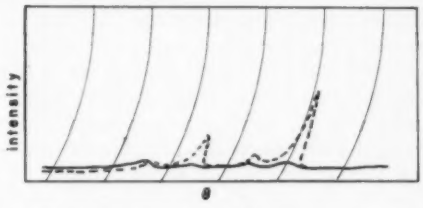

Fig. 8. X-ray patterns for AgO preparations; solid line, $AgO_{1.6}$; dotted line, AgO.

Using the method suggested by Brodd and Hackerman (7), the relative surface areas of Ag, Ag_2O, and AgO are 1 : 2.7 : 7.7. This was determined by measuring the double layer capacitance of a silver wire electrode and then also the capacitance of the same electrode after it was coated with Ag_2O, and finally when it was coated with AgO.

Oxygen evolution.—The third level of the charge curve is associated with the evolution of oxygen. Usually there is a gradual rise in voltage from the second to the third level. However, in experiments with silver wire electrodes it was noted that there were breaks in the part of the voltage curve between the second and third levels. These breaks occurred during a constant current charge and were noted whether the solution was agitated with nitrogen or oxygen, or was quiescent. Two breaks were noted in many instances, Fig. 1, but they did not appear on the discharge curve. These breaks were also observed when a sintered silver plate was charged in excess electrolyte.

When silver wire electrodes were treated with interrupted current, a break was often noted in the decay curve after oxygen evolution had begun, Fig. 5, right panel. This break was at a potential of about 0.4 v at room temperature and 0.33 v at 0°C. These breaks were observed for no more than a second or two, and occurred as the general voltage trend was upward. No such breaks were noted during the closed circuit part of the process.

Discussion

In seeking to account for the behavior of the silver electrode in alkaline solutions it is apparent that the OH^- ions are the solute species involved. They are involved in the oxygen evolution process (8, 9) and

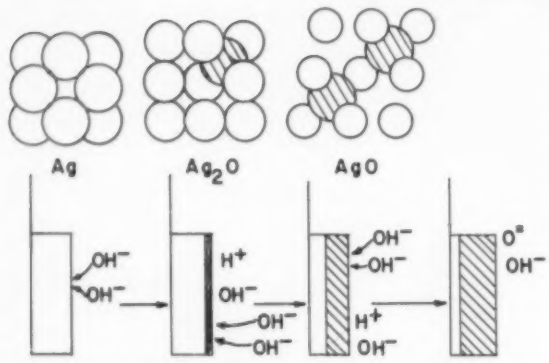

Fig. 9. Possible mechanism for silver oxide formation

are likely also involved in the other reactions. If water were the active species, then at constant current one would expect less formation of Ag_2O, e.g., at high KOH concentrations than at low concentrations. At the high KOH concentrations there would be comparatively fewer H_2O molecules and they would be less mobile because of the increased viscosity of the system. In actual fact, the per cent Ag converted to Ag_2O at constant current was greater in 42% KOH than in 8% KOH at all current densities used.

A possible mechanism for these oxidation processes is illustrated in Fig. 9. The lattice structures in the top panel are drawn to scale (10-12). The open circles represent Ag and the shaded circles oxygen. Since no data could be found for the ionic radius of Ag^{++}, an estimated value of 1.1Å was used. The other ionic radii used are those given by Pauling (13).

As a positive charge is placed on silver, the outermost valence electron is removed from each silver atom, producing Ag^+. This causes an expansion of the silver lattice and allows room for the inclusion of oxygen atoms or ions. The OH^- ions are drawn to this charged silver and the oxygen becomes separated from the hydrogen. The $O^=$ ions are then drawn into the Ag^+ lattice, forming Ag_2O.

	H°, kcal/mole	Reference
$H^+ (g) \rightarrow H^+ (aq)$	−255	(14)
$O^= (g) \rightarrow O^= (aq)$	−125	estimated
$OH^- (aq) \rightarrow OH^- (g)$	+92	(14)
$OH^- (g) \rightarrow O^= (g) + H^+ (g)$	+640	(15a)
$OH^- (aq) \rightarrow H^+ (aq) + O^= (aq)$	+352	

The lattice energy of Ag_2O is −715 kcal/mole (15b). According to the above data, this separation is energetically allowable.

The $O^=$ ions are rather immobile in this lattice and soon this reaction ceases because no more $O^=$ ions can be accommodated in the Ag^+ lattice. This is indicated also by the behavior of the silver electrode as shown on Fig. 3. This Ag_2O layer acts as a barrier to the flow of electrons and permits no ions to leave it except for a few Ag^+ ions which may go into solution. This accounts for the loss in weight shown on Fig. 3.

To continue the flow of current after the Ag_2O layer is formed, the potential on the electrode must be increased. This withdraws another electron from each Ag^+. There is then a greater repulsive force between the silver ions, and more $O^=$ ions must enter the lattice to preserve electroneutrality. As a result, the silver lattice is further distorted and expanded. Reaction then proceeds and the electrode gains in weight as AgO is formed. Because of the expanded lattice the $O^=$ ions can penetrate more deeply and thus the formation of AgO is greater than that of Ag_2O on the same electrode. This mechanism allows for the possibility that Ag can be transformed to AgO directly without the intermediate formation of Ag_2O. This appears to take place at constant potential charge with a polarization greater than 350 mv, Fig. 7.

The formation of AgO continues until the $O^=$ ions can no longer be absorbed by the electrode material at the rate demanded by the current flow. The potential then rises and another reaction takes place. The rise in potential here is slow compared to that between the formation of Ag_2O and that necessary for the formation of AgO. This rise corresponds to the occurrence of an additional reaction and not the replacement of one reaction by another. This additional reaction is the evolution of oxygen. The increase in potential is not sufficient to remove additional electrons from the Ag^{++} ions. The AgO formed is a fairly good electron conductor and the electrons needed for the flow of current may then arise from another reaction and be transferred through the AgO layer.

The potential rises here because, to continue the flow of current, $O^=$ ions can no longer migrate fast enough and more electrons cannot be removed from the Ag^{++} ions in the lattice. It is possible then that electrons are removed from the OH^- ions which are at the electrode surface,

$$OH^- \rightarrow OH + e \qquad [1]$$

and that these OH radicals then combine to form H_2O_2 which decomposes to give the oxygen.

$$2\ OH \rightarrow H_2O_2 \qquad [2]$$

$$H_2O_2 + OH^- \rightarrow H_2O + HO_2^- \qquad [3]$$

$$HO_2^- \rightarrow \tfrac{1}{2}\ O_2 + OH^- \qquad [4]$$

A serious objection to this mechanism is that the potential needed for reaction [1] is about 1.7 v on the scale used here (15c). This is considerably higher than that at which oxygen evolution occurs.

The evolution of oxygen does take place at potentials above that associated with the formation of HO_2^- (16). Furthermore, the breaks in that part of the voltage-time curves corresponding to oxygen evolution, Fig. 1 and 5, also occur at about the potential of the $OH^- - HO_2^-$ or $OH^- - O_2^-$ couples (15e and c). In general, at low current densities, the break is noted at the lower potential ($OH^- - O_2^-$), while as the current density increases the potential corresponds to the $OH^- - HO_2^-$ couple. Silver catalyzes the decomposition of peroxide and so the evolution of oxygen could easily proceed this way.

These facts suggest two possibilities for the oxy-

gen evolution reaction. Reactions [5]-[7] illustrate a mechanism

$$OH^- \rightarrow O^= + H^+$$

or

$$OH^- \rightarrow O^- + H^+ + e \quad [5]$$

$$2\,O^- \rightarrow O_2^- + e \quad [6]$$

$$O_2^- \rightarrow O_2 + e \quad [7]$$

involving the $OH^- - O_2^-$ couple. It is possible that the $O^=$ or O^- ions may emigrate from the AgO lattice as well as be formed from the OH^- ions in solution.

The other possibility is illustrated by a series of reactions consisting of [5], [8], [4]. Here again the oxygen ions from the solid may be involved.

$$O^- + OH^- \rightarrow HO_2^- + e \quad [8]$$

It is difficult to make a choice between these mechanisms. Both are permissible according to the ideas of Rüetschi and Delahay (8). Perhaps the latter is more consistent with the results and suggestions of Anbar and Taube (9). Measurement of the oxygen overvoltage could conceivably shed some light on this mechanism, but these measurements are, at best, difficult to make.

The ideas suggested here stress the fact that the mobility of the OH^- ion is an important factor in these oxidation processes. When this mobility is impaired, e.g., at low temperatures or at high KOH concentrations, the extent of oxide formation is also less because the OH^- ions cannot migrate fast enough to allow reaction to take place at the rate set by the current.

It has been noted that the polarization necessary to carry out the oxide formation is not very sensitive to current density. This indicates that the cause of the polarization is not primarily resistance. On the basis of the mechanism suggested here, this polarization would be due to the splitting of the OH^- ion. This would appear in the formation of each of the two oxides. In addition to this the formation of AgO would be polarized by the migration of $O^=$ ions in the Ag^{++} lattice.

Acknowledgment

Thanks are due to the Office of Naval Research under whose sponsorship this work was carried out, and to the Yardney Electric Corporation for supplying some of the materials. This work was performed under Contract N onr-1682(01) with the Office of Naval Research.

Manuscript received May 11, 1959. This paper was prepared for delivery before the Columbus Meeting, Oct. 18-22, 1959.

Any discussion of this paper will appear in a Discussion Section to be published in the June 1960 JOURNAL.

REFERENCES

1. R. Luther and F. Pokorny, *Z. anorg. u. allgem. Chem.*, **57**, 290 (1908).
2. I. A. Denison, *Trans. Electrochem. Soc.*, **90**, 387 (1946).
3. A. Hickling and D. Taylor, *Discussions Faraday Soc.*, No. 1, 277 (1947).
4. P. Jones, H. R. Thirsk, and W. F. K. Wynne-Jones, *Trans. Faraday Soc.*, **52**, 1003 (1956).
5. T. P. Dirkse and G. J. Werkema, *This Journal*, **106**, 88 (1959).
6. L. A. Vander Lugt, MS Thesis, Michigan State University, 1959.
7. R. J. Brodd and N. Hackerman, *This Journal*, **104**, 704 (1957).
8. P. Rüetschi and P. Delahay, *J. Chem. Phys.*, **23**, 556 (1955).
9. M. Anbar and H. Taube, *J. Am. Chem. Soc.*, **78**, 3252 (1956).
10. R. B. Wilsey, *Phil. Mag.*, **46**, 487 (1923).
11. P. Niggli, *Z. Krist.*, **57**, 253 (1922).
12. V. Scatturin, P. Bellon, and R. Zannetti, *Ricerca Sci.*, **27**, 2163 (1957).
13. L. Pauling, "The Nature of the Chemical Bond," 2nd ed., p. 346, Cornell University Press, Ithaca (1940).
14. E. J. Garrick, *Phil. Mag.*, **8**, 102 (1929).
15. W. M. Latimer, "Oxidation Potentials," 2nd ed., Prentice-Hall, Inc., New York (1952): *a*, p. 25; *b*, p. 20; *c*, p. 48; *e*, p. 45.
16. T. P. Dirkse and D. B. De Vries, *J. Phys. Chem.*, **63**, 107 (1959).

Effect of Sodium Pyrophosphate on Polarization and Corrosion of Tin

I. A. Ammar[1] and S. Riad

Department of Chemistry, Faculty of Science, Cairo University, Cairo, Egypt, U.A.R.

ABSTRACT

Corrosion rates and corrosion potentials have been measured for tin in eight different acid, alkaline, and neutral solutions. The corrosion potential, measured against the saturated calomel electrode, has been found to increase toward more active potentials with increase of concentration. It has been observed that sodium pyrophosphate decreases the corrosion rate and increases the corrosion potential toward more active values. This increase is proportional to the amount of pyrophosphate added. Cathodic and anodic polarization measurements have been carried out in an attempt to explain the function of sodium pyrophosphate as a corrosion inhibitor. The results have been compared with previous work on the inhibition of iron corrosion by polyphosphates.

Measurements of the rate of corrosion of tin and the related corrosion characteristics are important since tin is used as a protective coating for iron and copper (1). Inhibition of the corrosion of tin in hydrochloric and acetic acid solutions, by incorporating about 5% antimony in tin, was studied by Hoar (2). The corrosion of tinplate and its inhibition by chromate-containing solutions was studied by Kerr (3, 4). Electrodeposited coatings of Sn-Zn (5) and Sn-Ni (6) alloys were found to resist the corrosion of steel. Corrosion of tin in solutions containing chloride ions was studied by Britton and Michael (7) who observed that addition of sodium carbonate, bicarbonate, orthophosphate, chromate, and silicate prevented the corrosion of tin.

The present investigation was undertaken to study the possibility of using sodium pyrophosphate as an inhibitor for the corrosion of tin and to investigate the effect of this substance on the cathodic and anodic polarization measurements. Polyphosphates were found to have an inhibiting effect on the corrosion of iron (8). Pyrophosphate was chosen for the present investigation because it is more stable than metaphosphate (9). The mechanism of inhibition of iron corrosion by polyphosphates sometimes (10) was attributed to the laying down of a calcium carbonate film favored by the presence of polyphosphate. The present investigation, therefore, was extended to study the effect of calcium chloride on the rate of corrosion of tin.

Experimental

The electrolytic cell used for polarization measurements was similar to that used in overpotential work (11). It had two separate compartments for anode and cathode. One of these two compartments was provided with a capillary leading to a salt bridge via a glass tap. The barrel of a syringe, 10 cm long and 1 cm in diameter, was joined to the top of this compartment and was used to lower the test electrode so as to touch the tip of the capillary without introducing air inside the cell. A saturated calomel was used as a reference electrode. The cell was guarded against atmospheric oxygen with the use of ground glass joints and water-sealed taps. A subsidiary platinum electrode, in the form of a disk 1 cm^2 in area, was used in connection with the tin electrode. The cell also was used for the measurements of corrosion potentials. For measurements in air-free solutions, purified nitrogen was introduced into the cell and was divided between the two compartments by means of two taps. Nitrogen was purified by passing it through NaOH and pyrogallol solutions and then over copper heated to 450° to remove traces of oxygen left. Bubbling of nitrogen was stopped during potential measurements.

Tin electrodes were prepared from pure tin foil (over 99.99% Sn) in hydrogen atmosphere. This was carried out in a glass apparatus having a side arm (3 mm ID) containing a piece of platinum wire the middle of which was sealed to glass. After introducing the tin foil, the apparatus was closed by a ground glass joint and was deaerated by passing hydrogen for several hours. The metal then was melted and the melt was introduced into the side arm. The metal was allowed to cool under hydrogen, and the side arm was cut off the main apparatus. Part of the tin electrode was exposed by cutting the appropriate length of glass. The electrode then was sealed to the piston of the syringe, the barrel of which was joined to one of the compartments of the cell.

For corrosion tests, tin rods were prepared as described above and then were rolled into sheets 1 mm in thickness. Specimens (2 x 1.5 cm) were cut. They were abraded to 00 emery paper, degreased in hot benzene, and then were dried and weighed. Corrosion tests were carried out in a wide 100 ml jar provided with a loosely fitting wooden cover from which the electrode was suspended by a thread. In this manner oxygen concentration cells from top to bottom were minimized. All corrosion tests were carried out in aerated unstirred solutions for a period of three days. The specimen then was removed,

[1] Present address: Institut fur anorganische Chemie, Berlin, Germany.

rinsed with conductivity water, swabbed with a towel wetted with benzene, and finally was dried and weighed.

Measurements were carried out in solutions of hydrochloric, acetic, citric, and maleic acids, sodium hydroxide, sodium carbonate, sodium benzoate and sodium chloride. These were chosen to represent some of the solutions which contact tin in its various industrial applications. Solutions were prepared from "Analar" grade reagents and conductivity water. The sodium pyrophosphate[2] used contained 0.1% orthophosphate and 0.025% impurities such as Fe, K, and Pb. Solutions of pyrophosphate were prepared directly before the tests in order to minimize any possible reversion to the orthophosphate. All measurements were carried out at 30° in an air thermostat controlled to ±0.5°. Results were duplicated and the mean was computed. The spread in the corrosion rate was less than 1 mdd. All potentials were recorded vs. the saturated calomel electrode potential. The current density was expressed in amp/cm².

Results

Corrosion rates, in air-saturated solutions, are given in Table I for five concentrations ranging from 0.05 to 1.0M. The effect of sodium pyrophosphate on the corrosion rate was studied in 0.1M solutions for various concentrations of pyrophosphate. Results are given in Table II. Data for the corrosion rate in the presence of 0.01M $CaCl_2$, and in the presence of a mixture of 0.01M $CaCl_2$ and 0.01M $Na_4P_2O_7$ are given in Table III for six different solutions. The effect of $Na_4P_2O_7$ on the pH in 0.1M solutions is given in Table IV. The pH values in pure 0.1M solutions are included in Table IV for comparison. The pH values in presence of $CaCl_2$ are given in Table V. Measurements of the pH were carried out under the conditions of corrosion rate measurements.

The dependence of the potential of corroding tin on time was studied in deaerated and air-saturated solutions. Corrosion potentials were measured over a wider concentration range than corrosion rates. Except in Na_2CO_3 solutions, the steady-state corrosion potential E_c is reached within 5 min from the moment the electrode contacts the solution. In all solutions studied, E_c is active with respect to the saturated calomel potential. In deaerated solutions, E_c is more active than the corresponding value in air-saturated solutions. The effect of concentration on the corrosion potential was studied by measuring time-potential relations for five different concentrations in deaerated and air-saturated solutions. Except in NaCl solutions, E_c increases toward more active potentials with increase of concentration. The relation between E_c and log C, where C is the molarity, is linear for both deaerated and air-saturated solutions. Results are shown in Fig. 1 and 2 for aerated and deaerated solutions, respectively. In NaCl solutions (not shown in Fig. 2), E_c remains practically constant (560-570 mv more active than the saturated calomel potential) with increase of concentration from 0.05 to 1.0M. The effect of sodium pyrophosphate on the corrosion potential was

[2] Prepared by Fabrication Alemana, Germany.

Table I. Effect of concentration on corrosion rate in aerated pure solutions

Solution	Corrosion rate (mdd) in 0.05M	0.1M	0.25M	0.5M	1.0M
Hydrochloric acid	3	15	17	22	29
Acetic acid	5	11	14	16	18
Citric acid	13	18	20	23	26
Maleic acid	19	64	212	417	1083
Sodium hydroxide	12	20	23	24	29
Sodium carbonate	5	13	15	27	29
Sodium chloride	2	2	2	3	3
Sodium benzoate	3	3	4	5	6

Table II. Effect of pyrophosphate concentration on corrosion rate in 0.1M solutions

Solution	Corrosion rate (mdd) at different concentration of $Na_4P_2O_7$ 0.01M	0.025M	0.05M	0.25M
Hydrochloric acid	5	4	3	3
Acetic acid	9	7	6	3
Citric acid	17	15	13	10
Maleic acid	37	28	18	7
Sodium hydroxide	20	18	16	11
Sodium carbonate	9	7	6	5
Sodium benzoate	2	2	2	2
Sodium chloride	2	2	1	1

Table III. Effect of $CaCl_2$ on corrosion rate in 0.1M solutions

Solution	Corrosion rate (mdd) in presence of 0.01M $CaCl_2$	0.01M $CaCl_2$ + 0.01M $Na_4P_2O_7$
Hydrochloric acid	3	1
Acetic acid	1	1
Citric acid	4	3
Maleic acid	16	5
Sodium benzoate	1	1*
Sodium chloride	0	0*

* Solution is turbid.

Table IV. Effect of pyrophosphate concentration on the pH in 0.1M solutions

Solution	Concentration $Na_4P_2O_7$ Pure 0.1M	0.01M	0.025M	0.05M	0.25M
Hydrochloric acid	1.1	1.2	1.3	2.1	7.6
Acetic acid	2.6	4.0	4.5	5.3	7.8
Citric acid	1.8	2.5	2.8	3.4	6.0
Maleic acid	1.2	1.6	1.9	3.4	7.1
Sodium hydroxide	11.9	12.1	12.1	12.1	12.0
Sodium carbonate	11.1	11.1	11.1	11.0	10.9
Sodium benzoate	7.1	9.6	9.9	9.9	9.9
Sodium chloride	6.3	9.7	9.8	9.8	9.8

Table V. Effect of $CaCl_2$ on the pH in 0.1M solutions

Solution	Concentration $Na_4P_2O_7$ 0.01M $CaCl_2$	0.01M $CaCl_2$ + 0.01M $Na_4P_2O_7$
Hydrochloric acid	1.1	1.1
Acetic acid	2.7	3.7
Citric acid	1.9	2.3
Maleic acid	1.4	1.6
Sodium benzoate	7.1	9.3
Sodium chloride	6.3	9.3

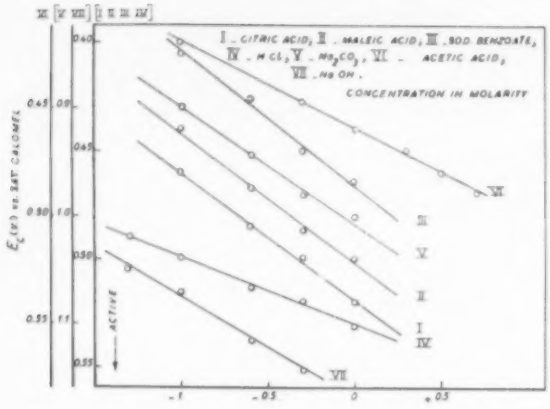

Fig. 1. Effect of concentration on corrosion potentials in aerated solutions.

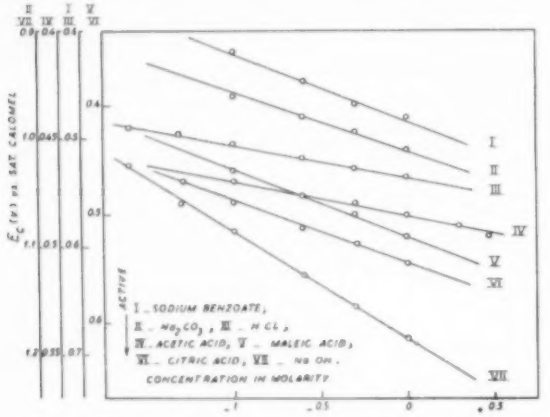
I - SODIUM BENZOATE,
II - Na_2CO_3, III - HCl,
IV - ACETIC ACID, V - MALEIC ACID,
VI - CITRIC ACID, VII - NaOH.
CONCENTRATION IN MOLARITY
ACTIVE

Fig. 2. Effect of concentration on corrosion potentials in deaerated solutions.

studied in 0.1M solutions. In presence of as little as 0.01M $Na_4P_2O_7$, E_c increases toward more active potentials in both deaerated and air-saturated solutions. Furthermore, this effect is proportional to the pyrophosphate concentration as is clear from the results, in deaerated 0.1*N* HCl, shown in Fig. 3.

Cathodic polarization measurements were carried out in deaerated 0.1M solutions of NaOH, HCl, acetic, and maleic acids. Measurements were started from low to high current densities. At each setting of current, the electrode was left polarized until the steady-state potential was reached. This usually took less than 5 min. Results in maleic acid and NaOH are shown in Fig. 4 and 5, respectively. Cathodic polarization curves for HCl and acetic acid are similar to those of maleic acid. It is clear from Fig. 4 and 5 that $Na_4P_2O_7$ increases the cathodic polarization toward more active values. This increase is proportional to the concentration of pyrophosphate added. The relation between cathodic polarization and the logarithm of the concentration of $Na_4P_2O_7$ is similar to Fig. 3. $CaCl_2$, however, does not change the cathodic polarization appreciably (Fig. 4). Similar conclusions are drawn for HCl and acetic acid. Previous work on iron (12) similarly has indicated that polyphosphates increase the cathodic polarization toward more active potentials.

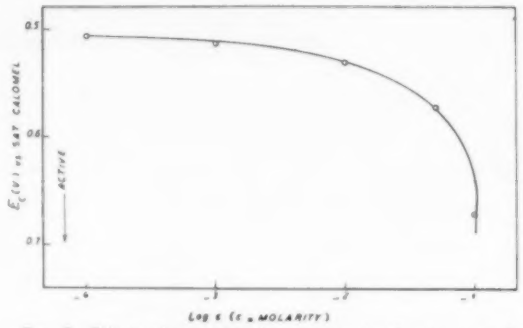

Fig. 3. Effect of pyrophosphate concentration on corrosion potential in deaerated 0.1N HCl.

Anodic polarization measurements were carried out in aerated 0.1M solutions of maleic acid and NaOH. In order to minimize the time effect, the electrode was left unpolarized until the corrosion potential was attained. Polarization then was commenced at a low current density, and the electrode was left polarized for nearly 1 hr until the steady-state potential was reached. With this slow technique, the potential changed from the active to the noble direction. Following this, measurements at higher current densities were taken. Results, at high current densities, are shown in Fig. 4 and 5, from which it is clear that $Na_4P_2O_7$ decreases the anodic polarization (potential becomes less noble) in 0.1N NaOH, and it has no effect on the anodic polarization in 0.1M maleic acid solution.

Discussion

It is clear from the data given in Table I that, in aerated solutions, the rate of corrosion of tin increases with increase of concentration. However, this increase is not marked in NaCl solutions as compared to the results in other solutions studied. The maximum rate of attack is observed in maleic acid solutions. Table II indicates that the corrosion rate, in acid and alkaline solutions, decreases with the increase of pyrophosphate concentration. In NaCl solution, the corrosion rate is decreased only

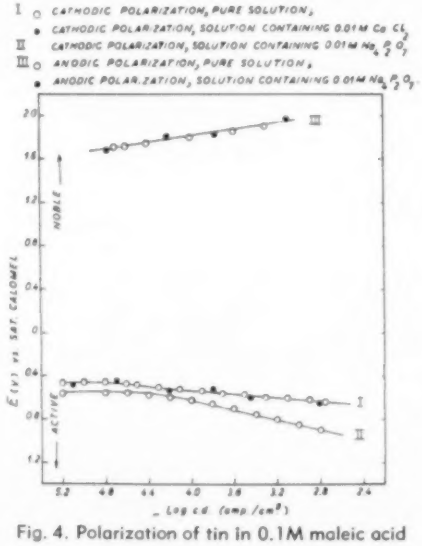
I ○ CATHODIC POLARIZATION, PURE SOLUTION,
● CATHODIC POLARIZATION, SOLUTION CONTAINING 0.01M Ca Cl2
II CATHODIC POLARIZATION, SOLUTION CONTAINING 0.01M $Na_4P_2O_7$
III ○ ANODIC POLARIZATION, PURE SOLUTION,
● ANODIC POLARIZATION, SOLUTION CONTAINING 0.01M $Na_4P_2O_7$
NOBLE
ACTIVE
Log c.d. (amp./cm²)

Fig. 4. Polarization of tin in 0.1M maleic acid

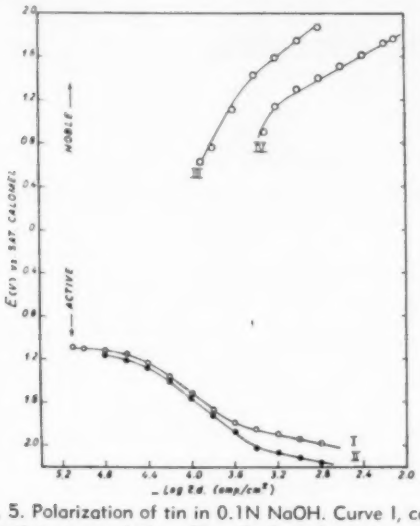

Fig. 5. Polarization of tin in 0.1N NaOH. Curve I, cathodic polarization, pure solution; II, cathodic polarization, solution containing 0.01M $Na_4P_2O_7$; III, anodic polarization, pure solution; IV, anodic polarization, solution containing 0.01M $Na_4P_2O_7$.

by 1 mdd at high pyrophosphate concentrations, whereas in sodium benzoate solution it is independent of pyrophosphate concentration. Hence, pyrophosphate is an effective inhibitor for the corrosion of tin in the acid and alkaline solutions studied. Previous work (8), on the inhibition of the corrosion of mild steel, has shown that polyphosphates are effective corrosion inhibitors in presence of dissolved oxygen. Moreover, it has been observed that addition of $CaCl_2$ accelerates the corrosion of mild steel in presence of dissolved oxygen (8). In the case of tin, $CaCl_2$ decreases the corrosion rate as it is clear from results given in Tables I and III. Addition of pyrophosphates to the solution containing $CaCl_2$ produces a further decrease in the corrosion rate in HCl, citric, and maleic acids (Table III).

The shift of cathodic polarization toward more active values (Fig. 4 and 5), produced by the addition of pyrophosphate, may be ascribed to the adsorption of pyrophosphate on tin cathodes thus lowering the available surface area for the cathodic reaction. Adsorption of pyrophosphate on local cathodic areas also may account for the change of corrosion potentials [given by the point of intersection of the anodic and cathodic polarization curves (13)] toward more active values, observed in solutions containing pyrophosphate. Thus, if the polarization of local cathodes is increased in presence of pyrophosphate (Fig. 4 and 5), while the polarization of local anodes is decreased (Fig. 5) or not affected (Fig. 4), the corrosion potential is shifted toward more active values. In the first case, the corrosion rate may not be affected as it is evident from the results in 0.1*N* NaOH (cf. Tables I and II). On the other hand, when cathodic polarization is increased in presence of pyrophosphate and anodic polarization is not affected, the corrosion rate decreases as is clear from the results in maleic acid solutions, given in Tables I and II.

The present investigation indicates that the rate of corrosion of tin in acid and alkaline solutions is greater than that observed in NaCl and sodium benzoate solutions (Table I). This may be explained on the basis of the amphoteric character of tin according to which tin is expected to dissolve in the acid and alkaline *p*H range more than in the neutral *p*H range (cf. Table IV). It is clear from Table IV that addition of pyrophosphate to acid solutions increases the *p*H to the neutral range, and, hence, it is expected that tin does not go into solution as readily in this *p*H range as it does in the extreme acid range. In alkaline solutions pyrophosphate has no appreciable effect on *p*H (Table IV). However, the possibility exists that, in such solutions, pyrophosphate may have a complexing action on tin with the result that the anodic polarization is decreased in presence of pyrophosphate as compared to the values in absence of pyrophosphate (Fig. 5). This effect is, however, compensated by the increase of cathodic polarization in presence of pyrophosphate. In salt solutions, pyrophosphate increases the *p*H (Table IV) and has no appreciable effect on the corrosion rate (Table II). This increase in *p*H would require more dissolution of tin, i.e., decrease of the anodic polarization. However, for the corrosion rate to remain constant, this effect also must be compensated by the increase of cathodic polarization.

It is clear from the results of the present investigation that $CaCl_2$ is not necessary for pyrophosphate to function as a corrosion inhibitor, in contradiction to the suggestion of Raistrick (10) that inhibition by polyphosphates is due to the laying down of a calcium carbonate film favored in presence of polyphosphates. However, $CaCl_2$ has no appreciable effect on *p*H (Table V) and it decreases the corrosion rate (Table III). This is not easy to explain since $CaCl_2$ has no effect on the cathodic polarization measurements (Fig. 4) while its effect on anodic polarization is irreproducible.

Acknowledgment

The authors wish to express their thanks to Professor A. R. Tourky for his interest in this work.

Manuscript received Sept. 11, 1958.

Any discussion of this paper will appear in a Discussion Section to be published in the June 1960 JOURNAL.

REFERENCES

1. U. Evans, "Metallic Corrosion Passivity and Protection," p. 404, Edward Arnold, London (1945).
2. T. P. Hoar, *J. Inst. Metals*, **55**, 135 1934).
3. R. Kerr, *J. Soc. Chem. Ind.*, **65**, 101 (1946).
4. R. Kerr, R. M. Angles, and K. Caulfield, *ibid.*, **66**, 5 (1947).
5. R. M. Angles and R. Kerr, *Engineering*, **161**, 289 (1946).
6. S. Britton and R. Angles, *Bull. Inst. Metal Finishing* (London), **3**, 259 (1953-1954).
7. S. Britton and D. Michael, *J. Applied Chem.*, **7**, 349 (1957).
8. H. Uhlig, D. Triadis, and M. Stern, *This Journal*, **102**, 59 (1955).
9. R. Morgan and R. Swoope, *Ind. Eng. Chem.*, **35**, 821 (1943).
10. B. Raistrick, *Chemistry & Industry*, **1952**, p. 408.
11. I. A. Ammar and S. Awad, *J. Phys. Chem.*, **60**, 837 (1956).
12. J. Mansa and W. Szybalski, *Acta Chem. Scand.*, **4**, 1275 (1950).
13. M. Stern and A. Geary, *This Journal*, **104**, 56 (1957).

Thin Film Formation on Zirconium

Robert E. Meyer

Chemistry Division, Oak Ridge National Laboratory,

operated by Union Carbide Corporation for the U. S. Atomic Energy Commission, Oak Ridge, Tennessee

ABSTRACT

Using an electrochemical method, rates of film growth in oxygenated sodium sulfate solutions have been measured on polycrystalline zirconium at temperatures ranging from 25° to 88°C. The resulting rate-time plots are roughly hyperbolic. A model is proposed which when treated by electrode kinetics is shown to give this type of behavior.

Recently, correlations have been observed between the polarization resistance of a corroding electrode and its corrosion rate (1-3). The polarization resistance of an electrode is defined as the derivative $dE/dI_{E\to E_r}$ where I is the net current flowing through the electrode at a measured potential E, and E_r is the rest potential. Theoretical justification for this correlation has been provided by Stern and Geary (4) who derive the following equation from the Tafel equation for the case where the rest potential of a corroding electrode is determined by the intersection of two logarithmic polarization curves

$$\frac{dE}{dI_{E\to E_r}} = \frac{b_a b_c}{(2.3)(I_{corr})(b_a + b_c)} \qquad [1]$$

Here, I_{corr} is the corrosion rate of the electrode, and b_a and b_c are the Tafel slopes ($dE/d \log I$) for the anodic and cathodic reactions. This equation has been derived from more fundamental quantities by Posey (5), who has presented a complete discussion of the kinetics of polyelectrodes under activation control. If the conditions for the use of Eq. [1] can be met, it provides an excellent method for measuring rates and should be applicable especially to systems whose rates may be too small for weight-loss or analytical methods. Because rates can be measured quickly while the sample remains in the solution without significantly disturbing the system, this method is applicable particularly to the determination of rate-time plots.

In order to use this method, it must be shown that the open-circuit potential is determined by the intersection of two logarithmic polarization curves, one anodic and one cathodic. Furthermore, there must be no oxidation process other than the corrosion process under consideration, i.e., one must make sure that no portion of the anodic current is the oxidation of hydrogen, water, ferrous ion, or other oxidizable species.[1] It should be evident also that the presence of a film does not necessarily preclude the method, for logarithmic potential-current behavior is possible also on film-covered electrodes.

[1] It is, of course, possible in many cases to take a second oxidation reaction into account and determine the corrosion rate from electrochemical measurements alone, but this involves the analysis of far more complex polarization behavior [see Stern (6) and Posey (5)].

In the experiments reported here, this method was applied to the measurement of film growth on zirconium immersed in oxygen-saturated 0.1 F Na_2SO_4 of pH 3.5. The reaction believed to occur is the oxidation of zirconium to zirconium oxide (7), ZrO_2. The cathodic or reduction process is therefore the reduction of oxygen and the anodic or oxidation process is the oxidation of zirconium. Because of the great insolubility of ZrO_2, all oxidized zirconium is assumed to be incorporated into the film. Other possible cathodic processes are the reduction of hydrogen ions or water and the reduction of the film. The latter process is thermodynamically improbable at these potentials, and measurements of hydrogen evolution (to be reported in a later publication) showed that the rates are negligible under the conditions encountered in these experiments.

The possible interfering anodic processes are the oxidation of impurities and the oxidation of water. Careful purification of the solution and cell can eliminate the former and also at the same time eliminate impurities that may interfere with the kinetics of the cathodic process. Significant water oxidation on these systems is not observed until one obtains potentials at least 1.5 v above the highest potentials encountered in this work. Therefore, it is probable that the rate of water oxidation is negligible at potentials near SCE.

Typical polarization behavior of this system is shown in Fig. 1. Here it is demonstrated that the reduction of oxygen follows an equation of the form

$$I_c = I_{o,c} \exp \frac{-\alpha_c z_c E \mathrm{F}}{RT} \qquad [2]$$

where α_c is the transfer coefficient of the cathodic process, z_c is the charge number, and $I_{o,c}$ is a constant whose numerical value depends on the reference potential to which values of E are referred. This equation is the Tafel equation written in the exponential form with $b_c = RT/\alpha_c z_c \mathrm{F}$.

An analogous equation is assumed for the anodic current, I_a, at constant film thickness, as follows

$$I_a = I_{o,a} \exp \frac{+\alpha_a z_a E \mathrm{F}}{RT} \qquad [3]$$

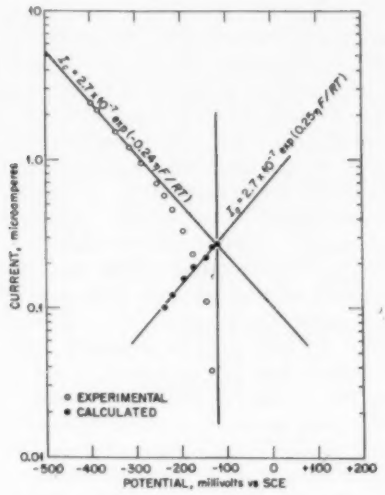

Fig. 1. Experimental current-potential plot in oxygenated Na_2SO_4 solution at 88°C.

where α_a and z_a are the transfer coefficient and charge number, respectively, of the anodic reaction. This assumption is made reasonable by the theoretical considerations described below which led to the derivation of Eq. [6]. An equation of the form of Eq. [3] has been reported valid for the anodizing of zirconium at constant film thickness by Adams and Van Rysselberghe (8).

Equation [1] can be solved for I_{corr} and rewritten in terms of the variables in Eq. [2] and [3] as follows

$$I_{corr} = \frac{dI}{dE_{E \to E_r}} \times \frac{RT}{F} \times \frac{1}{(\alpha_a z_a + \alpha_c z_c)} \qquad [4]$$

The quantities $\alpha_c z_c$ and $\alpha_a z_a$ can be determined from Tafel slopes, but generally it is better to determine $\alpha_a z_a$ indirectly. Excessive anodic polarization can affect the surface materially by forming significant quantities of film, and therefore it is best to avoid large anodic polarizations entirely. An indirect method[2] of determining $\alpha_a z_a$ which does not involve excessive polarization is illustrated in Fig. 1. Here the anodic polarization points are determined by the difference between the net current and the extrapolated cathodic current. The Tafel slope, and hence $\alpha_a z_a$, is determined then from the slope of the line through these points. At the end of an experiment, when there is no need for further measurements, it is possible to check the value of $\alpha_a z_a$ by direct anodic polarization. Of course, the voltage rises with time when zirconium is anodized at constant density, but if the current density is small enough, the voltage rise during the measurement will be negligible. At the end of an experiment, these small current densities are sufficient to obtain a Tafel slope, from which $\alpha_a z_a$ may be estimated.

The quantity $dI/dE_{E \to E_r}$ can be determined by plotting I vs. E on a linear scale and by determining the slope at $E = E_r$. Since the I vs. E plot is linear over a short potential range about the rest potential, the slope can be determined very easily from several polarizations at small overvoltages.

In general, $\alpha_a z_a$ and $\alpha_c z_c$ do not vary rapidly in an experiment and therefore need be determined only occasionally. Rate-time curves can be determined therefore by a series of small polarizations, which determine $dI/dE_{E \to E_r}$, along with a few complete cathodic polarization curves.

Normally it is desirable to obtain a longer linear Tafel region than shown in Fig. 1, but concentration polarization is likely to interfere if the current density is further increased. The linear Tafel slope was verified by a great many plots similar to Fig. 1, many of which had considerably longer linear regions.

It should be noted here that this method of measuring rates is independent of mechanism since it only requires that equations of the form of Eq. [2] be obeyed formally over the potential and current ranges used.

Experimental

The measurements were carried out in 100 cc Pyrex cells which contained the zirconium electrode, an inlet and exit for oxygen, a platinum polarizing electrode, and a Haber-Luggin capillary leading through an all-glass closed stopcock to a separate chamber which contained a saturated calomel electrode. Oxygen was introduced through the inlet vigorously in order to provide sufficient stirring and to insure saturation. No greases or waxes of any kind were used in the cell, the only nonglass material used being Teflon. The zirconium electrodes, which were machined from fine-grained ¼ in. crystal bar rod and had an area of 2.2 cm^2, were cylinders ⅜ in. long and ¼ in. in diameter. They were mounted on ¼ in. Teflon rod holders which effectively masked off one end of the cylinder, electrical contact being maintained by a stainless steel rod threaded into the center of the masked-off end of the cylinder. The steel rod was masked completely from the solution by passing it through a hole drilled down the axis of the ¼ in. Teflon rod.

Before immersion in the cell, the electrodes were cleaned and immersed in a H_2O-HNO_3-HF chemical polishing bath long enough to remove several mils of metal. They then were rinsed with triply distilled water several times and finally immersed for 2 min in boiling triply distilled H_2O. This procedure was carried out by rapidly transferring the electrode from beaker to beaker so that the liquid never was allowed to dry on the surface. If the polishing solution were allowed to dry on the surface, a white insoluble residue would be left which defied all attempts at removal except by a repeated immersion in the polishing solution. The electrodes then were placed in a dynamic greaseless vacuum system and annealed for several hours at 750°C. The hottest portion of the furnace contained a supply of zirconium chips which acted as a getter. The electrodes so treated undoubtedly had a residual thin film on the surface even before the 1-min exposure to air during the process of mounting the electrodes on the Teflon holder. The initial rates observed were still

[2] This and another method for determining the anodic Tafel slope knowing the complete cathodic polarization curve have been described by Stern and Roth (9).

faster than could be measured by the methods used, so that there seemed to be no point to taking elaborate precautions to minimize the initial film.

The solutions used were made up from triply distilled water, doubly recrystallized sodium sulfate, and a small amount of C.P. H_2SO_4. One of the water distillations was made from alkaline permanganate solution. The solutions were pre-electrolyzed between platinum electrodes a minimum of 24 hr at about 10 ma before use. At this current the potential of the cathode was well below the lowest potential observed on the zirconium electrode.

The cells were cleaned with ordinary dichromate cleaning solution and with a hot mixture of equal parts of water, concentrated HNO_3, and concentrated H_2SO_4. The latter solution very efficiently removed the last traces of greases and other contaminants from the surface of the cell. The cells then were rinsed thoroughly with triply distilled water, one of the rinses including a 24-hr soaking with hot stirred water.

Potentials were measured with a L&N Model 7664 *p*H and emf meter which was modified slightly so that its output could be fed into a 10-mv Brown recorder. This whole unit was calibrated periodically with a potentiometer, and the absolute accuracy was about ±1 mv on a 1000 mv range or ±0.5 mv on a 100 mv full-scale range. The high input impedance of the *p*H meter, about 10^{11} ohms, effectively prevented any polarization of the electrode by the measuring circuit and also made the meter suitable for measuring small currents by measuring the potential drop over high-value resistors.

The small currents used were supplied by a bank of radio "C" batteries connected in series so that up to 230 v could be obtained. In order to maintain constant current a large resistance was placed in series in the polarizing circuit. The resistors were connected to a battery of decade switches so that any resistance from 0 to 10^7 ohms could be obtained quickly. This variable resistance plus a second switch which selected several voltages provided a convenient way of obtaining any necessary current.

A typical experiment was carried out as follows: the cell was cleaned, and the solution and electrode prepared as described above. At the completion of the cooling period after the vacuum anneal the electrodes were mounted quickly on the electrode holder and immersed in the prepared solution with the potential-measuring device on. The potential was recorded continuously during the experiment, and both small and complete polarization curves were taken at appropriate intervals. Care was taken to insure that the polarization did not alter the course of the experiment significantly. In most cases a duplicate experiment was made without any polarization in order to see whether the potential-time behavior duplicated and to compare rates at the end of the duplicate experiment to rates of those experiments which had the normal amount of polarization.

Calculations and Results

Because each of the experiments necessarily involves a large amount of data, results are presented as plots of rates vs. time and the values of the polarization resistance and α will not be given. In order to draw a smooth curve between the experimentally determined points, a semi-empirical method of determining the rates from the potential was used. As was pointed out above, the cathodic current is given by Eq. [2]. Experimentally it was found that the constants $I_{o,c}$ and $\alpha_c z_c$ changed very little in a given experiment (if $I_{o,c}$ is defined always at the same reference potential). Therefore a plot of the corrosion potential vs. the logarithm of the corrosion rate, which is necessarily equal to the cathodic current at the corrosion potential, should be either a straight line of slope $RT/\alpha_c z_c F$ (for the case of constant $I_{o,c}$ and $\alpha_c z_c$) or a gently curving line (for the case of slightly varying $\alpha_c z_c$ and $I_{o,c}$). Such a plot is shown in Fig. 2 for an experiment at 88°C, the open circles on the plot representing points determined from Eq. [4]. Because the potential-time behavior is known from the continuous potential recording, the rate-time curve can be found by combining the rate-potential and potential-time plots. In Fig. 3, the potential-time behavior of this experiment (No. 4) is given along with the potential-time behavior of a number of other experiments at about the same temperature. In Fig. 4 and 5 the rate-time curves are shown for two experiments each at 25°, 46°, 66°, and 88°. Rates are given as total current; current density may be obtained by dividing the numbers in the graph by 2.2 cm², the area of the electrodes. The notable features of the rate-time curves are the very sharp initial decline and the gradual leveling off. The shapes of the curves are approximately hyperbolic in time and rate. The open circles on the one 88° experiment in Fig. 5 show points de-

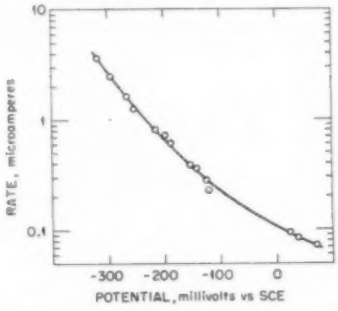

Fig. 2. Corrosion rate vs. open-circuit potential for zirconium in oxygenated Na_2SO_4 solution at 88°C.

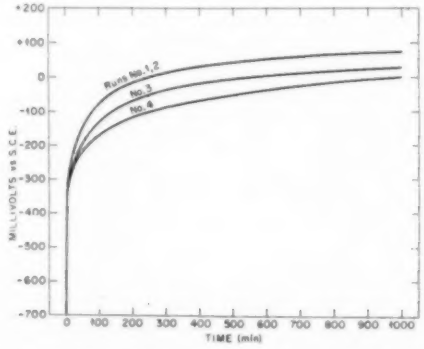

Fig. 3. Potential-time curves for crystal bar zirconium at 88°C in Na_2SO_4 solution.

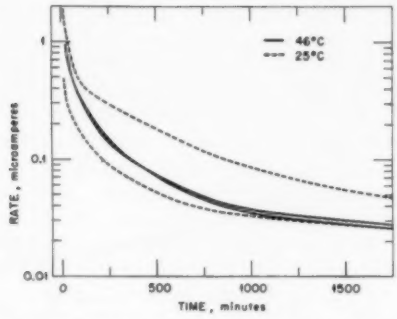

Fig. 4. Corrosion rate vs. time for zirconium in oxygenated Na_2SO_4 solution at 25° and 46°C.

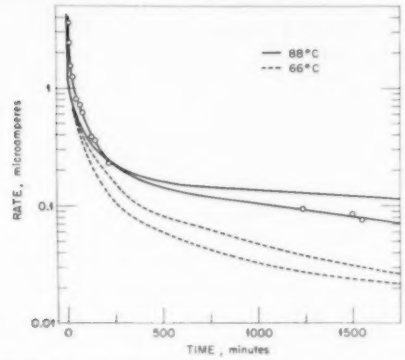

Fig. 5. Corrosion rate vs. time for zirconium in oxygenated Na_2SO_4 solution at 66° and 88°C.

termined directly by Eq. [4]; the rest of the curve was determined by the method described above.

It will be noted from Fig. 3 that the potential time curves do not exactly duplicate, although the general shape is the same. Because the rate changes by one power of ten for about every 300 mv change in potential, it is clear that a difference of 100 mv at a given time is not a serious irreproducibility. It is clearly impossible to duplicate precisely the surface of the electrode or the initial film thickness. The fact that the curves are as smooth as they are is of some significance, since such smooth curves could be obtained only if adequate solution purification and careful electrode preparation were carried out; otherwise jagged potential-time plots were observed.

As mentioned above, the constants $I_{o,c}$ and $\alpha_c z_c$ for the reduction of oxygen stayed fairly constant in a given experiment, i.e., the current-potential plots were almost superimposable. On the other hand, $\alpha_a z_a$ decreased with time, especially at 88°. In a typical experiment at 88°, the first determination of $\alpha_a z_a$ might yield a value as high as 0.3 or 0.35 while after several days $\alpha_a z_a$ might be as low as 0.1.

Discussion

Before attempting to describe the results in any mathematical form, some of the complexities of this system should be discussed. First, one has to be careful about applying the concept of a "single rate-determining step" since there are always two half-reactions present, anodic and cathodic, in any oxidation, and only if one were practically at equilibrium would it be justifiable to say that the other is a single rate-determining reaction. In the system considered here, neither the anodic nor the cathodic reaction is at equilibrium; hence, they both control the rate of the reaction. Furthermore, it is conceivable that in either the anodic or cathodic process there are two or more reaction barriers such that the concepts of consecutive reactions must be considered to analyze the system. Consecutive reactions are especially likely to occur in three-phase systems of the type considered here, when one must consider charged-particle transfer through the metal-film and film-solution interfaces and through the bulk of the film.

Another complexity that very likely occurs is the heterogeneous growth of the film. Variations in thickness and shape of the films can be produced easily by variations in activation energies and other kinetic factors which are caused by the presence of defects, grain boundaries, various exposed crystal faces, etc. Thus the actual growth of a film even in a carefully controlled experiment is very complex. The theoretical treatment of heterogeneous growth is extremely complex and, in common with most treatments of film growth, uniform growth will be assumed here.

The pertinent experimental facts that must be explained are the rapid decrease in rates, the decrease in α_a, and the rise in potential. The basic hypothesis that leads to an explanation of these observations is that a portion of the total potential drop occurs in the film and the field in the film decreases as the film thickens[2] and the potential changes. The field strength will be given by

$$F = \frac{V}{X} = \frac{V}{X_o + R\int I dt} \qquad [5]$$

where F is the field strength, V is the potential drop across the film, X is the film thickness, X_o is the initial film thickness, $\int I dt$ is the total charge passed, and R is the factor relating charge to thickness. If the structure of the film and the area of the electrode are known, R can be calculated easily. It will be assumed that the anodic current is controlled by a field-dependent rate-determining process within the film such that the activation energy will be lowered by the amount $(z_a elV)/(X_o + R\int I dt)$ where $(z_a e)$ is the charge of the moving particle and l is the distance through which the force acts. This rate-determining process could be the movement of an ion from one equilibrium position to another, and the location of the barrier to this movement could be either at one of the interfaces or in the bulk of the film. Neglecting any reverse current in the film, the anodic current will be given by

$$I_a = I_{b,a} \exp \frac{z_a elV}{(X_o + R\int I dt)kT} \qquad [6]$$

This equation, in the simpler form $I_a = A \exp BF$, where A and B are constants, has been verified ex-

[2] Such an explanation was proposed by Cabrera and Mott (11) in their treatment of thin films, but their subsequent treatment is different from that proposed here.

perimentally for the anodizing of zirconium by Charlesby (10); and a similar equation has been derived by Cabrera and Mott (11). The constant $I_{k,a}$ will contain a concentration term, a frequency factor, and an exponential term in activation energy. The assumption that reverse movement of the ions is negligible is good for high field strength or for a very high activation energy for movement in the reverse direction. The latter condition is most probable if the principal barrier to particle movement is at one of the interfaces. If there is a symmetrical energy barrier such as might occur in the bulk of a film, then the reverse current will not be negligible at low field strength.

The reduction of oxygen will entail a flow of electrons through the film against the field. It will be assumed that the height of this potential barrier in the film will determine the flow of electrons in the manner represented by

$$I_e = I_{k,e} \exp\ (-\alpha_e' eV/kT) \qquad [7]$$

The constant α_e' should be distinguished from α_a of Eq. [2] because the former affects only the film potential and the latter affects the total potential including the double-layer potential at the film-solution interface.[4] This assumption is not strictly valid and agrees only approximately with experiment. The experimental α_a value decreases during the course of the experiment although not nearly as much as α_a decreases. This decrease in α_a could easily be due to changes in α_e'. Electronic film resistances are assumed negligible since the films are on the order of 100Å or less thick.

Equations [6] and [7] may be combined with the elimination of eV/kT to give

$$X_o + R\int I dt = -\frac{z_a l \ln\ (I/I_{k,c})}{\alpha_c' \ln\ (I/I_{k,a})} \qquad [8]$$

recalling that $I_a = I_c = I$ at open circuit.

Differentiating with respect to time, Eq. [8] results in

$$\frac{dI}{dt} = -\frac{\alpha_c' R I^2 [\ln\ (I/I_{k,a})]^2}{z_a l \ln\ (I_{k,c}/I_{k,a})} \qquad [9]$$

or

$$\frac{dI}{dt} = -AI^2 [\ln(I/I_{k,a})]^2 \qquad [9a]$$

where $A = \dfrac{\alpha_c' R}{z_a l \ln\ (I_{k,c}/I_{k,a})}$.

Equation [9] can be integrated but the result is a series which is not easy to use. It is more convenient to integrate it graphically for various values of $(I/I_{k,a})$. Since the variation in the term $[\ln(I/I_{k,a})]^2$ is small compared to changes in I^2, a useful approximate integration can be made by assuming that $\ln(I/I_{k,a})$ is constant. This assumption may be further improved by the possibility that $I_{k,a}$ may decrease slightly with time along with I. Because particles in low activation energy positions are likely to react first in preference to particles in higher activation energy positions, the over-all average activation energy is likely to be increased and therefore $I_{k,a}$ decreased. If then $\ln(I/I_{k,a})$ is assumed constant, Eq. [9a] integrates to

$$1/I = A[\ln(I/I_{k,a})]^2 t + K \qquad [10]$$

where K is an integration constant. Equation [10] is, of course, a hyperbola.[5]

The behavior of these functions is shown in Fig. 6 where Eq. [10] is plotted along with the results of the graphical integration of Eq. [9]. In order to emphasize the differences of the shapes of the curves, the constants are chosen so that all functions will have the same values at currents (rates) of one and 100. There is obviously little difference in the shape of the curves unless $I/I_{k,a}$ is less than about 10^1, which will occur for small fields. Thus these equations would predict that the rate-time behavior is almost hyperbolic at high field strength (or the thickness-time behavior is almost logarithmic). In Fig. 7 it is shown that by the proper selection of the constants, the theoretical expressions can account for experimental plots. For the sake of clarity, only three rate-time curves are shown, but the others can easily be fitted also. Of course, with three arbitrary constants, A, K, and $I_{k,a}$, this is relatively easy, so that all that Fig. 7 shows is the possibility that the theoretical expressions can account for the experimental rate curves.

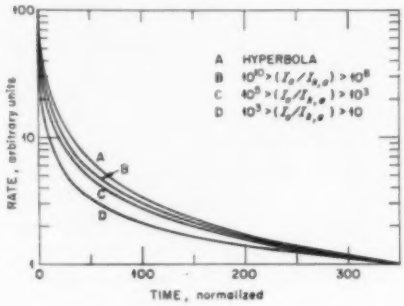

Fig. 6. Theoretical rate-time curves

[4] Experimental evidence obtained by the author suggests that the reduction of O_2 is best represented by a dual-barrier model, one barrier occurring at the film-solution double layer, and the other in the film as described above. For a more complete description of the dual-barrier model see Posey (12).

[5] This derivation is similar mathematically to a derivation presented by Vetter (13) for film growth at constant potential. It is interesting that film growth at constant potential and at open circuit follow essentially the same kinetics.

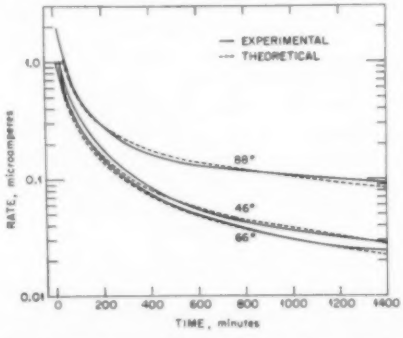

Fig. 7. Comparison of theoretical and experimental corrosion rates of crystal bar zirconium in oxygenated Na_2SO_4 solution.

It is appropriate to estimate the value of the constant A in order to see if it has the correct order of magnitude. This involves mainly an estimate of the quantity R, which relates charge to thickness of film. Assuming the film to be ZrO_2 of density 5.5 g/cc, R is equal to 5.79×10^{-6} cc/coulomb ÷ area. For these specimens of 2.2 cm^2, R is equal to 2.63×10^{-6} cm/coulomb. The constant α_c' will be assumed to be about one, l will be assumed to be 3×10^{-8} cm, z_a will be assumed to be 2 corresponding to oxide ion migration, and the term $\ln (I_{k,c}/I_{k,a})$ will be assumed to be of the order of magnitude of ten.[6] Using these values A turns out to be about 40 $coulombs^{-1}$. In Fig. 7, the 46° and 88° runs are fit by the graphically integrated form of Eq. [9] with A equal to 3.4 and 190, respectively, and $I_{k,a}$ assumed to be 1.1×10^{-9} A at 88°C and $10^{-12}A$ at 46°. The 66° run was fit by the hyperbola $1/I = 540\ (t + 960)$, t being the time in seconds (the graph gives time in minutes). Since a hyperbola was used, $I/I_{k,a}$ must be greater than about 10^5 and hence $[\ln(I/I_{k,a})]^2$ must be greater than about 130 and A, which is equal to $540/[\ln (I/I_{k,a})]^3$ according to Eq. [10], must be less than about 4. Of course these values depend on how one decides to fit the curve, but they do not change their order of magnitude for various attempts at fitting the curves. The determined values of A therefore seem to be correct as to order of magnitude.

The rise in potential which is observed in these experiments is simply the result of the decrease in anodic current at a given potential due to film thickening. In order that anodic and cathodic currents always remain equal, the potential must rise, since the anodic current must increase and the cathodic current decrease as the potential rises.

The effect of temperature is complicated as can be seen by comparing the rate expressions at various temperatures. In order to obtain meaningful data from the temperature effects, values of $I_{k,a}$ and $I_{k,c}$ would have to be known with considerable precision. However, comparison of the rate-time curves shows that, with the exception of one of the 25° experiments, the rates were considerably higher at 88° than at the other temperatures. There is therefore much more film growth in these experiments, and this accounts for the fact that the decrease in α_a was far more noticeable in the 88° experiments than in the other experiments. The experiments at 25°C should not be given much significance since there was considerably more scatter in the data leading to the (smoothed) rate-time curves shown in Fig. 4.

The expressions given here can account for the shape of the rate-time curves, but it is clear that more information is needed on the mechanisms of the cathodic and anodic processes. Probably such information is obtained best by isolating the individual processes and studying them alone. Such studies now are being carried out, and the reduction of various reducible species on film-covered zirconium will be the subject of a future communication.

[6] This estimate results from the probability that the activation energy for the anodic process is higher than that for the cathodic process. Admittedly this estimate of ten for the value of $\ln(I_{k,c}/I_{k,a})$ is only a guess.

Acknowledgment

The kind encouragement and helpful discussions of Dr. G. H. Cartledge, Dr. F. A. Posey, and Dr. A. L. Bacarella, all of this Laboratory, are gratefully acknowledged.

Manuscript received March 2, 1959.

Any discussion of this paper will appear in a Discussion Section to be published in the June 1960 JOURNAL.

REFERENCES

1. K. F. Bonhoeffer and W. Jena, *Z. Elektrochem.*, **55**, 151 (1951).
2. R. V. Skold and T. E. Larson, *Corrosion*, **13**, 69 (1957).
3. M. Stern, *ibid.*, **14**, 440t (1958).
4. M. Stern and A. L. Geary, *This Journal*, **104**, 56 (1957).
5. F. A. Posey, *ibid.*, **106**, 571 (1959).
6. M. Stern, *ibid.*, **104**, 645 (1957).
7. R. D. Misch, "Electrode Reactions of Zirconium Metal," in "The Metallurgy of Zirconium," p. 663, McGraw-Hill Book Co., New York (1955).
8. G. B. Adams, Jr. and P. Van Rysselberghe, *This Journal*, **102**, 502 (1955).
9. M. Stern and R. M. Roth, *ibid.*, **104**, 390 (1957).
10. A. Charlesby, *Acta Metallurgica*, **1**, 340 (1953).
11. N. Cabrera and N. F. Mott, *Repts. Prog. Phys.*, **12**, 163 (1948-1949).
12. F. A. Posey, G. H. Cartledge, and R. P. Yaffe, *This Journal*, **106**, 582 (1959).
13. K. J. Vetter, *Z. Elektrochem.*, **59**, 67 (1955).

The Oxidation of Iron-Nickel Alloys

III. Kinetics of Oxidation of Three Commercial Alloys

R. T. Foley and C. J. Guare

General Engineering Laboratory, General Electric Company, Schenectady, New York

ABSTRACT

Three commercial iron-nickel alloys, containing 30, 41, and 78% nickel, were oxidized over the range 600°-1000°C in two atmospheres, laboratory air, and a 21.7% O_2-78.3% N_2 mixture. The oxidation of these alloys follows a parabolic weight gain-time relationship during the 60-min reaction time. Replicate experiments generally showed that the precision in determining the parabolic rate constants was better in the O_2-N_2 mixture than in laboratory air. This effect is probably the result of day-to-day variations in composition of laboratory air. Temperature dependences of the reaction rates were determined with the Arrhenius-type equation. Both the reaction rates and the apparent energies of activation of the 30-41% alloys are consistent with a rate-determining process of cation diffusion through a spinel structure $Ni_x Fe_{3-x} O_4$. It is hypothesized that the apparent energy of activation for the 78% alloy is due to the influence of the 3.8% Mo on the physical character of the film. Anomalously high rates were observed in both atmospheres at the higher temperatures, and this is discussed with reference to "over-temperatures," resulting from heat generated at the surface by oxidation.

An earlier study (1) had as its objective outlining the mechanism of high-temperature (600°-900°C) oxidation of an iron-nickel alloy containing 42% nickel. It had been pointed out that the iron-nickel system was of theoretical interest because these two elements form a continuous series of substitutional solid solution alloys with both components oxidizable. Furthermore, iron-nickel alloys of various compositions are used industrially for such purposes as glass-to-metal sealing, as magnetic materials, and as materials with special thermal properties. The earlier study demonstrated that the mechanism of oxidation involved diffusion through a nickel ferrite reaction product film, and the variation of activation energies and oxidation rates with surface preparation was explained on the basis of diffusion through ferrite structures of varying percentages of nickel. This study extends this work to two other commercial alloys and special atmospheres. Oxidation was studied over the temperature range 600°-1000°C. The objective of this paper is to report and interpret kinetic data so that ultimately a complete understanding of the mechanism of oxidation of iron-nickel alloys may be realized. It is expected that work reported and underway in two other laboratories (2-4) as well as in our own, will achieve this contribution to general oxidation theory.

Experimental

Oxidation Studies

The oxidations were carried out employing a Chevenard thermobalance. In this instrument the sample to be oxidized is supported on a fused silica rod and the furnace, at the desired temperature, is lowered around it. The change in weight of the sample is recorded automatically as a function of time.

Experiments were run at 600°, 700°, 800°, 900°, and 1000°C. The temperature of the furnace was controlled to ±1.4°C according to a General Electric protable precision potentiometer. This instrument was calibrated to be accurate to 0.05%. Usually the oxidation was allowed to proceed for 60 min. Two atmospheres were employed. The first was static laboratory air. This certainly changed from day to day because of humidity variation and other influences, all of which have not fully been assessed in high-temperature oxidation work. (Some of the experiments described here were made several years apart.) The second atmosphere consisted of a controlled mixture, 21.7% oxygen and 78.3% nitrogen by volume flowing at a rate of 263 ml/min. The dew point of this mixture was −20°F. In all cases at least duplicate, and usually triplicate, samples were oxidized. Weight changes were taken from the thermobalance curve at 6-min intervals and replotted to establish the rate constant. The spread of the parabolic rate constants is apparent from the tables listing the results. Usually this spread was less than ±6% of an average value. Where poorer precision was obtained, the experiment had usually been run in laboratory air. In several instances the first duplicate runs were within 3% of an average value. The experiment repeated several months later gave values with about the same precision. However, the first average might vary from the second by 60%. This must be due to variation in the composition of the atmosphere; experiments are now being run to clarify this point.

Composition of alloys.—The three iron-nickel alloys investigated represent compositions of interest to the electrical and electronics industry. Alloy A was nominally 30% Ni, 70% Fe; Alloy B—41% Ni, 59% Fe; Alloy C—78% Ni, 18% Fe, and 4% Mo.

Complete analyses of these alloy strips before oxidation were given in a previous report (5). Reanalysis for carbon gave a corrected value of 0.001% rather than the 0.01% reported. This agrees with what would be expected from the heat treatments. The alloys were obtained[1] in the form of strip 0.050-0.076 cm thick. The sheared coupons were annealed for 2 hr at 1125°C in hydrogen and then cooled in hydrogen to room temperature. Before oxidation the panels of about 20 cm^2 area were cleaned chemically.

Surface preparation.—The alloy strips were chemically cleaned at 90°C for 2 min in an acid mixture and with a procedure described before (5). The intent was to oxidize a surface free of disturbed metal. Electron diffraction examination of a surface prepared by this method gave only the pattern corresponding to the iron-nickel alloy (1). An objection to acid cleaning a binary alloy might arise from the possibility of selective dissolution. Presumably in an iron-nickel alloy the iron would be selectively dissolved, yielding a nickel-rich surface which would exhibit a lower oxidation rate. The magnitude of this effect was assessed by preparing samples of the 41% nickel alloy for oxidation at 900°C in the controlled O_2/N_2 atmosphere, the only variation in treatment being the time of pickling. The parabolic rate constant varied as follows:

Time in acid bath at 90°C min	k_p (x 10^{10} g^2cm^{-4} sec^{-1}
2	4.00, 3.94 avg 3.96
4	3.77, 3.54 avg 3.66
6	3.77, 3.54 avg 3.66

The extended pickling decreased the measured oxidation rate by 7.5%.

Electron Diffraction Analyses of Films

Electron diffraction analyses by the reflection technique were made with a General Electric electron diffraction instrument. This instrument was equipped with an attached high-temperature furnace enabling one to study the oxidation products at the temperature of reaction. These experiments, as well as the equipment, are described in more detail in another report (5).

Treatment of Data

The oxidation rate for these iron-nickel alloys may be represented by the parabolic rate equation:

$$(\Delta m)^2 = b + k_p t \qquad [1]$$

where Δm is gain in weight in g/cm^2 of a sample oxidized for t seconds; k_p is the parabolic rate constant expressed in $g^2cm^{-4}sec^{-1}$; b is a constant (g^2cm^{-4}).

The temperature dependence for the reaction is best described by an Arrhenius type equation as:

$$k_p = Ae\frac{-\Delta E^*}{RT} \qquad [2]$$

in which ΔE^* is termed the apparent energy of activation and A the frequency factor. As discussed below, the significance of ΔE^* derived from the Arrhenius plot must be interpreted with caution at elevated temperatures.

[1] From the Carpenter Steel Company.

Table I. Parabolic rate constants for Alloy A (30% Ni), k_p (g^2 cm^{-4} sec^{-1})

t, °C	Laboratory air	O_2-N_2 mixture
600	1.18×10^{-12} 1.07 1.09	1.26×10^{-12} 1.28
700	1.39×10^{-11} 1.38	1.54×10^{-11} 1.38
800	9.4×10^{-11} 8.4	8.7×10^{-11} 8.2 8.7
900	1.32×10^{-9} 1.25 0.98	5.3×10^{-10} 5.1
1000	$a = 1.01 \times 10^{-9}$ $a = 0.98$ $a = 0.95$ --- $b = 1.75$ $b = 1.65$ $b = 2.05$	3.5×10^{-9} 3.2 3.2

Results

Results for Alloy A (30% Ni)

The parabolic rate constants, k_p in Eq. [1], are listed in Table I. Generally, the precision of the rate constants obtained in the controlled atmosphere is better than of those obtained in laboratory air. For all of the runs with alloy A, the average deviation from the mean for 2 or 3 runs was ±3.0% in the controlled atmosphere and ±5.4% in laboratory air. If duplicate runs were made in laboratory air on the same day, however, the precision would be ±2-3%. At 600°, 700°, and 800°C there is apparently no definite influence of the atmosphere by way of increased or decreased rate. At 900°C the rate in the laboratory air is greater than that in the controlled atmosphere by a factor of 2 and at 1000°C by a factor of 3.

The parabolic relationship gives an excellent representation for the data for all the controlled atmosphere data and most of the data in laboratory air. However, in the latter case at 900°C, there is a slight tendency for the plots to be concave upward. At 1000°C the k_p definitely increases after an oxidation time of about 20 min, and it is necessary to

Table II. Temperature dependence of oxidation reactions

Alloy	Atmosphere	"A" frequency factor, g^2 cm^{-4} sec^{-1}	ΔE^*, apparent energy of activation, cal/mole
A (30% Ni)	Laboratory air	0.044	41,800
	O_2-N_2 mixture	0.024	41,100
B (41% Ni)	Laboratory air	0.082	44,600
	O_2-N_2 mixture	0.020	40,900
	Ref. (1)	0.012	40,800
C (78% Ni)	Laboratory air	1.28×10^{-2}	38,230
	O_2-N_2 mixture	3.10×10^{-4}	35,450

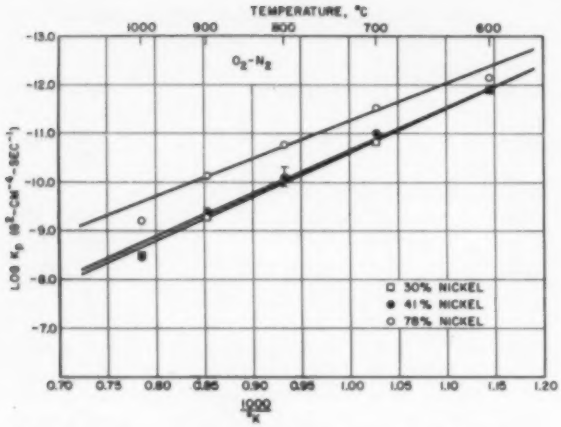

Fig. 1. Temperature dependence of oxidation rate of iron-nickel alloys oxidized in a controlled O_2-N_2 atmosphere.

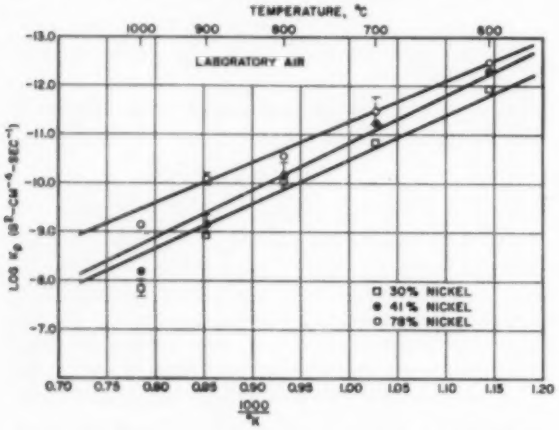

Fig. 2. Temperature dependence of oxidation rate of iron-nickel alloys oxidized in laboratory air.

represent the data by two stages. These two stages are represented by "a" and "b" in Table I. This is a reproducible effect. After the initial oxidation stage the rate almost doubles.

The temperature dependence of the reaction is described by "A" and "ΔE^*" in Eq. [2]. These quantities are given in Table II, and the curves are plotted in Fig. 1 and 2. The 5 points in the O_2-N_2 atmosphere fall close to the linear plot, but the 900° and 1000° points obtained in laboratory air fall in a direction indicating greater reaction. This point is discussed below.

Alloy B (41% Ni)

Rate constants describing the oxidation behavior of the 41% alloy are given in Table III. For comparison, results obtained about 4 years ago (1) on an alloy of almost the same composition are given. (The present alloy contained 40.9% Ni, the former contained 41.8%.) These results agree well with the present and the differences in the results are most likely due to variation in laboratory air.

In all cases excellent representation by Eq. [1] was achieved. The precision of the results obtained in the controlled atmosphere was again better than that of the laboratory air, 4.1% and 7.2%, respectively. In the last case the four 800°C values were considered as two groups. This is a good example of the variation in results, mentioned above, which is sometimes obtained when experiments are run in laboratory air many weeks apart.

The atmosphere effect in this case is not straightforward. Oxidation in laboratory air at 600° and 700°C proceeds at a rate distinctly less than in the controlled atmosphere. At 800° the rates are about the same, whereas at the higher temperature the laboratory air rate is double that in the controlled atmosphere.

The temperature dependence of the oxidation reaction is described in Table II and in Fig. 1 and 2. The actual plot of values obtained in the O_2-N_2 mixture is approximately linear within experimental error. The 900° and 1000°C values obtained in laboratory air fall off in the direction of the higher rate similar to the behavior of the 30% alloy.

Alloy C (78% Ni)

Rate constants for this alloy are listed in Table IV. The precision of runs made in the controlled O_2-N_2 atmosphere was ±6.6%, while that in laboratory air was ±15.2%. The considerable spread in results in laboratory air is explained by the variation in the composition of this atmosphere over the months the experiments were run. These data were represented quite well by a single parabolic equation of the Eq. [1] type with the exception of the 1000°C run in air. In this situation after an oxidation time of about 30 min, the parabolic plot followed a second straight line of lower slope. These two phases of reaction are given by "a" and "b" in Table III.

There was no consistent pattern established on comparison of rates in laboratory air and in the O_2-N_2 mixture. The spread of results in the laboratory air made this comparison difficult.

The temperature dependence of the reaction is given by "A" and "ΔE^*" values in Table II. In both atmospheres the 1000° point falls below the curve, indicating a higher rate of reaction than would be expected from extrapolation from the four lower

Table III. Parabolic rate constants for Alloy B (41% Ni), k_p (g^2 cm^{-4} sec^{-1})

t, °C	Laboratory air	O_2-N_2 mixture	42% Alloy (Ref. 1)
600	5.0×10^{-13} 5.1	1.14×10^{-12} 1.40	9.5×10^{-13}
700	5.6×10^{-12} 6.0	9.6×10^{-12} 9.9	7.9×10^{-12}
800	3.71×10^{-11} 4.40 1.22 1.17	4.87×10^{-11} 1.12 1.19	4.53×10^{-11}
900	4.46×10^{-10} 7.75 8.58 10.8	3.79×10^{-10} 3.89 4.65 4.00 3.94	3.67×10^{-10}
1000	7.2×10^{-9} 6.5	3.51×10^{-9} 3.51	

Table IV. Parabolic rate constants for Alloy C (78% Ni), k_p (g^2 cm^{-4} sec^{-1})

t, °C	Laboratory air	O_2-N_2 mixture
600	4.0×10^{-12}	7.0×10^{-12}
	2.8	7.3
		7.2
700	2.76×10^{-12}	3.17×10^{-12}
	1.96	3.28
	6.1	2.61
	5.9	2.96
800	2.93×10^{-11}	1.62×10^{-11}
	2.71	1.62
	2.76	1.71
	2.77	1.85
900	6.6×10^{-11}	8.5×10^{-11}
	6.3	6.2
	11.0	7.7
	9.8	7.6
1000	a = 8.4×10^{-10}	6.8×10^{-10}
	8.4	5.9
	b = 6.8	5.5
	6.1	

temperatures. The apparent energy of activation lower than that of alloy A or alloy B is significant.

Discussion

The "A" and "ΔE^*" values of Eq. [2] describe the temperature dependence for the oxidation of the three alloys and offer some clue as to the mechanism of oxidation. Based on this work and other work carried out in this laboratory, it is estimated that a value of about 41,000 cal/mole represents the heat of activation of diffusion and the heat of formation of vacancies through a structure of the composition $Ni_x Fe_{3-x} O_4$. This value is approximated by the 30% and 41% alloy. It is recognized that the oxide film on the 30% alloy and the 41% alloy is at least a duplex structure with the spinel growing at the metal-oxide interface and Fe_2O_3 further removed from the metal (1, 5). The composition of the spinel varies, being richer in Ni close to the alloy itself. Because of the duplex nature of the film and because of the variation of Ni/Fe ratio in the spinel, a theoretical derivation of the reaction rate would be difficult.

The rates summarized by the values in Table II indicate that all three of these alloys are more resistant to oxidation than iron, but not as resistant as the so-called "heat resistant alloys," typified by iron alloys containing 18% chromium, 8% nickel. This again is related to the rate-determining process, diffusion through the spinel structure. As has been pointed out by Yearian and co-workers (6), the more resistant alloys form a Cr_2O_3 type film while the more reactive alloys (in the heat resistant class) form spinel type structures upon oxidation. On the other hand, in comparison with pure iron these alloys are oxidation resistant. With alloys containing as much as 30% Ni, the formation of FeO at the alloy-oxide interface is suppressed. Diffusion of cations through the FeO structure is about 20 times as rapid as through Fe_3O_4 (3). Comparison of our results for the 30% alloy with those of Stanley (7) for iron yields rate ratios of 200-1000 rather than 20 expected on this basis. The lower rate is directly related to the Ni substitution in the spinel structure. Therefore, these alloys occupy a position on the oxidation resistant scale intermediate between iron (readily oxidized) and austenitic stainless steels (heat resistant).

The low apparent activation energy of Alloy C must be related to the presence of Mo in the alloy. Apparent activation energies of 40,000-45,000 cal/mole would be expected if the rate-determining step were diffusion through either the spinel structure or NiO, both of which are present in this alloy during oxidation at elevated temperatures. Electron diffraction examination of the alloys at elevated temperature indicates that MoO_3 is probably present in the first formed film (5). This point was not as well established as desired and more work is being done now to clarify this point. However, these prior observations fit those of Iitaka and co-workers (8) who found MoO_3 at the metal-oxide interface after oxidation of alloys of somewhat similar composition. The expectation that MoO_3 will simply evaporate and lead to catastrophic oxidation is an oversimplification. The Mo content, the Fe content, and the temperature all bear on the behavior (9). The effect of Mo, however, may be one of influencing the physical character of the film. This has been demonstrated to be a significant factor in oxidation processes, particularly where thermal cycling is involved (10).

In Fig. 1 and 2 it is very apparent that deviations occur at 900° and 1000°C, from the simple Arrhenius plot. These deviations from the Arrhenius plot may arise from changes in mechanism over the temperature range (11) or the production of local "over temperatures" on the reacting surface (12). Aside from these "experimental" causes, even on a theoretical basis one would not expect ΔE^* to be completely independent of temperature. This has been pointed out by Moelwyn-Hughes (13) and others. It is assumed here, as a first approximation, that, for a given alloy, the mechanism does not change to any considerable extent over this temperature range and an attempt is made to estimate the significance of the "over temperature."

When the reaction

$$\text{metal} + \text{gas} = \text{reaction product}$$

occurs rapidly and is accompanied by a high heat of reaction, it would be expected that the temperature of the sample would rise sensibly during the first few minutes of the reaction. This has been observed, for example, in the oxidation of iron near its melting point (14) and recently measured by Meussner and Birchenall (15). In the latter experimental work a temperature rise of 88°C was observed for the reaction between iron and sulfur at 900°C. In fact, this effect discouraged measurement of the reaction rate over 900°. Schmahl, Baumann, and Schenck (12) measured "over temperatures" during the oxidation of iron in the temperature range of 910°-950°C, to account for deviations from the parabolic law. Direct measurements of the rise in sample temperature were compared with calculated values. The calcu-

Table V. Comparison of calculated and measured over-temperatures

Alloy	Atmosphere		From Arrhenius plot (Fig. 1 and 2)	Calculated
A (30%)	Air	900°	32°	27°
		1000°	126°	106°
	O_2/N_2	900°	0°	31°
		1000°	34°	71°
B (41%)	Air	900°	43°	25°
		1000°	106°	70°
	O_2/N_2	900°	0°	18°
		1000°	52°	85°
C (78%)	Air	900°	0°	14°
		1000°	70°	39°
	O_2/N_2	900°	0°	8°
		1000°	92°	34°

lation was based on all of the heat evolved going into heating the iron panel. Following the method of Schmahl, *et al.*, we have calculated temperature rises for the three alloys. The heat evolved equivalent to the amount of oxidation occurring in the first 1½ min—the linear portion of the weight gain-time curve—was calculated. Values for the heats of formation for Fe_3O_4 of 261,700 at 900°C, and 261,800 cal at 1000°C, and for NiO, 56,770 at 900° and 56,650 cal at 1000°C were used (16). Heat capacity data (17) allowed an estimation of the temperature rise in the approximately 4-g sample employed in the experiments. This calculated value was then compared with the value on the basis that the entire deviation from the Arrhenius plot was "over temperature." Table V compares these values and there is a rough correspondence. This treatment introduces large errors, mainly in considering how the heat is dissipated. The assumption that no heat is lost by convection or radiation is obviously an oversimplification and would make the "calculated" values too high. Also, the k_p values given for 900° and 1000°C are based on a 60-min oxidation period rather than the 1½ min initial reaction time. This thermal effect is being studied more exactly because in the 1000°C range it must have an important influence on oxidation rates and their interpretation to develop an understanding of mechanism.

In a qualitative way this would in part account for the greater deviation from the Arrhenius plot observed for the 30% and 41% alloy in the (stagnant) air atmosphere in contrast to that observed in the (flowing) controlled O_2/N_2 mixture. Heat would be carried away in the gas stream in the latter case.

The oxidation of Ni-Fe alloys containing 5, 10, 20, 30% Ni over periods of up to several hundred hours has been reported by Benard and Moreau (18). The kinetics for the 20% alloy is reported up to about 15 hr. The oxidation follows a $y^n = kt$ relationship, y being the amount of oxygen picked up in time, t. At 675°C $n = 2$, indicating agreement with the parabolic relationship. At 800° $n = 2.4$ up to 5 hr and then changes to $n = 1.6$. At 900° the break in the plot is at 2 hr. Up till then $n = 2.6$ and above that 1.22. The authors postulate that during the first stage of the process the controlling factor is the diffusion of iron in the zone of the alloy depleted by a selective oxidation mechanism. During the second phase the controlling rate is the diffusion of oxygen in the superficial oxide layer. Benard and Moreau consider the significant mechanism for the Fe-Ni system to be one of selective oxidation. Some of Sachs's (19) work with low Ni alloys seems to agree in a general way. Their mechanism is based on the reduction of NiO with FeO. In our electron diffraction examination of films we have not seen FeO as a principle constituent and indeed it is rare when the patterns suggest this compound at all. Birchenall, *et al.*, have pointed out that the NiO makes for its instability (3). Our results do not support this selective oxidation mechanism. Perhaps the reason lies in the fact that these investigators have worked with alloys lower in nickel content for long times. Our work deals with relatively thin films. In our work subscale formation was not significant as it was during the lengthy experiments of Benard and Moreau.

We regard the oxidation mechanism for the 30% and 41% alloy as primarily one involving diffusion of cations through a spinel type film and for the 78% alloy diffusion through a film composed of spinel and NiO. In the latter case the MoO_2 enters into the film in a manner as yet unexplained but now under investigation in our laboratory.

Manuscript received Nov. 1, 1956. This paper was prepared for delivery before the Cleveland Meeting, Sept. 30-Oct. 4, 1956.

Any discussion of this paper will appear in a Discussion Section to be published in the June 1960 JOURNAL.

REFERENCES

1. R. T. Foley, J. U. Druck, and R. E. Fryxell, *This Journal*, **102**, 440 (1955).
2. M. J. Brabers, W. J. Heideger, and C. E. Birchenall, *J. Chim. Phys.*, **53**, 810 (1956).
3. M. J. Brabers and C. E. Birchenall, *Corrosion*, **14**, 179 (1958).
4. S. W. Kennedy, L. D. Calvert, and M. Cohen, *Trans. Am. Inst. Mining Met. Engrs.*, **215**, 64 (1959).
5. R. T. Foley, C. J. Guare, and H. R. Schmidt, *This Journal*, **104**, 413 (1957).
6. H. J. Yearian, E. C. Randell, and T. A. Longo, *Corrosion*, **12**, 515 (1956); H. J. Yearian, H. E. Boren, and R. E. Warr, *ibid.*, **12**, 561 (1956).
7. J. K. Stanley, J. von Hoene, and R. T. Huntoon, *Trans. Am. Soc. Metals*, **43**, 426 (1951).
8. I. Iitaka, T. Nakayama, and K. Sekiguchi, *J. Sci. Research Inst. (Japan)*, **45**, 57 (1955).
9. W. C. Leslie and M. G. Fontana, "Pittsburgh International Conference on Surface Reactions," p. 175, Corrosion Publishing Co., Pittsburgh, Pa. (1948).
10. J. F. Radavich, ASTM Special Technical Publication #171 (1955).
11. E. A. Gulbransen and K. F. Andrew, *This Journal*, **106**, 294 (1959).
12. N. G. Schmahl, H. Baumann, and H. Schenck, *Arch. Eisenhüttenw.*, **27**, 707 (1956).
13. E. A. Moelwyn-Hughes, "Physical Chemistry," p. 1111, Pergamon Press, London (1957).
14. W. E. Jominy and D. W. Murphy, *Trans. Am. Soc. Steel Treating*, **18**, 19 (1930).
15. R. A. Meussner and C. E. Birchenall, *Corrosion*, **13**, 677 (1957).
16. J. P. Coughlin, Bureau of Mines Bulletin 542, U. S. Printing Office, Washington (1954).
17. "Thermodynamic Properties of the Elements," American Chemical Society, Washington (1956).
18. J. Benard and J. Moreau, *Rev. Met.*, **47**, 317 (1950); *Compt. rend.*, **232**, 1842 (1951).
19. K. Sachs, *J. Iron Steel Inst.*, **185**, 348 (1957).

Oxidation Studies on the Nickel-Chromium and Nickel-Chromium-Aluminum Heater Alloys

Earl A. Gulbransen and Kenneth F. Andrew

Research Laboratories, Westinghouse Electric Corporation, Pittsburgh, Pennsylvania

ABSTRACT

A systematic study was made of the oxidation resistance of five 80Ni-20Cr heater alloys and one 4Al-19Cr-77Ni alloy. Kinetic and crystal structure studies were made over the temperature range of 500° to 1100°C. The adhesion of the oxide film to the alloy was tested by the strain oxidation technique, and the over-all performance was evaluated by the ASTM useful life tests. The rate of oxidation of the several alloys could not be correlated with the ASTM useful life results, while the strain oxidation tests could be correlated with the ASTM useful life tests. Cr_2O_3 was the major oxide formed on the 80Ni-20Cr alloys at 1100°C. Although Al_2O_3 and Cr_2O_3 were observed below 1000°C on the 4Al-19Cr-77Ni alloy, no Al_2O_3 was observed in the oxide scale at 1100°C. A thermodynamic and kinetic interpretation was made of the results.

Due to their good oxidation resistant properties, the 80 nickel-20 chromium series of heater alloys are used for severe service conditions. The addition of silicon and small amounts of calcium, zirconium, cerium, etc., has resulted in a 600% improvement in the performance of these alloys over the past 40 years as measured by the ASTM useful life test (1) for heater alloys (2-4).

Several studies have been made on these alloys to determine the chemical and physical basis for the improved performance. Using a historical series of alloys, Gulbransen and Andrew (2) showed that the rate of oxidation at constant temperature could not be correlated with ASTM useful life test results. Crystal structure studies (3, 4) of eight alloys also showed no correlation with useful life test results.

This paper presents new studies on the oxidation of the 80Ni-20Cr series of alloys and of a 75Ni-19Cr-4Al alloy. Manganese and silicon compositions were varied in the 80Ni-20Cr series of alloys. These studies include: (*a*) kinetic studies from 500° to 1100°C to determine the rate of oxidation as a function of temperature, (*b*) strain oxidation studies to evaluate the adherence of the oxide to the alloy, and (*c*) crystal structure studies on the oxide scale to determine its structure and composition. These studies are interpreted by thermochemical analyses of the chemical reactions occurring in the system and by oxidation rate theory.

An extensive review of the scientific literature was given in earlier papers (2-4). The technical aspects of heater alloys have been reviewed by Hessenbruch (5). The recent work of Pfeiffer (6) should be noted.

Experimental

Method.—A vacuum microbalance was used for all of the rate studies. Its construction and use have been described (7). In addition to our standard quartz microbalance having a sensitivity of 0.91 μg/0.001 cm deflection, a low sensitivity microbalance of 3.30 μg/0.001 cm sensitivity was used. Two sizes of specimens 0.0127 cm thick were used. The first weighed 0.6826 g and had a surface area of about 14 cm^2. The second weighed 0.5300 g and had a surface area of about 10.5 cm^2.

Samples.—The alloys were prepared, analyzed, and life tested by the Hoskins Company and by the Driver-Harris Company. Table I gives a list of the alloys, their analyses, and the results of the ASTM useful life tests (1). Alloys containing Si were represented by two alloys with a constant Mn content, while alloys containing Mn were represented by three alloys having a given Si composition. Minor changes in composition result in a threefold change in the ASTM useful life value at 1177°C.

Specimens were abraded using 1/0 to 4/0 polishing papers under purified kerosene and then cleaned with petroleum ether, soap and water, distilled water and alcohol.

Table I. Chemical analyses and useful life test data, Ni-Cr and Al-Ni-Cr alloys

Alloy	Classification	Weight %								Useful life,	
		C	Mn	Si	Cr	Ni	Fe	Ca	Al	hrs	T°C
491	Low Mn, intermediate Si	≈0.06	0.05	1.03	≈20.00	Bal.	≈0.25	0.020	0.13	105	1177
492	High Mn, intermediate Si	≈0.06	2.30	1.01	≈20.00	Bal.	≈0.25	0.035	0.15	106	1177
493	Low Mn, low Si	≈0.06	0.04	0.23	≈20.00	Bal.	≈0.25	0.028	0.20	63	1177
494	Low Mn, intermediate Si	≈0.06	0.02	0.82	≈20.00	Bal.	≈0.25	0.040	0.17	124	1177
495	Low Mn, high Si	≈0.06	0.02	2.09	≈20.00	Bal.	≈0.25	0.039	0.15	178	1177
245	High Si, high Al	≈0.03		1.44	≈19.38	Bal.			4.05	>178	1177

Table II. Oxide film thickness and oxide color 7.6 cm of Hg of O_2, 2 hr of reaction except where noted

Temp.	Alloy 493 Thickness		Color	Alloy 495 Thickness		Color	Alloy 245 Thickness		Color
	μg/cm²	A ($\rho = 1$)		μg/cm²	A ($\rho = 1$)		μg/cm²	A ($\rho = 1$)	
550	3.66	223	Straw	4.25	259	Purple	—	—	—
650	6.13	374	Purple	6.04	368	Purple	—	—	—
750	6.37	389	Blue	13.8	842	Straw-green	—	—	—
850	17.9	1,092	Blue-gray	35.1	2,141	Blue-green	—	—	—
875	—	—	—	—	—	—	116.0*	7,076	Gray
900	—	—	—	—	—	—	166.0*	10,126	Gray
950	43.1	2,629	Gray	120.0	7,320	Gray	299.0*	18,239	Gray
1000	93.8	5,722	Gray	173.0	10,553	Gray	492.0*	30,012	Gray
1050	169.0	10,309	Gray	277.0	16,897	Gray	675.0*	41,175	Gray
1100	244.0	14,884	Gray	365.0	22,265	Gray	917.0*	55,937	Gray

* 6-hr test.

The furnace tube, reaction system, and gas preparation system have been described (7, 8). Furnace temperature was maintained constant to ±1.5°C.

Strain oxidation.—The ASTM useful life test (1) involves an alternate heating and cooling cycle at 2-min intervals. At 1177°C several hundred thousands of cycles may be required to determine the useful life of a given alloy. The ASTM test involves both a test of the over-all resistance to oxidation and a test of the effect of stress developed by heating and cooling on the oxide-metal interface.

Gulbransen and Andrew developed a microgravimetric test (9) for study of the effect of a single large strain of 2% on the oxidation process. This strain oxidation test involves the following operations: (*a*) oxidizing the alloy to a given weight gain, (*b*) removal of sample from reaction system and straining 1, 2, or 4%, (*c*) reoxidation of the sample to evaluate the effect of strain on the oxidation behavior.

The effect of a strain can be studied quantitatively by comparison of the rate of oxidation before and after application of a strain. Strain can damage the oxide-metal interface and the oxide without visual evidence of cracking.

X-ray diffraction method.—Electrochemical (10) and chemical methods were used for stripping the oxide from the metal. For high Si alloys the oxide films were removed by the iodine-methanol chemical method. Oxide films were washed carefully in distilled water before being rolled on a glass capillary tube for mounting in the x-ray camera.

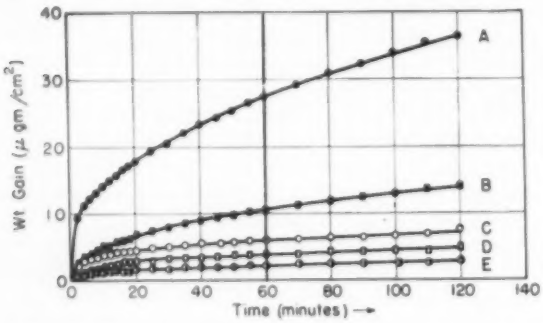

Fig. 1. Effect of temperature on oxidation of Ni-Cr alloy 493, 7.6 cm of Hg of O_2, abraded through 4/0. Curve A, 900°C; B, 800°C; C, 700°C; D, 600°C; E, 500°C.

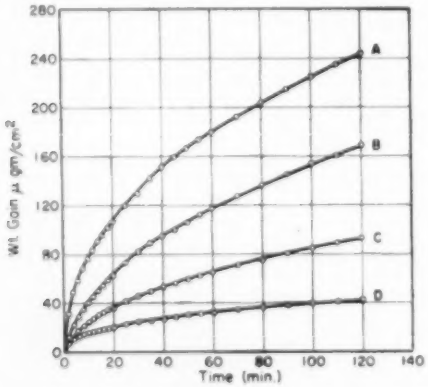

Fig. 2. Effect of temperature on oxidation of Ni-Cr alloy 493, 7.6 cm of Hg of O_2, abraded through 4/0. Curve A, 1100°C; B, 1050°C; C, 1000°C; D, 950°C.

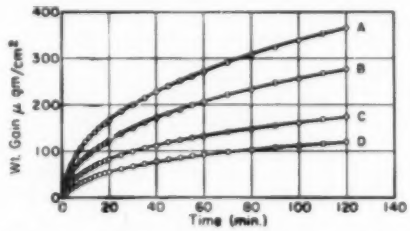

Fig. 3. Effect of temperature on oxidation of Ni-Cr alloy 495, 7.6 cm of Hg of O_2, abraded through 4/0. Curve A, 1100°C; B, 1050°C; C, 1000°C; D, 950°C.

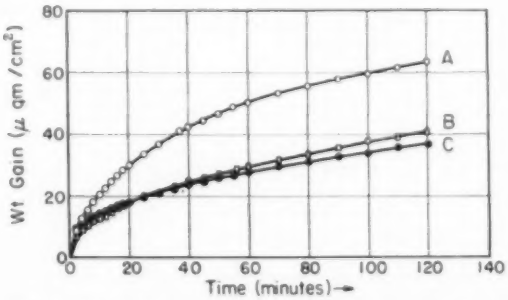

Fig. 4. Effect of Si on oxidation of Ni-Cr alloys, 900°C, 7.6 cm of Hg of O_2, abraded through 4/0. Curve A, 495, 2.09% Si; B, 494, 0.82% Si; C, 493, 0.23% Si.

Table III. Parabolic rate law constants (A) and heats of activation for oxidation of five nickel-chromium alloys at three temperatures

A in $(g/cm^2)^2/sec$, ΔH in calories per mole

Alloy	Analyses	Useful life, hr	750°C		900°C		1100°C	
			A	ΔH	A	ΔH	A	ΔH
495	2.09 Si, 0.02 Mn + Ca	178	2.14×10^{-14}	40,850	4.10×10^{-13}	61,200	1.7×10^{-11}	61,200
493	0.23 Si, 0.04 Mn + Ca	63	4.06×10^{-15}	49,730	1.26×10^{-13}	49,730	7.08×10^{-13}	76,350
492	1.01 Si, 2.30 Mn + Ca	106	3.31×10^{-14}	44,850	5.89×10^{-13}	44,850		
491	1.03 Si, 0.05 Mn + Ca	105	1.0×10^{-14}	50,830	2.78×10^{-13}	50,830		
245	1.44 Si, 4.05 Al, 19.38 Cr	>178	1.67×10^{-14}	65,300	1.22×10^{-13}	65,300	5.28×10^{-11}	

Table IV. Summary results effect of strain on oxidation of Ni-Cr alloys oxidized 900°C, 0.1 atm oxygen

Alloy	Class	Film Thickness $\mu g/cm^2$	% Strain	$(g/cm^2)^2/sec$ Parabolic rate law constants		Useful life 1177°C hr
				Before	After	
495	High Si, low Mn + trace elements	44.5	2	2.82×10^{-13}	1.6×10^{-13}	178
491	Intermediate Si, low Mn + trace elements	47.1	2	1.97×10^{-13}	1.77×10^{-13}	105
492	Intermediate Si, high Mn + trace elements	43.7	2	5.89×10^{-13}	4.63×10^{-13}	106
493	Low Si, low Mn + trace elements	45.4	2	5.62×10^{-14}	9.81×10^{-14}	63

All of the diffraction patterns were made using filtered CrK_α radiation from a fine focus x-ray diffraction tube. Diffraction patterns were made at room temperature using a 9 cm Unicam camera.

Results

Oxidation studies were made in the vacuum microbalance over the temperature range of 500° to 1100°C. Before oxygen was added, the apparatus was evacuated to a pressure of 10^{-6} mm Hg or less. The furnace was then raised about the sample and furnace tube, and thermal equilibrium was allowed to occur. Above 900°C decarburization of the alloy by the room temperature oxide occurred for some of the alloys (11). Weight gain was calculated in units of micrograms per square centimeter.

X-ray diffraction analyses showed that the oxide scales were Cr_2O_3 and $NiO \cdot Cr_2O_3$. To estimate the thickness in angstroms from the weight gain in micrograms per square centimeter a factor of 61 was used. This factor assumes Cr_2O_3 to be the oxide and a surface roughness ratio of unity.

Kinetic Studies

Alloy 493 (low Si, low Mn).—Figures 1 and 2 show weight gain vs. time curves for the oxidation of alloy 493 for the two temperature ranges 500°-900°C and 900°-1100°C. All of the curves show a rapid initial reaction, with the rate of reaction decreasing as the film thickens. Two series of temper colors were observed on the alloys at 900°C before the gray colored oxide formed. Table II shows a summary of the colors of the oxide films and the thickness after 2 hr of reaction. This alloy showed the lowest rate of oxidation of the series of alloys studied.

Alloy 495 (high Si, low Mn).—Figure 3 shows weight gain curves for alloy 495 for the temperature range 950°-1100°C. The results at 500°-900°C were similar to those for alloy 493. Alloy 495 having a higher Si content oxidizes at a more rapid rate than alloy 493. Figure 4 shows a comparison of three alloys at 900°C. Silicon increases the initial rate of oxidation of the 80 Ni-20 Cr alloys for all temperatures studied. ASTM useful life tests show the high Si alloy to have the longest life.

Effect of Mn.—An earlier study showed that Mn may have a deleterious effect on the oxidation process due to its very high vapor pressure. Small quantities of Mn are probably in the alloy as sulfide and oxide. However, larger amounts of the order of 1 and 2% must be present in solid solution in the alloy.

Since the trace elements Ca, Al, and Zr were not controlled in the earlier study two special alloys were prepared in which only the Mn content was varied. These are alloys 492 and 491 of Table I. Figure 5 shows a comparison at 900°C. The high Mn alloy containing 2.30% Mn and 1.01% Si gave a higher rate of oxidation than alloy 491 containing

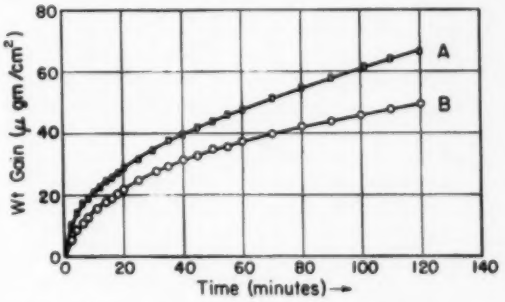

Fig. 5. Effect of Mn on oxidation of Ni-Cr alloys, 900°C, 7.6 cm of Hg of O_2, abraded through 4/0. Curve A, 492, 2.30% Mn; B, 491, 0.05% Mn.

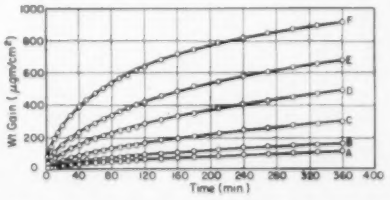

Fig.6. Effect of temperature on oxidation of alloy 245, 7.6 cm of Hg of O_2, abraded through 4/0. Curve A, 875°C; B, 900°C, C, 950°C; D, 1000°C; E, 1050°C; F, 1100°C.

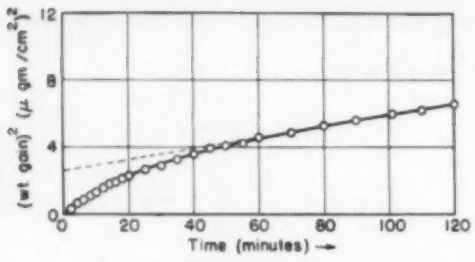

Fig. 7. Parabolic plot oxidation of Ni-Cr alloy 493, 500°C, 7.6 cm of Hg of O_2, abraded through 4/0.

0.05% Mn and 1.03% Si. ASTM useful life data were nearly identical.

Alloy 245 (high Si, high Mn).—Since Al has been shown to greatly improve the Fe-Cr series of heater alloys (12) a special Ni-Cr alloy containing 4.05% Al was studied. Figure 6 shows a 6-hr weight gain curve for this alloy from 875° to 1100°C. A comparison of Fig. 6 with Fig. 2 and 3 shows alloy 245 to oxidize at a more rapid rate than alloys 493 and 495. Table II shows the color of the oxides after 6 hr of reaction and the oxide thickness. Figure 6 shows that the total amount of oxidation after 6 hr is increasing with temperature from 875° to 1100°C. For the 5Al-22Cr-Fe alloys the total amount of oxidation remains nearly constant for the temperature range 950°-1050°C. Addition of Al to the Ni-Cr alloys does not have the marked effect on the oxidation reaction that was found for the Al-Cr-Fe alloys.

Parabolic rate law correlation.—A number of empirical rate laws have been proposed to interpret the rate of oxidation of metals and alloys. The parabolic rate law was used here since it has been derived from fundamental physical concepts involving the formation and diffusion of ions and electrons (13, 14). The equation states that $W^2 = A\,t + C$. Here W was the weight gain, t was the time, and A and C were constants.

Since the composition of the oxide was a function of time and temperature no one rate law could explain the complete time and temperature behavior. We used parabolic rate law plots to indicate changes in the oxide composition and to show whether the protective properties were improving or deteriorating.

To test the application of the parabolic rate law, graphs were made of the square of the weight gain vs. time. Figures 7, 8, and 9 show three plots for alloy 493. The 500°C plot shown in Fig. 7 indicates that the slope decreases continuously. Previous crystal structure studies (4) showed the initial oxide was NiO. After 30 hr of oxidation the oxide was identified as Cr_2O_3. The change in the parabolic rate law constants in Fig. 7 may be related to the change in oxide composition. Figures 8 and 9 at 900° and 1100°C show better agreement with the parabolic rate law after the initial deviation.

Temperature dependence.—To determine the temperature dependence of the parabolic rate law constants A, we use the relation $A = B\,e^{-\Delta H/RT}$. Here ΔH is the heat of activation of diffusion and heat of formation of the defects, B is a constant, and R the gas law constant. More elaborate rate expressions may be used for A so that the entropy terms may be evaluated (15). However, the complex nature of the alloy and oxide makes a complete interpretation very difficult. ΔH was evaluated from log A vs. $1/T$ plots of the rate law data.

Figures 10, 11, and 12 show plots of log A vs. $1/T$ for alloys 493, 495, and 245. All of the alloys gave two or more straight lines. The change in slopes may be related to crystal structure or composition changes in the oxide. Table III shows a summary of the parabolic rate law constants and heats of activation for three temperatures for all of the alloys and a comparison of these data with ASTM useful life tests.

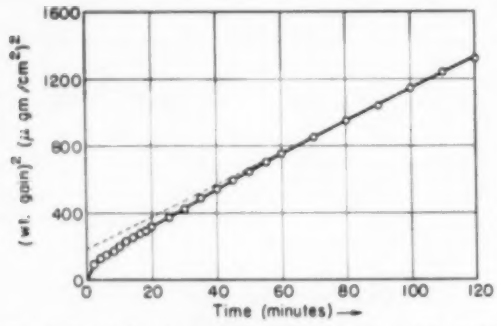

Fig. 8. Parabolic plot oxidation of Ni-Cr alloy 493, 900°C, 7.6 cm of Hg of O_2, abraded through 4/0.

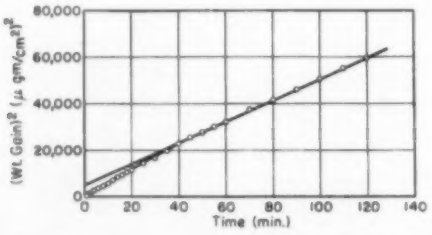

Fig. 9. Oxidation of Ni-Cr alloy 493, 1100°C, 7.6 cm of O_2, abraded through 4/0, parabolic plot. $A = 7.08 \times 10^{-12}$ $(g/cm^2)^2/sec$.

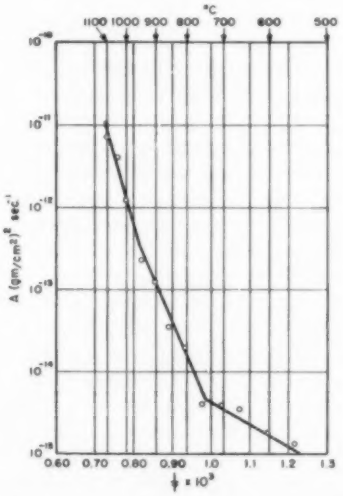

Fig. 10. Oxidation of Ni-Cr alloy 493 (low Si, low Mn), Log A vs. 1/T, ΔH = 76,250 cal/mole (950°-1100°C); ΔH = 49,730 cal/mole (750°-950°C).

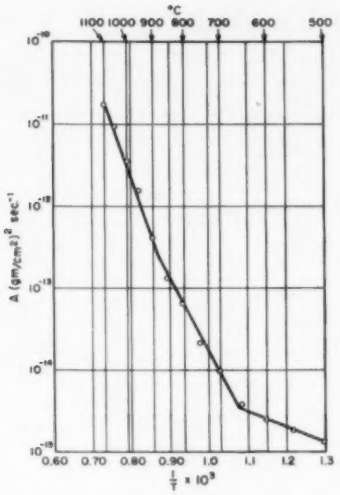

Fig. 11. Oxidation of Ni-Cr alloy 495 (high Si, low Mn). Log A vs. 1/T, $\Delta H = 61{,}200$ cal/mole (880°-1100°C); $\Delta H = 40{,}850$ cal/mole (650°-880°C).

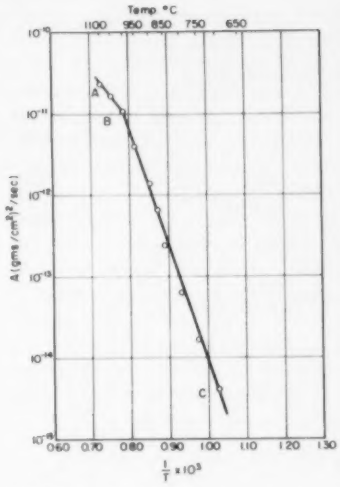

Fig. 12. Oxidation of alloy 245. Log A vs. 1/T, $\Delta H_{880} = 65{,}300$ cal/mole.

Strain Oxidation Studies

Samples of alloys 491, 492, 493, and 495 were oxidized individually at 900°C in 7.6 cm Hg of O_2 until a film of 45 $\mu g/cm^2$ was formed. The samples were removed and stretched 2% in a tensile testing machine. The marred surface held in the grips was removed and 4.5-cm length samples used for the reoxidation study.

Parabolic rate law plots of the data show that a 2% strain increased the parabolic rate law constants for the low silicon alloy 493 from 5.73×10^{-14} to 9.81×10^{-14} $(g/cm^2)^2$ sec^{-1}. A similar plot for the high Si alloy showed the parabolic rate law constants to decrease from 2.82×10^{-13} to 1.6×10^{-13} $(g/cm^2)^2$ sec^{-1} as a result of the 2 percent strain. Visually 2% strain has not effected the oxide-metal interface.

In addition to the long-term effect on the rate of oxidation a short-term effect was noticed especially on the low Si alloy 493. A rapid pickup of oxygen occurred on reoxidation. This reaction heals some of the damage in the oxide film. A very small short-term effect was noticed for the high Si alloy.

A summary of the effects of strain on the oxidation of the 80 Ni-20 Cr alloys is shown in Table IV.

These experiments indicate that minor elements such as Si and Ca in the alloy can greatly effect the resistance of the oxide and oxide-metal interface to stresses and strains. It is of interest to note that the results of the strain-oxidation test correlate with the ASTM useful life tests.

Crystal Structure Studies

Alloys.—X-ray diffraction studies were made on the alloys to test for the presence of second phases and the effect of minor elements on the lattice parameters of the alloy.

Table V shows the results of x-ray diffraction studies on alloys 493, 495, and 245. The alloys all have the face-centered cubic structure. A trace reflection was found at 2.122Å which suggests the presence of trace amounts of a second phase in the alloy. Three reflections were used in the calculation of the unit cell size a_o. Alloy 495 of the Ni-Cr series had the smallest value for a_o and the best ASTM useful life test. The effect of Al in replacing Ni is to increase the unit cell size.

Table V. Lattice parameters of alloys and pure nickel

Alloy	Composition	Lattice parameter a_o Å
493	Low Si, low Mn + trace elements	3.542 ±0.002
495	High Si, low Mn + trace elements	3.540 ±0.002
245	High Si, high Al	3.547 ±0.002
Ni(16)	Pure	3.52387

Oxide scales.—Crystal structure studies were made on the oxide scales over the temperature range 800°-1100°C. Results are shown in Table VI. A comparison of the crystal structures formed on alloys 493 and 495 shows similar oxide compositions at high temperatures. At 850°C alloy 493 showed Cr_2O_3 plus a trace of NiO while alloy 495 showed Cr_2O_3 alone. Several unidentified reflections were found in both alloys scales. We conclude that small composition differences exist in the oxide films. However, it is unlikely that the observed differences in oxide composition can be correlated with the major differences in performance as measured by the ASTM life test.

Alloy 245 showed $Cr_2O_3 + \alpha - Al_2O_3$ at 850°C. However, at 1100°C the oxide was Cr_2O_3 plus a spinel having a lattice parameter of 8.32Å. The spinel parameter can be compared to a value of 8.32Å for $NiO \cdot Cr_2O_3$ (16) or a value of 8.06Å found for $NiO \cdot Al_2O_3$ (16). The fact that $\alpha - Al_2O_3$ appears in the film at 800°-1000°C and not at 1100°C may be significant. In the 5Al-23Cr-72Fe alloy series Al_2O_3 forms in preference to Cr_2O_3 even at 1100°C.

X-ray diffraction analyses of the oxide scales is subjected to several limitations. (*A*) SiO_2 and other amorphous oxides may not be observed. (*B*) Oxides in amounts of 1-5% or less may not be recorded. (*C*) Oxides may be present in solid solution and not be recorded. (*D*) The chemical or electrochemical

Table VI. Summary crystal structure studies on Ni-Cr and Ni-Cr-Al alloys

Alloy 495, high Si, low Mn		Alloy 493, low Si, low Mn		Alloy 245, high Si, high Al	
Temp, °C	Crystal structures	Temp, °C	Crystal structures	Temp, °C	Crystal structures
1100		1100	Cr_2O_3 s.a. spinel 8.325*	1100	Cr_2O_3 spinel $a_o = 8.32$*
1050	Cr_2O_3 tr. sp. 8.33*	1050	Cr_2O_3 tr. sp. a_o 8.34*		
1000		1000	Cr_2O_3 s.a. sp. 8.33*	1000	Cr_2O_3, NiO spinel $a_o = 8.33$* s.a. $\alpha - Al_2O_3$
950	Cr_2O_3 s.a. sp. 8.33*	950	Cr_2O_3		
900		900		900	Cr_2O_3, NiO spinel $a_o = 8.33$* s.a. $\alpha - Al_2O_3$
850	Cr_2O_3	850	Cr_2O_3 tr. NiO		
				800	Cr_2O_3, $\alpha - Al_2O_3$

* Probably $NiO \cdot Cr_2O_3$; s.a. = small amount; tr. = trace.

stripping techniques also removed carbides, nitrides as well as oxides which can give extraneous reflections in the x-ray diffraction pattern.

Electron diffraction analyses was also attempted for the thinner oxide films. Many unidentified lines were present in addition to the oxide reflections. These we attribute to carbides, nitrides, etc.

Before a complete picture can be obtained of the oxide composition and crystal structure both x-ray diffraction and electron diffraction methods must be improved. Chemical analyses of these films must also be developed.

Discussion

Effects of Alloying Elements in Oxidation

Alloying elements can affect the nature of the oxidation reaction in several ways. First, the alloying element can affect the thermodynamic activity of the various metals in the alloys (17), the phase diagram of the alloy system, and the substructure of the alloy. Second, the alloying element can affect the composition, crystal structure, and physical and chemical properties of the oxide film (4). The alloying element may participate in the oxide film as follows: (*a*) form its own oxide in the outer layer of the oxide film at the oxide-gas interface, (*b*) form a mixed oxide in the outer layer or in the bulk of the oxide film, (*c*) form a mixed valency oxide changing the electrical and ionic transport properties of the oxide, (*d*) form its own oxide or compound with other oxides at the metal oxide interface, (*e*) remain in the metal at the metal-oxide interface, and (*f*) form a volatile reaction product.

The individual effect of the alloying element depends on its ionic size, charge, mobility, and thermodynamic activity. Since the chemical activity of the several oxides and the mobilities of the several ion species are temperature dependent, the specific effect of an alloying element may change with temperature.

Most of the elements which improve the performance of the 80Ni-20Cr alloy series are those which form very stable oxides and which do not participate in forming spinels or other oxides in the bulk of the oxide scale. These are: Si, Ca, Zr, Th, Ce, etc. To remain at the oxide-metal interface these elements form oxides which do not react with the major metallic components in the alloy.

Thermochemical Calculations

Table VII shows the principle types of chemical reactions which may occur during the oxidation of Ni-Cr and Ni-Cr-Al alloys. The composition of the oxide film and the distribution of the several oxides within the oxide is determined by the thermodynamic equilibria, the rates of the several chemical reactions, and by diffusion processes in the alloy (17). Calculations are made here only for the equilibrium state involving pure oxides and pure metals since information is not available on rates of diffusion of the metals in the alloys and in the oxides or on the chemical activities of the metals in the alloys.

A standard state of unit activity is assumed for the component metals in the alloy. Compared to the

Table VII. Types of surface reactions occurring in Ni-Cr and Al-Ni-Cr alloys

A. Direct oxidation
$2Cr(s) + 3/2\,O_2(g) \rightleftarrows Cr_2O_3(s)$, etc.
B. Solid phase reactions
$2Al(s) + Cr_2O_3(s) \rightleftarrows Al_2O_3(s) + 2Cr(s)$, etc.
C. Formation of spinels
$NiO(s) + Cr_2O_3(s) \rightleftarrows NiO \cdot Cr_2O_3(s)$, etc.
D. Formation of silicates
$Al_2O_3(s) + SiO_2(s) \rightleftarrows Al_2O_3 \cdot SiO_2(s)$, etc.
E. Decarburization
$Cr_2O_3(s) + 3C(\text{solid soln.}) \rightleftarrows 2Cr(s) + 3CO(g)$, etc.
F. Vaporization
$Cr(s) \rightleftarrows Cr(g)$, etc.

Table VIII. Dissociation pressures of the oxides

Temp, °C	$-\text{Log } PO_2$ (atm.)					
	NiO	Cr_2O_3	Al_2O_3	SiO_2	MnO	Fe_2O_3
25	75.4	121.8	184.6	144.6	127.2	85.8
200	43.8	73.4	112.4	87.6	77.4	50.8
400	27.6	48.9	75.7	58.8	52.1	33.0
600	19.0	35.6	55.8	43.2	38.4	23.4
800	13.6	27.3	43.3	33.5	29.8	17.4
1000	9.8	21.6	34.7	26.8	24.0	13.3
1200	7.0	17.4	28.4	21.9	19.6	10.3

Table IX. Solid phase reactions of nickel, chromium, and aluminum oxides

1. $3NiO(s) + 2Cr(s) \rightleftarrows Cr_2O_3(s) + 3Ni(s)$
2. $3NiO(s) + 2Al(s) \rightleftarrows Al_2O_3(s) + 3Ni(s)$
3. $2NiO(s) + Si(s) \rightleftarrows SiO_2(s) + 2Ni(s)$
4. $NiO(s) + Mn(s) \rightleftarrows MnO(s) + Ni(s)$
5. $Cr_2O_3(s) + 2Al(s, g) \rightleftarrows Al_2O_3(s) + 2Cr(s)$

Temp, °C	$\log_{10} K$ Reaction 1	Reaction 2	Reaction 3	Reaction 4	Reaction 5
25	69.7	163.8	69.2	25.9	94.2
200	44.4	102.9	43.8	16.8	58.5
400	32.0	72.1	31.2	12.3	40.1
600	25.0	55.2	24.2	9.7	30.2
800	20.6	44.6	19.9	8.1	24.0
1000	17.7	37.4	17.0	7.1	19.7
1200	15.7	32.1	14.9	6.3	16.4

Table X. Vapor pressure of metals

Temp, °C	$\log_{10} K_P$ (atm.) Ni	Cr	Al	Si	Mn	Fe
900	−11.0	−10.17	−7.6	−11.8	−5.3	
1000	−9.6	−8.8	−6.5	−10.3	−4.4	−9.67
1100	−8.2	−7.63	−5.5	−8.9	−3.5	−8.58
1200	−7.2		−4.7	−7.9	−2.8	−7.62

free energy change of the reaction the activity correction is small. Table VIII shows the dissociation pressures of the oxides from 25°C to 1200°C, as calculated from equations given by Kubaschewski and Evans (18). All of the oxides are stable in the oxidation atmospheres used.

Table IX shows calculations on the equilibrium constants for the several solid phase reactions which determine in part the composition of the oxide scale. Nickel oxide is reduced by Cr, Al, Si, and Mn. Chromium oxide is reduced by Al. For the 80Ni-20Cr alloys the equilibrium oxide should be largely Cr_2O_3. Cr_2O_3 was found experimentally by x-ray crystal structure studies shown in Table VI to be the main oxide in the scale. Although thermodynamic calculations cannot be made for the spinels, $NiO \cdot Cr_2O_3$ appears to be a stable compound since it is found also in the oxide scales.

For alloy 245 containing 4.05% Al, thermochemical calculations suggest the oxide should be Al_2O_3. This compound was observed except at 1100° where Cr_2O_3 and $NiO \cdot Cr_2O_3$ were observed.

Table X shows the vapor pressures of the several metals involved in these alloys. The vapor pressures of Ni, Al, Si, and Mn were calculated from the compilation of Stull and Sinke (19). Data for Fe and Cr were taken from a recent work by Gulbransen and Andrew (7).

According to calculations, Al should volatilize at high temperatures from the metal in vacuum or react at the surface to form Al_2O_3 in oxygen. Since Al_2O_3 forms at 800° and 1000°C but not at 1100°C, Al may be lost from the oxide film possibly as a lower oxide of Al.

Orientation Relationships

Tightly adherent oxide scales are one of the important characteristics of high heat resistant alloys. One of the factors in good adhesion is the matching of lattice parameters in the oxide and metal structures. Matching of lattice parameters is also important in determining the epitaxial relationships.

Bénard has suggested two rules for the directing influence of crystal structures in oxidation (20): (*a*) the oxide tends to orient itself to the metal structure to produce as near a coincidence as possible of the repeat distances between the metal atom in the two structures, and (*b*) planes of high atomic density in the oxide tend to orient to high density atomic planes in the metal consistent with the geometry of the two structures.

The orientation relationships of NiO on face-centered cubic Ni has been studied by Lawless, Young, and Gwathmey (21) and by Newkirk and Martin (22). The (111) plane of NiO was found to grow on both the (001) and (111) planes of the metal. A parallelism was found between the [110] directions of oxide and metal. Newkirk and Martin (22) calculate a 15.6% disregistry between the oxide and metal structures. If these relationships are correct, we must conclude that Bénard's simple rules (20) do not hold for NiO on Ni.

We have made an analyses of the simple repeat distances of $NiO \cdot Cr_2O_3$ formed on Ni-Cr-Al and Ni-Cr face-centered cubic alloys following Bénard's rules. A minimum disregistry is found for the growth of the (100) plane of $NiO \cdot Cr_2O_3$ spinel on the (111) plane of the alloy and a parallelism of the [100] direction of the oxide with the [111] direction of the alloy. However, a large disregistry is found for the [110] direction. Due to the influence of atoms outside of the lattice planes involved, the simple picture of coincidence of repeat distances does not apply for face-centered cubic structures. A more detailed picture of the orientation relationships must be developed to explain the good adherence of $NiO \cdot Cr_2O_3$ in Ni-Cr alloys.

We have not made an analyses of the simple repeat distances of Cr_2O_3 formed on the Ni-Cr and Ni-Cr-Al alloys due to the complexities of the Cr_2O_3 structure. Single crystal studies should be made to determine the orientation relationships for the oxides formed on these good oxidation resistant alloys.

Summary

1. Vacuum microbalance measurements were made on the oxidation of a series of 80Ni-20Cr and a 75Ni-19Cr-4Al heater alloys over the temperature range of 500°-1100°C.

2. Silicon and manganese compositions were varied in the 80Ni-20Cr series of alloy.

3. Kinetic studies showed the low Si and low Mn alloy oxidized at a lower rate than the alloy containing 2% Si. No correlation was formed between ASTM heater life tests and the rate of oxidation of a series of heater alloys.

4. Kinetic data were fitted to the parabolic rate law. However, a number of deviations were observed. For all experiments the initial parabolic rate law constant was larger than the final values found for thicker films. This change was attributed to chemical transitions occurring in the oxide films.

5. Parabolic rate law data plotted on a logarithmic plot as a function of 1/T showed two or three straight lines. Heats of activation for the several temperature ranges for each alloy were determined.

6. Strain oxidation studies on the alloys showed good correlation with ASTM life tests. This study suggests that the resistance of the oxide-metal interface to stresses or strain is the most important factor in determining the practical performance of heater alloys. Silicon and the other minor elements appear to help the metal resist the effects of stresses or strains at the oxide-metal interface.

7. X-ray diffraction crystal structure studies were made on three alloys over the temperature range. Cr_2O_3 and $NiO \cdot Cr_2O_3$ spinel were the principal oxides formed for the 80Ni-20Cr alloys. α-Al_2O_3 was found, in addition, on the 75Ni-19Cr-4Al alloy at 800° and 1000°C but not at 1100°C. The latter observation was unexpected.

8. Rate data and crystal structure observation were interpreted from thermochemical calculations in the several chemical reactions occurring in the system. Orientation relationships were also discussed.

Manuscript received Dec. 19, 1958. This paper was prepared for delivery before the Philadelphia Meeting, May 3-7, 1959.

Any discussion of this paper will appear in a Discussion Section to be published in the June 1960 JOURNAL.

REFERENCES

1. F. E. Bash and J. W. Harsch, *Am. Soc. Testing Materials Proc.*, **29**, Pt. II, 506 (1929).
2. E. A. Gulbransen and K. F. Andrew, *This Journal*, **101**, 163 (1954).
3. J. W. Hickman and E. A. Gulbransen, *Trans. Am. Inst. Mining Met. Engrs.*, **180**, 519 (1949).
4. E. A. Gulbransen and W. R. McMillan, *Ind. Eng. Chem.*, **45**, 1734 (1953).
5. W. Hessenbruch, "Metalle and Legierungen fur Hohe Temperaturen," Berlin, Julius Springer (1940).
6. H. Pfeiffer, *Werkstoffe u. Korrosion*, **10**, 573 (1957).
7. E. A. Gulbransen, "Advances in Catalysis," Vol. V, pp. 119-175, Academic Press Inc., New York (1953).
8. E. A. Gulbransen, *Trans. Electrochem. Soc.*, **81**, 187 (1942).
9. E. A. Gulbransen and K. F. Andrew, A.S.T.M. Technical Publication No. 171, p. 35, February 2, 1955.
10. E. A. Gulbransen, R. T. Phelps, J. W. Hickman, *Ind. Eng. Chem. Anal. Ed.*, **18**, 391 (1946).
11. E. A. Gulbransen, W. S. Wysong, and K. F. Andrew, *Trans. Am. Inst. Mining Met. Engrs.*, **180**, 565 (1949); T. D. 2438.
12. E. A. Gulbransen and K. F. Andrew, *This Journal*, **106**, 294 (1959).
13. C. Wagner, *Z. Physik, Chem.*, **(B) 21**, 25 (1933).
14. C. Wagner, "Atom Movements," American Society for Metals, pp. 153-173, Cleveland, Ohio (1951).
15. E. A. Gulbransen, *Ann. N. Y. Acad. Sci.*, **58**, 830 (1954).
16. J. D. H. Donnay and W. Nowacki, "Crystal Data" Memoir No. 60, The Geological Society of America, April 1, 1954, New York.
17. C. Wagner, *This Journal*, **103**, 571 (1956).
18. O. Kubaschewski and E. D. Evans, John Wiley & Sons, Inc., New York (1956) Book.
19. D. R. Stull and G. C. Sinke, "Thermodynamic Properties of the Elements," Am. Chem. Soc., Washington, D. C., November, 1956.
20. J. Bénard, *Bull soc. chim. France*, **13**, 511 (1946).
21. K. R. Lawless, F. W. Young, Jr., and A. T. Gwathmey, *J. chim. phys.*, **53**, 667 (1957).
22. J. B. Newkirk and W. G. Martin, *Trans. Am. Inst. Mining Met. Engrs.*, **212**, 398 (1958).

The Action of Nickel and Cobalt in Electroluminescent Zinc Sulfide Phosphors

Paul Goldberg

Sylvania Research Laboratories, Bayside, New York

ABSTRACT

Nickel and cobalt produce many of the effects in electroluminescent phosphors that are known for photo- and cathodoluminescent zinc sulfide. In addition, these elements bring to electroluminescent phosphors other changes in properties which are of practical and theoretical interest. Among these are (*a*) enhancement of emittance in blue-emitting phosphors, (b) marked changes in emittance-voltage and emittance-frequency characteristics, and (c) simplification of the brightness wave forms. The frequency and brightness wave effects can be understood in terms of "fast" and "slow" recombination processes which are influenced differently by the iron-group elements. The enhancement of electroluminescence is of uncertain origin but may arise from changes in the photocapacitive properties of the powder crystals due to the iron-group elements. The similarities and differences of nickel and cobalt in both blue and green-emitting phosphors are discussed.

The sensitivity of zinc sulfide phosphors to iron-group elements has a long history (1). Nickel, cobalt, and iron influence the intensity of luminous emission and the rate of luminescence decay in phosphors excited by ultraviolet or cathode rays (2-4). At concentrations much less than the activator content their action is to suppress the emission strongly. Consequently they are termed "killers" or "quenchers." The interpretation of these effects involves trapping and/or recombination of free holes and electrons (3, 5-7) at the killer site. The iron-group elements can influence excitation processes by

introducing absorption bands (8) and also weak emission bands (9).

The purpose of this paper is to discuss the way iron-group elements act in electroluminescent (EL) phosphors. Lehmann already has demonstrated that these elements depress the emittance and induce superlinear emittance-frequency characteristics (10).

In the experiments described below the EL emittance and brightness wave forms were followed as a function of voltage, frequency, and concentration of the iron-group elements. In addition to the effects seen by Lehmann it was found that: (*a*) The emittance of blue-emitting phosphors was increased with additions of 10^{-5} g at./mole or less of the iron-group elements. (*b*) In the range 10^{-5} to 10^{-4} g at./mole of Ni or Co dependencies of emittance on voltage and frequency may undergo marked changes. (*c*) With additions of 10^{-5} to 10^{-4} g at./mole of Ni the brightness waves take on a simplified form.

The ordinary names such as "killers" or "quenchers" given to these elements in the zinc sulfide system are clearly inadequate here. Therefore, in the remainder of this report reference will be made to the elements as "modifiers."

Nickel and cobalt have been shown to influence the dielectric properties of photoluminescent zinc sulfide (11). Also, it is known that the dielectric properties of EL phosphors are of consequence in their response in an electric field (12). Therefore studies were made to trace the importance of these observations on the materials of this report.

Experimental Technique

Phosphors.—The phosphors studied are of the ZnS:Cu,Cl type and contain roughly 3 x 10^{-4} g at. Cu/mole in the case of blue-emitting materials and 1.5 x 10^{-3} g at. Cu/mole for the green-emitting group. The modifiers were introduced during the preparation as aliquots of solutions of the following Johnson-Mathey salts: $Co(NO_3)_2 \cdot 6H_2O$ and $NiSO_4 \cdot 7H_2O$. Not all of the modifier enters the lattice in these preparations as shown in Table I.

For 1 x 10^{-4} g at. Ni/mole and above, the known (8) absorption band of Ni in ZnS appears as a distinct yellow body color.

In subsequent discussions the concentration of modifiers is specified in terms of the amount added in the preparation.

Optical and electrical measurements.—Emittance data were obtained from cells 25 x 25 x 0.125 mm in size with a castor oil dielectric. Brass and transparent conductive glass (500 ohms/square) served as electrode materials. An RCA 1P22 photomultiplier detector was used in conjunction with a Photovolt Model 520 photometer. A rough measure of the emission color was obtained as the blue/green (B/G) ratio with a Corning 4010 filter measuring the green and 5543 and 3389 filters together measuring the blue. The detector for obtaining the brightness waves was a Du Mont 6292 photomultiplier. Dielectric properties of the phosphors were obtained with cells similar to those described above at a field strength too low to give electroluminescent emission. The electrical loss and capacitance data were measured with a Q meter (Boonton Radio Co. Model 260-A) in both a dark environment and under room (fluorescent) illumination.

Table I.

Modifier added in the preparation, g at./mole	Ni found in phosphors (green emission) g at./mole	Co found in phosphors (blue emission) g at./mole
Zero (control)	1.3×10^{-6}[a]	$<8 \times 10^{-7}$[a]
1×10^{-6}[b]	1.3×10^{-6}	—
3×10^{-6}	3.6×10^{-6}[b]	—
1×10^{-5}	0.48×10^{-5}	1.2×10^{-5}[b]
3×10^{-5}	1.1×10^{-5}	2.3×10^{-5}
1×10^{-4}	0.46×10^{-4}	0.69×10^{-4}
3×10^{-4}	2.3×10^{-4}	1.65×10^{-4}
1×10^{-3}	0.43×10^{-3}	0.49×10^{-3}

[a] Measured by spectrographic analysis, the other data by wet chemical analysis.
[b] The apparent excess found over that added may arise from analytical inaccuracy at low levels of added modifier. The analytical error amounts to $\pm 0.15 \times 10^{-6}$ at the level of 1 x 10^{-6}, and 10% or less at all higher concentrations.

Experimental Results

Frequency Dependence of the Luminous Emittance

Green-emission.—Figure 1 shows the log-log plot of the integrated light output or emittance (L) as a function of frequency (f) for a family of green-emitting EL phosphors with varying amounts of Ni

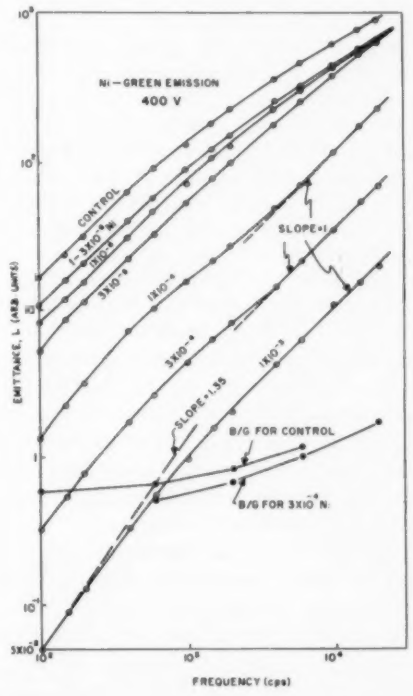

Fig. 1. Emittance-frequency characteristics of green-emitting electroluminescent phosphors with various nickel concentrations, at 400 v. Data for 1 x 10^{-6} and 3 x 10^{-6} g at. Ni/mole are coincident within experimental error.

at 400 v (rms). This family shows many of the characteristics of modifier activity: (*a*) For Ni concentrations up 3 x 10^{-5} g at./mole the *L-f* curves show linearity from 100 cps to nearly 1 kc. At higher frequencies the dependence is sublinear. This is similar to the known behavior of ordinary EL phosphors (15-17). (*b*) The *L-f* characteristics show linear portions at Ni concentrations of 1 x 10^{-4} g at./mole and higher, from frequencies of a few kilocycles up to the limit of measurement at 20 kc.[1] This stands in pronounced contrast to the usual sublinear behavior which sets in at lower frequencies. The effect is approximately independent of voltage. There is a continuing decrease in the average emittance for greater additions of nickel. (*c*) Superlinearity in the *L-f* characteristics appears at 1 x 10^{-4} g at. Ni/mole and higher. The effect disappears for a given Ni concentration at frequencies above 1 kc and is replaced by the linear behavior described above. The superlinearity is more severe in Co-containing phosphors. As will be shown later, *L* may increase as rapidly as the third power of the frequency. (*d*) There is a convergence at high frequencies of the curves of Ni in range 1 x 10^{-6} to 3 x 10^{-5} g at./mole. (Alternatively, this may be expressed as a decrease in the ability of Ni to suppress electroluminescence as the frequency is increased. The difference in emittance of about 40% between the control sample and that with 1 x 10^{-6} g at. Ni/mole was not found in subsequent preparations.) (*e*) The blue band is quenched more than the green band at higher Ni concentrations. Figure 1 shows the decrease in the B/G ratio upon incorporation of 3 x 10^{-4} g at. Ni/mole. The shift toward the green holds too for phosphors emitting mainly blue light.

The superlinearity and convergence phenomena described above are also brought on by Co. This element however does not provide linear *L-f* characteristics in the kilocycle region for any green-emitting phosphors studied here. Other differences between Co and Ni will be mentioned subsequently.

As a modifier, iron acts somewhat differently. It depresses the brightness with almost no change in the shape of the *L-f* curves. A weak red emission attributable to Fe was observed under field excitation. A similar band was reported previously by Gergely (9) for photoluminescent excitation.

It has been mentioned by others that emittance-frequency investigations should be coupled with temperature studies in order that ambiguous results be avoided (18, 19). However, the shape of the emittance-temperature characteristics of these materials with and without Ni shows a general insensitivity to frequency, except for a scale factor.

Blue-emission.—An analogous pattern to that discussed above is found in EL phosphors emitting mainly blue light. There is however one main difference. The lowest concentrations of modifier effect an enhancement in emittance. Figure 2 shows the *L-f* characteristics of blue-emitting ZnS:Cu,Cl at various Co concentrations in the range 3 x 10^{-7} to 1 x 10^{-3} g at. Co/mole. The phosphors with 3 x 10^{-7} to 3 x 10^{-4} g at. Co/mole are all brighter than the control at higher frequencies. This increase partially obscures the convergence effect described previously. However, both the superlinearity and linearity relationships are evident. The existence of the enhancement effect has been suggested by Burns (20).

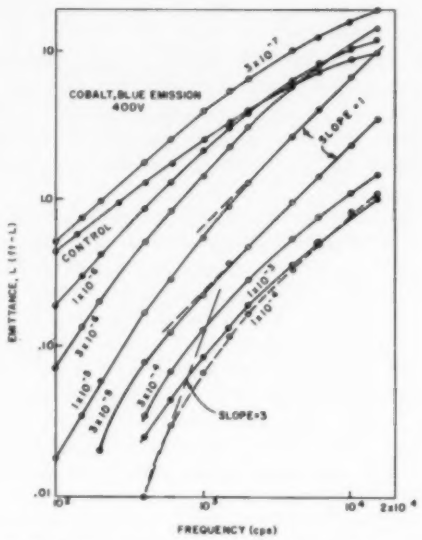

Fig. 2. Emittance-frequency characteristics of blue-emitting El phosphors with various Co concentrations.

The integrated light output of phosphors containing Ni behave in much the same way as described above for Co although not as strongly. Figure 3 shows a family of curves at various levels of Ni. Cobalt induces superlinearity at 1 x 10^{-6} g at./mole which becomes pronounced at 10^{-4} g at./mole ($L \sim f^3$). Nickel first induces superlinearity at 1 x 10^{-4} g at./mole, and as in Fig. 1, the effect is weak. The emittance enhancement also has been observed for Fe and Cr additions.

The photoluminescence of these materials, in contrast to the electroluminescence, decreases monotonically with increasing modifier content. This is largely in agreement with the work of Arpiarian for the ZnS:Cu, Cl system (2).

A significant difference between Ni and Co in these phosphors is the reappearance of sublinearity in the range 1 x 10^{-4} to 1 x 10^{-3} g at. Co/mole. There is no equivalent to this in the Ni-containing family (cf. Fig. 2 and 3).[2]

Voltage Dependence

The voltage dependence of emittance of EL phosphors can be represented by a variety of empirical formulas. One of these, which receives some support from theory is

$$L = A \cdot f(V) \cdot \exp(-bV^{-1/2})$$

where *L* is the luminous emittance, *V* the rms volt-

[1] The linearity of *L-f* characteristics should be tested with a detector which counts photons. Such results would be unambiguous in spite of color shifts in the emission with frequency. The linearity, e.g., for 1 x 10^{-4} g at. Ni/mole shown in Fig. 1, measured with an RCA 1P22 photomultiplier, is therefore open to some question due to the color shift. In other results, however, e.g. Fig. 3, the linearity is quantitative since color shifts are minimal.

[2] The reason the curve for 1 x 10^{-4} Co in Fig. 2 falls below that of 3 x 10^{-4} is not evident. Chemical analyses for Co in the finished phosphors cannot account for it (see Table I) although small temperature gradients during the synthesis may.

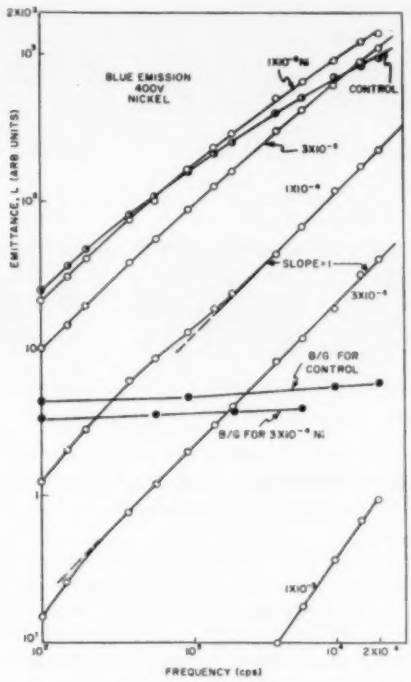

Fig. 3. Emittance-frequency characteristics of blue-emitting EL phosphors with various Ni concentrations.

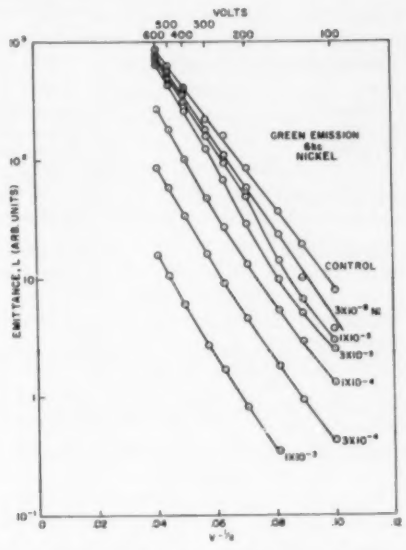

Fig. 4. Emittance-voltage characteristics of green-emitting EL phosphors with various Ni concentrations; L ~ exp(—b $V^{-1/2}$).

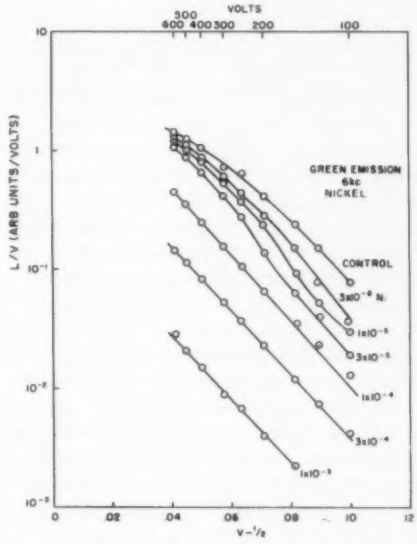

Fig. 5. Data of Fig. 4 plotted according to L/V ~ exp(—b $V^{-1/2}$).

age; A and b are arbitrary constants (15, 18). Experimental work by various investigators shows two functionalities; $f(V)$ = constant (15, 18) or $f(V) = V$ (21). The $f(V)$ term is related to the particular trap distribution in the phosphor (18).

Blue-emission.—Here the behavior on increasing the nickel concentration is almost completely described by changes in the value of the constant A in Eq. [1] with $f(V)$ = const. A similar result was reported by Lehmann for his phosphors (10).

Green-emission.—Phosphors containing either Ni or Co show both functionalities depending on the concentration of modifier. Figure 4 shows the L-V characteristics of the same group of phosphors appearing in Fig. 1, at a constant frequency of 6 kc. It is evident that at Ni contents greater than 1 x 10^{-4} g at./mole, a new voltage dependence has fully developed. This voltage dependence corresponds to $f(V)$ equal to V. Figure 5 presents the data of Fig. 4 replotted such that $f(V)$ equals V (ordinate is L/V). The effect also is found for Co at a concentration one order of magnitude less than for Ni. The change in shape of the voltage characteristic is frequency-dependent. Experiments at 2, 6, and 20 kc all show the effect described above. At 100 and 600 cps, however, no change in shape was detected.

Table II summarizes some of the principal findings on the modifier action on emittance functionalities.

Brightness Wave Forms

Brightness waves have been used widely as a means of following electronic processes relating to electroluminescence in both powders (15, 19, 22-25) and single crystals (26). If the exciting voltage is sinusoidal, the waves show a major (primary) peak and at least one minor (secondary) peak per half cycle of voltage. Also there is usually a continuous component in that the light does not fall to zero at any time during a cycle. Destriau used the intensity of this continuous component as a measure of the mean lifetime of luminescent centers in the excited state (27).

The brightness wave characteristics are changed for phosphors containing modifiers. Figures 6a and 6b show the brightness waves of green-emitting phosphors containing no Ni and 1 x 10^{-4} g at. Ni/mole, respectively, for frequencies of 100 cps, 1 kc and 10 kc at 400 v. The central line in the figures indicates the level of zero light. The principal feature

Table II.

Dominant emission	Frequency dependence	Voltage dependence
Blue—No modifier	Sublinear above 100-200 cps	$L \sim \exp V^{-1/2}$
Low Ni conc., $<10^{-4}$	Sublinear above $\sim$ 600 cps	$L \sim \exp V^{-1/2}$
High Ni conc., $\geq 10^{-4}$	Linear to 20 kc*, superlinear below $\sim$ 400 cps	$L \sim \exp V^{-1/2}$
Low Co conc., $<10^{-5}$	Superlinear below 1 kc	$L \sim \exp V^{-1/2}$
Intermediate Co conc., $\sim 10^{-5}$	Linear to 20 kc, strongly superlinear below $\sim$ 1 kc	$L \sim \exp V^{-1/2}$
High Co conc., $>3 \times 10^{-5}$	Superlinear below $\sim$ 1 kc, sublinear above 1 kc	$L \sim \exp V^{-1/2}$
Green—No modifier	Sublinear above $\sim$ 400 cps	$L \sim \exp V^{-1/2}$
Low Ni conc., $<10^{-4}$	Sublinear above $\sim$ 500-1000 cps	Transition (See Figs. 4, 5)
High Ni conc., $\geq 10^{-4}$	Linear to 20 kc, superlinear below 1 kc	$L \sim V \exp V^{-1/2}$
Low Co conc., $<10^{-5}$ High Co conc., $>3 \times 10^{-5}$	Superlinear below 1 kc, sublinear at higher frequencies	Transition $L \sim V \exp V^{-1/2}$

* 20 kc is the limit of the frequency range examined.

Table III. Dielectric properties of blue-emitting electroluminescent phosphors

	Resistive photocurrent,* μa	ΔK, %	Electro-luminescence enhancement, %, at 15 kc, 400 v	
3×10^{-7} Co [2]	26	6.8	100	(Fig. 2)
No Co [2]	18	29		
1×10^{-6} Ni	10	6.6	45	(Fig. 3)
No Ni	14	30		

* The photocurrent is calculated from the voltage applied by the Q meter oscillator and the equivalent parallel resistance of the test cell.

[2] *Note added in proof:* Activation analyses of these samples show Co concentrations of 1.5×10^{-7} g at./mole for "No Co" and 2.0×10^{-6} g at./mole for "3×10^{-7} Co."

of these curves is the nearly complete absence of secondary peaks and continuous components in the phosphor containing Ni. At lower Ni content an intermediate behavior obtains: reduced height of the secondary peak and also a change in its phase to the descending portion of the primary peak.

The same phenomena result for blue-emitting phosphors. Figures 7a and 7b illustrate equivalent curves for two phosphors previously represented in Fig. 3. The brightness waves of the two Ni-doped phosphors are nearly identical. The phosphors in Figs. 6b and 7b are the same ones which show linear L-f characteristics in Figs. 1 and 3, respectively.

Cobalt-bearing phosphors show a different brightness wave pattern. All phosphors shown in Fig. 2 have brightness waves with a nearly constant continuous component, amounting to about 20% of the amplitude of the primary peaks. At 3×10^{-6} g at. Co/mole in that group however, the secondary peak has vanished fully. It reappears again at the same phase angle for all higher Co concentrations.

Dielectric Properties and the Electroluminescent Enhancement Effect

By increasing the matrix dielectric constant one obtains a greater field strength in the phosphor (12). Conversely it may be expected that an increase in the phosphor dielectric constant will reduce the field strength in the phosphor and result in reduced emittance.

In ZnS-type phosphors the dielectric constant increases under photo-excitation (13, 14). It is reasonable that a phosphor, excited to electroluminescence, will absorb part of its own radiation, especially in the blue region. It may then experience the ordinary photocapacitive effect by virtue of that absorption.

Roux has shown that the photocapacitive effect is suppressed by Ni and Co (11). The phosphors in this report which show enhanced emittance in the presence of modifiers may do so because of the suppressed photocapacitive effect and, therefore, because of a resulting higher field strength in the phosphor.

It is difficult to investigate dielectric effects of this sort under conditions of EL excitation because the electrical properties of the cells are dominated by voltage- and frequency-dependent losses (28). However, some information can be obtained by following the dielectric changes in the phosphor induced by external illumination. As mentioned above, this bears a relation to some of the processes in an EL cell, since the emitted radiation itself serves as a source of "external" illumination.

Data given in Table III obtain for phosphors showing electroluminescent enhancement. The results are expressed as the photocurrent and per cent increase in the dielectric constant of the phosphor-matrix mixture on exposure to room light.

The data are consistent with the idea that quenching of the photocapacitive effect is responsible for the electroluminescence enhancement. This is supported by observations that the enhancement occurs almost exclusively in blue-emitting phosphors

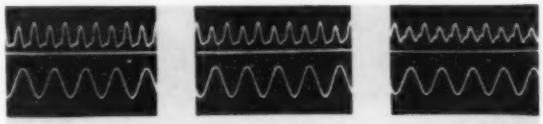

Fig. 6a. Brightness and voltage wave forms at three frequencies for the control phosphor of Fig. 1 (green-emission).

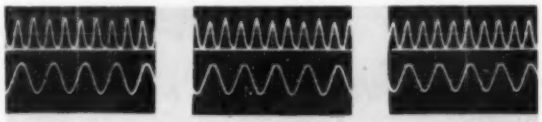

Fig. 6b. Equivalent curves for the specimen in Fig. 1 containing 1×10^{-4} g at. Ni/mole.

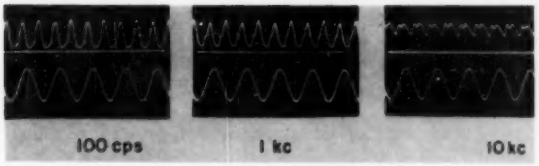

Fig. 7a. Brightness and voltage wave forms at three frequencies for the control phosphor of Fig. 3 (blue-emmission).

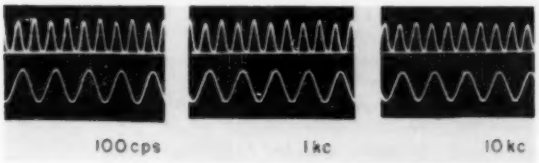

Fig. 7b. Equivalent curves for the specimen in Fig. 3 containing 1 x 10^{-4} g at. Ni/mole.

where self-absorption will tend to be greater than for emission predominantly in the green. Nevertheless, other factors will have to be considered before a definitive explanation of the enhancement is available. Among these are: (*a*) the degree of self-absorption of EL emission in phosphors, (*b*) the effect of such absorption on the phosphor dielectric constant and conductivity, and (*c*) the detailed field distribution changes within the grains resulting from the self-absorption.

The photocurrent data show that the enhancement is not related to that arising from the photoconductive effects recently reported by Ivey (29) and by Thornton (30). These workers state that external illumination is responsible for shifting the voltage distribution in phosphor crystals in favor of the barrier due to a more conductive bulk. Data in Table I show that the conductivity without Ni is greater than with Ni.

Discussion

Electroluminescence excitation is assumed to arise from impact ionization of luminescent centers by high energy electrons accelerated in a region of high field strength (31, 32). The electrons are swept away from the ionized centers by the field to remote parts of the crystal and contribute to a polarization field or become trapped. The voltage reversal brings many of the electrons back to the excitation region where radiative recombinations occur. The trapped electrons either cannot return at all (deep traps) or return at a later time (shallow traps) following field or thermal release (15, 18, 19, 25). Trapping of these electrons may enhance the continuous component (24). It has been proposed by Zalm, Haake, and others, that electron trapping is responsible for the secondary peak (15, 19).

This physical picture of excitation and recombination will serve as a basis for interpreting the experiments illustrating modifier action. Because Ni and Co behave differently in several respects, e.g., brightness waves and frequency response, they will be discussed separately. We shall refer to an unimpeded electronic recombination as a "fast" process. The delayed emission due to trapping or other causes will be viewed as a "slow" process.

The following model is proposed to account for the experimental result for Ni-bearing phosphors. Nickel offers to both trapped and conduction electrons a radiationless recombination site with a large capture cross section. At intermediate nickel concentrations (1 x 10^{-4} g at./mole) effectively all of the trapped electrons and some conduction electrons are brought back to the activator ground states through these recombination sites. This eliminates the contributions of the slow processes to the brightness waves, namely, the secondary peak and continuous component. Nonradiative escape of electrons from traps in zinc sulfide phosphors containing Ni has been suggested by Leverenz (1) and Kallman and Sucov (33). Only the fast process remains which can follow the field at all audio frequencies. The resulting linear *L-f* relationship of these phosphors up to 20 kc means that the area under each primary peak remains constant with frequency and is dependent only on the voltage. As the frequency is changed, the number of primary peaks per unit of time changes proportionately giving a linear *L-f* response.

At lower Ni concentrations (less than 1 x 10^{-4} g at./mole), the situation is somewhat more complicated. There are not enough recombination sites for all the trapped electrons to be affected. Furthermore, a finite relaxation time is required for the recombination sites to dissipate electronic energy radiationlessly and thereby return electrons to their ground states. The result of this is shown in Fig. 1. At low frequencies (e.g., 100 cps) Ni effects a reduction in brightness at the lowest concentrations. At high frequencies, where the number of conduction and trapped electrons is much larger, the radiationless recombination sites are swamped. The sites are neither numerous enough nor fast enough to be effective. Thus at 10 to 20 kc hardly any quenching action is observed for concentrations up to 3 x 10^{-5} g at. Ni/mole. Further increases in modifier concentration provide sufficient recombination centers, and the emittance is diminished at all frequencies. The concept of rapid capture and relatively slow release by radiationless recombination centers was suggested by Nail, *et al.* (4) as one explanation of superlinear photoluminescence in (Zn,Cd)S:Ag, Cl-Ni.

When large numbers of free electrons are produced by a voltage increase rather than by a frequency increase, the same result is observed. Figure 4 shows that for low modifier levels, the quenching action is more effective at low voltage (small supply of free electrons) than at high voltage (large supply of free electrons).

Zalm suggests that superlinearity in brightness-frequency characteristics is to be expected if the escape of holes to the valence band from ionized centers occurs (15). It is in these terms that the superlinearity seen in Fig. 1, 2, and 3 can be described. The presence of the modifier atom is assumed *ad hoc* to promote the escape of holes. Following this escape the electrons and holes recombine radiationlessly. The escape of holes to the valence band may have an appreciable relaxation time.

When the period of a cycle becomes smaller than this relaxation time superlinearity disappears. This is the case for frequencies above 1 kc in most of the samples studied.

The differences between Co and Ni as a modifier of electroluminescence has a direct counterpart in differences found in photoluminescence (3) and glow curve data (5). It can be argued, although with some reservations, that Ni serves as a recombination center but introduces no new trapping levels of importance to electroluminescence, while Co does both. One can then associate the continuous component and secondary peak in the brightness waves of Co-doped phosphors with this trapping level as well as the return to sublinearity in the L-f curves of Fig. 2. This argument is admittedly incomplete in that sublinearity returns in Fig. 2 at 1×10^{-4} g at. Co/mole while the secondary peak returns at 1×10^{-5} g at. Co/mole.

In one sense Co and Ni act alike. They both are able to change the shape of the voltage characteristic of green-emitting phosphors at frequencies above 1 kc (see Table II). This behavior is then a function of the activator (and/or coactivator) concentration as it is not found in blue-emitting phosphors. Thus it may be related to the particular trap distribution within the phosphor.

Duboc (34) and Klasens (35) discuss the processes in a two-level model which can introduce various functionalities in photoluminescence of photoconduction vs. exciting intensity. In spite of this, it does not seem profitable at the present time to fit the electroluminescence data into the band scheme in detail greater than that already done above. One must make assumptions to fit the models of Duboc and Klasens: (*a*) that the frequency in the electroluminescence case and the exciting light intensity in the photoluminescence case are comparable variables, and (*b*) that ZnS:Cu,Cl-Co/Ni is adequately represented by a two-state band scheme. These assumptions seem too restrictive for the present.

Acknowledgments

It is a pleasure to thank Drs. D. H. Baird, B. E. Bartels, A. L. Solomon, and R. N. Summergrad for many helpful discussions. The able assistance of J. W. Culp, S. Faria, and J. T. Ragusin in the synthesis of phosphors and in carrying out some of the measurements is acknowledged gratefully. Thanks are due J. Cosgrove and R. Weberling for analytical data.

Manuscript received April 17, 1959. This paper was prepared for delivery before the New York Meeting, April 27-May 1, 1958.

Any discussion of this paper will appear in a Discussion Section to be published in the June 1960 JOURNAL.

REFERENCES

1. H. W. Leverenz, "An Introduction to Luminescence of Solids," pp. 333-337, John Wiley & Sons, New York (1950).
2. N. Arpiarian, *J. Phys. Radium*, **17**, 674 (1956).
3. W. Hoogenstraaten and H. A. Klasens, *This Journal*, **100**, 366 (1953).
4. N. R. Nail, F. Urbach, and D. Pearlman, *J. Opt. Soc. Am.*, **39**, 690 (1949).
5. W. Hoogenstraaten, *This Journal*, **100**, 356 (1953).
6. S. Roberts and F. E. Williams, *J. Opt. Soc. Am.*, **40**, 516 (1950).
7. M. Schoen, *Z. Naturforsch.*, **66**, 251 (1951).
8. H. A. Klasens, *This Journal*, **100**, 72 (1953).
9. G. Gergely, *J. Phys. Radium*, **17**, 679 (1956).
10. W. Lehmann, *Phys. Rev.*, **101**, 489 (1956).
11. J. Roux, *J. Phys. Radium*, **17**, 813 (1956).
12. S. Roberts, *J. Opt. Soc. Am.*, **42**, 850 (1952).
13. G. F. J. Garlick, "Progress in Semiconductors—1," p. 99, John Wiley & Sons, New York (1956).
14. S. Roberts, *J. Opt. Soc. Am.*, **43**, 590 (1953).
15. P. Zalm, *Philips Research Repts.*, **11**, 353, 417 (1956).
16. S. Nudelman and F. Matossi, *This Journal*, **103**, 34 (1956).
17. C. W. Jerome and W. C. Gungle, *ibid.*, **100**, 34 (1953).
18. C. F. Alfrey and J. B. Taylor, *Brit. J. Applied Phys.*, Supplement No. 4, S44 (1954).
19. C. H. Haake, *J. Opt. Soc. Am.*, **47**, 881 (1957).
20. L. Burns, U. S. Pat. 2,774,902 (Dec. 18, 1953).
21. F. A. Schwertz, J. J. Mazenko, and E. R. Michalik, *Phys. Rev.*, **98**, 1133 (1955).
22. J. Mattler, *J. Phys. Radium*, **17**, 725 (1956).
23. F. Matossi and S. Nudelman, *Phys. Rev.*, **99**, 1100 (1955).
24. W. A. Thornton, *ibid.*, **102**, 38 (1956).
25. F. F. Morehead, Jr., *This Journal*, **105**, 461 (1958).
26. D. R. Frankl, J. L. Birman, G. F. Neumark, and A. Lempicki, *J. Phys. Radium*, **17**, 731 (1956).
27. G. Destriau, *ibid.*, **16**, 798 (1955).
28. W. Lehmann, *This Journal*, **103**, 24 (1956); **105**, 585 (1958).
29. H. F. Ivey, *Bull. Am. Phys. Soc.*, Ser. II, **3**, 273 (1958).
30. W. A. Thornton, *ibid.*, Ser. 11, **3**, 273 (1958).
31. D. Curie, *J. Phys. Radium*, **13**, 317 (1952).
32. W. W. Piper and F. E. Williams, *Phys. Rev.*, **87**, 151 (1952).
33. H. Kallman and E. Sucov, *ibid.*, **109**, 1473 (1958).
34. C. A. Duboc, *Brit. J. Appl. Phys.*, Suppl. No. 4, S 107 (1954).
35. H. A. Klasens, *J. Phys. Chem. Solids*, **7**, 175 (1958).

Optical Properties of Tin- and Lead-Activated Calcium Metasilicate Phosphors

Richard W. Mooney

Chemical and Metallurgical Division, Sylvania Electric Products Inc., Towanda, Pennsylvania

ABSTRACT

The preparation and optical properties of two new tin-activated calcium metasilicate phosphors are described. The more efficient of these is a β-$CaSiO_3$:Sn phosphor emitting in the visible at about 520 mμ. The optical properties of the tin-activated species are compared to their lead-activated analogues; and from considerations of crystal structure as affected by firing temperature and activator concentration, it is concluded that changes in spectra result from changes in crystal structure and not from the degree of aggregation of the activator ions. It is suggested that the emission spectra correspond to the $^2P_1^\circ \rightarrow {}^1S_0$ and the $^1P_1^\circ \rightarrow {}^1S_0$ transitions of the lead- and tin-activator centers.

Calcium metasilicate activated by lead and manganese is a well-known phosphor with a visible emission band at 610 mμ and an ultraviolet emission band at about 350 mμ (1-3). A study of the effect of crystal structure (4) showed that the inversion temperature of β-$CaSiO_3$ (wollastonite) to α-$CaSiO_3$ (pseudowollastonite) is raised with increasing manganese concentration in agreement with results reported by Voos (5), who showed that $MnSiO_3$ (rhodonite), being an isomorph of β-$CaSiO_3$, forms mixed crystals with wollastonite. A more recent study (6) of the influence of crystal structure on β-$CaSiO_3$:Pb + Mn showed that at temperatures where both wollastonite and pseudowollastonite are formed, the manganese crystallizes in the wollastonite lattice to the extent that a red shift is produced by the concentration of manganese in the β-$CaSiO_3$ structure. It was shown also that the addition of magnesium oxide to calcium metasilicate increased the inversion temperature of β-$CaSiO_3$ to α-$CaSiO_3$, whereas the addition of strontium oxide lowered the inversion temperature thus favoring the formation of pseudowollastonite.

The calcium silicates activated by lead alone were studied in detail by Studer and Fonda (7). They found several emission bands in the ultraviolet which they attributed to differences in crystal structure as follows: two bands at 300 mμ and 385 mμ to α-$CaSiO_3$:Pb, a 345 mμ band to β-$CaSiO_3$:Pb, and a 334 mμ band to β-Ca_2SiO_4:Pb. The corresponding excitation spectra varied widely with several maxima between 200 and 300 mμ. In a later study of the mechanism of sensitized luminescence of solids, Schulman and co-workers (8) claimed that the differences in emission were due to differences in the nature of the lead activator center rather than to changes in crystal structure. Specifically, they claimed that the emission bands at 290 and 390 mμ in $CaSiO_3$:Pb were caused by Pb^{2+} singlet centers, i.e., Pb^{2+} activator ions which had no other Pb^{2+} nearest neighbors; whereas the single-band emission at 340 mμ observed at higher lead concentrations was attributed to the occurrence of Pb^{2+}-Pb^{2+} doublets or higher aggregates of Pb^{2+} ions, i. e., centers which had 2 or more Pb^{2+} ions in neighboring cation positions.

Due to the similarities in electronic configuration between lead and tin and the resulting similarities in chemical behavior, it was thought that tin also might function as an activator in the calcium silicate system. In addition, previous work on tin-activated phosphates (9) had shown that many of the tin-activated phosphors were moderately efficient. A study of the calcium silicate system activated by tin has shown that there are at least four phosphors present, two having metasilicate structures and two having orthosilicate structures. This paper gives the preparation and properties of tin-activated β-$CaSiO_3$ (wollastonite) and tin-activated α-$CaSiO_3$ (pseudowollastonite) and compares their spectra with their closely related lead-activated analogues. The preparation and properties of the tin-activated calcium orthosilicates will be reported in a later paper.

Experimental Procedure

Calcium carbonate and silicic acid were mixed in a mole ratio of 1.00 to 1.20 together with 0.01-10.0 mole % of stannic or stannous oxide for the tin-activated phosphors, or lead oxide for the lead-activated phosphors. The mixture was pebble-milled in a deionized water slurry, dried at 110°-120°C, and fired in silica trays at temperatures varying from 980°-1320°C depending on the particular crystal form desired. For maximum efficiency it was necessary to fire in a steam atmosphere, and since the tin-activated phosphors luminesce only when the tin is in a lower valence state, a reducing atmosphere, usually a mixture of hydrogen and steam, was maintained. The steam and hydrogen contents of the firing atmosphere were controlled carefully in order to obtain reproducible results.

The crystal structures of the phosphors were determined by conventional x-ray diffraction techniques using CuKα radiation from a Philips Norelco unit. In the majority of cases, identification was made by means of Debye-Scherrer powder patterns taken with large diameter (114.6 mm) cameras. In

Table I. Effect of tin-activator concentration on the inversion temperature for β- to α-$CaSiO_3$*

Firing temperature, °C	Mole fraction of Sn retained in phosphor				
	0	0.00045	0.00075	0.0058	0.042
1150	β	β	$\alpha(\beta)$	$\alpha(\beta)$	α
1120	β	β	β	β	$\beta(\alpha)$

* Minor constituent given in parentheses.

a few cases, diffractometer tracings were taken on a Norelco wide-range goniometer at a scanning speed of 1/4°/min. As would be expected, the two methods were in excellent agreement.

The quantitative analyses for per cent tin and per cent lead were made as follows. For tin the sample was dissolved in HCl, treated with lead to reduce any stannic tin to the stannous state, and then titrated at 10°C with a standard iodine solution. The determination of per cent lead was slightly more complicated. The sample was first decomposed with HF plus H_2SO_4 followed by a Na_2CO_3 fusion. The resulting $PbCO_3$ was dissolved in HNO_3 and precipitated as $PbMoO_4$ by a solution of $(NH_4)_2MoO_4$. The precipitate was filtered, washed, and fired. The activator contents are expressed in this paper as gram-atom tin or lead per gram-mole of $CaSiO_3$, i.e., as mole fraction.

The excitation-emission radiometer[1] used for the measurements of excitation and emission spectra will be described in detail elsewhere (10). Basically, it is a double monochromator system with a high-pressure xenon arc source and a 1P28 photomultiplier detector. A combination of optical and electrical components provides for constant-energy-level illumination of the sample during excitation measurements and gives an emission spectrum which is proportional to the true energy output of the sample regardless of source fluctuations or detector sensitivity as a function of wave length.

Results with $CaSiO_3$:Sn

A preliminary study of firing temperature disclosed that the more efficient β-$CaSiO_3$:Sn phosphor was obtained with good brightness between 1090° and 1150°C, whereas the less efficient α-$CaSiO_3$:Sn phosphor always was obtained at temperatures above 1150°C. Later it was found that the inversion temperature for β- to α-$CaSiO_3$ was dependent on the activator concentration as shown in Table I. In general, the results were in reasonable agreement with the phase diagram of Levin, McMurdie, and Hall (11) who list the inversion temperature of β- to α-$CaSiO_3$ as 1125°C.

It also was shown that the addition of other divalent cations changed the inversion temperature. For instance, the addition of oxides or fluorides of magnesium, zinc, or cadmium increased the optimum firing temperature for β-$CaSiO_3$:Sn to 1200°C and over, thus indicating an increase in the inversion temperature or a stabilization of the wollastonite structure. Conversely, the addition of the carbonates or fluorides of strontium and barium lowered the optimum firing temperature indicating a stabilization of the pseudowollastonite structure. For barium fluoride, for instance, optimum brightness was obtained at 980°C. These results agree in principle with those of Lange and Kressin (6) in that the addition of ions smaller than calcium, such as magnesium, stabilize the β-$CaSiO_3$ structure, whereas the addition of ions larger than calcium, such as strontium, stabilize the α-$CaSiO_3$ structure.

The phosphor β-$CaSiO_3$:Sn emits in the green with a peak of about 518 mμ when excited by 254 mμ radiation. The corresponding excitation spectrum has a maximum at 246 mμ. Plots of emission and excitation spectra of β-$CaSiO_3$:Sn are shown in the top half of Fig. 1. The emission spectrum is non-Gaussian indicating the possibility of a second unresolved emission band on the high-energy side of the peak. All samples identified as β in Table I gave an emission spectrum as shown in Fig. 1 with the exception of the sample containing the least tin (4.5 x10^{-4} gram-atom Sn/$CaSiO_3$) fired at both 1120° and 1150°C, for which an emission peak at 400 mμ as well as the usual peak at 518 mμ was obtained. This peak was not observed in unactivated samples. The excitation spectrum is characteristic of that obtained for tin-activated phosphors, i.e., broad, indicating the presence of several unresolved absorption bands. The fluorescence of β-$CaSiO_3$:Sn persists at low brightness after the exciting radiation is removed. No quantitative measurements of decay time were made.

The phosphor α-$CaSiO_3$:Sn is weakly fluorescent having two emission bands peaking at 562 and 450 mμ as shown in the top half of Fig. 2. All samples identified as α by x-ray diffraction gave the two peaks shown in Fig. 2 again with the exception of the sample having the least tin (4.5 x 10^{-4} gram-atom Sn/$CaSiO_3$). This sample fired at 1205°, 1260°, and 1320°C showed evidence of the 400 mμ band, although its definition was not as good as that obtained with the β-structure due to the 450 mμ band in the α-$CaSiO_3$:Sn phosphor. Those samples identified as a mixture of α- and β-$CaSiO_3$:Sn in Table I gave a broad band emission extending from 562 to

[1] Built by the Perkin-Elmer Corporation, Norwalk, Conn.

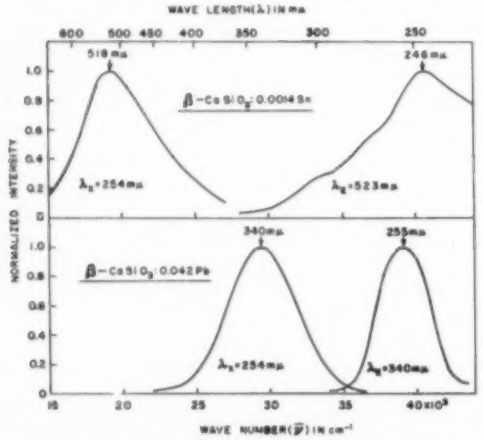

Fig. 1. Excitation and emission spectra of β-$CaSiO_3$:Sn and β-$CaSiO_3$:Pb with activator concentrations given in atoms retained in the fired phosphor per mole $CaSiO_3$.

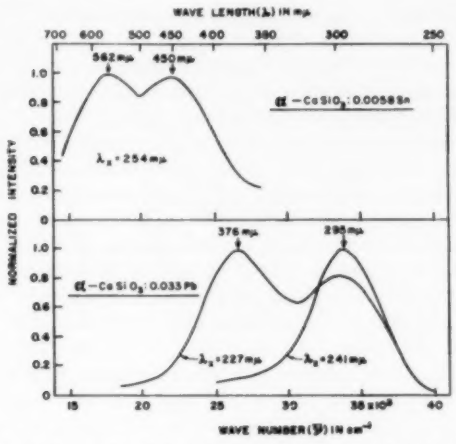

Fig. 2. Emission spectra of α-$CaSiO_3$:Sn and α-$CaSiO_3$Pb with activator concentrations given in atoms retained in the fired phosphor per mole $CaSiO_3$.

450 mμ, since the superposition of the α- and β-$CaSiO_3$:Sn emission gave bands at 562, 518 and 450 mμ which overlapped each other. There was no evidence of the 518 mμ band ascribed to β-$CaSiO_3$:Sn in samples fired at 1205°, 1260°, and 1320°C for the lowest or the highest tin concentration (mole fractions of 4.5×10^{-4} and 4.2×10^{-2}, respectively). The excitation spectra again consisted of several absorption bands as shown in the top half of Fig. 3. It is noteworthy that emission in the lower energy band (562 mμ) is favored by absorption at higher energies, i.e., the excitation spectrum is shifted toward higher energies for fluorescence in the red.

The addition of manganese gave rise to a new emission band at 610 mμ in addition to the band at 518 mμ. Manganese is especially effective in stabilizing the low temperature or β-form of $CaSiO_3$ and, therefore, firing temperatures as high as 1260°C with manganese present still gave the β-$CaSiO_3$ structure. The phosphor β-$CaSiO_3$:Sn + Mn is very similar to the well-known phosphor β-$CaSiO_3$:Pb + Mn (1-3) with the obvious difference in emission between tin- and lead-activation being demonstrated by the presence of the 518 mμ band due to tin rather than the 350 mμ band due to lead. Due to the close proximity of the tin band at 518 mμ and the manganese band at 619 mμ, an increase in manganese concentration produced an apparent shift in the peak emission due to a decrease in intensity of the tin band and an increase in intensity of the manganese band. The tendency of manganese to crystallize in the rhodonite-wollastonite structure stabilized the β-$CaSiO_3$ form over wide Ca/Si ratios (even up to 2.00/1.00 where Ca_2SiO_4 should form) as well as wide temperature ranges.

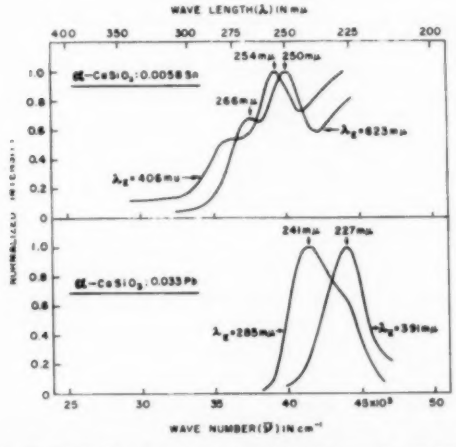

Fig. 3. Excitation spectra of α-$CaSiO_3$:Sn and α-$CaSiO_3$:Pb with activator concentrations given in atoms retained in the fired phosphor per mole $CaSiO_3$.

Results with $CaSiO_3$:Pb

A corresponding study of the lead-activated calcium metasilicates gave very similar results to those obtained on the tin-activated system. Thus, β-$CaSiO_3$:Pb was obtained below 1150°C, whereas the less efficient α-$CaSiO_3$:Pb phosphor always was obtained above 1150°C. Again the particular modification obtained at temperatures close to the transition temperature was dependent on the activator concentration (see Table II).

The β-$CaSiO_3$:Pb phosphor emits in the ultraviolet at about 340 mμ when excited by 254-mμ radiation. The corresponding excitation spectrum has its maximum at 255 mμ. Both the emission and the excitation spectra have Gaussian distributions as shown in the bottom half of Fig. 1. All samples identified as β in Table II had excitation and emission spectra as above. There was no evidence of a second emission band at very low concentrations, but the peak of the emission band did shift slightly from 337 to 350 mμ in going from the lowest to the highest lead concentration.

All lead-activated calcium metasilicates fired above 1150°C had the α-$CaSiO_3$ structure and displayed emission and excitation spectra characteristic of those shown in the bottom halves of Fig. 2 and 3. Thus α-$CaSiO_3$:Pb has two emission bands at 295 and 376 mμ and two corresponding excitation bands at 241 and 227 mμ. It is interesting, however, that irradiation in the lower-energy band at 241 mμ produced the higher energy band at 295 mμ, whereas irradiation in the higher energy band at 227 mμ caused the lower energy band at 376 mμ to appear. That is, the direct energy relationship between excitation and emission that one normally would expect is reversed. Those samples in Table II which were identified as a mixture of α- and β-$CaSiO_3$ gave all three emission bands depending upon the wave length of excitation. However, the greater absorption of β-$CaSiO_3$:Pb compared to α-$CaSiO_3$:Pb at the

Table II. Effect of lead-activator concentration on the inversion temperature for β- to α-$CaSiO_3$*

Firing temperature, °C	Mole fraction of Pb retained in phosphor				
	0	0.001	0.01	0.064	0.085
1150	β	$\beta(\alpha)$	$\alpha(\beta)$	$\alpha(\beta)$	α
1120	β	$\beta(\alpha)$	$\beta(\alpha)$	$\beta(\alpha)$	$\alpha(\beta)$

* Minor constituent given in parentheses.

higher wave lengths made the β-$CaSiO_3$: Pb emission spectra predominant even for the sample containing 0.085 Pb/$CaSiO_3$ fired at 1120°C and identified as primarily α-$CaSiO_3$ (see Table II). Therefore, the emission spectra of lead-activated $CaSiO_3$ fired in the neighborhood of the inversion temperature exhibited the following characteristics with increasing lead content. At very low lead concentrations, the β-$CaSiO_3$: Pb band appeared at 337 mμ. As the structure changed to a mixture of β- plus α-$CaSiO_3$, all three bands appeared, and finally the β-$CaSiO_3$: Pb band now at 350 mμ was again the only band found at high lead concentrations. On the contrary, samples fired at 1260°C having the lowest (0.001) and the highest (0.085) lead concentrations exhibited only the typical α-$CaSiO_3$: Pb bands.

Discussion

The obvious conclusion to be drawn from these results is that the excitation and emission spectra of tin- and lead-activated calcium metasilicates are determined primarily by the particular activator used and the crystal structure of the matrix in which the activator is found. This conclusion is in agreement with the original work on lead-activated calcium metasilicates by Studer and Fonda (7), but is in sharp disagreement with the later work by Schulman, Ginther, and Klick (8), who ascribed the differences in spectra observed on lead-activated calcium metasilicates to the occurrence of singlet Pb^{2+} activator centers at low lead concentrations and doublet Pb^{2+}-Pb^{2+} activator centers at higher lead concentrations.

According to this later work, the singlet Pb^{2+} centers are excited only by absorption in the 235 mμ band, which is shown by Fig. 3 to be in reality two bands peaked at 227 and 241 mμ, and which gives a double-band emission peaked at 290 and 390 mμ (295 and 376 mμ according to Fig. 2). In this work, these paired excitation and emission bands are ascribed to the phosphor, α-$CaSiO_3$: Pb.

The 255 mμ absorption band with single-band emission peaking at 340 mμ was assigned to the presence of Pb^{2+}-Pb^{2+} doublets by Schulman, *et al.* However, while the experimental agreement between the measured spectra is excellent (see Fig. 1), the present work claims that these bands are associated with the β-$CaSiO_3$: Pb phosphor.

The evidence for these assumptions is given by a comparison of the spectra of the lead-activated calcium metasilicates as a function of activator concentration and firing temperature coupled with x-ray identification of the crystal structures of the phosphors. Thus, as related under results, phosphors fired at temperatures close to the inversion temperature (1125°C), i.e., at 1120° and 1150°C, have varying spectra depending upon the activator concentration and its effect on crystal structure. At very low lead concentrations, the spectra are characteristic of β-$CaSiO_3$: Pb as would be expected from the x-ray identification. At intermediate lead concentrations, the spectra are mixtures of that expected from β- and α-$CaSiO_3$: Pb. However, at the highest lead concentrations, the spectra are once more characteristic of β-$CaSiO_3$: Pb, whereas one would expect to find the α-$CaSiO_3$: Pb spectrum in view of the x-ray identification. To explain this result, it must be remembered that with increasing lead concentrations, the phosphors are becoming less efficient due to concentration quenching; and, since the α-$CaSiO_3$: Pb phosphor is inefficient even at low activator concentrations, its emission at high lead concentrations is below the limits of detection of the instrument. These results are in rough agreement with the observation of Schulman, *et al.*, as would be expected, since they used a firing temperature of 1150°C where both β- and α-$CaSiO_3$ may be formed under the right conditions.

The above observations are not convincing proof since the spectra of the phosphors are confused by crystal structure changes. However, it has been noted that firings above 1150°C gave only the α-$CaSiO_3$ structure. If the differences in spectra are due to the occurrence of lead singlet or doublet centers, these differences should depend only upon the activator concentration and not on the firing temperature with its effect upon crystal structure. Therefore, the experimental observation that lead-activated calcium metasilicates fired at 1260°C exhibited only the spectral characteristics of α-$CaSiO_3$: Pb as shown in Fig. 2 and 3 and never the spectrum of β-$CaSiO_3$: Pb as shown in Fig. 1, completely independent of activator concentration leads to the conclusion that the spectra are determined by the crystal structure and not by the degree of aggregation of the activator ions. The same conclusion also may be reached from the results on the tin-activated calcium metasilicate system.

The previous observation (8) that irradiation in the 235 mμ absorption band does not excite the visible Mn^{2+} emission in $CaSiO_3$: Pb + Mn is explained easily by the fact that Mn crystallizes preferentially in the β-$CaSiO_3$ lattice (5, 6) and therefore it is necessary to excite the Pb atoms in β-$CaSiO_3$: Pb, which absorbs at 255 mμ, but not at 235 mμ.

As usual in studies of this type, it is easier to demonstrate the incorrectness of a previous model than it is to propose with any degree of assurance a model which does explain the experimental observations. Due to the complexity of the silicate crystal structures and the resulting complex symmetry of their crystalline fields, it is not possible to explain the results in a quantitative manner as has been done for KCl: Tl (12). However, some rather interesting speculations concerning the nature and origin of the emission bands may be made. For instance, since the electronic configurations of the ground states of Tl II (Tl^+) and Pb III (Pb^{2+}) are identical and that of Sn III (Sn^{2+}) is very similar, having a $5s^2\ {}^1S_0$ ground state instead of the $6s^2\ {}^1S_0$ ground state of Tl II and Pb III, one might expect lead- and tin-activated phosphors to behave generally much like thallium-activated systems.

Therefore, proceeding by analogy with KCl: Tl, the higher energy emission bands in both tin- and lead-activated α-$CaSiO_3$ might be assumed to arise from the ${}^1P_1^\circ \rightarrow {}^1S_0$ transition and the lower energy bands to arise from the ${}^3P_1^\circ \rightarrow {}^1S_0$ transition of the activator

centers. Similarly, in view of its relative position with reference to the emission bands in the α-structure, the single band in tin- and lead-activated β-$CaSiO_3$ could be assigned arbitrarily to the $^3P_1^\circ \rightarrow {}^1S_0$ transition. Such assignments of energy levels are not inconsistent with the trends that one should expect by comparison to the same energy level transitions for the free ions (13). However, the assignment of the $^3P_1^\circ \rightarrow {}^1S_0$ transition to the green emission band in β-$CaSiO_3$:Sn is not consistent with the phosphorescence observed, which suggests a forbidden transition, whereas the $^3P_1^\circ \rightarrow {}^1S_0$ transition is allowed if the selection rule $\Delta S = 0$ does not hold due to imperfect LS coupling.

In summary, it has been shown that the spectra of tin- and lead-activated calcium metasilicates are associated with the particular structure produced, i.e., α- or β-$CaSiO_3$ and not with the degree of aggregation of the activator ions. Instead it is suggested that the emission bands in both tin- and lead-activated α-$CaSiO_3$ are related to the $^3P_1^\circ \rightarrow {}^1S_0$ and the $^1P_1^\circ \rightarrow {}^1S_0$ transitions of the activator ions and that the single emission band in β-$CaSiO_3$:Sn or Pb is related to the $^3P_1^\circ \rightarrow {}^1S_0$ transition, although the reason for the occurrence of a $^1P_1^\circ \rightarrow {}^1S_0$ transition in the α-$CaSiO_3$ structure and not in the β-$CaSiO_3$ structure is not understood.

Acknowledgment

The author is indebted to several of his colleagues for their help with the preparations and measurements. Specifically, the author wishes to thank Mr. F. N. Shaffer for his aid and advice in the preparation of the first Sn-activated metasilicates, Dr. C. W. W. Hoffman for the x-ray identifications, and Mr. G. J. Meisenhelter for the analytical determinations. The author also wishes to acknowledge the advice and encouragement of Dr. J. S. Smith during the progress of this work.

Manuscript received May 18, 1959. This paper was prepared for delivery before the Philadelphia Meeting, May 3-7, 1959.

Any discussion of this paper will appear in a Discussion Section to be published in the June 1960 JOURNAL.

REFERENCES

1. J. B. Merrill and J. H. Schulman, *J. Opt. Soc. Amer.*, **38**, 471 (1948).
2. H. C. Froelich, *This Journal*, **93**, 101 (1948).
3. K. H. Butler, *ibid.*, **95**, 267 (1949).
4. G. R. Fonda and H. C. Froelich, *ibid.*, **93**, 114 (1948).
5. E. Voos, *Z. anorg. u. allgem. Chem.*, **222**, 201 (1935).
6. H. Lange and G. Kressin, *Z. Physik*, **142**, 380 (1955).
7. F. J. Studer and G. R. Fonda, *J. Opt. Soc. Amer.*, **39**, 655 (1949).
8. J. H. Schulman, R. J. Ginther, and C. C. Klick, *This Journal*, **97**, 123 (1950).
9. K. H. Butler, *ibid.*, **100**, 250 (1953).
10. W. Slavin, R. W. Mooney, and D. T. Palumbo, To be published.
11. E. M. Levin, H. F. McMurdie, and F. P. Hall, "Phase Diagrams for Ceramists," p. 48, The American Ceramic Society, Columbus, Ohio (1956).
12. F. E. Williams, *J. Opt. Soc. Amer.*, **47**, 869 (1957).
13. C. E. Moore, "Atomic Energy Levels," Vol. III, NBS Circular #467 (1958).

Phase Equilibria and Manganese-Activated Fluorescence in the System $Zn_3(PO_4)_2$-$Mg_3(PO_4)_2$

J. F. Sarver, Fred L. Katnack,[1] and F. A. Hummel

Department of Ceramic Technology, College of Mineral Industries, The Pennsylvania State University, University Park, Pennsylvania

ABSTRACT

Determination of the phase relationships on the $Zn_3(PO_4)_2$-$Mg_3(PO_4)_2$ join by the quench method has enabled the previously designated "gamma zinc phosphate" to be identified as a solid solution of zinc orthophosphate in magnesium orthophosphate. $Mg_3(PO_4)_2$ takes 95 mole % $Zn_3(PO_4)_2$ into solid solution at 1000°C. β-$Zn_3(PO_4)_2$ takes a small amount of $Mg_3(PO_4)_2$ into solid solution (about 3 mole % at 1000°) and, in order to satisfy the requirements of the Phase Rule, α-$Zn_3(PO_4)_2$ must take a small amount of $Mg_3(PO_4)_2$ into solution. The previously determined $Zn_3(PO_4)_2$-$Mn_3(PO_4)_2$ relationships are discussed in terms of the new data for the zinc-magnesium orthorphosphate system. Solid solution relationships in the system MgO-ZnO-P_2O_5 are diagrammed and discussed.

Data on peak emission and brightness of the β-$Zn_3(PO_4)_2$ solid solution and the $Mg_3(PO_4)_2$ solid solution were obtained using molar substitutions of manganese as an activator. The brightness of the β-$(Zn,Mg)_3(PO_4)_2$:Mn solid solutions compares favorably with commercial β-$Zn_3(PO_4)_2$:Mn phosphors and the N.B.S. standard. The manganese-activated phosphors near the high zinc end of the $Mg_3(PO_4)_2$ solid solution series are very bright relative to the β-$Zn_3(PO_4)_2$:Mn standard, but they peak near 6280Å, which may in part account for the higher brightness.

This paper is the last of a series which was intended to establish the identity and the manganese-activated emission characteristics of the α, β, and "gamma" zinc orthophosphate family of cathode-ray excitable phosphors. A second purpose in accumulating these data was to establish a general picture of the phase relationships in the system MgO-ZnO-P_2O_5.

The work of Smith (1) led to the development of these red fluorescing T.V. phosphors and the adoption of the alpha, beta, and "gamma" nomenclature.

Katnack and Hummel (2) established the nature of the alpha to beta zinc orthophosphate inversion and later Hummel and Katnack (3) furnished data on the manganese-activated cathode-ray emission characteristics of all the zinc phosphate compounds.

Recent work by Sarver and Hummel (4) established the nature of manganese-activated cathode-ray emission in the system $Mg(PO_3)_2$-$Zn(PO_3)_2$.

Experimental Procedure

Phase relationships.—The equilibrium relationships in the system were established using the seventeen compositions shown in Table I. The raw materials used were C.P. grades of ZnO, basic magnesium carbonate, and dibasic ammonium phosphate, $(NH_4)_2HPO_4$. The starting material for quench determinations in compositions 1-7 was a fused and recrystallized melt which had been held at 750°C for 24 hr. The starting material for the remaining portion of the work (compositions 8-17) was a calcine which had been heated to 200°C for 24 hr.

Phase identifications were made by petrographic and x-ray diffraction examination, using nickel-filtered CuKα radiation for the latter method.

Fluorescence.—Two sets of data on manganese-activated, cathode ray emission were obtained. The first series included data on the β-$(Zn,Mg)_3(PO_4)_2$:Mn solid solutions and a wide range of $(Mg,Zn)_3(PO_4)_2$:Mn ternary solid solutions. The second series included a brief investigation of the manganese activator concentration on the peak emission and brightness of one of the brightest compositions in the high zinc end of the $(Mg,Zn)_3(PO_4)_2$ solid solutions.

Spectral distribution curves were obtained with a demountable cathode-ray tube operating at 16 kv anode potential, 1.0 μa/cm^2 beam current density on a standard scan T.V. raster of 65 cm^2 area.

Brightness under the above conditions was measured using an eye-corrected Weston foot-lambert meter.

Results and Discussion

Phase Relationships on the Orthophosphate Join

The quench and heat treatment data shown in Table I were used to construct the equilibrium diagram shown in Fig. 1. The system is characterized by a small region of β-$Zn_3(PO_4)_2$ solid solutions, a still smaller region of α-$Zn_3(PO_4)_2$ solid solutions, and a very large region of $Mg_3(PO_4)_2$ solid solutions. The x-ray diffraction data for the β-$Zn_3(PO_4)_2$ and

[1] Present address: Radio Corporation of America, Somerville, N. J.

Table I. Compositions, quench data, and heat treatments for the system $Zn_3(PO_4)_2$-$Mg_3(PO_4)_2$

Comp. No.	Mole per cent $Zn_3(PO_4)_2$	Mole per cent $Mg_3(PO_4)_2$	Temp, °C/24 hr	Phases present
1	100	0	900	α-Z_2P
			1000	β-Z_2P
2	99	1	950	β-Z_2P_{ss}
			995	β-Z_2P_{ss}
3	98	2	921	α-Z_2P_{ss} + M_3P_{ss}
			929	β-Z_2P_{ss} + M_3P_{ss}
			933	β-Z_2P_{ss} + M_3P_{ss}
			950	β-Z_2P_{ss} + M_3P_{ss}
			998	β-Z_2P_{ss}
4	97	3	920	M_3P_{ss}
			950	β-Z_2P_{ss} + M_3P_{ss}
			1000	β-Z_2P_{ss} + M_3P_{ss}
			1045	β-Z_2P_{ss}
5	96	4	958	M_3P_{ss}
			995	β-Z_2P_{ss} + M_3P_{ss}
			1035	β-Z_2P_{ss} + M_3P_{ss}
			1045	β-Z_2P_{ss}*
6	95	5	995	M_3P_{ss}
			1035	β-Z_2P_{ss} + M_3P_{ss}
7	94	6	1040	M_3P_{ss}
8	90	10	1050	M_3P_{ss}
9	80	20	1050	M_3P_{ss}
10	70	30	1050	M_3P_{ss}
11	60	40	1050	M_3P_{ss}
12	50	50	1161	M_3P_{ss}
			1180	M_3P_{ss}*
13	40	60	1050	M_3P_{ss}
14	30	70	1050	M_3P_{ss}
15	20	80	1050	M_3P_{ss}
16	10	90	1050	M_3P_{ss}
17	0	100	1050	M_3P_{ss}

* Evidence of melting.

Note: Compositions 1 through 7 and 12 were treated in quenching furnaces. The remaining compositions were heat treated in Globar furnaces.

α-Z_2P = α-$Zn_3(PO_4)_2$
β-Z_2P = β-$Zn_3(PO_4)_2$
M_3P = $Mg_3(PO_4)_2$

α-$Zn_3(PO_4)_2$ phases have been presented in a previous paper (2). The presence of magnesium in solid solution in the α and β phases produced no appreciable shift in the position of the lines in the x-ray diffraction pattern.

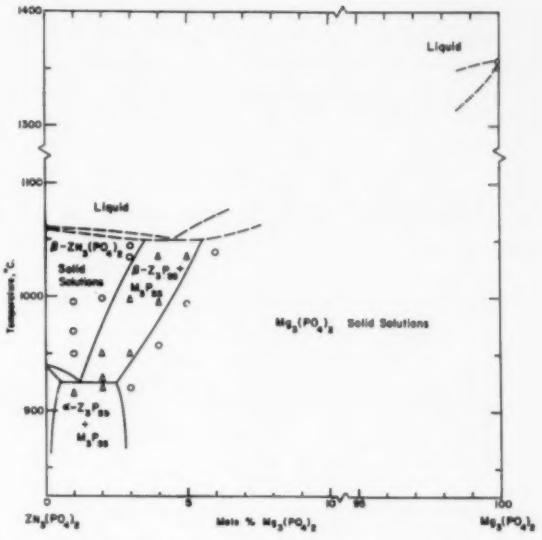

Fig. 1. Phase relationships on the $Zn_3(PO_4)_2$-$Mg_3(PO_4)_2$ join

The x-ray diffraction data for $Mg_3(PO_4)_2$, solid solutions containing 20, 40, 60, 80, and 95 mole % $Zn_3(PO_4)_2$, and the previously reported (3) manganese "gamma zinc orthophosphate" are listed in Table II. The patterns of the magnesium orthophosphate solid solutions are shown in Fig. 2 for convenience in following the changes which occur. A detailed study of the x-ray diffraction patterns of all the members of the $Mg_3(PO_4)_2$ solid solution compositions (7-17) listed in Table I showed that the series was actually continuous from pure $Mg_3(PO_4)_2$ to 95 mole % $Zn_3(PO_4)_2$. Petrographic examination confirmed the one phase nature of the compositions in this region.

Since the system was not glass-forming, the liquidus relationships were not determined and the phase boundaries in the high-temperature region are shown as dashed lines due to this uncertainty. Berek (5) reported the melting point of $Mg_3(PO_4)_2$

Table II. X-ray diffraction data for $(Zn,Mn)_3(PO_4)_2$,* $(Zn_{0.95}Mg_{0.05})_3(PO_4)_2$, Mg_3PO_4, and four intermediate solid solutions

$(Zn, Mn)_3(PO_4)_2$*			$(Zn_{0.95}Mg_{0.05})_3(PO_4)_2$			80Z_2P-20M_3P		60Z_2P-40M_3P		40Z_2P-60M_3P		20Z_2P-80M_3P		$Mg_3(PO_4)_2$		
2θ	d	I/I_o	2θ	d	I/I_o	2θ	I/I_o	2θ	I/I_o	2θ	I/I_o	2θ	I/I_o	2θ	d	I/I_o
15.9	5.57	10												15.9	5.57	14
			20.4	4.35	80	20.4	70	20.4	75	20.4	54	20.4	45	20.4	4.35	32
20.5	4.33	90†	20.6	4.31	37	20.6	41	20.6	59	20.6	46	20.6	37	20.6	4.31	28
21.1	4.21	5	21.1	4.21	8	21.2	12	21.3	19	21.5	22	21.5	27	21.6	4.11	39
22.3	3.99	40	22.1	4.02	40	22.1	31	22.0	33	22.0	40	21.8	27	21.8	4.08	49
23.0	3.87	25	23.0	3.87	25	23.0	27	23.0	40	23.1	48	23.1	61	23.1	3.85	91
24.2	3.68	5	24.4	3.65	5	24.4	5	24.4	6	24.4	6	24.4	15	24.3	3.66	35
26.1	3.41	100	25.9	3.44	100	25.9	100	25.9	100	25.9	100	25.9	100	25.9	3.44	100
27.6	3.23	20	27.6	3.23	26	27.7	26	27.8	29	27.9	26	27.9	22	27.9	3.20	19
29.5	3.03	20	29.5	3.03	27	29.6	26	29.6	30	29.7	26	29.7	22	29.8	3.00	22
30.8	2.90	10	30.7	2.91	10											
31.9	2.81	25	32.0	2.80	10	32.0	17	32.0	9	32.0	9	32.0	17	32.0	2.80	17
32.9	2.72	15	32.8	2.73	13	32.8	10	32.7	9	32.6	9	32.5	8	32.3	2.77	7
34.0	2.64	10	34.1	2.64	5	—	—	—	—	—	—	—	—	—	—	—
35.6	2.52	35	35.6	2.52	51	35.6	54	35.7	55	35.6	22	35.5	21	35.4	2.54	12
35.8	2.51	35	—	—	—	—	—	—	—	35.8	37	35.8	32	35.9	2.50	28
36.6	2.46	55	36.6	2.46	40	36.8	42	37.0	41	37.2	34	37.2	36	37.2	2.42	34

* Hummel and Katnack (3).
† May be a doublet.

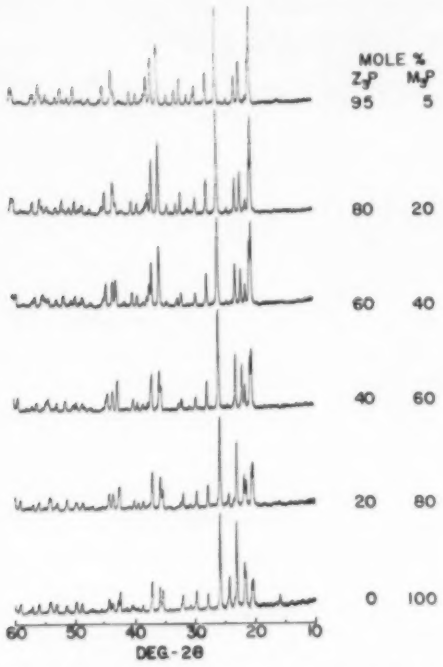

Fig. 2. X-ray diffraction patterns for magnesium orthophosphate solid solutions.

as 1357°C, and this value has been used in constructing Fig. 1.

A word about the previously determined relationships on the $Zn_3(PO_4)_2$-$Mn_3(PO_4)_2$ join (3) is now in order. The close structural relationship between the long series of (Mg, Zn)$_3(PO_4)_2$ solid solutions and the (Zn, Mn)$_3(PO_4)_2$ solid solutions ("gamma zinc orthophosphate") is now apparent from the data in Table II. It had been mentioned (3) and it is well known that oxidation of manganese hinders the complete determination of phase relationships in such a system when working in air. If a pure $Mn_3(PO_4)_2$ phase could be made by synthesis in nitrogen or other protective atmosphere, it is possible that a large range of (Zn,Mn)$_3(PO_4)_2$ solid solutions would exist, analogous to the zinc-magnesium series. Even without the benefit of a protective atmosphere to assure the retention of divalent manganese, it has been shown (3) that quite a broad region of ternary solid solutions do exist.

The Ternary System MgO-ZnO-P_2O_5

The subsolidus solid solution relationships in the ternary system are shown in Fig. 3.

The MgO-ZnO relationships were determined by firing mixtures of the oxides at 1300°C for 8 hr. Using nickel-filtered CuKα radiation ($\lambda = 1.5405$Å) and 10% by weight of silicon metal as an internal standard, diffraction patterns were run at ½° (2θ)/min. The results for MgO and the solid solution limit (ZnO in MgO) are shown in Table III.

The lattice expansion due to the inclusion of 32 mole % zinc oxide was 0.7%. Similar data for compositions near ZnO indicated about 3% of solid solution at 1300°C.

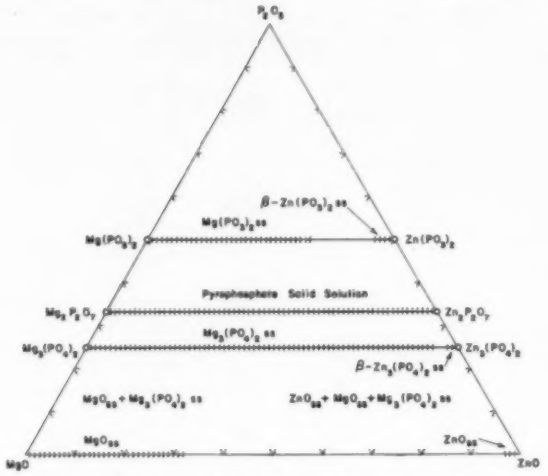

Fig. 3. Subsolidus solid solution relationships in the system MgO-ZnO-P_2O_5 (mole per cent).

Data on the orthophosphate join have been presented above and the data on the solid solutions on the metaphosphate join were presented previously (4).

According to some unpublished data obtained several years ago (6), it is probable that a complete (or nearly complete) series of pyrophosphate solid solutions exist. The generally high solid solubility of the zinc compounds in their magnesium analogues is thus apparent.

Fluorescence

Compositions shown in Table IV were fired at 1000°C for 48 hr, using 1 mole % MnO as an activator.

These results show that a little $Mg_3(PO_4)_2$ added to β-$Zn_3(PO_4)_2$ improves the brightness of the β solid solution, and that excessive amounts will damage brightness. A substantial shift in the position of peak intensity occurs with small additions of $Mg_3(PO_4)_2$.

The $Mg_3(PO_4)_2$ solid solutions containing high amounts of zinc are perhaps brighter than the β-type phosphors, but unfortunately the peak intensities are shifted to the neighborhood of 6300Å. Even the low intensity $Mg_3(PO_4)_2$ peaks at 6320Å.

It appears that there may be a minimum in the position of peak intensity in the solid series in the neighborhood of 70-80 mole % $Zn_3(PO_4)_2$.

Table III. Comparison of unit cell dimensions of MgO and $(Mg_{0.68}Zn_{0.32})O$

			MgO			
hkl	2θ obs.	2θ corrected	d, Å	I	I/I_o	a_o
111	37.00	36.95	2.433	9	11	4.214
200	42.96	42.95	2.104	84	100	4.208
220	62.36	62.36	1.488	44	52	4.209
311	74.75	74.75	1.2689	6	7	4.208
322	78.70	78.70	1.2148	12	14	4.208
			$(Mg_{0.68}Zn_{0.32})O$			
111	36.63	36.73	2.447	25	38	4.238
200	42.55	42.65	2.120	66	100	4.240
220	61.80	61.85	1.4988	33	50	4.239
311	74.10	74.15	1.2777	9	14	4.238
222	78.00	78.05	1.2233	7	11	4.238

Table IV. Brightness and peak intensity of β-$(Zn,Mg)_3(PO_4)_2$ and $(Mg, Zn)_3(PO_4)_2$ ("gamma") solid solutions

Comp. No.	$Zn_3(PO_4)_2$	$Mg_3(PO_4)_2$	Phases	Peak intensity, A	Relative brightness
1	100.0	0.0	β-Z_3P	6360	116
2	99.5	0.5	β-Z_3P_{ss}	6380	118
3	99.0	1.0	β-Z_3P_{ss}	6400	90
4	98.5	1.5	β-Z_3P_{ss}	6400	105
5	98.0	2.0	β-Z_3P_{ss} + M_3P_{ss}	6300	119
6	95.0	5.0	M_3P_{ss}	6300	133
7	90.0	10.0	M_3P_{ss}	6280	133
8	80.0	20.0	M_3P_{ss}	6260	121
9	70.0	30.0	M_3P_{ss}	6260	87
10	60.0	40.0	M_3P_{ss}	6270	91
11	50.0	50.0	M_3P_{ss}	6290	66
12	40.0	60.0	M_3P_{ss}	6280	43
13	30.0	70.0	M_3P_{ss}	6300	26
14	20.0	80.0	M_3P_{ss}	6300	22
15	10.0	90.0	M_3P_{ss}	6310	14
16	0.0	100.0	M_3P_{ss}	6320	12
N.B.S. Zinc Orthophosphate: Mn				6380	100
G.E. 1092-1, Lot 11 $Zn_3(PO_4)_2$: Mn				6380	117

Table V. Effect of activator concentration on the brightness of $(Zn_{0.95}, Mg_{0.05})_3(PO_4)_2$ solid solution

Comp.	Mole % $Mn_3(PO_4)_2$ substituted for $Mg_3(PO_4)_2$	Heat treatment, °C for 48 hr	Peak intensity, A	Relative brightness
1	0.01	1000	6300	131
2	0.015	975	6280	123
3	0.020	950	6280	127
4	0.025	925	6280	124
5	Composition 6, Table IV		6300	120
NBS Zinc Orthophosphate: Mn			6380	100
G.E. 1092-1, Lot 11 β-$Zn_3(PO_4)_2$: Mn			6380	124

On the basis of the results shown in Table IV, a series of compositions was made to check the effect of activator concentration in the brightest $(Zn_{0.95}, Mg_{0.05})_3(PO_4)_2$ ("gamma") solid solution, as shown in Table V. These samples were fired at temperatures (see Table V) which were designed to prevent the formation of any unwanted β phase. It must be remembered that the $(Zn_{0.95}, Mn_{0.05})_3(PO_4)_2$ solid solution would transform to the β structure at temperatures around 940°C (3). If fired too high, the intermediate solid solutions would also begin to transform. Unfortunately, this technique does not permit a direct comparison of the brightness of phosphors fired at the same temperature. X-ray diffraction patterns of the fired samples showed them to be pure $Mg_3(PO_4)_2$ solid solutions.

This series of compositions shows that the solid solution is relatively insensitive to large changes in activator concentration. It should be noted that composition 6 when first measured gave a relative brightness of 133 compared to 120 when used as a comparative standard in the series in Table V. These differences are probably mainly due to variations in sample preparation and measuring technique.

The peak intensities hover around 6280-6300Å, indicating not quite as good "redness" as the beta phosphors.

Conclusions

1. "Gamma zinc phosphate" or "gamma zinc orthophosphate" has been shown to be an extended series of solid solutions of zinc orthophosphate in $Mg_3(PO_4)_2$.

2. Analogous series of $(Zn,Mg)_3(PO_4)_2$ and $(Zn,Mn)_3(PO_4)_2$ solid solutions exist in their respective ternary systems and probably form solid solutions in the quarternary system ZnO-MgO-MnO-P_2O_5.

3. The high zinc members of the $Mg_3(PO_4)_2$ solid solutions have good brightness and form the basis of a well-defined series of red cathode-ray phosphors. The brightness and peak emission of these phosphors are relatively insensitive to the amount of Mn^{++} which is substituted for Mg^{++} in the structure.

Acknowledgment

Emission data were obtained through cooperation of Marjorie Brines of the Chemical Products Plant, General Electric Co. The investigation was made possible by the support of the Chemical Products Plant, General Electric Co., Cleveland, Ohio.

Contribution #58-81 from the Department of Ceramic Technology, College of Mineral Industries, The Pennsylvania State University, University Park, Pa.

Manuscript received April 6, 1959. This paper was prepared for delivery before the Philadelphia Meeting, May 3-7, 1959.

Any discussion of this paper will appear in a Discussion Section to be published in the June 1960 JOURNAL.

REFERENCES

1. A. L. Smith, *This Journal*, **98**, 363 (1951).
2. F. L. Katnack and F. A. Hummel, *ibid.*, **105**, 125 (1958).
3. F. A. Hummel and F. L. Katnack, *ibid.*, **105**, 528 (1958).
4. J. F. Sarver and F. A. Hummel, *ibid.*, **106**, 500 (1959).
5. Jozef Berak, *Roczniki Chem.*, **32**, 17 (1958).
6. R. M. Smith and F. A. Hummel, Unpublished data on the pyrophosphate join, 1950.

Cadmium Sulfide Photoconductive Sintered Layers

Martha J. B. Thomas and Edward J. Zdanuk[1]

Engineering Laboratories, Sylvania Electric Products Inc., Salem, Massachusetts

ABSTRACT

The preparation and performance of sintered photoconductive cadmium sulfide layers have been described. Although the photoconductive characteristics are directly dependent on composition, layer preparative techniques, and geometry of the unit, these parameters may be predicted and controlled to give a resultant reproducible layer of desired electrical and optical characteristics.

The use of photoconductive cadmium sulfide in electronic devices, such as light amplifiers and image converters, has increased greatly during the past few years (1-4). These devices usually have necessitated fabrication of photoconductive layers of large surface area. Such layers can be achieved most readily by means of powdered layer (5), sintered layer (1, 3), dielectric imbedment, or evaporated film (7) techniques. Sintered layers have become particularly popular in device fabrication because of their superior sensitivity (5, 8) uniformity, high mechanical strength, and ease of formation (5, 8).

Although a considerable amount of work has been done in determining the electrical and optical characteristics of pure cadmium sulfide and cadmium sulfide matrices in which traces of impurities such as copper and the halogens have been incorporated, these studies were conducted in the main on single crystals (9-11).

This paper describes some of the optical and electrical characteristics of sintered layers of cadmium sulfide and demonstrates the dependence of these characteristics on the initial chemical formulation and on the method of forming the final sintered layer.[2]

Experimental

Figure 1 presents schematically the process involved in the preparation of the sintered layer.

Phosphor quality cadmium sulfide (Sylvania or RCA) and analytical reagent quality cadmium chloride and copper chloride were used. A formulation found to be particularly suitable for general sintered layer application had the following composition:—1 mole cadmium sulfide; 0.3 mole of cadmium chloride; 8 x 10^{-4} gram atoms of copper added as copper chloride or basic copper carbonate. All components were ground prior to blending. The blended composite, usually 100 g, was given an initial bulk firing for 35 min in covered porcelain crucibles. This resulted in a small amount of sintering and preliminary distribution of activator components into the cadmium sulfide. The partially sintered cadmium sulfide was milled in xylene to insure sufficiently fine particle size to yield a smooth-appearing sintered layer; to the suspension sufficient organic binder (ethyl-cellulose type) was added in order to insure a coherent layer during film formation prior to sintering. Usually this photoconductor suspension was sprayed although layers prepared with flow-on and doctor blade techniques gave identical results.

The sprayed layer was dried at room temperature for at least ½ hr during which most of the organic solvent volatilized. The layer was sintered in an electric muffle furnace in an air atmosphere, normally for 10 min at 550°C. Dependence of layer characteristics on presintering and sintering temperatures is discussed later.

Preparation of Test Cells

Standard cells.—Standard test cells of the geometry indicated in Fig. 2 were used for the determination of the desired characteristics. The cells were made on 1 x 2½ x ⅛ in. Pyrex slides which had been coated with a conductive film of transparent semiconducting tin oxide. The desired electrode structure with ⅛ x ¼ in. gaps was prepared by sand blasting the conductive film through a pattern mask. The slides were then thoroughly washed and dried in an oven at 150°C. The photoconductor suspension was sprayed in square patches between the electrodes using a suitable mask. Each slide had six in-

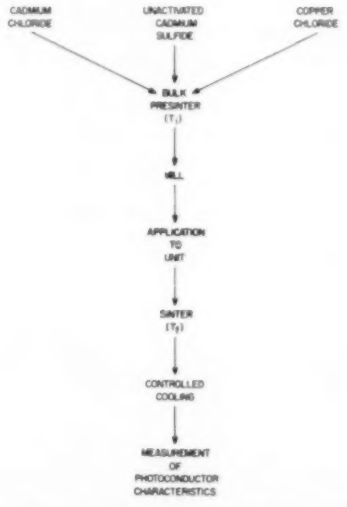

Fig. 1. Flow diagram of preparation of sintered layer

[1] Present address: Research Division, Raytheon Manufacturing Co., Waltham, Mass.

[2] After this paper had been submitted for publication a technical report was issued by Lincoln Laboratories (13). This report, which has limited circulation, describes similar studies of CdS sintered layers and supplements the present paper.

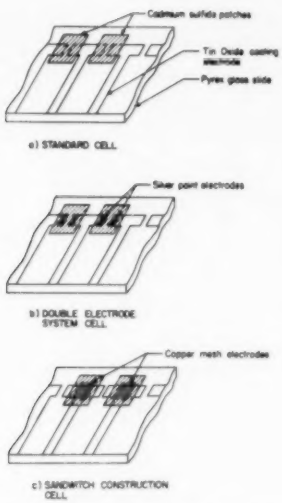

Fig. 2. Types of photoconductive cells used in measurement of photoconductor characteristics.

dividual test cells and measurements of electrical and optical properties of each individual cell were made. Values of the central four cells were found to be reproducible and consistent. The end cells yielded very erratic results, which will be discussed later in the paper.

Double electrode cells.—Double electrode cells (Fig. 2B) were made from the standard test cells by painting silver electrodes (Du Pont air dry conductive silver) on the top surface duplicating the gap structure of the tin oxide electrodes on the undersurface of the photoconductive layer.

Sandwich.—Sandwich cells (Fig. 2C) were also fashioned from the basic standard test cells by applying a ¼ x ¼ in. patch of very fine electroformed copper mesh. This copper mesh, 500 lines to the inch, was applied to the surface by a silicone adhesive. To have the measurement on these sandwich cells reflect only the volume conduction of the photoconductive layer, a mask of an opaque material, e.g., black plastic tape, was applied to prevent activation by light around the edges.

Electrode materials.—All surface conductivity measurements were made with cells having electrodes of semiconducting tin oxide. However, measurements made with cells using fired-on platinum electrodes did not differ significantly. The effect of any reaction of the sintered layer with electrode material as exemplified by the two types of electrodes is apparently confined to the interface between layer and electrode. Such reactions change primarily the resistance of the contact between electrode and layer. This contact resistance is a small fraction of the resistance of the layer and is only slightly photosensitive. Also, it tends to be eliminated in a surface conductivity measurement which is the difference between a light and dark photoresponse. In systems where an asymmetrical electrode system exists and rectifying phenomena are likely, difference in electrode material becomes important.

Techniques and methods of measurement.—The photosensitivity of the prepared layers was measured with a d-c applied voltage of 600 v and with an exciting light of 10 ft-L from a green electroluminescent lamp. For standard measurements this exciting light illuminated the electrode gap from the glass side. Rise and decay characteristics were determined by observing the photoconductor response on an oscilloscope screen. The "dark current" I_{30} was taken as the current measured 30 sec after the removal of the exciting light. Decay time γ_{10} represents the time necessary to reach 10% of photocurrent upon removal of activating light. Spectral response curves were determined using a Beckman D. U. spectrophotometer as a monochromator. By variation of the slit width, an equal quantity of energy at various wave lengths was allowed to excite the photoconductor cell with 600 v d-c applied potential. Slit width variations during measurements gave

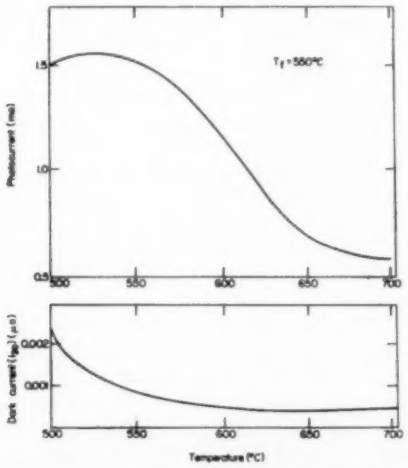

Fig. 3. Effect of presintering temperature on photoconductor characteristics. Final sintering of layer at 550°C for 10 min (600 v d-c potential, 10 ft-L, green El lamp excitation).

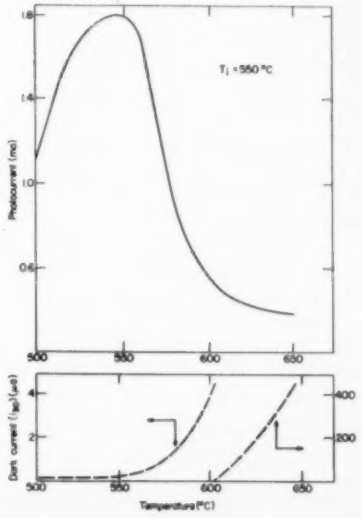

Fig. 4. Effect of sintering temperature on photoconductor characteristic. Presinter of layer at 550°C for 35 min (600 v d-c potential, 10 ft-L green El lamp excitation).

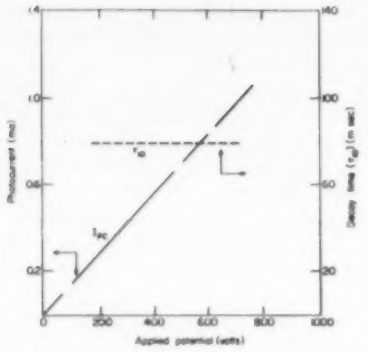

Fig. 5. Effect of applied potential on photoconductor characteristics (10 ft-L green El lamp excitation).

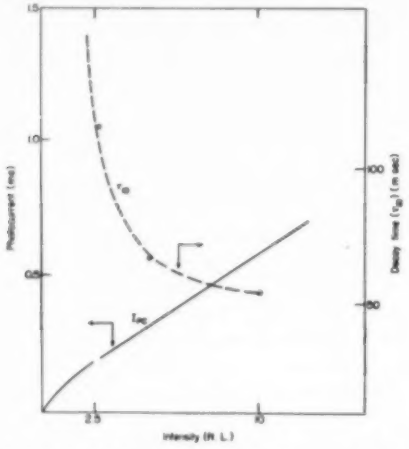

Fig. 6. Effect of intensity of illumination on photoconductor characteristics (green El lamp excitation, 600 v d-c potential applied).

a half intensity band width varying from 14 mμ at 550 to 18 mμ at 700 μ. This small variation of band widths in the peak response region resulted in a negligible shift in peak positions. The response was determined with an RCA electronic microammeter.

Reflectance measurements were made on a modified reflectance attachment to the Beckman D. U. spectrophotometer using basic magnesium carbonate as reference.

Effect of presintering temperature (T_i).—In an effort to establish conditions necessary to obtain maximum photosensitivity, a step-wise variation of the conditions at each part of the process was conducted. Figure 3 represents the effect of the variation of presintering temperature on the photocurrent and dark current. In each case, a 100 g mass of the photoconductor was fired in a covered crucible for a period of 20 min. The final sintering of the test slides was at a temperature of 550°C for 10 min. It will be noted that the greatest ratio of photocurrent to dark current occurs at T_i 550°C. Higher temperatures cause a decrease in the photocurrent while lower temperatures result in a layer which has relatively high dark current. This is probably the result of incomplete sintering combined with a relatively large amount of residual unincorporated $CdCl_2$.

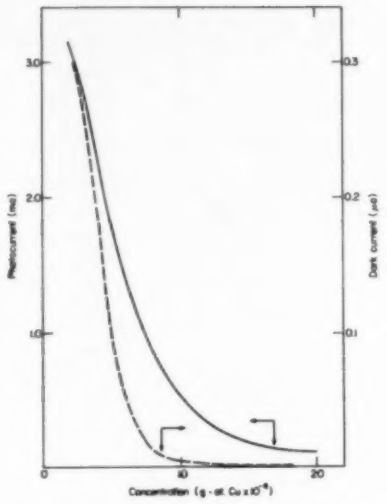

Fig. 7. Effect of copper concentration of photoconductor characteristics. (600 v d-c potential, 10 ft-L green El lamp excitation).

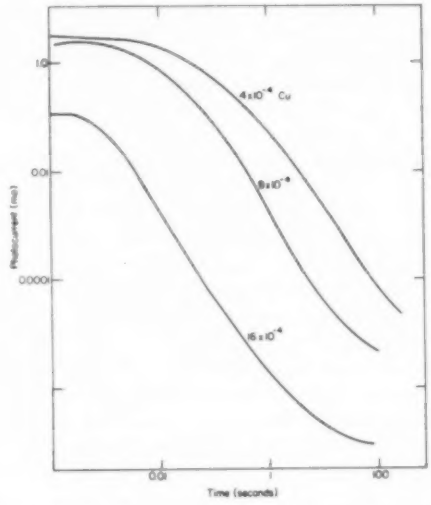

Fig. 8. Effect of copper concentration on decay characteristics of sintered layer cadmium sulfide (600 v d-c potential, 10 ft-L green El lamp excitation).

Effect of sintering temperature (T_f).—The temperature of sintering has a particularly great effect on both the photocurrent and the dark current. In all cases the slides were fired for a period of 10 min at temperatures from 500° to 700°C. With increasing temperatures the dark current increases until the material shows a high dark conductivity with little or no photoconductivity (Fig. 4). As a result of these observations a standard prefiring temperature and sintering temperature of 550°C was chosen for all samples. Cells with layer thickness of about 5 mils prepared under these conditions were used to determine the dependence of the photocurrent and the decay time on the applied voltage and the light intensity. The photocurrent varied linearly with increased voltage over the range of 100-800 v while voltage variation had little or no effect on the decay time γ_{10} (Fig. 5). A linear relationship was also ob-

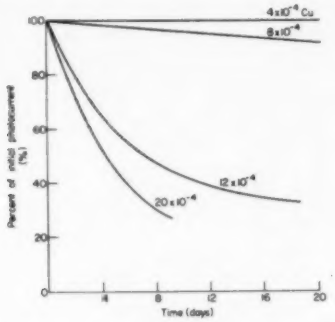

Fig. 9. Effect of copper concentration on shelf life (600 v d-c potential, 10 ft-L green El lamp excitation).

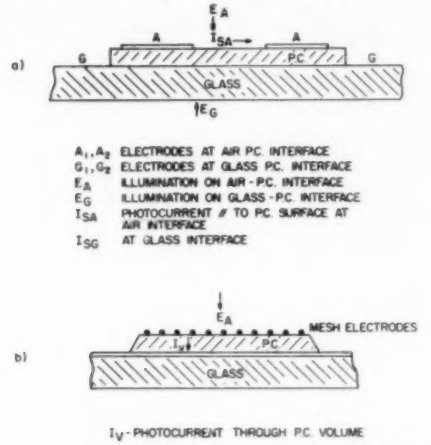
a)
b)
GLASS
PC
MESH ELECTRODES
A1, A2 ELECTRODES AT AIR PC. INTERFACE
G1, G2 ELECTRODES AT GLASS PC. INTERFACE
EA ILLUMINATION ON AIR - PC. INTERFACE
EG ILLUMINATION ON GLASS - PC. INTERFACE
ISA PHOTOCURRENT // TO PC. SURFACE AT AIR INTERFACE
ISG AT GLASS INTERFACE
IV - PHOTOCURRENT THROUGH P.C. VOLUME

Fig. 10. Notations used describing photoconducting characteristics of layer.

served over most of the intensity range, although at the low intensities some divergence was noted. The decay rate appeared to be quite dependent on the intensity of excitation, being relatively slow at the lower intensities (Fig. 6).

All cell data are reported for excitation with 10 ft-L of green EL light and for 600 v applied potential. Whenever necessary the above linear relationships are applied for conversion to these conditions.

Effect of copper concentration.—Confirming what had been found in single crystal studies, (5, 9, 10, 12, 13), increasing copper concentration results in a decrease of both photocurrent and dark current (Fig. 7) with concurrent change of the body color of the sintered layer from yellow to a black-brown.

Increased copper concentration,[3] although decreasing the photocurrent of the layer, did increase the rate of decay to a considerable (Fig. 8) extent. However, this increased copper effected a decrease of the relative shelf life of the prepared layer (Fig. 9). Test slides measured to obtain these data were subjected to normal laboratory conditions including usual winter humidity variations indoors and fluorescent lighting. Measurements were made in every case at about the same time of day. In all cases the photoconductivity appeared to reach a steady state after the observed decay.

[3] All concentrations expressed in this paper are in units of gram atoms per mole of CdS.

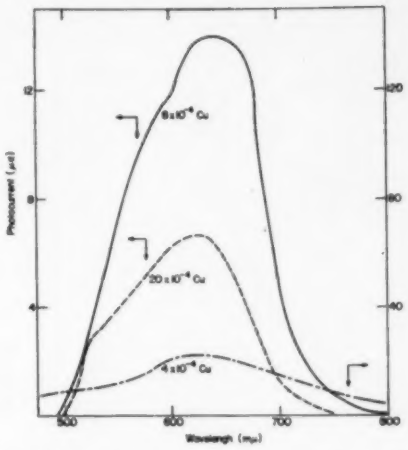

Fig. 11. Spectral response $I_{SG}{}^{G}$ for cadmium sulfide sintered layers (600 v d-c potential).

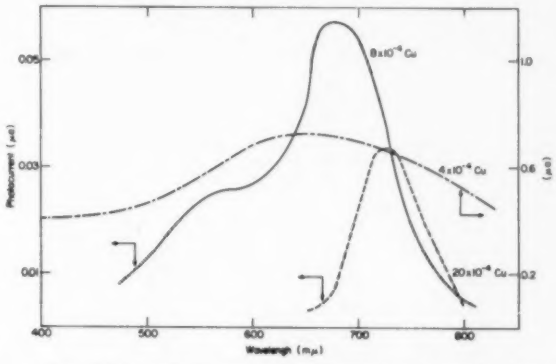

Fig. 12. Spectral response $I_{SG}{}^{A}$ cadmium sulfide sintered layers (600 v d-c potential).

Spectral response.—Although photoconductors have been further classified by the determination of their spectral response, there have been inconsistencies with respect to the published data. Variations in spectral response characteristics of cadmium sulfide photoconductor have been attributed not only to chemical composition but also to its physical state (5) and mode of operation (1). No definitive study of these parameters has been reported.

A consideration of a sintered layer photoconductor reveals the role of the cell structure or geometry on characteristics. Figure 10a represents a magnified view of a test cell showing the arrangement of the various parts involved in the measurement of surface-like conductivity. In the conductivity measurements used to evaluate the effects of different firing temperatures and different copper concentrations, illumination had been in all cases from the glass-CdS interface side (E_G) and voltage had been applied across the tin oxide electrodes in the plane of the same interface. Under these conditions the photocurrent will be designated by $I_{SG}{}^{G}$; the superscript G giving the direction from which the sample is illuminated, in this case the glass side, and the subscript SG indicating a surface-like conduction with voltage across the electrodes in the glass-CdS interface, G.

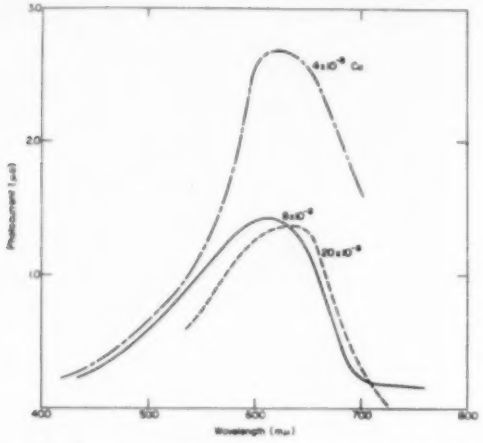

Fig. 13. Spectral response $I_{RA}{}^{A}$ for cadmium sulfide sintered layers (600 v d-c potential).

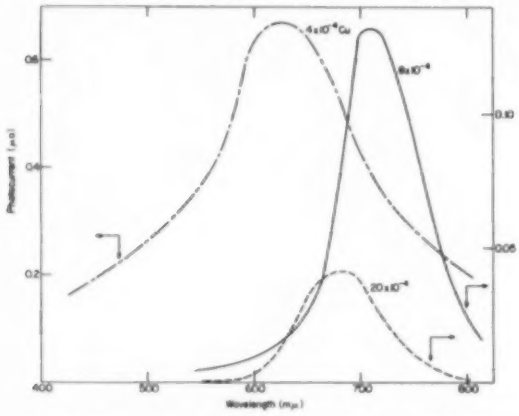

Fig. 14. Spectral response $I_{RA}{}^{G}$ for cadmium sulfide sintered layers (600 v d-c potential).

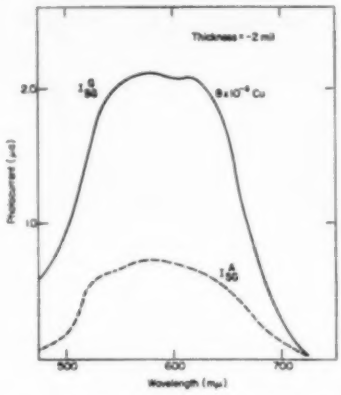

Fig. 15. Spectral response of 2-mil cadmium sulfide layer (600 v d-c potential).

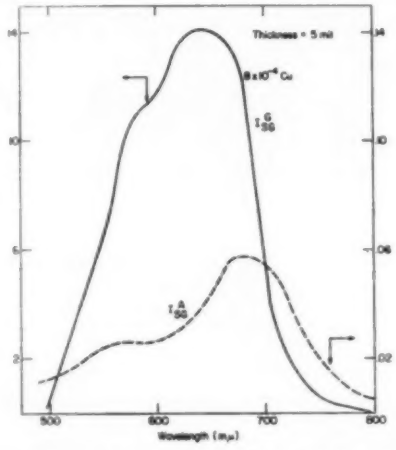

Fig. 16. Spectral response of 5-mil cadmium sulfide layer (600 v d-c potential).

The second surface, i.e., the air photoconductor interface can also be used to evaluate the sintered layer. Voltage was applied across silver electrodes painted on this surface, and the photocurrent $I_{RA}{}^{G}$ produced by exciting from the photoconductor glass side was determined.

Two additional surface type photocurrents may be determined if the direction of excitation is reversed. These currents may be symbolized as $I_{RG}{}^{A}$ and $I_{RA}{}^{A}$ using the same conventions as above.

Thus, the four possible surface photocurrents can be designated by $I_{RA}{}^{G}$, $I_{RG}{}^{G}$, $I_{RG}{}^{A}$, and $I_{RA}{}^{A}$.

In addition to the above surface-like conductivities, the contribution of any current produced within the body of the layer for the particular geometry of the cell should be determined. Using the standard-type cell and adding mesh electrodes to the air surface, the photocurrent through the photoconductor volume may be measured (Fig. 10b). Again, a current may be developed by exciting either through the glass or air interface yielding two possible types of volume currents ($I_V{}^{A}$ and $I_V{}^{G}$).

$I_{RG}{}^{G}$.—The spectral response of photoconductors excited through the glass with voltage applied across electrodes in the glass-photoconductor interface ($I_{RG}{}^{G}$) is shown in Fig. 11. Although the relative magnitude of the photocurrent varies with copper concentration, the optimum wave length or maximum-response occurs in all cases at a wave length of 625 mμ.

$I_{RG}{}^{A}$.—If the excitation occurs at the air-photoconductor interface, spectral response curves for variable copper concentrations show a dependence of the position of their maximum on copper concentration (Fig. 12).

$I_{RA}{}^{A}$, $I_{RA}{}^{G}$.—The spectral response of the sintered layer as characterized by these two currents is shown in Fig. 13 and 14. There appears to be essentially no shift in the peak response toward longer wave length with increasing copper in these cases.

Effect of layer thickness on photoconductor characteristics.—Since the spectral response of the surface photocurrent appeared to vary with the surface excited, a variation of the chemical composition of the two surfaces might be suspected. If the thickness of the layer were decreased progressively, at some point it might be expected that this surface composition variation should disappear. Figures 15 and 16 represent spectral response curves ($I_{RG}{}^{A}$, $I_{RG}{}^{G}$) using cell layer thicknesses of 2 and 5 mils, respectively. In contrast to the 5-mil layer there is no difference in the shape and maxima of the spectral response

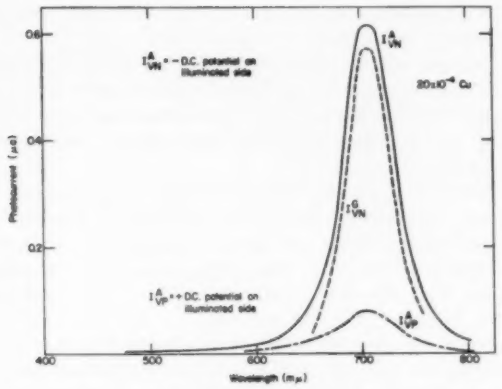

Fig. 17. Spectral response I_V for cadmium sulfide sintered layers (600 v d-c potential 10 ft-L green El lamp excitation).

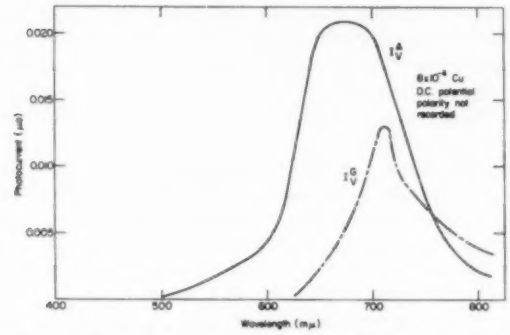

Fig. 18. Spectral response I_V for cadmium sulfide sintered layers (600 v d-c potential 10 ft-L green El lamp excitation).

curves in the case of the 2-mil layer. Also, the body color of thin layers was considerably lighter than that of the 5-mil layer even though the copper concentrations were identical. This difference can be attributed to the loss of a greater amount of chloride from the thin layer. This chloride is necessary for effective incorporation of copper into the lattice.

Volume conductivity I_V.—The spectral response of the volume type current I_V was determined with sintered layers of various copper concentrations. Curves for 8 x 10^{-4} and 20 x 10^{-4} copper are shown in Fig. 17 and 18. The characteristics of these curves are somewhat similar to $I_{SO}{}^{A}$ and $I_{SA}{}^{G}$. The layer with the lower copper concentration shows a difference in peak position depending on which side was illuminated. The layer with the higher copper showed no lack of symmetry. It should be noted that Fig. 18 indicates a rectification phenomenon the magnitude of which is dependent on the direction of illumination.

Reflectance curves.—Figure 19 represents the surface (air-photoconductor 5 mil) reflectance of the photoconductive layer. As may be seen from the curves, the body color becomes progressively darker with increased copper concentration.

Effect of firing atmospheres.—The importance of firing conditions with respect to both atmosphere and surroundings was exemplified by the different photoconductive properties associated with the end patches of the standard cells. To determine more accurately the importance of the composition of the firing atmosphere, the effect of variations on concentration of (*a*) oxygen and (*b*) cadmium chloride in the firing atmosphere on the photoconductivity of the layers was studied. In the former case, the layers were fired in atmospheres of various oxygen-argon mixtures. There is no doubt that some oxygen is required to achieve an optimum in sensitivity of the cadmium sulfide layer (Fig. 20), but it also appears that the beneficial effect of oxygen may be introduced in the presinter firing or the final sintering. The effect of oxygen on dark current is of importance only when long firing times are used. Some advantage may be gained if the oxygen content of the firing is kept small (about 2%). This is in agreement with improvement of photoconductive characteristics observed with restrictive firings in small volumes. However, conditions close to optimum are achieved simply by firing in air in a small electric muffle furnace for a time and at the temperature indicated earlier.

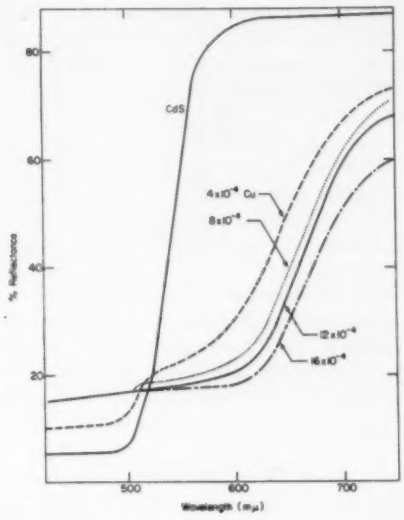

Fig. 19. Reflectance curves of photoconductor layers with variable copper concentrations.

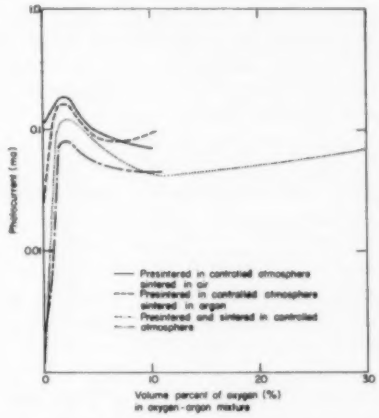
Photocurrent (ma)
Volume percent of oxygen (%) in oxygen-argon mixture
Presintered in controlled atmosphere sintered in air
Presintered in controlled atmosphere sintered in argon
Presintered and sintered in controlled atmosphere

Fig. 20. Effect of oxygen in firing atmosphere on photocurrent $I_{SO}{}^{G}$ (600 v d-c potential 10 ft-L green El lamp excitation).

An atmosphere rich in cadmium chloride or some other chloride-containing compound is also necessary in the fabrication of a sensitive photoconducting layer. When the major portion of the halide is removed by repeated washing of an activated cadmium sulfide material (presintered only) until the wash liquid showed no test for chloride, the resultant sintered layer was pale yellow in color, powdery in character, and low in photoconductive characteristics. However, this same layer may be made sensitive by resintering in a closed volume with cadmium chloride crystals added to provide a suitable atmosphere. A similar effect may be achieved if the layer were exposed to a hydrogen chloride atmosphere prior to resintering. The resintered layer was not only photoconductive, but also the body color was nearly identical to that of the control.

Discussion of Results

Sintered layers of cadmium sulfide photoconductor (copper chloride-coactivated) can be prepared with a sensitivity ratio (ratio of photocurrent and dark current after 30 sec) of 10^7. In general, such layers have characteristics quite similar to those reported with respect to the single crystals. The sintered layer characteristics are, however, directly dependent on the method of preparation and the geometry of the system in which the layer is used.

In the system chosen for investigation, a system which is of practical application to device manufacture, the two surfaces have been shown to be chemically and physically quite different, and hence the optical and electrical responses are dependent on the geometry of excitation. These variations may be explained by differences in the relative activator-coactivator concentrations. During sintering, the halide coactivator is volatilized quite readily. Because of the large excess of cadmium chloride used in formulation, there is sufficient halide available so that some will remain within the photoconducting material itself as well as in the atmosphere surrounding the material. During sintering, the halide volatilizes evenly throughout the layer. Once this halide has diffused to the surface, however, it escapes into the atmosphere. Thus the surface of the layer may be considered as a diffusion boundary between an atmosphere of low chloride concentration and the relatively chloride-rich cadmium sulfide bulk. Upon cooling, some halide is reabsorbed by the surface of the layer. Such processes could explain a concentration variation of halide across the layer. During the sintering the copper concentration would simply equilibrate throughout the layer since copper is not volatile at the sintering temperatures.

Experimentally, the ease of migration of the chloride ion out of the cadmium sulfide lattice has been shown by the successful reactivation of a nonphotoconductive (chloride-free) CdS by means of a simple exposure to cadmium chloride or hydrogen chloride vapors. The unevenness of reabsorptions of the coactivator during cooling is indicated both by the difference in color between the two layer surfaces (especially at higher copper concentrations) and by the dependence of this body color variation on the thickness of the layer.

Assuming that sintering under the conditions used does result in a difference in coactivator concentration within the layer, the spectral response curves may be explained utilizing data obtained in single-crystal work.

Wood (14) ascribed the spectral response peak at 520 mμ to a stimulation of photoconduction resulting from lattice defects in the crystal associated with presence of chloride. The 700 mμ peak on the other hand, was directly associated with copper-type active centers. Considering the $I_{SG}{}^{G}$ spectral energy curves, the peak is in all cases about 625 mμ. This type of curve could result from the combined effects of Cu and Cl centers. Increasing the copper concentration should have little or no effect on the position of the peak response provided that there is sufficient chloride to keep the relative ratio of copper to chloride centers constant. The constancy of ratio would be dependent then on the initial composition of the photoconductor blend, the thickness of the layer, and duplicating of firing times and temperatures of layer.

With respect to the air-photoconductor interface ($I_{SG}{}^{A}$), the spectral response is found to shift toward the longer wave lengths with increasing copper concentration. Again applying the work of Wood, it may be assumed that this shift is the result of a higher ratio of Cu to Cl type centers. This increase in Cu over Cl-type centers would be the result of the lower chloride concentration existing at the surface. Accompanying this increase in the relative number of copper-type centers with respect to the chloride-type centers will be a deepening in the body color of the surface. This body color shift results in a more efficient absorption of longer wave lengths which, combined with the greater effectiveness of activation due to higher copper center concentration, further shifts the spectral response peak toward the red. The copper center concentration is not entirely dependent on initial copper concentration but is interrelated to chloride concentration.

The darkening of the body color associated with increasing copper observed primarily at the air photoconductor interface introduces the possibility of affecting the position of the spectral response peak by a simple filtering action, i.e., modifying the composition of the activating radiation reaching the portion of the layer involved in the conductance measurements by other portions of the layer which are not involved at all or to a much lesser degree.

The greatest effect of this filtering action is observed in the spectral response curves of $I_{SA}{}^{G}$ and $I_{SG}{}^{A}$ type photoconduction. In these cases the most effective wave length will be that which can penetrate through almost the entire layer and activate that part of the layer in the region of the electrodes on the surface opposite the illuminated surface. Since the longer wave lengths are more penetrating, the peak spectral response as measured by these conductances will be further toward the red than the peak responses of the other conductances. In $I_{SA}{}^{G}$ and $I_{SG}{}^{A}$ measurements the easily absorbed shorter wave

lengths will be filtered out by that portion of the layer which is least effective in contributing to the conductance. It will be noted that the peaks of the spectral responses I_{so}^{A} and I_{sA}^{G} do in fact occur at longer wave lengths. The volume conductance is also dependent on the body color of the layer but to a slightly lesser extent than in the above situation. In this case light absorbed by any part of the layer can contribute effectively to the volume-like photoconduction. The peak response of these spectral response curves lies roughly between the two types of surface conduction responses.

Acknowledgments

Sincere thanks are due to C. Lagos, T. Barry, B. Rybinski, and R. Levitt for the preparation and measurement of many of the photoconducting layers. For frequent and helpful discussions and constructive criticisms the authors are indebted to Dr. K. H. Butler and F. Koury of the Engineering Laboratories as well as M. Zimmerman and R. Billups of the Lincoln Laboratories, M.I.T.

Part of the work reported here was carried out as a cooperative project with the Lincoln Laboratory, a technical center operated by the Massachussetts Institute of Technology with joint support of the Army, Navy, and Air Force under contract.

Manuscript received May 2, 1959. This paper was prepared for delivery before the New York Meeting, April 27-May 1, 1958.

Any discussion of this paper will appear in a Discussion Section to be published in the June 1960 JOURNAL.

REFERENCES

1. G. Diemer, H. A. Klasens, and J. G. Santen, *Philips Research Repts.*, **10**, 401, (1955).
2. J. E. Rosenthal, *Proc. I.R.E.*, **43**, 1882, (1955).
3. E. E. Loebner, *ibid.*, **43**, 1897, (1955).
4. B. Kazan and F. H. Nicoll, *Proc. I.R.E.*, **43**, 1888, (1955).
5. S. M. Thomsen and R. H. Bube, *Rev. Sci. Inst.*, **26**, 664, (1955).
6. G. Kuwabara, *J. Phys. Soc. Japan*, **9**, 992, (1954).
7. E. Schwarz, *Proc. Phys. Soc.*, **62A**, 530, (1949); *ibid*, **63B**, 624 (1950); *ibid.*, **64B**, 821 (1951).
8. B. T. Kalomiets, *Doklady Akad Nauk S.S.S.R.*, **83**, 561 (1952).
9. W. Veith, *Compt. rend.*, **230**, 947, (1950); *Z. angew. Phys.*, **7**, 1, (1955).
10. D. Goerćke, *P. Annalender Tele Communications*, **6**, 325 (1951).
11. J. Gottesman, *J. Opt. Soc. Amer.*, **44**, 368, (1954).
12. R. H. Bube and S. M. Thomsen, *J. Chem. Phys.*, **23**, 15 (1955).
13. F. A. Kroeger, H. J. Vink, and J. van der Boomgaard, *Z. physik. Chem.*, **203**, 1, (1954).
14. J. Wood, *J. Electronics and Control*, **3**, 225 (1957).
15. R. R. Billups, W. L. Gardner, and M. D. Zimmerman, Technical Report #200, Lincoln Laboratory, M.I.T., Lexington, Mass.

The Nature of Alumina in Quenched Cryolite-Alumina Melts

Perry A. Foster, Jr.

Alcoa Research Laboratories, Aluminum Company of America, New Kensington, Pennsylvania

ABSTRACT

The equilibrium primary phases that precipitate from cryolite-alumina melts are cryolite, to the left of the eutectic, and corundum, to the right of the eutectic. No solid solubility of alumina in the cryolite phase was found. Evidence is presented in the form of photomicrographs and x-ray powder patterns that a new alumina phase is obtained by extremely rapid quenching of the liquid. The x-ray pattern of this phase is similar to the aluminum silicate, mullite. It is thought to result from the disproportionation of an oxyfluoride complex in the melt and is perhaps a skeletal arrangement with some of the characteristics of the oxyfluoride precursor. This new alumina phase is metastable and transforms through eta-alumina to corundum on heating.

Although quenching methods are well established and have been used extensively to elucidate the phase relationships in many nonmetallic systems, little use has been made of the technique in studies of the alumina-cryolite system.

Zintl and Morawietz (1) reported that x-ray powder patterns showed only cryolite in quenched cryolite fusion products containing 5 and 10% alumina. Similar experiments with 15% alumina quenches showed corundum as well as cryolite, indicating that the solubility limit had been exceeded at the temperature employed. It is believed this temperature was approximately 1000°C. Zintl and Morawietz (1) also reported that the densities of those quenched products in which no corundum was found were the same as cryolite. Calculated densities, based on a mechanical mixture and the two types of solid solution, ruled out all but the primary or substitutional solid solution model. Zintl reasoned that it was probably impossible to quench fast enough from above the liquidus to preserve the molecular arrangement of that phase field, and that what one obtained was something characteristic of a lower temperature: in this case, a primary solid solution with an alumina dimer (Al_2AlO_4) substituted for Na_3AlF_6 in the cryolite lattice.

Ginsberg and Bohm (2) repeated Zintl's experiments and found that for alumina contents less than 12%, x-ray showed only cryolite in both slowly cooled and quenched samples. However, an aluminum sulfate extraction gave quantitative recovery of alumina for the slowly cooled specimens and a

40% recovery for the quenched specimens. They concluded that alumina is in solid solution at a concentration of 7-8% in the quenched melt.

Grjotheim (3) obtained cooling curves for melts of several compositions from 9 down to 5% alumina at a rather slow cooling rate of 0.7°/min. Eutectic halts were noted for all these compositions. At 2.5%, the halt was not established definitely. Grjotheim felt this might be due either to solid solubility or to the small amount of eutectic which forms at this composition producing an undectable heat effect.

The purpose of the present work is to determine the nature of alumina in alumina-cryolite melts quenched from above the liquidus; to determine the extent of solid solution on the low alumina side of the eutectic; and to obtain information concerning possible new compound formation on the high-alumina side of the eutectic. This is part of a larger program underway in these Laboratories to elucidate the phase relationships in the cryolite-aluminum system.

Experimental

Hand-picked natural Greenland cryolite was employed. The most prevalent impurities are: silicon (SiO_2) 0.14%, potassium (KF) 0.055%, calcium (CaF) 0.01%, and lithium (LiF) 0.035%. The alumina used was Alcoa, A-10 Grade. The most common impurities in this material are: soda, 0.092%, and silica, 0.19%.

The starting materials were prepared by prefusing, under argon, 5-g mixtures of cryolite and alumina in a covered platinum crucible at 1015° ±10°C. The fusion temperature was maintained for 5 min before slowly cooling to room temperature. Weight losses due to moisture and decomposition were of the order of 0.2%. The fused material was crushed to pass 200 mesh and then mixed thoroughly. Two 1-g samples were analyzed for alumina by extraction with a hot aluminum chloride solution. If these two determinations agreed within the usual experimental error, the gross sample qualified as the source material for the 20 mg quenching charge. Prefusing of high alumina samples (14-18%) presented some difficulty. Temperatures higher than 1015°C would be necessary to effect complete solution. However, cryolite begins to decompose above this temperature, evolving $NaAlF_4$, and consequently enriching the melt in NaF. It was found from duplicate alumina determinations of a number of different high alumina compositions that the fine grinding and mechanical homogenizing procedure, after partial fusion at 1015°C, was effective in obtaining a uniform distribution of unreacted and precipitated alumina.

Quenching Procedure

Small platinum-tubes, 3-mm ID with 0.01-mm wall, were cut to lengths of approximately 1.5 cm. One end was crimped shut and fused with a Burrell "Kup-L-Weld" Thermocouple Welder, and 20 mg of a prefused, homogenized alumina-cryolite composition was loaded into the tube. The tube was flattened to remove some of the air; then the open end was arced shut. The tube was inserted into a platinum foil envelope, which was threaded with a platinum fuse wire, and suspended from two hooked conductors within 1 mm of a calibrated platinum, platinum-10% rhodium thermocouple (4). This assembly was inserted into a platinum-wound resistance furnace.

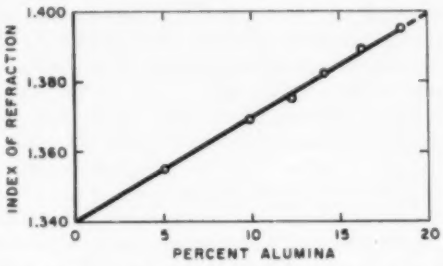

Fig. 1. Variation of the quenched liquid index of refraction with alumina content.

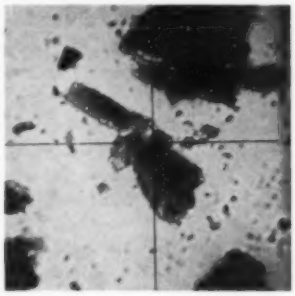

Fig. 2. Quenched liquid, 5% Al_2O_3. X250

The complete liquification of all compositions was insured by initially treating the samples at 1100°C for 30 min. Following this heat treatment, the temperature was lowered slowly to, and controlled at, the level required for that particular investigation. That temperature was maintained for a period of time sufficient to establish chemical and physical equilibrium. The sample was released from the hot-zone of the furnace into a quenching medium by running current through the hooked leads, thereby melting the fuse wire. The optimum time at temperature was determined by experience after microscopic examination of a number of samples.

The index of refraction of the various phases was observed, using the Becke line method. Positive identification was made from x-ray powder diffraction patterns.

Results and Discussion

X-ray powder diffraction patterns of cryolite-alumina melts having alumina contents ranging from 5-18.5%, quenched from above the liquidus, showed only cryolite lines. These observations were in agreement with those of Zintl and Morawietz (1) and Ginsberg and Bohm (2). However, the refractive index increased with increased alumina content (Fig. 1), thus appearing to contradict x-ray findings, which showed a constant parameter regardless of alumina content. The quenched liquid particles were quite opaque and had a fine mosaic crystalline structure (Fig. 2). This feature prohibited obtaining a very precise index. Nevertheless, the increase in re-

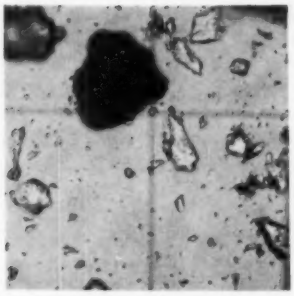

Fig. 3. Primary phase cryolite-quenched liquid, 5% Al_2O_3. X210.

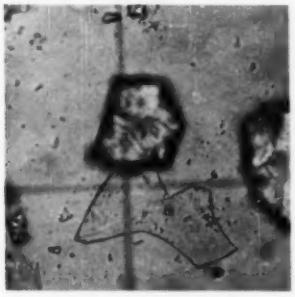

Fig. 4 Sub-solidus cryolite and alumina, 5% Al_2O_3. X210

fractive index above that of cryolite (1.339) was pronounced and nearly linear with alumina content.

If, as Zintl and Ginsberg suggested and the early phase diagram of Roush and Miyake (5) would predict, the primary phase on the low alumina side of the eutectic is a solid solution containing between 7 and 11% alumina, the index of refraction of that phase should be significantly greater than that of cryolite. The indices of refraction of the two phases present in quenches originating slightly below the liquidus along the 5% alumina isopleth indicated that the primary phase is cryolite (the well-formed clear crystals in Fig. 3). The dark, mosaic, quenched liquid particles constitute the other equilibrium phase. Quenches originating from lower and lower temperatures showed an increasing amount of cryolite crystals, as would be expected from the lever arm principle. Quenches from below the eutectic boundary (approximately 960°C) showed microscopically two equilibrium solid phases (Fig. 4). One phase (immediately above the crosshair)[1] is cryolite that precipitates below the liquidus and continues to do so until the composition of the liquid and the temperature of the melt are such (eutectic point) that a second solid phase (flat plate immediately at the crosshair) commences to form. The second phase had the refractive index of corundum. A density separation was performed on a sample quenched from just below the eutectic boundary. Methylene iodide, with a density of 3.33, was used as the separating medium. X-ray analyses showed that the light fraction was principally cryolite and the heavy fraction principally corundum.

Quenches along an isopleth on the high alumina side of the eutectic showed microscopically, and by x-ray, that the primary phase particle is corundum. This was consistent with the preceding observation that corundum appears below the solidus on the low alumina side of the eutectic. It is significant that x-ray diffraction techniques were not sensitive enough to show corundum in a specimen similar to that shown in Fig. 4. This could explain why Ginsberg, employing only x-ray techniques, was unable to observe corundum in either slowly cooled or quenched samples of low alumina content.

Thus it appears possible to quench from above the liquidus and preserve a phase that is not characteristic of anything that occurs at lower temperatures in the diagram. Attention, therefore, is focused on the nature of alumina as it exists in the sample quenched from above the liquidus.

The general consensus in the literature favors some sort of reaction between alumina and cryolite in the molten state to produce oxyfluoride complexes or aluminates, or both. For example, Treadwell (6) proposed $(F_2AlO_2AlF_2)^{=}$; Grunert (7), $AlOF_5^{\equiv}$ and $AlOF_3^{=}$; Boner (8), $AlOF_2^{-}$; Rolin (9), AlO_2^{-} and AlO^{+}; and Forland, *et al.*, (10), $AlO_2F_2^{\equiv}$.

Edwards, *et al.* (11) made density measurements on melts over a range of compositions above the liquidus. These measurements showed that, as the alumina content increased, the density of the melt decreased steadily below that of cryolite towards a minimum, indicating a chemical interaction. Frank and Foster (12), employing radioactive aluminum, demonstrated the complete exchange between the aluminum atoms of cryolite and alumina on fusion. This would not occur if alumina simply dissolved without ionization or dissociation in cryolite. The same workers (13) made density calculations using various possible reaction schemes to get a fit with Edwards' density curve. The best fit was obtained

Fig. 5. Mullitized alumina, extracted from quenched liquid. X210.

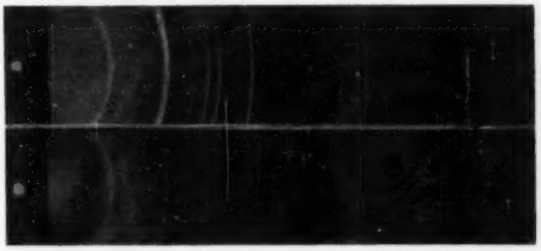

Fig. 6. X-ray powder diffraction patterns of (a) (top) mullite, $3Al_2O_3 \cdot 2SiO_2$, (b) (bottom) m-alumina.

[1] The focus of this particle was sacrificed in order to obtain a definition of the flat corundum plate at the crosshairs.

Table I. *d* Values and relative line intensities

m-Al_2O_3			Mullite, $3Al_2O_3 \cdot 2SiO_2$		
Line No.	d, A	I/I_o	Line No.	d, A	I/I_o
1	5.45	V. stg.	1	5.42	Med.
2	3.47	V. stg.	2	3.42	V. stg.
3	2.92	Med. wk.	3	2.90	Med. wk.
4	2.72	Stg.	4	2.72	Med.
5	2.59	Stg.	5	2.56	Med.
6	2.46	V. wk.	6	2.44	Wk.
7	2.34	Stg.	7	2.30	Med. wk.
8	2.24	Stg.	8	2.22	Stg.
9	2.15	Med.	9	2.13	Med. wk.
10	2.06	V. wk.	10	1.89	Wk.
11	1.99	V. wk.	11	1.845	Med. wk.
12	1.88	Med. wk.	12	1.71	Med.
13	1.73	Med.	13	1.70	Med.
14	1.61	Med. wk.	14	1.60	Med.
15	1.55	Med. stg.	15	1.58	Wk.
16	1.492	Wk.	16	1.522	Stg.
17	1.461	Wk.	17	1.46	Med. wk.
18	1.41	V. wk.	18	1.445	Med.
19	1.346	Wk.	19	1.426	Wk.
20	1.288	Med. stg.	20	1.409	Med.

with an equilbrium between Na_3AlF_6, $NaAlF_4$, NaF, $Na_2AlO_2F_3$, and $NaAlO_2$.

The identification of the primary phase on the high alumina side of the eutectic as corundum rules out the possibility of a stable solid oxyfluoride compound. X-ray powder patterns of the quenched liquid showed only cryolite, implying that the oxyfluorides are too unstable to retain their configuration on quenching, or are not present in sufficient amounts for detection. Of particular interest, then, is the structural form of the alumina in the quenched liquid particles.

The quantitative separation of alumina in alumina-cryolite fusion products customarily is performed by leaching with hot, 30%, aluminum chloride solution, followed by repeated washing and, finally, ignition of the residue at 1100°C. This procedure yields alumina contents with a precision of ±0.1% with a 1-g sample. With minor modifications, satisfactory precision was also obtained with the small samples, whether quenched or slowly cooled. X-ray diffraction patterns of the ignited residues invariably showed large proportions of corundum, with small amounts of beta- and zeta-alumina, and, occasionally, other forms. To retain the alumina structure as it existed in the quenched liquid, the ignition step was eliminated.

The x-ray patterns of the extraction residues showed a large amount of material that was similar to the aluminum silicate, mullite, $3Al_2O_3 \cdot 2SiO_2$, and a small amount of material resembling the lithium-containing zeta-alumina, although, in this case, the material was lithium free. This was true, regardless of the alumina content, within the concentration range of the experiments. Figure 6 compares Debye patterns of the mullite-like alumina (hereafter referred to as m-alumina for convenience) and true mullite. Table I lists the *d* values and relative line intensities.

Table II. X-ray analyses of heated m-alumina

X-ray analysis of the starting materials	Heating conditions	X-ray analysis after heating
m-Alumina	250°C 1 hr	m-Alumina
m-Alumina	300°C 1 hr	m-Alumina; eta-alumina
m-Alumina	600°C 1 hr	m-Alumina; eta-alumina
m-Alumina	650°C 1 hr	Eta-alumina
m-Alumina	700°C 1 hr	Eta-alumina
m-Alumina	750°C 1 hr	Eta-alumina; corundum
m-Alumina	775°C 1 hr	Corundum

The aluminum chloride extraction residues for compositions on the high alumina side of the eutectic, but originating at a temperature below the liquidus, contained a mixture of m-alumina and corundum. Corundum is the primary phase in this region of the phase diagram. Extraction residues of samples quenched from below the liquidus on the low alumina side of the eutectic contained only the m-alumina. The primary phase in this region, cryolite, is soluble in hot aluminum chloride solution. Residues from quenches originating below the solidus, regardless of their composition relative to the eutectic, contained only corundum, indicating that the amount of m-alumina present is a function of the amount of quenched liquid.

True mullite ($3Al_2O_3 \cdot 2SiO_2$) contains 13.2% silicon. Qualitative spectroscopic analysis of the m-alumina showed a silicon concentration near 1%. This can be accounted for by the accumulation of the silicon present in the original cryolite and alumina. It is not enough, of course, to account for the similarity to true mullite.

The m-alumina was heated at various temperatures to determine its stability. Table II lists the results of x-ray analyses of these materials. The conversion of m-alumina to corundum on heating demonstrates that it is a metastable phase.

Generally, x-ray analysis was too insensitive to detect m-alumina in the quenched liquid. Its occasional detection demonstrated, however, that the m-alumina is a component of the quenched liquid and was not produced during the aluminum chloride extraction. A refractive index of 1.604 ± 0.016 was determined for the extracted m-alumina. A more precise determination was not possible because of the extremely fine particle size of the precipitate (Fig. 5).

Conclusions

The following is offered to explain the observations of this work. Alumina dissolves in cryolite by a reaction mechanism to produce one or more species (perhaps oxyfluorides) that are stable only in the melt. These compounds disproportionate on equilibrium freezing to cryolite and corundum, which then are stable to room temperature. On the cryolite side of the eutectic, cryolite freezes as the primary

phase. If the liquid is rapidly quenched, however, there is insufficient time for the alumina from the disproportionation to recrystallize as corundum. Rather, it assumes the mullite-like configuration, which tentatively might be considered a skeletal arrangement having some characteristics of its oxyfluoride precursor. The quenched liquid is thus an intimate mechanical mixture of cryolite and m-alumina with an observable refractive index that is actually an average index of the two phases, taken in appropriate proportions.

Manuscript received Sept. 9, 1958.

Any discussion of this paper will appear in a Discussion Section to be published in the June 1960 JOURNAL.

REFERENCES

1. E. Zintl and W. Morawietz, Z. *anorg. u. allgem. Chem.*, **240**, 145 (1939).
2. H. Ginsberg and A. Bohm, Z. *Elektrochem.*, **61**, 313 (1957).
3. K. Grjotheim, "Contribution to the Theory of the Aluminum Electrolysis," p. 90, Institute of Silicate Science, Trondheim, Norway (1956).
4. P. A. Foster, *J. Phys. Chem.*, **61**, 1005 (1957).
5. G. A. Roush and M. Miyake, *Trans. Am. Electrochem. Soc.*, **48**, 153 (1925).
6. W. D. Treadwell, *Schweiz. Arch. angew. Wiss. u. Tech.*, **6**, 69 (1940).
7. E. Grunert, *Z. Electrochem.*, **48**, 393 (1942).
8. J. E. Boner, *Helv. Chim. Acta*, **33**, 1137 (1950).
9. M. Rolin, *Ann. Phys.*, Series 12, **6**, 970 (1951).
10. T. Forland, H. Storegraven, and S. Urnes, Symp. sull 'elettrolisi dell 'alluminio, October 12, 1953, Milan, Italy.
11. J. D. Edwards, C. S. Taylor, L. A. Cosgrove, and A. S. Russell, *This Journal*, **100**, 508 (1953).
12. W. B. Frank and L. M. Foster, *J. Phys. Chem.*, **61**, 1531 (1957).
13. W. B. Frank and L. M. Foster, Alcoa Research Laboratories, to be published.

A Study of the Iodide Niobium Process

Robert F. Rolsten[1]

Eastern Laboratory, E. I. du Pont de Nemours & Company, Gibbstown, New Jersey

ABSTRACT

It was established that the rate of deposition of niobium by the thermal decomposition of niobium iodides can be expressed in units of moles of niobium deposited per unit length of a deposition element per unit of time. The rate of deposition of niobium was studied (*a*) with deposition temperatures from 750° to 1100°C, (*b*) with feed material temperatures from 240° to 470°C, and (*c*) with crude niobium with different surface areas.

Van Arkel (1) prepared single crystal tungsten rods by the thermal decomposition of tungsten hexachloride on a resistively heated wire in an evacuated flask in 1923. Van Arkel, deBoer, and Fast (2-7) subsequently extended the technique to the preparation of other metals from their volatile halides. The metal iodides have been used extensively since they exhibit a low thermal stability. In addition, iodine is particularly well adapted as the basis for such a process because it reacts readily with most elements to form compounds which are moderately stable in the vapor state and which dissociate at a high temperature. Furthermore, iodine does not react directly with most oxides.

Fast (8) studied the rate of formation of titanium by the thermal decomposition of gaseous titanium iodides. The temperature of the deposition element was maintained constant while the temperature of the feed material was varied. The deposition rate increased from a minimum at room temperature to a maximum at about 175°C, decreased to a second minimum at about 300°-470°C, and then increased again to 520°C, the highest feed temperature employed in the series of measurements. However, Fast (8) noted, from experiments where the deposition bulb was fabricated from Supermax glass, that the deposition rate at a feed temperature of 620°C was considerably higher than at 520°C. Fast (7), Döring and Molière (9), and Emelyanov, Bystrov, and Evstyukhin (10) observed a deposition rate of zirconium vs. bath temperature curve that was similar in shape to the curve observed by Fast (8) for titanium.

It was reported (11) recently that high-purity niobium[2] could be prepared by an iodide decomposition process. The purpose of the investigation reported here was to determine the effect that such factors as (*a*) deposition and feed temperatures, (*b*) reactivity of the crude (feed) niobium to be refined, and (*c*) the predominant gas and condensed solid phase species would have on the rate of deposition of niobium.

Experimental

The deposition unit employed throughout this investigation is shown in Fig. 1. A 64-mm diameter Vycor cylinder was equipped with a 15-mm OD quartz reentrant tube or finger. The crease or constriction in the deposition bulb was 50 mm in diameter and 45 mm from the bottom of the cylinder. This crease served to position the 50 mm diameter perforated molybdenum retaining cylinder. Molybdenum does not form a volatile iodide under the experimental conditions for deposition and, consequently, is not transferred. The impure niobium was contained in the annular space between the Vycor bulb and the molybdenum cylinder.

[1] Present address: U.S. Borax Research Corporation, 412 Crescent Way, Anaheim, California.

[2] Niobium metal prepared by the thermal decomposition of the niobium iodides can be designated as iodide niobium.

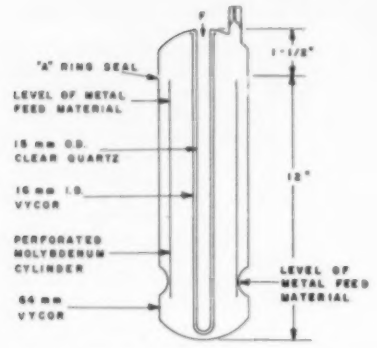

Fig. 1. Reentrant-type apparatus for the preparation of metals.

In a typical experiment, the deposition unit was thoroughly cleaned, charged with impure niobium, and the head assembly attached to the deposition bulb by fusing the Vycor at "A". Thermocouples were fastened to the wall of the deposition bulb, covered with a single layer of ⅛ in. thick asbestos cloth, and wound with 14 gauge Nichrome wire. This unit was positioned centrally in the 6 x 18 in. cavity of the empty salt bath and then connected (glass-to-glass) to a vacuum system composed of a 3-turn glass coil to eliminate fracture due to vibration or expansion, a McLeod gauge, a cold trap, a mercury diffusion, and a mechanical pump. Fifteen grams of resublimed iodine were added to an auxiliary bulb (reservoir) held in dry ice. The space between the steel wall of the salt furnace and the Nichrome heating element was packed with high-temperature insulating wool. The deposition bulb, with the crude metal was vacuum outgassed at 800°-850°C, and heat was supplied from the Nichrome element coiled around the deposition bulb. After the pressure in the system was maintained at 10^{-5} mm Hg or less for 48 hr, the Nichrome element was disconnected, the system cooled to room temperature under vacuum, and the wool insulation removed from the furnace. A salt mixture ($NaNO_3$-KNO_3-$NaNO_2$) was added to the tank of the furnace and was melted with power supplied from the furnace. The liquid salt was agitated with an auger-type screw that lifted salt from the bottom of the tank and distributed it at various levels and directions to the top of the tank. The temperature of the deposition bulb, located 2 in. from the bottom of the tank and 2 in. beneath the surface of the salt, was maintained at ±3°C. Deposition temperatures were attained independently and measured with a platinum-platinum 10% rhodium thermocouple located in the center of the Nichrome wire helical heating element, indicated by "F" in Fig. 1. At the termination of the deposition experiment, liquid salt was siphoned from the salt tank and the residual niobium iodide within the deposition bulb was condensed on the walls of the cold Vycor bulb. The temperature of the deposition element was maintained at 900°-1000°C to prevent any iodide from condensing upon the niobium deposit.

In some experiments, the deposition bulb was positioned centrally within a 100-mm ID furnace. Thermocouples were fastened to the wall of the deposition bulb. Additional thermocouples were located at ½ in. intervals from the top to the bottom of the 24 in. long furnace, and they extended ¼ in. from the inside wall of the furnace into the air gap between the furnace and deposition bulb.

The weight of metal deposited was determined directly by weighing. The Vycor tube with the niobium deposit was compressed between polished stainless steel (No. 316) plates. The ductile deposit deformed while the Vycor tube shattered and thus provided an easy method of separation.

The crude (feed) niobium used in this work was in the form of 4-10 mil sheet and 12 mm diameter by 4 mm thick sintered powder pellets. Both forms are available commercially. Typical analytical results, in weight per cent, of the starting and iodide niobium, are summarized below:

	Oxygen	Nitrogen	Hydrogen	Carbon	Iron	Silicon	Tantalum
Pellets	0.435	0.018	0.0021	0.050	0.05	0.1	~0.5
Iodide (from pellets)	0.064	0.001	0.0008	<0.001	<0.005	0.006	—
Sheet	0.195	0.012	0.0009	0.006	0.01	0.01	~0.4
Iodide (from sheet)	0.043-0.062	<0.001	0.0001	<0.001	<0.005	0.001	0.04-0.18

Oxygen and hydrogen were determined by vacuum fusion analyses utilizing a platinum bath at 1900°C, nitrogen by micro-Kjeldahl, carbon with a Leco No. 515 Carbon Determinator, and iron, tantalum, and silicon by spectrographic analysis.

Results and Discussion

Runnalls and Pidgeon (12) and Döring and Molière (9) reported that the deposition rate of titanium and zirconium, from their respective iodides, was dependent on the surface area of small diameter (0.13 to 0.75 mm) deposition elements. Shapiro (13) reported that the deposition rate of zirconium was independent of the surface area for cylindrical deposition elements with diameters between 2 and 25 mm. This was observed from zirconium (filament) deposition temperatures in the range from 1100° to 1450°C. In addition, Shapiro (13) observed that the rate of deposition of zirconium remained constant at a given bath or feed material temperature and concluded that the vapor pressure, the value of which is determined by the coldest spot in the vessel and which value would thus remain constant for a given feed (bath) temperature, fixed the rate of deposition at a given deposition temperature.

Five deposition experiments were made utilizing a liquid salt bath with the feed temperature and deposition temperature of 244° and 1000°C, respectively. The initial diameter of the Vycor deposition element was 19 mm. Each experiment was made with 450 g of niobium pellets. The results from these five

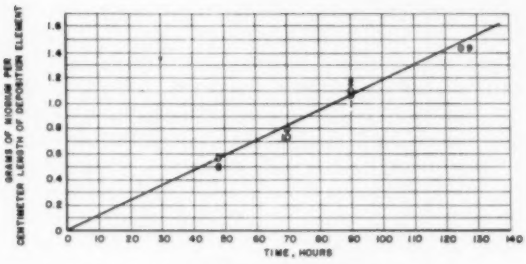

Fig. 2. Deposition element growth vs. time

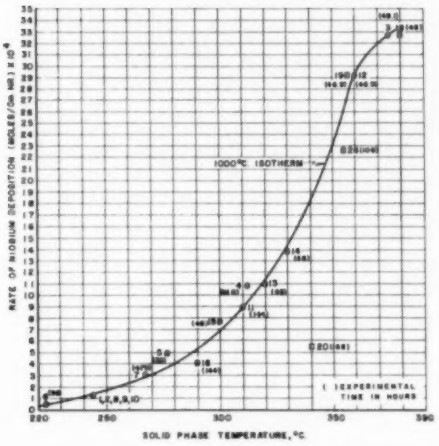

Fig. 3. Dependence of deposition rate on the condensed iodide temperature. Niobium pellet: ⊙ = salt bath; □ = air bath.

experiments, 1, 2, 8, 9, and 10, are shown graphically in Fig. 2, a plot of the grams of niobium deposited per centimeter of length of deposition element vs. the deposition time in hours. These data can be expressed by a straight line over the time interval from zero to 125 hr. Experiments 1 and 2 were made under identical conditions with the deposition time of 90 hr, to indicate the reproducibility of the measurements. The grams of metal deposited per centimeter of length of deposition element were 1.064 and 1.080 for experiments 1 and 2, respectively.

The constancy of deposition rate with time, with the steadily increasing surface area, clearly shows that the decomposition of the iodide on the deposition element cannot be rate controlling. If it were, the increased area of the deposition element would certainly affect the deposition rate. This leaves either (*a*) diffusion of iodide to or iodine from the deposition element or (*b*) the rate of reaction of the liberated iodine with the crude niobium as the possible rate controlling steps.

A total of sixteen experiments (charge of 450 g of niobium pellets) were made in the salt bath with a deposition temperature of 1000°C and feed temperatures from 224° to 375°C. The results from these experiments are summarized in Fig. 3, a plot of the deposition rate in moles of niobium per centimeter of length of the deposition element per hour vs. the condensed iodide[3] temperature. The experimental times, in hours, are reported in parentheses in Fig. 3. The low deposition rate of 0.00005 moles cm^{-1} hr^{-1} was observed at 224°C, and this rate steadily increased to the maximum of 0.00326 moles cm^{-1} hr^{-1} at 375°C, the highest temperature used in this series of experiments. It can be seen that the smooth curve which represents the data changes slope at about 350°C, which indicates that the maximum deposition rate may occur in the temperature range of 380° to 400°C for the 1000°C deposition isotherm.

Sixteen experiments (charge of 450 g of niobium pellets) were made in an air bath with a deposition temperature of 1000°C and at feed temperatures from 335° to 458°C. The results from the experiments for the 1000°C isotherm are summarized in Fig. 4, a plot of the deposition rate vs. feed temperature. The latter temperatures, measured at the surface of the deposition bulb, were about 90°C higher than the temperatures of the air bath. It can be seen that the low rate of 0.00050 moles cm^{-1} hr^{-1} was observed at the lowest condensed iodide temperature (335°C) employed. This rate increased steadily to a maximum of 0.0033 moles cm^{-1} hr^{-1} at about 370°-375°C and then decreased to a second minimum at about 410° to 440°C. From this minimum, the deposition rate again increased to 0.0015 moles cm^{-1} hr^{-1} which was observed at 458°C, the highest condensed iodide temperature employed.

There is a close similarity in the general shape of the deposition rate-temperature curves shown in Fig. 3 and 4. The best agreement occurs in the temperature range from 350° to 380°C, where both sets of data show a maximum in the deposition rate. However, considerable deviation occurs at about 340°C. For example, in experiment 20 (air bath) the observed deposition rate was 0.00054 moles cm^{-1} hr^{-1} while the deposition rate for the corresponding experiment (salt bath) was 0.00178 moles cm^{-1} hr^{-1}. The fact that the individual sets of data given in Fig. 3 and 4 can be expressed by a smooth curve, that is, each set of data are internally consistent but mutually consistent only over a limited range, strongly indicates that some unknown factor entered into the reaction process. In order to make experiment 20 (340°C) agree with the curve shown

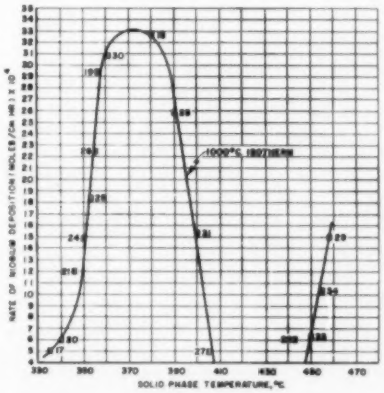

Fig. 4. Dependence of deposition rate on the condensed iodide temperature. Air bath-niobium pellet.

[3] The expressions, "condensed iodide temperature" and "deposition bulb temperature" are considered to be synonymous in this paper.

in Fig. 3, an error in temperature measurement of 50°C would have to be accounted for. It should be remembered, however, that the deposition bulb operated in the liquid salt would be susceptible to more accurate temperature measurement and operation at a more uniform temperature than the deposition bulb operated in the air bath. In addition the wall temperature of the bulb would be much closer to the temperature of the liquid salt.

Twenty-two experiments were made in which each charge consisted of 15 g of resublimed iodine and 500-600 g of 4-10 mil niobium sheet. All experiments were conducted in an air bath, and the temperature of the wall of the deposition bulb was about 70°C higher than the temperature of the air bath. Fifteen of these experiments were made with a deposition temperature of 1000°C and feed temperatures from 310° to 470°C, and five experiments were made with a deposition temperature of 1100°C and feed temperatures from 305° to 405°C. In addition, two experiments, 53 and 55, were made with the deposition temperature of 750° and 900°C, respectively. These deposition rate data are summarized in Fig. 5. It can be seen that the rate data for the 1000° and 1100°C isotherms are quite similar in shape to the curves given in Fig. 3 and 4. All curves start out at a low deposition rate, increase to a maximum rate at about 380°C, and then the rate decreases to a maximum at about 430°C. The deposition rate increases at condensed iodide temperatures greater than 430°C.

The most pronounced difference in the deposition rate data obtained by using sheet (Fig. 5) or pellet niobium (Fig. 4) as the starting material can be seen in the maximum rate of deposition that was attained for the 1000°C isotherms. For example, the maximum rate of 0.00082 moles cm^{-1} hr^{-1} was obtained with sheet niobium feed while the maximum rate of 0.00332 moles cm^{-1} hr^{-1} was obtained with

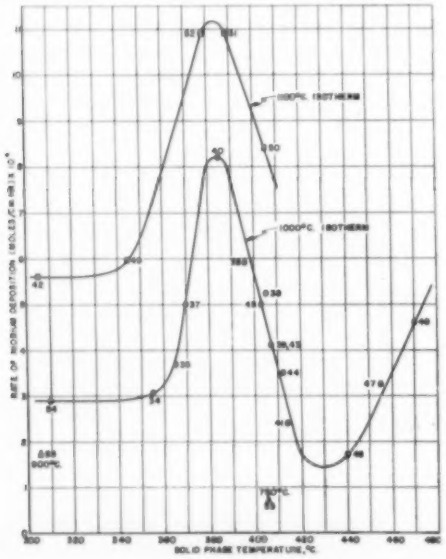

Fig. 5. Plot of deposition rate of niobium vs. condensed iodide temperature, air bath-niobium sheet.

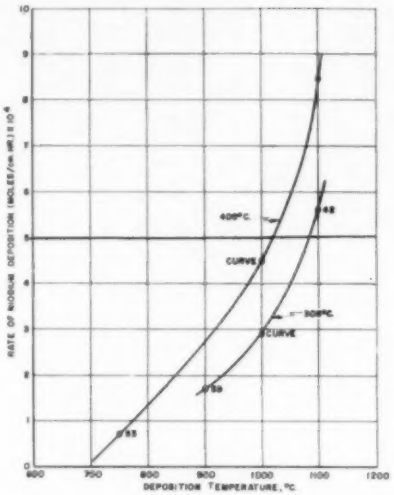

Fig. 6. Plot of deposition rate of niobium vs. deposition temperature.

niobium pellets as feed. Since the conditions under which the above experiments were conducted were identical except for the difference in the feed niobium, it is clear that the reaction of the feed material with the liberated iodine can determine the rate of deposition. Thus, the high surface area niobium pellets can react quickly with the liberated iodine to form iodide. Consequently the iodine pressure does not play as prominent a role in the deposition process when niobium pellets are used as the feed material.

The effect of the deposition temperature on the deposition rate of niobium at constant condensed iodide temperature can be seen in Fig. 6. The condensed iodide isotherm, 405°C, indicated that the deposition rate increased from 0.00007 moles cm^{-1} hr^{-1} at 750°C to 0.00084 moles cm^{-1} hr^{-1} at 1100°C. A similar curve was obtained for the 305°C isotherm. Extrapolation of the 405°C curve to zero deposition rate indicated that the minimum deposition temperature for niobium, that is, the temperature above which the niobium iodides are thermally unstable, would be somewhere in the range of 700°C. The minimum deposition temperature for the 305°C isotherm would, however, be expected to occur at a temperature below 700°C since the total pressure would be less than for the 405°C isotherm. Therefore, the two curves would cross.

In expressing the data given above in Fig. 3, 4, and 5, it was assumed that:

1. The method of expressing the deposition rate, moles cm^{-1} hr^{-1}, was valid for all feed temperatures and not just for the one temperature (244°C) investigated. The feed temperatures, which determine the total pressure in the system, were such as to permit deposition to be controlled by diffusion and the operating conditions did not permit deposition to occur in either the free molecule (lower pressure) or in the diffusion plus convection regions (higher pressure).

2. The deposition mechanism remained the same for all condensed iodide temperatures, that is, for

both the maximum and the minimum total pressures within the deposition bulb.

3. Only iodine and niobium iodides (not oxyiodide or hydrogen, etc.) contributed to the total pressure of the system.

The deposition rate of niobium must certainly be dependent on the availability of niobium iodide(s) at the deposition element. The quantity of gaseous niobium iodide depends on the reactivity of the crude niobium, the stability of the iodides in contact with excess niobium, and the vapor and disproportionation pressures of the various iodides. Therefore, a cursory study of the niobium iodides was made in order to determine the effect of the various iodides on the deposition process.

Niobium pentaiodide was prepared (14) by the reaction of iodide niobium and resublimed iodine in an evacuated tube at 280°-290°C. A high partial pressure of iodine was maintained during the reaction to stabilize the temperature sensitive pentaiodide. The excess iodine was sublimed at 114°C from the large bronze colored, plate-like crystals of the pentaiodide. Niobium was determined as Nb_2O_5 by dissolving and precipitating the sample in freshly filtered NH_4OH, filtering, and igniting in air in a platinum crucible. Iodine was determined by the modified (15) Volhard technique. Anal. calcd. for NbI_5: Nb, 12.77; I, 87.23; found: Nb, 12.81, 12.70, 13.1, 12.70; I, 87.33, 87.55, 87.52, 87.24, 87.17. Crystals of the pentaiodide were placed in a calibrated 10-ml pycnometer (inside a dry box) and the density was determined at 25°C by evacuating the pycnometer bulb containing the pure pentaiodide and then distilling, under vacuum, absolute carbon tetrachloride onto the solid sample. Density values for five different samples were 4.98, 5.04, 5.19, 5.14, and 5.08 g cc^{-1}. This pycnometric density can be compared to the x-ray density of 5.24 g cc^{-1} for the orthorhombic pentaiodide that contains 16 formula weights per unit cell.

A sample of this pentaiodide was placed in a Pyrex tube, equipped with a break seal that was broken under vacuum, and heated at 243°C for 145 hr. Iodine was liberated and the nonvolatile residue was observed to have an I/Nb ratio of 2.97. A second sample of pure pentaiodide was treated in the manner described above, but heated to 250°C. The observed I/Nb ratio was 3.07. X-ray diffraction data obtained from the two niobium iodide samples, $NbI_{2.97}$ and $NbI_{3.07}$, are in essential agreement.

Niobium pentaiodide was heated (16) to 270°C for 48 hr in 0.8 mm pressure of iodine to yield dark gray, metallic-appearing crystals of NbI_4 which were in the form of elongated hexagonal plates and fine needles. Heating a higher iodide to 425°-430°C for 48 hr in a partial pressure of iodine resulted (16) in the formation of pure NbI_5.

Samples of NbI_5 were placed in a Pyrex tube, equipped with a break seal that was broken under vacuum, and heated to 450°C for 123 hr. Material started to sublime at 250° to 260°C, and a brown to bronze colored solid was evolved at a temperature between 430°-450°C. Samples of this residue were observed to have an I/Nb ratio of 1.74. The condensed solid iodide phase removed from the deposition bulb at the termination of an experiment with the condensed iodide and deposition temperatures of 310° and 1000°C, respectively, was observed to have an I/Nb ratio of 2.74. In another experiment, some of the gaseous iodide was removed from the deposition bulb while deposition was in progress and was observed to have an I/Nb ratio of 3.12. The crude niobium was maintained at 430°C with the deposition element at 1000°C. It should be recognized that the solid iodide remaining after a deposition experiment necessarily does not have to be the same as the solid iodide existing during the experiment.

A possible explanation for the shape of the deposition rate vs. feed material temperature curves is now offered. It should be recognized that the following explanation for the deposition of niobium from its volatile iodides parallels the explanation offered by Fast (7, 8) for the zirconium-zirconium iodide and the titanium-titanium iodide systems. Pure niobium pentaiodide is not stable (forms lower iodides) at temperatures of about 200°C in vacuum or when heated in the presence of excess niobium. This thermal instability should be more pronounced inside the deposition bulb where a temperature gradient exists in the crude niobium. Metal at the surface of the molybdenum retaining screen, due to the location of the deposition element (~1000°C), will be considerably hotter than the metal at the wall of the deposition element. Therefore, the niobium at the retaining screen, due to its higher temperature, will be more chemically active toward the liberated iodine. This will prevent the development of a high partial pressure of iodine and this effect will tend to reduce further the thermal stability of the pentaiodide ($NbI_5 \rightarrow NbI_4 + \frac{1}{2} I_2$). The net result is that NbI_5 should not be an important condensed iodide species within the deposition bulb. This seems to have been realized since the solid iodide phase, with the condensed iodide and deposition temperatures of 310° and 1000°C, respectively, was observed to be I:Nb = 2.74.

Solid niobium tetraiodide was not observed in the deposition bulb after any of the experiments and, consequently, it may not be an important condensed iodide species. It should be noted, however, that in the case of tantalum, a compound corresponding to I:Ta = 3.91 was removed from the deposition bulb at the conclusion of a deposition experiment. Corbett and Seabaugh (16) reported that the heating of a higher iodide to 425° to 430°C in a partial pressure of iodine yielded NbI_5. The temperature of the crude niobium at the molybdenum retaining screen within the deposition bulb may be at this temperature level. The fact should not be overlooked, however, that the tetraiodide could enter into the deposition process according to the reactions at 300°C: $NbI_{4(c)} \rightarrow NbI_{4(g)}$ and $2NbI_{4(c)} \rightarrow NbI_{5(g)} + NbI_{3(c)}$. In any event, the quantity of iodide in the gas phase (a low partial pressure) is quite small in the condensed iodide temperature range of 300°-340°C which results in a low deposition rate. In the condensed iodide temperature range where the deposi-

tion rate is at a minimum (~300°C) to the maximum (~380°C), the quantity of iodide in the gas phase was increased as a result of the reactions specified above or for the following: $NbI_{3(c)} \rightarrow NbI_{3(g)}$ and $2NbI_{3(c)} \rightarrow NbI_{4(g)} + NbI_{2(c)}$.

The increase in deposition rate with the condensed iodide temperature in the lower temperature range can be explained on the basis of an increase in vapor pressure of the iodide; however, the behavior from the maximum (~380°C) to the minimum (~400°C) apparently has no simple explanation. Although there is an increase in the quantity of the nonvolatile, thermally stable, lower iodide in the condensed iodide temperature range of 380°-400°C, this alone should not cause the deposition rate to diminish. There can be a pressure over a mixture of solid lower iodides and this pressure, providing there is no solid solubility between the iodide species, will be independent of the quantity of the solid species present. The nonvolatile lower iodide could, however, coat the crude niobium and presumably prevent the iodine liberated at the deposition element from reacting with the crude niobium which would permit the partial pressure of iodine to increase. Thus, any increase in condensed iodide temperature would permit the formation of more lower iodide to coat the crude niobium and prevent the reaction between the niobium and iodine. This would result in a still higher partial pressure of iodine with a necessary shift in the equilibrium and could conceivably permit the iodine to attack and remove niobium from the deposition element. Thus, the net or apparent deposition rate would be quite small.

Upon further increasing the condensed iodide temperature, that is, from about 440° to at least 470°C, the diiodide can enter into the deposition process as a result of the possible reactions:

$$NbI_{2(c)} \rightarrow NbI_{2(g)},\ 2NbI_{2(c)} \rightarrow NbI_{4(g)} + Nb$$
$$\text{and } 2NbI_{2(c)} \rightarrow NbI_{(c)} + NbI_{3(c)}$$

and the deposition rate again increases. In one deposition experiment (sheet niobium was used as the crude) a sample of the gaseous species (iodide and iodine) was removed from the deposition bulb and observed to be I:Nb = 3.12. This would of course indicate that NbI_4 is the principal gaseous iodide within the deposition bulb at condensed iodide temperatures from 430° to 470°C.

The difference in thermal stability of the various niobium iodides manifests itself in that the same deposition rate of niobium can be obtained from at least three different condensed iodide temperatures. For example, the deposition rate of 0.0015 moles cm^{-1} hr^{-1} can be obtained with condensed iodide temperatures of 350°, 399°, and 459°C as shown in Fig. 4.

Acknowledgment

The author wishes to thank the Pigments Department of the Du Pont Company for the use of their facilities for this research program.

Manuscript received May 15, 1959. This paper was prepared for delivery before the Columbus Meeting, Oct. 18-22, 1959.

Any discussion of this paper will appear in a Discussion Section to be published in the June 1960 JOURNAL.

REFERENCES

1. A. E. van Arkel, *Physica*, **3**, 76 (1923).
2. A. E. van Arkel and J. H. deBoer, U. S. Pat. 1,671,-213, May 29 1928.
3. A. E. van Arkel and J. H. deBoer, *Z. anorg. u. allgem. Chem.*, **148**, 345 (1925).
4. J. H. deBoer and J. D. Fast, *ibid.*, **153**, 1 (1926).
5. Idem., **187**, 177 (1930).
6. J. H. deBoer, *Ind. Eng. Chem.*, **19**, 1256 (1927).
7. J. D. Fast, *Z. anorg. u. allgem. Chem.*, **239**, 145 (1938).
8. Idem., **241**, 42 (1939).
9. H. Döring and K. Molière, *Z. Elektrochem.*, **56**, 403 (1952).
10. V. S. Emelyanov, P. D. Bystrov, and A. E. Evstyukhin, *J. Atomic Energy, U.S.S.R.*, **1**, No. 1, **43** (1956); English translation, *J. Nuclear Energy*, **3**, 121 (1956).
11. R. F. Rolsten, *Trans. AIME*, **1959**, 472.
12. O. J. C. Runnalls and L. M. Pidgeon, *J. Metals*, **4**, 843 (1952).
13. "The Metallurgy of Zirconium," B. Lustman and F. Kerze, Jr., Editors, Chap. 5, McGraw-Hill Book Co., New York (1955).
14. R. F. Rolsten, *J. Am. Chem. Soc.*, **79**, 5409 (1957).
15. J. R. Caldwell and H. B. Moyer, *Ind. Eng. Chem., Anal. Ed.*, **7**, 38 (1935).
16. J. D. Corbett and P. X. Seabaugh, *J. Inorg. Nuc. Chem.*, **6**, No. 3, 207 (1958).

Reactions in the Niobium-Hydrogen System

W. M. Albrecht, W. D. Goode, and M. W. Mallett

Battelle Memorial Institute, Columbus, Ohio

ABSTRACT

Equilibria and elevated-temperature x-ray studies show that a solid solution of hydrogen in niobium is produced throughout most of the system. A miscibility gap was found at low temperatures and pressures with a critical point at about 140°C, 0.01 mm of mercury hydrogen pressure, and 0.3 H/Nb. Sorption rates at 300°-550°C were initially linear. At higher temperatures, sorption rates were controlled by diffusion in the metal matrix. Diffusion coefficients at 600°-700°C can be expressed by:

$$D = 0.0215 \exp\left[(-9370 \pm 600)/RT\right]$$

Desorption rates were slower than those predicted by diffusion.

In a previous study (1), the authors investigated the equilibria in the niobium-hydrogen system in the ranges 100°-900°C, 10-1000 mm of mercury hydrogen pressure, and at atomic ratios of hydrogen to niobium, H/Nb, of 0.01-0.85. A single-phase solid solution was produced throughout most of the system. However, the presence of a two-phase region in the system was indicated at low temperatures and hydrogen pressures. The present study was made to establish more definitely the extent of this region. Equilibria were established at pressures lower than those of the preceding work. Equilibrium products were identified by x-ray diffraction. Also, studies were made of the kinetics of the reaction of hydrogen with niobium and of the diffusion of hydrogen in the metal.

Paxton and Sheehan (2) measured the solubility of hydrogen in niobium at 1 atm pressure to establish partially the phase diagram of the system. They also made permeability experiments to measure the rate of diffusion of hydrogen in the metal. Gulbransen and Andrew (3) have reported the kinetics of the reaction of hydrogen with niobium for 200° to 900°C at hydrogen pressures up to 57 mm Hg. Both of these studies have a bearing on the present investigation.

Material

The original niobium bars were cut and fabricated to approximately 0.3 to 0.9 cm rods and to 0.03 cm sheet. Samples for the reaction rate and diffusion studies were vacuum annealed at 1150°C for ½ hr. Analysis of the fabricated niobium after annealing has been reported (1). The major impurities were 0.15 w/o Ta and 0.043 w/o oxygen. All other impurities were below 0.02 w/o.

Pure hydrogen was obtained from the thermal decomposition of uranium hydride prepared from dry tank hydrogen and degassed uranium chips.

Experimental Methods

The method to obtain equilibria data has been described (1). However, for this work, the micro-Sieverts apparatus was equipped with a differential oil manometer to measure pressures in the range 0.1-50 mm Hg. Briefly, data were obtained as follows. A measured amount of hydrogen was added to the calibrated reaction tube containing 3-4 g of sheet (0.03 cm thick) niobium. At the desired temperature, the system was allowed to come to constant (equilibrium) pressure as measured on the differential oil manometer. The equilibrium composition was calculated from the equilibrium pressure, specimen weight, volume of gas addition, and volume capacity of the reaction system at the experimental temperature.

Sorption rates were measured with another modified Sieverts apparatus (4). Essentially, the apparatus consists of a reaction tube, pressure regulator, gas buret, and a high vacuum-pumping system. Cylindrical specimens approximately 0.3, 0.6, and 0.9 cm in diameter and 1-3 cm long were dry abraded through 240-, 400-, and 600-grit silicon carbide paper. Each specimen was weighed, measured, and spot welded to a Pt-Pt + 10% Rh thermocouple. After a light final polish with dry 600-grit silicon carbide paper, the sample was hung in the reaction tube and sealed to the Sieverts apparatus. The system was evacuated to less than 0.01 μ of mercury, then heated to the temperature of the run.

The reaction was initiated by admitting hydrogen through the pressure regulator to the reaction tube. The buret was kept balanced at atmospheric pressure at all times. Readings of the buret were taken at convenient time intervals depending on the speed of the reaction. The amount of gas reacted with the sample was the difference between the volume added from the buret and the volume remaining in the gas phase in the calibrated dead space of the reaction tube.

Diffusion coefficients for hydrogen in niobium were determined from sorption rate data obtained at 600°-700°C. A few experiments were made to determine diffusion rates by a technique based on measuring rates of outgassing of specimens in a vacuum of 10^{-6} to 10^{-5} mm Hg at various temperatures. The apparatus and procedure have been described previously (5, 6). The rates of hydrogen outgassing were measured for 0.6 cm diameter niobium cylin-

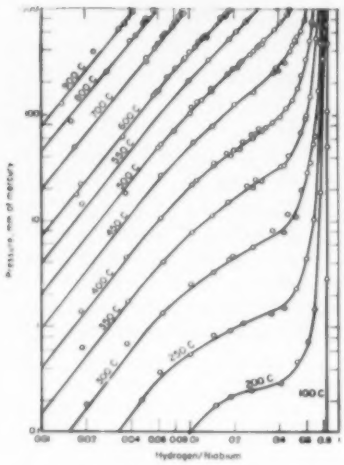

Fig. 1. Logarithmic plot of isotherms in the niobium-hydrogen system.

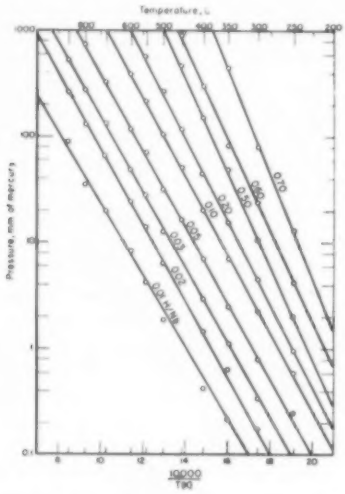

Fig. 2. Representative isopleths for the niobium-hydrogen system.

ders initially containing 0.03 to 0.06 H/Nb atomic ratio.

Results and Discussions

Equilibria

Equilibrium data obtained in the present study have been combined with those previously reported for the niobium-hydrogen system to give comprehensive coverage of the ranges 100°-900°C, 0.1-1000 mm Hg pressure, and 0.01-0.85 H/Nb ratios. Figure 1 is a logarithmic plot of equilibrium pressure against composition for various temperatures. It is seen that none of the isotherms show invariant pressures. This indicates that there is no two-phase region within these ranges. Equilibrium data could not be obtained at lower temperatures and pressures because of the extremely long times required.

Equilibria in the niobium-hydrogen system were interpreted in terms of the conditions required to form various products (solid solutions) having definite H/Nb ratios as discussed in the previous paper

Table I. Thermodynamic data for formation of various niobium-hydrogen compositions

Composition H/Nb ratio	Constants in $\log_{10} P_{mm} = -A/T + B$		$-\overline{\Delta H}$, kcal/mole H_2	$-\overline{\Delta S}$, cal/mole H_2-degree
	A	B		
0.01	3478	4.833	15.90 ±0.20	8.93 ±0.25
0.02	3592	5.490	16.40 ±0.13	11.94 ±0.18
0.03	3567	5.770	16.33 ±0.07	13.22 ±0.09
0.05	3575	6.170	16.40 ±0.11	15.05 ±0.15
0.10	3688	6.801	16.90 ±0.12	17.94 ±0.14
0.20	3953	7.548	18.09 ±0.04	21.36 ±0.06
0.30	4149	8.030	18.99 ±0.05	23.57 ±0.07
0.40	4301	8.403	19.70 ±0.12	25.27 ±0.19
0.50	4424	8.765	20.20 ±0.14	26.93 ±0.23
0.60	4319	8.895	19.80 ±0.29	27.52 ±0.47
0.70	5005	10.670	22.90 ±0.71	35.65 ±0.97

(1). For a given composition, the equilibria can be expressed by the equation,

$$\log_{10} P_{mm} = -[A/T(K)] + B \qquad [1]$$

From plots of the logarithm of the equilibrium pressure against reciprocal temperature, various isopleths are obtained from which the constants, A and B, can be calculated. Several representative isopleths are shown in Fig. 2. Values of the constants determined by the method of least squares are given in Table I. Using the familiar Gibbs-Helmholtz and van't Hoff equations, and defining the activity of hydrogen as equal to the inverse hydrogen pressure in atmospheres, the constants can be defined as,

$$A = -\overline{\Delta H}/2.303\ R \qquad [2]$$

and

$$B = -\overline{\Delta S}/2.303\ R + \log 760 \qquad [3]$$

Partial molar heats of solution, $\overline{\Delta H}$, and partial molar entropies, $\overline{\Delta S}$, calculated from Eq. [2] and [3] are also given in Table I. It is seen that there is a general increase in the magnitude of the partial molar heat of solution and entropy with hydrogen composition.

X-ray diffraction measurements were made at room temperature to 400°C on niobium and on specimens containing 0.097, 0.24, and 0.54 H/Nb ratios. Data were obtained from x-ray patterns of

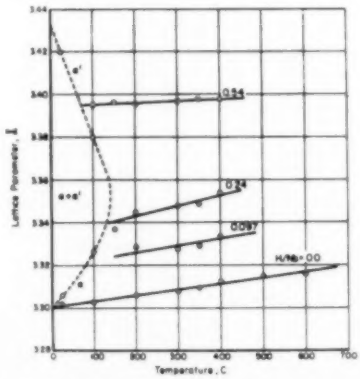

Fig. 3. Variation of lattice parameter with temperature and composition.

the specimens contained in sealed quartz capillaries. In all cases body-centered cubic structures were found. The variation of lattice parameters with temperature and composition are shown in Fig. 3. Specimens having compositions of 0.097 and 0.54 H/Nb contained two phases at room temperature and a single phase at 100°C and above. The specimen having a 0.24 H/Nb ratio showed two phases at room temperature and 100°C and one phase at 150°C and above. In the single phases, the lattice parameters increased with temperature and with hydrogen content. From the data for niobium, the thermal expansion coefficient for the metal was calculated to be 7.9×10^{-6}/°C. This is in good agreement with the handbook value of 7.1×10^{-6}/°C (7). It can be seen in Fig. 3 that the thermal expansion of the specimens containing hydrogen is approximately the same as that of the metal. The change in lattice parameter with hydrogen concentration was calculated to be 0.0023 ± 0.0002Å/1a/o hydrogen.

X-ray data in Fig. 3 can be used to outline a two-phase region in the niobium-hydrogen system. The limits of the two-phase region were calculated to be 0.024-0.75 H/Nb ratios at room temperature and 0.099-0.52 H/Nb ratio at 100°C. Also, by extrapolating the equilibrium data to lower pressures, isobars of 0.01 and 0.001 mm Hg were calculated which pass through the two-phase region. The phase diagram showing various isobars for the niobium-hydrogen system is presented in Fig. 4. It is seen that the critical point where the two phases become identical is at about 140°C, 0.01 mm of mercury hydrogen pressure, and 0.3 H/Nb ratio. It should be noted that the designation of the high-hydrogen phase which was reported (1) previously as beta has been changed to alpha prime. This is in keeping with the customary nomenclature for solid solutions showing a miscibility gap.

Values for hydrogen solubility in niobium at 1 atm pressure were reported recently by Paxton and Sheehan (2). Their results are compared with those of Sieverts and Moritz (8) and of this study in Table II. It is seen that solubilities of Paxton and Sheehan

Table II. Comparison of equilibria data at 1 atm pressure for the niobium-hydrogen system

Temp, °C	Equilibrium composition, H/Nb		
	Paxton and Sheehan	Sieverts and Moritz	Present study
800	0.047	0.051	0.051
600	0.16	0.15	0.16
500	0.22	0.39	0.42
400	0.55	0.64	0.68
300	0.66	0.73	0.77

below 600°C are considerably lower than those of the other studies. On the basis of the solubility study and high-temperature x-ray data, Paxton constructed a phase diagram for the niobium-hydrogen system showing the presence of the hydrides, Nb_2H having a hexagonal structure, and NbH having a body-centered cubic structure. The presence of the hydride Nb_2H is not indicated in the present study. Such a hexagonal structure has been attributed to impurities, probably nitrides, by Brauer and Hermann (9). The NbH structure of Paxton and Sheehan corresponds to the alpha prime structure of the present study.

Sorption Kinetics and Diffusion

Kinetic data for the sorption of hydrogen by niobium to produce compositions of 0.05, 0.10, 0.50, and 0.70 H/Nb were determined in the range 300°-700°C. Experimental conditions of temperature and pressure were determined from the isopleth (Fig. 2) of the desired product. Representative rate data are shown in Fig. 5 and 6. For every reaction up to 550°C, the initial sorption rate was linear (see Fig. 5). After a time depending on the conditions of the run, the rate decreased and stopped when equilibrium was established. Usually the reactions remained linear until about 40-50% of saturation was attained. At 300° to 450°C only the initial part of the sorption curves were obtained because of the very long times required to reach equilibrium. At 600°-700°C no initial linear rate was noted (see Fig. 6). A summary of all the linear rate constants ob-

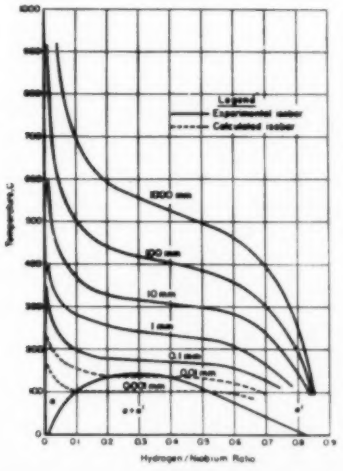

Fig. 4. Phase diagram of the niobium-hydrogen system showing various isobars.

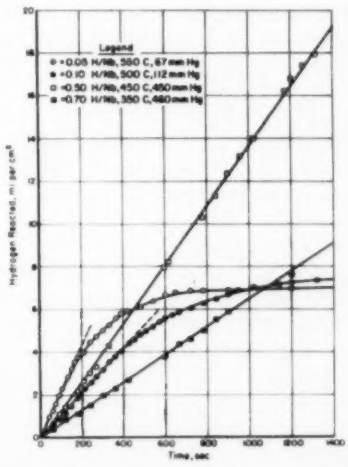

Fig. 5. Representative rate data for the reaction of hydrogen with niobium.

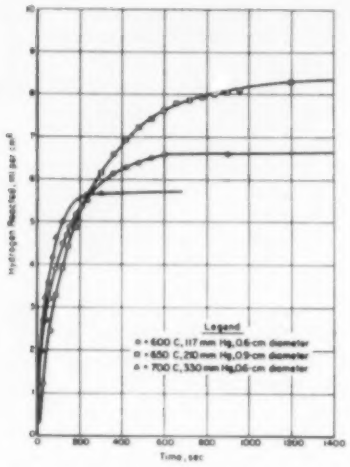

Fig. 6. Representative rate data for reaction of hydrogen with niobium to produce 0.05 H/Nb.

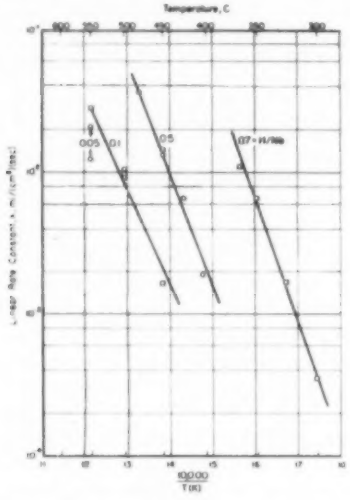

Fig. 7. Variation of linear rate constant with temperature for sorption of hydrogen in niobium.

tained at 300°-550°C is given in Table III. The variation of the initial linear rate constants with temperature for the various compositions is shown in an Arrhenius plot in Fig. 7. Data for the equation,

$$k = A \exp [-Q/RT] \qquad [4]$$

for each composition are given in Table IV. It was found that at a given temperature the initial linear rate increased with increasing hydrogen composition of the product. Also, the activation energies increased with H/Nb ratio.

Gulbransen and Andrew (3) found no consistent rate type for the niobium-hydrogen reaction from 250° to 900°C at pressures up to 5 cm. A linear reaction rate was reported only at 300°C and 21 mm of mercury hydrogen pressure. At these conditions, a composition of 0.6 H/Nb would be produced. The rate constant calculated from their data is 1.6 x 10^{-4} ml/cm²/sec. This rate constant is in line with the present work. However, at 700° and 900°C Gulbransen and Andrew found rather slow reaction

Table III. Summary of linear rate constants for the initial reaction to produce various hydrogen-niobium compositions

Composition, H/Nb	Temp, °C	Pressure, mm Hg	Rate constant × 10^3, ml/cm²-sec
0.05	550	67	21
	550	69	12
0.1	450	52	1.7
	500	112	9.1
	500	114	10
	550	218	29
0.5	400	145	1.9
	425	261	6.6
	450	450	14
	450	480	14
	480	744	37
0.7	300	83	0.35
	325	210	1.7
	350	460	6.7
	366	745	11

Table IV. Rate equations for the initial linear reaction to produce various hydrogen solutions

	Constants in the Arrhenius equation	
Composition, H/Nb	Frequency factor, A	Activation energy, Q, kcal/mole
0.10	1.32×10^7	32.6 ±1.0
0.50	1.39×10^9	36.4 ±1.3
0.70	2.18×10^{11}	38.7 ±1.5

rates. They show reactions continuing up to 2 hr using 3.3 mil (0.008 cm) thick specimens. In the present study, a specimen 0.6 cm in diameter attained equilibrium solubility in about 5 min at 700°C (see Fig. 6).

At 600°-700°C the sorption curves could be described by a diffusion equation in which sorption is initially parabolic. Modifying the derivation of Demarez, *et al.* (10) the solution of Fick's second law for diffusion in a finite cylinder can be expressed as

$$C/C_s = 1 - \frac{32}{\pi^2} \sum_{n=0}^{\infty} \sum_{m=1}^{\infty} \frac{1}{\beta^2_m (2n+1)^2} \exp\left\{-Dt\left[\frac{(2n+1)^2\pi^2}{l^2} + \frac{\beta^2_m}{a^2}\right]\right\} \qquad [5]$$

where: C = average hydrogen concentration at time, t; C_s = final equilibrium hydrogen concentration; β_m = a root of the Bessel function, $J_0(\beta)$; D = diffusion coefficient; l = length of cylinder; and a = radius of cylinder.

The cylindrical specimens used in the sorption experiments had a length five times the radius ($l/a = 5$). Substituting $5a$ and l, Eq. [3] becomes,

$$C/C_s = 1 - \frac{32}{\pi^2} \sum_{n=0}^{\infty} \sum_{m=1}^{\infty} \frac{1}{\beta^2_m (2n+1)^2} \exp\left\{\frac{-Dt}{a^2}\left[\frac{(2n+1)^2\pi^2}{25} + \beta^2_m\right]\right\} \qquad [6]$$

The theoretical curve obtained from Eq. [6] is shown in Fig. 8, in which C/C_s is plotted against

$(Dt/a^2)^{1/2}$ so as to yield a straight line for the initial parabolic behavior. The parabolic rate is followed until about 40% of saturation ($C/C_o = 0.4$) is attained. If the sorption of hydrogen is diffusion controlled, a proper choice of D would result in the experimental curves coinciding with that of theory. The excellent agreement of several experimental curves at 600°, 650°, and 700°C with theory is also seen in Fig. 8. It should be pointed out that the sorption curves obtained at the lower temperatures (350°-550°C) did not follow the theoretical diffusion curve. Probably some surface reaction affected the sorption rates.

The diffusion coefficients that were calculated from sorption and desorption rate data are summarized in Table V. It is seen that the diffusion coefficients from the outgassing (desorption) experiments are somewhat lower than those obtained from sorption rates. There was a poor agreement of the desorption rates with diffusion theory so that diffusion coefficients calculated from desorption are of doubtful worth. The diffusion rates obtained from sorption data give the best values for the diffusion coefficients for hydrogen in niobium.

Diffusion coefficients reported by Paxton and Sheehan (2) and included in Table V are considerably lower than those of the present work. Paxton and Sheehan infer that a slow surface reaction in the permeation experiments may have affected their values of D. This is highly probable since they found that the niobium permeation membranes became discolored during their experiments.

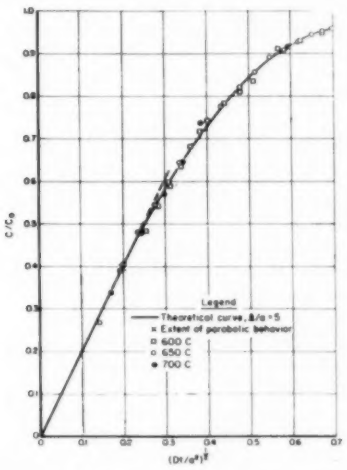

Fig. 8. Theoretical and experimental diffusion curves for sorption of hydrogen in niobium.

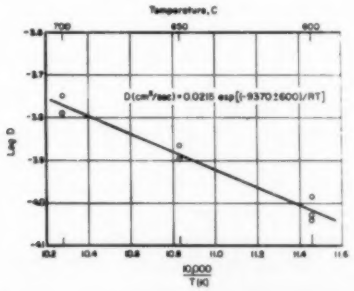

Fig. 9. Temperature variation of diffusion coefficients for hydrogen in niobium.

Table V. Diffusion coefficients for the niobium-hydrogen system

Temp, °C	Diffusion coefficient, $D \times 10^5$, cm² sec⁻¹		
	This work		
	From sorption	From desorption	Paxton and Sheehan (2)
500	—	0.58	0.00011
600	10	2.4	0.00063
600	9.4	—	0.001
600	9.2	—	—
650	14	4.3	—
650	13	—	—
700	16	—	0.0063
700	18	—	0.0036

The variation of the diffusion coefficient with temperature is described by the equation,

$$D = D_o \exp(-E/RT) \quad [7]$$

Data obtained from sorption rates are shown in Fig. 9. The equation for the best straight line through the points as determined by the method of least squares is

$$D = 0.0215 \exp[(-9370 \pm 600)/RT] \quad [8]$$

where 9370 ± 600 cal/g-atom is the activation energy. The entropy of diffusion can be calculated from D_o and E using the theory of Wert and Zener (11,12) for interstitial diffusion. For a body-centered-cubic lattice

$$D_o = 1/6\, a_o^2\, \nu \exp(\Delta S/R) \quad [9]$$

where a_o is the lattice constant and ν is the frequency of vibration of a solute atom in an interstitial position. The vibration frequency can be approximated from the relationship,

$$\nu = (E/2m\lambda^2)^{1/2} \quad [10]$$

where E is approximately equal to the activation energy, m is the mass of the solute atom, and λ is the distance between the interstitial positions ($\lambda = a_o/2$). From Eq. [7] and [8], ΔS for diffusion of hydrogen in niobium was calculated to be 3.8 cal/g-atom degree. According to theory this low positive value of ΔS is characteristic of interstitial diffusion and not diffusion through grain boundaries or other short circuiting paths.

Conclusions

Equilibria and x-ray studies show that in the ranges 100°-900°C, 0.1 to 1000 mm Hg pressure, and 0.01 to 0.85 H/Nb ratios the niobium-hydrogen system consists of a single-phase solid solution in which the basic body-centered-cubic structure of the metal expands as the hydrogen concentration increases. Equilibria in the system are best described by a series of isopleths since the heat of solution increases with hydrogen content. A two-phase region showing a miscibility gap was found at relatively low temperatures and pressures. Calculations based on the equilibrium and x-ray data place the critical point

where the two phases become identical at about 140°C, 0.01 mm of mercury hydrogen pressure, and 0.3 H/Nb ratio. The two phases, alpha and alpha prime, are both body-centered-cubic structures differing only in lattice parameter and are considered to be solid solutions of hydrogen in niobium.

Rates were obtained for the sorption of hydrogen by niobium to produce several solid solutions having hydrogen compositions of 0.05, 0.10, 0.50, and 0.70 H/Nb. The initial rates determined from 300° to 550°C were linear and increased with temperature and composition. At 600°-700°C sorption rates were diffusion controlled.

The diffusion coefficients obtained from desorption are lower than those obtained for sorption. Actually the desorption curves show a poor agreement with diffusion theory. Apparently some surface reaction influences the desorption rate.

Acknowledgment

The authors wish to express their thanks to Mr. D. A. Vaughan for making the many x-ray measurements. Work on this project was performed under AEC Contract W-7405-Eng-92.

Manuscript received April 27, 1959. This paper was prepared for delivery before the Columbus Meeting, Oct. 18-22, 1959.

Any discussion of this paper will appear in a Discussion Section to be published in the June 1960 JOURNAL.

REFERENCES

1. W. M. Albrecht, M. W. Mallett, and W. D. Goode, *This Journal*, **105**, 219 (1958).
2. H. W. Paxton and J. M. Sheehan, Report No. NYO-8040, Atomic Energy Commission (September, 1957).
3. A. E. Gulbransen and K. F. Andrew, *Trans. AIME*, **188**, 586 (1950).
4. W. M. Albrecht and M. W. Mallett, *This Journal*, **103**, 404 (1956).
5. C. B. Griffith and M. W. Mallett, "Vacuum Metallurgy," p. 147, Electrochemical Society, Inc., New York (1955).
6. W. M. Albrecht and M. W. Mallett, *Trans. AIME*, **212**, 204 (1958).
7. "Metals Handbook," American Society for Metals, Cleveland, Ohio, 1948-20.
8. A. Sieverts and H. Moritz, *Z. anorg. u. allgem. Chem.*, **247**, 124 (1941).
9. G. Brauer and R. Hermann, *ibid.*, **274**, 11 (1953).
10. A. Demarez, A. J. Hock, and F. A. Meunier, *Acta Met.*, **2**, 214 (1954).
11. C. Wert, and C. Zener, *Phys. Rev.*, **76**, 1169 (1949).
12. C. Zener, *J. Appl. Phys.*, **22**, 272 (1951).

Some Investigations of the Ag/AgCl in LiCl-KCl Eutectic Reference Electrode

Ling Yang and Robert G. Hudson

Metals Research Laboratory, Carnegie Institute of Technology, Pittsburgh, Pennsylvania

ABSTRACT

In electrochemical studies of metal chlorides dissolved in LiCl-KCl eutectic melt it is often desired to convert the metal-metal ion oxidation potentials E_c relative to a Ag/AgCl in LiCl-KCl eutectic reference electrode to those E_b based on the chlorine reference electrode. Such conversion can be made by using the emf E_c of the Ag/AgCl in LiCl-KCl eutectic/Cl_2 cell, and involves a correction term ΔE. By using cases where both E_c and E_b can be determined independently, studies have been made of the variation of ΔE with the nature and concentration of the metal ions in the melt, the temperature of the melt, the concentration of AgCl in the reference electrode, and the nature of the membrane separating the reference and metal electrodes. This information gives an estimate of the reliability of data obtained when the two reference electrodes are interchanged.

In electrochemical studies of chloride melts, the thermodynamic properties of metal chlorides dissolved in molten chloride solvents are often calculated from observed potentials between the metal electrodes and a chlorine reference electrode in these melts. The standard potentials may be determined experimentally or calculated from thermodynamic data (1). The information gained has been very helpful to our understanding of the constitution of these systems. There are occasions, however, where the chlorine electrode cannot be used directly. For instance, if the metallic ion of the chloride melt has more than one stable valence state under prevailing experimental conditions and chlorine gas can oxidize it from the lower to the higher state, the potential of the metal and its lower valence ion can be studied only with other reference electrodes. However, for the calculation of thermodynamic properties of the dissolved metal chloride, the observed potential must be converted to the chlorine reference electrode scale.

This problem occurred in our study of thermodynamic properties of polyvalent metal chlorides (MCl_n) dissolved in LiCl-KCl eutectic melt. A suitable reference electrode (2-9) was that suggested by Bockris, et al. (9), namely Ag/AgCl in LiCl-KCl eutectic/Pyrex membrane, which is of interest because of its simple construction. The Pyrex membrane avoids mixing of the electrolytes.

To convert the observed oxidation potential of a metal to such a reference electrode, to that of the same metal to a chlorine reference, we must know

Table I. Observed emf's of cell [c]

Mole fraction of AgCl, N	Temp, °K	Pressure, Cl_2, atm	E_c observed, v	dE_c/dT, v/°C
0.0146	768	0.976	1.1474	$+8.66 \times 10^{-5}$
	801		1.1493	
	823		1.1524	
0.0367	775	0.979	1.0834	-3.00×10^{-5}
	796		1.0825	
	804		1.0826	
	825		1.0818	
0.0452	769	0.968	1.0694	-3.33×10^{-5}
	798		1.0687	
	824		1.0680	
0.1966	767	0.975	0.9835	-1.55×10^{-4}
	803		0.9771	
	823		0.9743	
0.5025	767	0.975	0.9388	-2.33×10^{-4}
	773		0.9346	
	797		0.9294	
	825		0.9203	
1.0000	770	0.980	0.9010	-2.92×10^{-4}
	790		0.8950	
	810		0.8895	
	825		0.8842	

how they are related. Let E_a, E_b, and E_c represent, respectively, the emf's of the cells

M/MCl_n in LiCl-KCl eutectic/Pyrex membrane/AgCl in LiCl KCl eutectic/Ag [a]

M/MCl_n in LiCl-KCl eutectic/Cl_2 [b]

Ag/AgCl in LiCl-KCl eutectic/Cl_2 [c]

The cell reactions are

$M + n\,Ag^+ = M^{+n} + n\,Ag$ [A]

$M + n/2Cl_2 = M^{+n} + n\,Cl^-$ (MCl_n in LiCl-KCl eutectic) [B]

$n\,Ag + n/2\,Cl_2 = n\,Ag^+ + n\,Cl^-$ (AgCl in LiCl-KCl eutectic) [C]

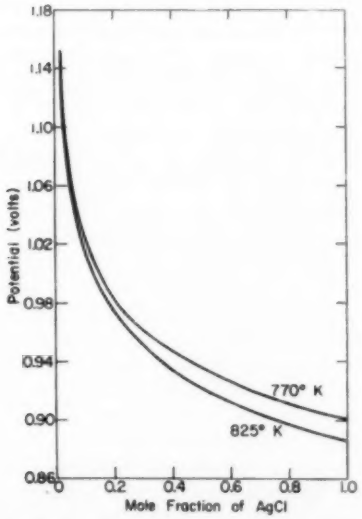

Fig. 1. Emf's E_c of cell [c] for various concentrations of AgCl.

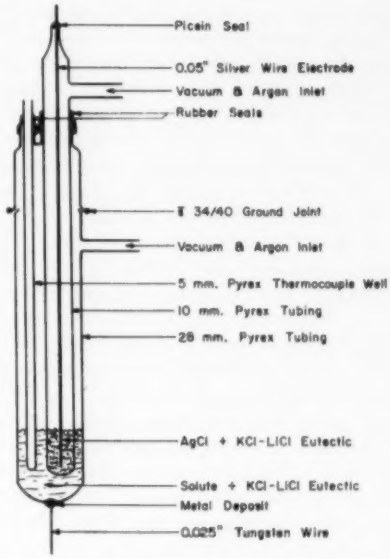

Fig. 2. Cell arrangement for measuring E_a

Define the quantity $\Delta E = E_a + E_c - E_b$. It can be shown from thermodynamics that

$$\Delta E = (1/\mathbf{F})\,[\mu(Cl^-\text{ of } MCl_n \text{ in eutectic}) - \mu\,(Cl^-\text{ of AgCl in eutectic})] + E_m \qquad [1]$$

where the μ's are chemical potentials and E_m is the membrane potential in cell [a]. The conversion of E_a to E_b thus requires a knowledge of both E_c and ΔE. Sufficient data do not yet exist to calculate ΔE from Eq. [1]. Our paper attempts an experimental evaluation of ΔE from measured values of E_a, E_b, and E_c.

Determination of E_c

Potentials of metal-chlorine cells have already been studied over a range of temperatures and concentrations (10). The data E_c for the AgCl melts are quoted in Table I. It can be shown from these that mixtures of AgCl and LiCl-KCl eutectic behave as regular solutions, with AgCl deviating positively from Raoult's law.

The derivative dE_c/dT was obtained from the slope of a plot of E_c [after correction to $(Cl_2) = 1$] vs. T, it is essentially constant for a given composition, and its sign changes at a mole fraction N(AgCl) of about 0.03. The data of Table I, after correction to $(Cl_2) = 1$ and to 770° and 825°K, are plotted in Fig. 1. This figure can be used to estimate any value of E_c within or near the concentration and temperature ranges shown.

Experimental Estimation of ΔE

As shown in Eq. [1], ΔE consists of two parts, one due to the difference of chemical potential of chloride ion in the two melts, the other due to the membrane potential E_m. Bockris, *et al.* (9) compared the observed emf's of the concentration cells

Ag/AgCl (0.13M) in LiCl-KCl eutectic/Pyrex membrane/AgCl (0.05-1.3M) in LiCl-KCl eutectic/Ag [d]

with those calculated from the Nernst equation, by assuming the activity coefficient of Ag^+ constant in the range of compositions used. They concluded that the discrepancies were mainly due to the differences of activities of alkali metal ions across the membrane. In general, however, the situation may not be so simple, especially when the metal chloride solute on one side of the membrane is different from that on the other side. Exact evaluation of ΔE is impossible without knowing the conditions prevailing at the two melt-membrane interfaces and that inside the membrane, as well as the transport mechanism through the membrane. So far the study of membrane potential has been confined mostly to aqueous solutions (11); molten salt systems have not received much attention.

In spite of these difficulties, useful information may be obtained on the magnitude of ΔE by studying cases where independent measurements can be made on both E_a and E_b. In our previous investigations (10), measurements have been made of E_b. Therefore if we determine the corresponding values of E_a against AgCl reference electrodes whose E_c evaluated from Fig. 1, we should be able to calculate ΔE and find out how it is affected by the nature and concentration of the metal chloride in the melt, the concentration of AgCl in the reference electrode, the temperature, and the membrane material, e.g. Pyrex, Vycor, or quartz.

Measurement of E_a.—E_a was measured by using the arrangement shown in Fig. 2. The AgCl reference electrode consisted of a 0.05 in. diameter Ag wire (99.99% pure) dipped in a LiCl-KCl eutectic melt containing AgCl of the desired concentration and situated inside a Pyrex (Vycor or quartz) tube.

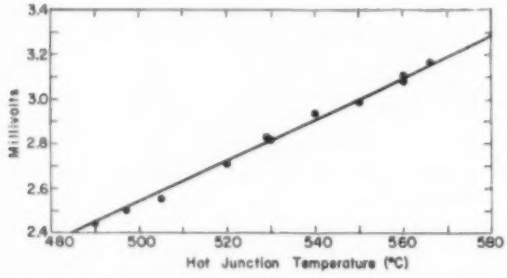

Fig. 3. Tungsten-silver thermal emf, cold junction 0°C, cold terminal of tungsten positive.

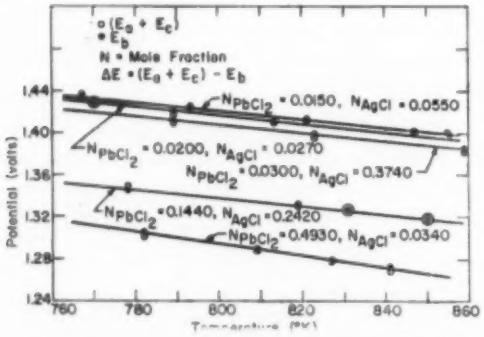
o (Ea + Ec)
• Eb
N = Mole Fraction
ΔE = (Ea + Ec) - Eb
NPbCl2 = 0.0150, NAgCl = 0.0550
NPbCl2 = 0.0200, NAgCl = 0.0270
NPbCl2 = 0.0300, NAgCl = 0.3740
NPbCl2 = 0.1440, NAgCl = 0.2420
NPbCl2 = 0.4930, NAgCl = 0.0340
Potential (volts)

Fig. 4. Comparison of $E_a + E_c$ with E_b; $PbCl_2$ melts.

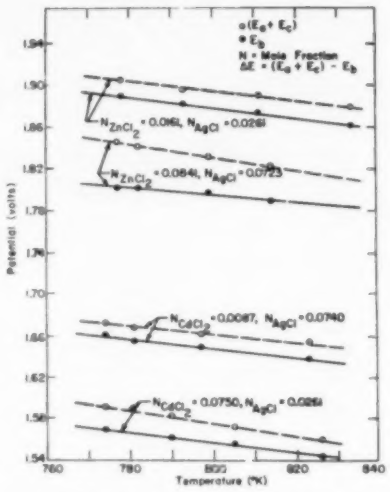
o (Ea + Ec)
• Eb
N = Mole Fraction
ΔE = (Ea + Ec) - Eb
NZnCl2 = 0.0161, NAgCl = 0.0261
NZnCl2 = 0.0848, NAgCl = 0.0723
NCdCl2 = 0.0087, NAgCl = 0.0740
NCdCl2 = 0.0750, NAgCl = 0.0251
Potential (volts)
Temperature (°K)

Fig. 5. Comparison of $E_a + E_c$ with E_b; $ZnCl_2$ and $CdCl_2$ melts.

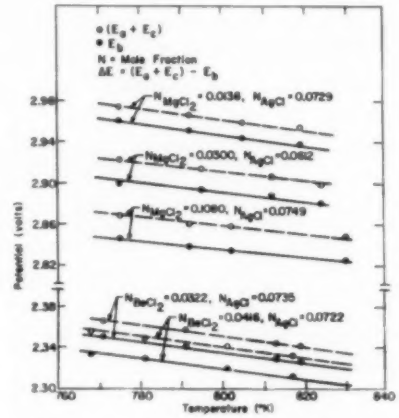
o (Ea + Ec)
• Eb
N = Mole Fraction
ΔE = (Ea + Ec) - Eb
NMgCl2 = 0.0038, NAgCl = 0.0729
NMgCl2 = 0.0300, NAgCl = 0.082
NMgCl2 = 0.1080, NAgCl = 0.0749
NBeCl2 = 0.0322, NAgCl = 0.0735
NBeCl2 = 0.0446, NAgCl = 0.0722
Potential (volts)
Temperature (°K)

Fig. 6. Comparison of $E_a + E_c$ with E_b; $MgCl_2$ and $BeCl_2$ melts.

The bottom of the tube was sealed and blown thin to form the membrane. The exact thickness of the membrane was unknown but was found immaterial to the results obtained. The metal electrode consisted of the desired metal electrodeposited from the melt containing the metal chloride on a 0.025 in. tungsten wire sealed to the bottom of the cell. Deposition was carried out by using a graphite anode (not shown in Fig. 2) which was then withdrawn. The chlorine gas evolved was removed by pumping and the cell filled with purified argon. The potential between the Ag electrode and the metal electrode was followed to 0.1 mv on a Brown recorder connected in series with a L&N K-2 potentiometer and another potentiometer covering a range of 0-10 v until a steady value was reached. The temperature of the melt, as indicated by a calibrated chromel-alumel thermocouple, was changed to different values and the corresponding steady potentials recorded. Finally the melt was brought back to the original temperature and the steady potential reached was compared with that obtained before. The agreement was usually within ±2 mv. In addi-

Table II. Effect of membrane materials on $\Delta E = E_a + E_c - E_b$

MCl_n	N (MCl_n)	N (AgCl)	Temp, °K	E_a, mv Pyrex	E_a, mv Vycor	E_a, mv quartz	E_c	E_b, mv	ΔE, mv Pyrex	ΔE, mv Vycor	ΔE, mv quartz
AgCl	0.016	0.245	780	0.173	0.183	—	0.970	1141	2	12	—
			787	0.173	0.183	—	0.970	1141	2	11	—
			816	0.183	0.190	—	0.963	1145	1	8	—
$PbCl_2$	0.030	0.136	795	0.411	0.416	0.417	1.003	1410	4	9	10
$ZnCl_2$	0.016	0.026	778	0.800	0.826	0.826	1.104	1888	16	42	42
	0.084	0.072	778	0.802	0.820	0.819	1.042	1806	37	56	55
			799	0.791	0.807	0.808	1.040	1796	35	51	52
			815	0.782	0.799	0.801	1.039	1786	33	52	54

tion, the reversibility of the electrode reactions was established by the close agreement (within ±1 mv) between the steady potential obtained in the above manner and that obtained after a few milliamperes had been drawn from the cell for about 2 min. For metals which attack glass, such as La and Y, the tungsten wire was inserted from the top of the cell so that the metal deposit was not in contact with glass. Although only one Ag/AgCl reference electrode is shown in Fig. 2, in actual measurements, four or five of them can be put in the same melt for the study of the effect of AgCl concentration in the reference electrode or the nature of the membrane

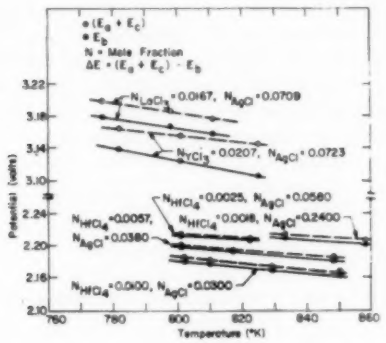
$(E_a + E_c)$
E_b
N = Mole Fraction
$\Delta E = (E_a + E_c) - E_b$
N_{LaCl_3} = 0.0167, N_{AgCl} = 0.0709
N_{YCl_3} = 0.0207, N_{AgCl} = 0.0723
N_{HfCl_4} = 0.0025, N_{AgCl} = 0.0580
N_{HfCl_4} = 0.0057, N_{AgCl} = 0.0380
N_{HfCl_4} = 0.0018, N_{AgCl} = 0.2400
N_{HfCl_4} = 0.000, N_{AgCl} = 0.0300
Potential (volts)
Temperature (°K)

Fig. 7. Comparison of $E_a + E_c$ with E_b; $LaCl_3$, YCl_3, and $HfCl_4$ melts.

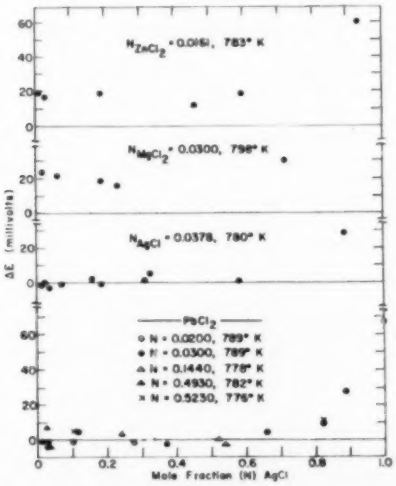

Fig. 8. Effect of AgCl concentration in the reference electrode on ΔE.

material on ΔE. The observed steady potential, after correction for the emf of the Ag-W thermocouple (Fig. 3), is E_a. The correction was made by converting the thermal emf's of Fig. 3 to those for a cold junction at room temperature. Thermal emf data were determined experimentally by coupling the tungsten wire and the silver wire used in this work. Methods for purifying and heating the melts were the same as described previously (10).

After the run, the AgCl reference electrode was raised out of the melt. Both the AgCl and the MCl_n melts were cooled quickly in an argon atmosphere and analyzed. On the basis of the analytical results, E_c was interpolated or extrapolated from Fig. 1, and E_b was taken from our previous data (10). ΔE was then computed from the data.

Variation of ΔE with various factors.—Results obtained are shown in Fig. 4-8, which can be summarized as follows:

1. *Nature of* MCl_n.—ΔE is negligible when MCl_n is AgCl (Fig. 8) and is less than a few millivolts for $PbCl_2$ (Fig. 4). This is true for a wide range of AgCl and $PbCl_2$ concentrations. For the others (Fig. 5-8), ΔE amounts to 5-40 mv. It is interesting to note that melts containing Ag^{++} and Pb^{++} which have less tendency to form complex ions with the chloride ions of the solvent have negligible ΔE, while those containing Be^{++}, Mg^{++}, Zn^{++}, Cd^{++}, which have been shown

Table III. Studies of charge carriers through Pyrex membrane

(a) AgCl, 525°C, 12 v, 5.0 ma, 2.36 hr

	Initial composition, % Ag	Final composition, % Ag	Ag gained, mg exp.	Ag gained, mg calcd.	Ag lost, mg exp.	Ag lost, mg calcd.
Positive side, AgCl (2.0904 g)	28.12	30.29	45.4	47.5		
Negative side, AgCl (2.0434 g)	28.12	25.93			44.8	47.5

(b) $ZnCl_2$, 533°C, 12 v, 8.0 ma, 2.31 hr

	Initial composition, % metal	Final composition, % metal	Zn gained, mg exp.	Zn gained, mg calcd.	Ag lost, mg exp.	Ag lost, mg calcd.
Positive side, $ZnCl_2$ (3.8168 g)	1.70	2.27	21.7	22.6		
Negative side, AgCl (1.2131 g)	11.99	5.97			73.1	74.5

to have a higher tendency to form complex ions exhibit higher ΔE (10).

2. *Concentration of* MCl_n.—For those melts having appreciable ΔE values, ΔE decreases as the concentration of MCl_n decreases (Fig. 5 and 6).

3. *Temperature.*—In the temperature range used in this work, ΔE does not seem to vary appreciably with temperature (Fig. 4-7), except for YCl_3 (Fig. 7).

4. AgCl *concentration of the reference electrode.*—Change of the AgCl concentration of the reference electrode over a wide range does not seem to affect ΔE appreciably (Fig. 8). However, for $N_{AgCl} > 0.6$, ΔE becomes abnormally high (Fig. 8).

5. *Membrane material.*—As shown in Table II, ΔE values for Vycor and quartz membranes are about the same, and they are higher than for Pyrex. Vycor and quartz are therefore less suitable membrane materials than Pyrex.

Some Transport Studies

In addition to the above investigations on ΔE, a few experiments have been performed to determine whether metal ions other than the Li^+ and K^+ are responsible for carrying the current through the Pyrex membrane. These were carried out by using the following cell arrangements with M = Ag or Zn,

M/MCl_n in LiCl-KCl eutectic/Pyrex membrane/

AgCl in LiCl-KCl eutectic/Ag [e]

A known amount of current was passed through each cell so that the Ag or Zn at the left dissolved into the melt while the Ag^+ in the melt at the right deposited out as Ag. The increase in the amount of Ag^+ or Zn^{++} in the melt at the left and the decrease in the amount of Ag in the melt at the right of the glass membrane were then determined by chemical analysis and compared with what would be expected on the basis of the amount of current passed through the cell if the membrane is impermeable to Ag^+ and Zn^{++}. The Ag^+ and the Zn^{++} contents of the melts were determined by precipitation and weighing as AgCl and $Zn(C_9H_6ON)_2$, respectively. The current of electrolysis was controlled manually and its time integral was determined by using a silver coulometer. Results are shown in Table III.

It can be seen that the amount of current carried by the Ag^+ or Zn^{++} through the Pyrex membrane, if any, cannot be more than a few per cent. Spectroscopic analyses of the glass used for making the membrane showed that it contains 0.02% Li_2O, 0.05% K_2O, and less than 0.0005% Ag_2O. The glass membrane in the AgCl cell, recovered after the electrolysis, was found to contain 0.75% Li_2O, 0.12% K_2O, and 0.001% Ag_2O. The large increase in the Li content seems to indicate that Li^+ is the predominant current carrier through the Pyrex membrane.

Reproducibility and Stability

The reproducibility of the Ag/AgCl in LiCl-KCl eutectic/Pyrex membrane reference electrode was studied by comparing the potentials of various reference electrodes made from melts of the same AgCl concentration N(AgCl) = 0.030 or 0.1020. Agreement was found to be within ±2 mv. The stability of this reference electrode was also investigated by following the change of the potential of AgCl concentration cells with N(AgCl) in the range 0.060 to 0.200, in LiCl-KCl eutectic melts with time. It was found that if oxygen and moisture were excluded from the melt, the change in potential was less than a few millivolts after the cells had been maintained at about 800°K for 40 hr.

The investigations described above cover some of the characteristics of the silver chloride-Pyrex reference electrode. Although the information available still does not allow us to calculate ΔE theoretically, these studies may serve to evaluate the reliability of potential data obtained in changing reference electrodes from AgCl to chlorine.

Acknowledgments

The authors wish to thank Drs. G. Derge and G. M. Pound of Carnegie Institute of Technology and Mr. Frank Kerze, Jr., of the U. S. Atomic Energy Commission for their interest in this work and their valuable help. They also are indebted to Drs. C. L. McCabe and P. Fugassi of Carnegie Institute of Technology, Dr. J. O'M. Bockris of the University of Pennsylvania and Dr. S. Senderoff of the National Carbon Company for stimulating discussions. This work is a part of a research program sponsored by the U. S. Atomic Energy Commission under Contract No. AT(30-1)-1432 and was presented at the June 1958 Symposium on Analytical Techniques for Molten Systems, sponsored by the American Chemical Society.

Manuscript received March 5, 1959.

Any discussion of this paper will appear in a Discussion Section to be published in the June 1960 JOURNAL.

REFERENCES

1. W. J. Hamer, M. S. Malmberg, and B. Rubin, *This Journal*, **103**, 8 (1956).
2. S. Senderoff and A. Brenner, *ibid.*, **101**, 31 (1954).
3. S. N. Flengas and E. Rideal, *Proc. Roy. Soc.*, **A223**, 443 (1956).
4. Yu K. Delimarskii and R. S. Khaimovich, *Ukrain. Khim. Zhr.*, **15**, 340 (1949).
5. Yu K. Delimarskii and A. A. Kolotii, *ibid.*, **16**, 438 (1950); **20**, 1169 (1954).
6. K. Hauffe and A. L. Vierk, *Z. Elektrochem.*, **53**, 151 (1949).
7. S. N. Flengas and T. R. Ingraham, *Canadian J. Chem.*, **35**, 1139, 1254 (1957); *This Journal*, **106**, 714 (1959).
8. H. A. Laitinen and C. H. Liu, *J. Am. Chem. Soc.*, **80**, 1015 (1958).
9. J. O'M Bockris, G. J. Hills, D. Inman, and L. Young, *J. Sci. Instrument*, **33**, 438 (1956).
10. L. Yang and R. G. Hudson, to be published in *Trans. Am. Metallurgical Society, AIME.*
11. "Membrane Phenomena," Discussion of the Faraday Society (1957).

The Oxygen-Evolution Reaction at Gold Anodes

II. Overpotential Measurements and Reaction Mechanism in Sulfuric Acid Solutions

Sidney Barnartt

Research Laboratories, Westinghouse Electric Corporation, Pittsburgh, Pennsylvania

ABSTRACT

The oxygen-evolution reaction at gold anodes was studied in sulfuric acid solutions, with and without added potassium sulfate, over the pH range 0 to 2.7 at 25°C. Overpotential measurements were made with an accuracy of ±1 mv in a cell having uniform current distribution over a spherical anode. Within current density limits imposed by the cell and the solution, Tafel's equation was obeyed to ±1 mv. The Tafel slope was $b = 2.303(3RT/4F)$ in each solution. At constant current density the overpotential was independent of pH or neutral salt additions. Several proposed mechanisms of the oxygen evolution reaction predict this independence, but in each case the theoretical Tafel slope is smaller than the observed value.

Overpotential data in the literature relating to the oxygen-evolution reaction have not been sufficiently accurate to settle the reaction mechanism unequivocally. In a previous paper (1) the factors involved in obtaining accurate overpotential measurements were evaluated with reference to a new cell design. Within current density (c.d.) limits dictated by this cell, it was found that steady-state measurements of oxygen overpotential at gold anodes in 0.1M H_2SO_4 were reproducible to ± 1 mv. Within the same deviation the overpotential (η) varied with c.d. (i) in accordance with Tafel's Eq. (2):

$$\eta = a + b \log i = a' + b \log i' \qquad [1]$$

where $i' = qi$ is the apparent c.d., q is the surface roughness, a and b are constants and $a' = a - b \log q$ is the extrapolated overpotential at 1 amp cm^{-2} apparent c.d. These measurements are extended in the present paper to include the effects of pH and neutral salt additions, effects which are diagnostic of the reaction mechanism (3-5).

Experimental Procedure

The experimental procedure was that of the previous paper, cell II and the solid gold electrode described therein (1) being used for almost all of the overpotential measurements. The electrode was polished to an almost mirror-bright surface with diamond polishing compound, ending with 3μ particle size. It was precleaned with solvents, cathodic treatment in hot 3M NaOH and immersion in 10M HNO_3. It was then made anode in 1M H_2SO_4 at 5 x 10^{-2} amp cm^{-2} for 5 min, the thin oxide layer thus formed being dissolved in 5M HCl, after which the electrode was rinsed thoroughly and inserted in the cell.

Sulfuric acid was distilled, and water redistilled from alkaline permanganate, in all-Pyrex stills. Reagent-grade K_2SO_4 was used without further purification; the experiments described below indicated that no deleterious impurities were present. Sulfuric acid solutions of concentration 0.01 to 1M, some with 0.5M K_2SO_4 added, were studied at 25.0°C. Overpotentials were determined by use of a saturated calomel reference electrode, as previously described (1).

The lower limit to the c.d. range for accurate measurements in 0.1M H_2SO_4 has been shown to be 3 x 10^{-5} amp cm^{-2}, and was attributed to cathodically produced H_2O_2 (1). Depolarization by H_2O_2 should depend on the cathode and cell geometry used, and not on solution concentration. Thus the lower c.d. limit of 3 x 10^{-5} was expected for all of the solutions studied, and this was found to be the case.

Although a brown film of hydrated Au_2O_3 formed slowly and continuously over the gold anode in each solution, the current efficiency for film formation was assumed to be sufficiently small to be negligible, as was shown for 0.1M H_2SO_4 (1).

The upper c.d. limit for accurate measurements varies with concentration and is determined either by the IR drop between the capillary tip and the electrode surface (V_{IR}) or by concentration polarization. The IR drop may be computed (1) from the equation:

$$V_{IR} = (ir_o^2/\kappa)\,[1/r_o - 1/(r_o + 3d - d/3)] \qquad [2]$$

where κ is the solution conductivity in mhos per centimeter, $r_o = 0.50$ cm is the radius of the spherical electrode, and $d = 0.02$ cm is the diameter of the capillary tip, the latter being positioned at a distance $3d$ from the electrode surface. The maximum c.d. i_l for making accurate IR drop corrections is obtained from Eq. [2] by setting $V_{IR} = 0.01$ v (1).

In order to avoid concentration polarization effects an upper limit of 3% was selected as the maximum allowable change in H_2SO_4 concentration at the anode. The c.d. i_c corresponding to this concentration change was calculated from the equation:

$$\Delta C = 10^3(1 - t_+)\, i\, l/2FD \qquad [3]$$

by setting $\Delta C = 0.03\, C_o$, where ΔC is the increase in acid concentration at the anode surface, C_o the bulk concentration (mole/l), l the thickness of the diffu-

sion layer, **F** the faraday, D the diffusion coefficient, and t_+ is the hydrogen ion tranference number.[1] For the sulfuric acid solutions studied, the mean values $l = 0.005$ cm for gas-bubbling conditions (7), $t_+ = 0.82$ (8) and $D = 1.9 \times 10^{-5}$ cm^2 sec^{-1} (9) were substituted into Eq. [3] to obtain:

$$i_2 = 0.12\, C_o \qquad [4]$$

Table I lists the calculated values of i_1 and i_2. The smaller of these was taken to be the maximum allowable c.d. for each solution and was not exceeded in this investigation, as shown in the last column.

Results

For each solution studied, oxygen overpotential varied with c.d. in accordance with Tafel's equation. Average values of the measured Tafel constants are given in Table II. The overpotential at an apparent c.d. $i' = 10^{-4}$ amp cm^{-2} ($\eta_1 = a' - 4b$) is included as a reference value within the actual c.d. range studied. Also tabulated is the apparent exchange current density qi_o; this quantity may be calculated from

$$qi_o = 10^{-a'/b} \qquad [5]$$

and is of the order of magnitude of 10^{-22} amp cm^{-2}.

The maximum deviation of the experimental overpotential values from the Tafel lines described in Table II was ± 1 mv, with the exception that at 10^{-2} amp cm^{-2} apparent c.d. the η-values in 1M and 0.5M H_2SO_4 were 3-4 mv high. The latter discrepancy, although small, was reproducible. In each solution, the steady-state overpotential readings obtained with decreasing and increasing currents agreed within ±1 mv and duplicate runs with fresh batches of solution showed the same good agreement previously reported for 0.1M H_2SO_4 (1).

The variation of overpotential with pH at constant c.d. is shown for typical runs in Fig. 1. There is no consistent change in overpotential with acid concentration or with salt addition. The small variations from the mean values (lines of Fig. 1) found for 1M and 0.05M H_2SO_4 reflect changes in the Tafel a and not in the slope b. The mean values yield a linear Tafel plot with deviations ≦ 1 mv, as shown in Fig. 2; the constants from this plot are appended to Table II. The mean slope of 0.045_2 may be closely represented by $b = 2.303\ (3RT/4\mathbf{F})$, which is 0.0443 at 25°C.

The only pertinent[2] data in the literature for gold in sulfuric acid solutions is that of Hickling and Hill (11), for electroplated gold in 0.5M H_2SO_4 at 20°C. These are also plotted in Fig. 2 for comparison, the vertical length of each point representing their stated reproducibility of ± 10 mv. The latter data indicated a slope of 0.07, a value appreciably greater than that found in the present work taking into consideration the 5° temperature difference. The actual experimental points, however, are in good agreement with the curve of Fig. 2 at 10^{-4} and 10^{-3} amp cm^{-2} apparent c.d., taking $\partial\eta/\partial T = -3$ mv/degree (19). The deviation at 10^{-5} amp cm^{-2} indicates depolarization by competing anodic reactions.

[1] Equation [3] is an approximation applicable to ideal solutions. Corrections for deviations from ideality (6) were ignored because only small concentration changes are considered here.

[2] Other work on this system (12-15) did not include studies of steady-state overpotential.

Table I. Upper current density limit imposed by *IR* drop or concentration polarization calculations

Solution	κ, at 25°C, ohm^{-1} cm^{-1}	i_1, V_{IR} = 10 mv, amp cm^{-2}	i_2, ΔC = 0.03 C_o, amp cm^{-2}	Actual c.d. limit studied, amp cm^{-2}
1.00M H_2SO_4	0.39	0.08	0.12	0.01
0.50M H_2SO_4	0.21	0.04	0.06	0.01
0.10M H_2SO_4	0.046	0.01	0.012	0.01
0.050M H_2SO_4	0.025	0.005	0.006	0.005
0.010M H_2SO_4	0.0062	0.001	0.0012	0.001
0.10M H_2SO_4 + 0.50M K_2SO_4	0.099	0.02	0.012	0.005
0.010M H_2SO_4 + 0.50M K_2SO_4	0.085	0.02	0.0012	0.001

Table II. Measured Tafel constants for oxygen evolution at gold anodes in sulfuric acid solutions, 25.0° C

Solution	pH*	a', v	b, v	$\eta_1 = a' - 4b$, v	10^{22} qi_o,** amp cm^{-2}
1.00M H_2SO_4	0.05	0.988	0.046_2	0.807	5
0.50M H_2SO_4	0.38	0.983	0.046_2	0.798	6
0.10M H_2SO_4†	1.01	0.977	0.045_5	0.797	2
0.05M H_2SO_4	1.28	0.975	0.045_2	0.794	3
0.01M H_2SO_4	1.86	0.975	0.044_8	0.796	2
0.10M H_2SO_4 + 0.50M K_2SO_4	1.63	0.980	0.045_2	0.799	2
0.01M H_2SO_4 + 0.50M K_2SO_4	2.71	0.979	0.045_5	0.797	3
Mean Tafel Line††		0.979	0.045_2	0.798	3

* Standardized with 0.1M HCl, $pH_2 = 1.10$ at 25°C (10).
** qi_o is the exchange current per apparent cm^2 of electrode surface.
† Data from previous paper (1).
†† From Fig. 2.

Discussion

Theoretical values of the Tafel slope and of other parameters useful for interpretation of the experimental data have been compiled by Bockris (4) for various mechanisms of anodic oxygen evolution. Three of the mechanisms include rate-determining steps for which overpotential is predicted to be independent of pH or neutral salt additions in acid solutions, in agreement with the experimental results of the present study. These mechanisms are listed in Table III. In each case the predicted slope is smaller than the experimental value.

The theoretical slopes of Table III involve no assumptions as to the value of the symmetry factor β (3, 4), but do involve assumptions concerning the degree of coverage of the electrode surface with adsorbed radicals. The combination mechanism Ib, for example, wherein the slow step is the combina-

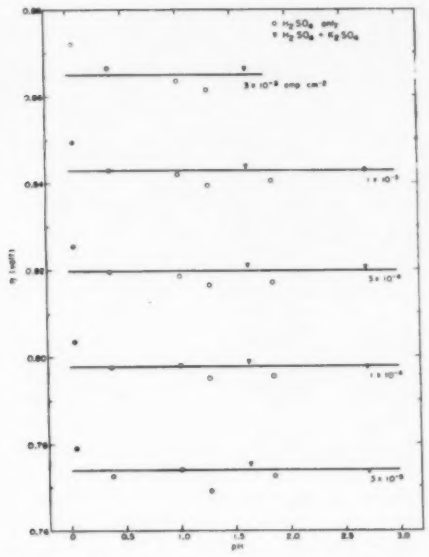

Fig. 1. Variation of oxygen overpotential with pH at constant apparent c.d., gold anodes in sulfuric acid solutions at 25.0°C.

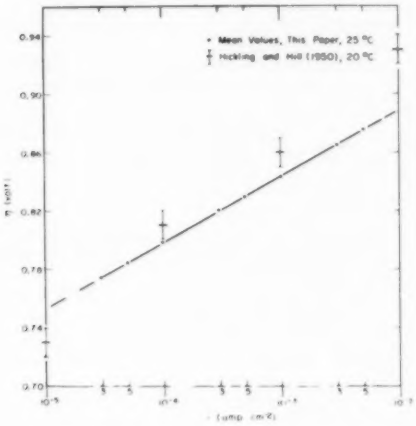

Fig. 2. Oxygen overpotential at gold anodes in sulfuric acid solutions, plotted vs. apparent c.d.

tion of two adsorbed hydroxyl radicals, corresponds to the Tafel slope listed ($RT/2\mathbf{F}$) only when coverage of the electrode surface with OH is very small. If the surface coverage is relatively high, the slope may be greater; this has been shown for an analogous case, the combination mechanism of hydrogen evolution (30). Thus the observed slope of 3/4 $RT/\mathbf{F}$ may correspond to one of the rate-determining steps listed in Table III when adsorption effects are taken into consideration. It may be concluded that the present data for gold are not in strict accord with any one of the mechanisms listed by Bockris (4). Further experimental data are needed to settle the mechanism unequivocally.

Oxygen overpotential at platinum in sulfuric acid solutions has been investigated by Bockris and Huq (16) under conditions of extreme purification (without, however, insuring uniform current distribution over the anode). The mean Tafel slope, measured in H_2SO_4 solutions with and without excess Na_2SO_4, was $b/2.303 = 3RT/2\mathbf{F}$ (± approximately 10%). This is double the value reported here for gold. Not one of the proposed mechanisms predict this slope (4), and the authors assumed that it was sufficiently close to $2RT/\mathbf{F}$ to indicate a discharge mechanism. With the additional assumption of $\beta = 0.5$, measurements of stoichiometric number plus pH and neutral salt effects led to the conclusion that discharge of water molecules is the rate-determining step on platinum.

The value $3RT/2\mathbf{F}$ observed by Bockris and Huq is the same as that previously found for platinum in 1933 by Hoar (17). A slope of less than half this value has been found recently for dilute solutions by Kheifets and Rivlin (29). Several earlier papers (see Table IV), however, reported the value $2RT/\mathbf{F}$, in agreement with the discharge mechanism.

The discharge mechanism is generally assumed also for lead anodes (covered with β-PbO_2) in sulfuric acid solutions on the basis of a slope of $2RT/\mathbf{F}$, although the other confirming parameters have not been measured for this metal. It is interesting that an α-PbO_2 electrode (over platinum) behaved quite differently, giving the slope (3/4) $RT/\mathbf{F}$ which was found here for gold.[3]

Reliable data for oxygen evolution on iron are exiguous. At pH 4, values of both b and i_o found by Wade and Hackerman (18) are remarkably close to those found here for gold. At a slightly lower pH (2.5), however, an appreciable decrease in b and in i_o (the latter by a factor of 10^6) was reported; this strong pH dependence merits confirmation.

In alkaline solutions, oxygen overpotential measurements to date have been discrepant (5). It may be concluded that little basis exists for selecting any one of the currently proposed mechanisms of anodic oxygen evolution as having general applicability for sulfuric acid solutions. There is a pronounced paucity of reliable experimental para-

[3] Revised data of Rüetschi, *et al.* (31) show a significantly higher slope for α-PbO_2 in 4.4M H_2SO_4 at 30°C, namely, 1.2 $RT/\mathbf{F}$.

Table III. Tafel slopes for mechanisms of anodic oxygen evolution in acid solutions, in which overpotential is independent of pH or neutral salt additions

		Mechanism	Rate-determining step	b/2.303
I	1a.	$H_2O \rightarrow OH + H^+ + e$		
	1b.	$2\,OH \rightarrow O + H_2O$	1b	$RT/2\mathbf{F}$
	1c.	$2\,O \rightarrow O_2$	1c	$RT/4\mathbf{F}$
II	2a.	$H_2O \rightarrow OH + H^+ + e$		
	2b.	$2\,OH \rightarrow H_2O_2$	2b	$RT/2\mathbf{F}$
	2c.	$H_2O_2 + OH \rightarrow HO_2 + H_2O$	2c	$RT/3\mathbf{F}$
	2d.	$HO_2 + OH \rightarrow O_2 + H_2O$	2d	$RT/4\mathbf{F}$
III	3a.	$H_2O \rightarrow OH + H^+ + e$		
	3b.	$2\,OH \rightarrow O + H_2O$	3b	$RT/2\mathbf{F}$
	3c.	$O + OH \rightarrow HO_2$	3c	$RT/3\mathbf{F}$
	3d.	$HO_2 + OH \rightarrow O_2 + H_2O$	3d	$RT/4\mathbf{F}$
		Experimental, Au/H_2SO_4 solutions (this investigation)		$3\,RT/4\mathbf{F}$

Table IV. Tafel slopes for the oxygen-evolution reaction on various anodes in H_2SO_4 solutions

Anode metal; Oxide surface		H_2SO_4 molarity	t, °C	Apparent c.d. range, amp cm^{-2}	$b/2.303$ observed	qi_o amp cm^{-2}	Ref.
Au; $Au_2O_3 \cdot 3H_2O$ (1, 24)		0.01 to 1	25	3×10^{-5} to 10^{-2}	$3RT/4F$*	$(2 \text{ to } 6) \times 10^{-8}$	This paper
Pt;	(a)	0.0005 to 0.05	25	10^{-7} to 10^{-4}	$3RT/2F$**	$(1 \text{ to } 3) \times 10^{-10}$	(16)
PtO, PtO_2φ (25, 26)	(b)	0.05	25	10^{-7} to 10^{-5}	$3RT/2F$	3×10^{-11}	(17)
	(c)	0.05	10 to 30	2×10^{-4} to 5×10^{-3}	$2RT/F$	—	(20)
	(d)	0.04 to 0.5	21.6 (±1)	5×10^{-3} to 10^{-1}	$2RT/3F$***	—	(29)
	(e)	0.1	0 to 80	10^{-7} to 10^{-2}	$2RT/F$	2×10^{-9} (at 35°)	(19)
	(f)	0.5	20	10^{-5} to 1	$2RT/F$	10^{-9}	(22)
	(g)	1	25	5×10^{-4} to 5×10^{-2}	$2RT/F$	—	(21)
Pb;	(a)	1	25	5×10^{-4} to 5×10^{-2}	$2RT/F$	—†	(21)
PbO_2	(b)	3.8	30	not reported	$2RT/F$	10^{-10}	(23)
(Pt) β-PbO_2	(c)	4.4	31.8	7×10^{-5} to 2×10^{-3}	$2RT/F$	6×10^{-10}	(28)
(Pt) α-PbO_2	(d)	4.4	31.8	10^{-4} to 2×10^{-3}	$3RT/4F$	2×10^{-10}	(28)
Feφφ	(a)	pH 4.0	5	5×10^{-7} to 10^{-4}	$3RT/4F$	2×10^{-21}††	(18)
	(b)	pH 2.5	5	3×10^{-6} to 10^{-4}	$RT/2F$	2×10^{-27}††	(18)

* b and η unchanged by addition of excess K_2SO_4.
** b unaffected but η changed by addition of excess Na_2SO_4.
*** b increased rapidly with concentration above 0.5M.
φ Probably hydrated (27).
φφ No surface film with properties approaching that of a known bulk oxide.
† qi_o increased continuously with time.
†† $q = 1$; solution contained 0.1M Na_2SO_4.

meters, which are needed to validate a proposed mechanism. Therefore future studies of the oxygen-evolution reaction should stress the accumulation of accurate overpotential measurements.

Manuscript received May 22, 1959. This paper was prepared for delivery before the Philadelphia Meeting, May 3-7, 1959.

Any discussion of this paper will appear in a Discussion Section to be published in the June 1960 JOURNAL.

REFERENCES

1. S. Barnartt, *This Journal*, **106**, 722 (1959).
2. J. Tafel, *Z. physik. Chem.*, **50**, 641 (1905).
3. R. Parsons, *Trans. Faraday Soc.*, **47**, 1332 (1951).
4. J. O'M. Bockris, *J. Chem. Phys.*, **24**, 817 (1956).
5. J. O'M. Bockris, Editor, "Modern Aspects of Electrochemistry," Butterworths Publications Ltd., London (1954).
6. H. S. Harned and B. B. Owen, "The Physical Chemistry of Electrolytic Solutions," 2nd ed., p. 86, Reinhold Publishing Corp., New York (1950).
7. C. V. King, *This Journal*, **102**, 193 (1955).
8. W. J. Hamer, *J. Am. Chem. Soc.*, **57**, 662 (1935).
9. E. A. Hollingshead and A. R. Gordon, *J. Chem. Phys.*, **8**, 423 (1940).
10. R. G. Bates, "Electrometric pH Determinations," p. 47, John Wiley & Sons, Inc., New York (1954).
11. A. Hickling and S. Hill, *Trans. Faraday Soc.*, **46**, 550 (1950).
12. G. Armstrong, F. R. Himsworth, and J. A. V. Butler, *Proc. Roy. Soc.*, **143A**, 89 (1933).
13. G. Deborin and B. Erschler, *Acta Physicochim. URSS*, **13**, 347 (1940).
14. A. Hickling, *Trans. Faraday Soc.*, **42**, 518 (1946).
15. S. E. S. El Wakkad and A. M. S. El Din, *J. Chem. Soc.*, **1954**, 3098.
16. J. O'M. Bockris and A. K. M. S. Huq, *Proc. Roy. Soc.*, **A237**, 227 (1956).
17. T. P. Hoar, *ibid.*, **142A**, 628 (1933).
18. W. H. Wade and N. Hackerman, *Trans. Faraday Soc.*, **53**, 1636 (1957).
19. F. P. Bowden, *Proc. Roy. Soc.*, **126A**, 107 (1929).
20. W. Roiter and R. Jampolskaja, *Acta Physicochim. URSS*, **7**, 247 (1937).
21. P. Jones, R. Lind, and W. F. K. Wynne-Jones, *Trans. Faraday Soc.*, **50**, 972 (1954).
22. A. Hickling and S. Hill, *ibid.*, **46**, 550 (1950).
23. P. Rüetschi and B. D. Cahan, *This Journal*, **104**, 406 (1957).
24. F. Jirsa and O. Buryànek, *Z. Elektrochem.*, **29**, 126 (1923).
25. F. C. Anson and J. J. Lingane, *J. Am. Chem. Soc.*, **79**, 4901 (1957).
26. S. E. S. El Wakkad and S. H. Emara, *J. Chem. Soc.*, **1952**, 461.
27. S. Altmann and R. H. Busch, *Trans. Faraday Soc.*, **45**, 720 (1949).
28. P. Rüetschi and B. D. Cahan, *This Journal*, **105**, 369 (1958).
29. V. L. Kheifets and I. Ya. Rivlin, *Zhur. Priklad. Khim.*, **28**, 1291 (1955).
30. R. Parsons, *Trans. Faraday Soc.*, **54**, 1053 (1958).
31. P. Rüetschi, R. T. Angstadt and B. D. Cahan, *This Journal*, **106**, 547 (1959).

Technical Note

The Formation of Carbides at the Interface of Liquid Germanium and Graphite

A. Epstein[1] and I. G. Geib

Department of Physics, Purdue University, Lafayette, Indiana

In the course of an investigation into the properties of liquid germanium, it was found that Ge solidified in contact with graphite becomes joined to it if a metal soluble in liquid Ge is added. When pure graphite and pure Ge are used, a good mechanical joint is not obtained.

Spectroscopically pure Ge (10-15 g) was placed in a porcelain crucible and heated to about 1000°C at a pressure of about 10^{-4} mm Hg. A hollow spectroscopically pure graphite cylinder of 22 mm internal diameter and about 25 mm height and an inner, concentric cylindrical graphite probe of diameter 3.2 mm were lowered into the molten Ge and were maintained at the stated temperature for periods from 8 to 12 hr. When the entire apparatus was brought to room temperature, the graphite cylinder could be lifted out of the Ge ingot without difficulty. The procedure was repeated with currents of 5-10 amp maintained while the Ge was molten, but the presence of the radial electric field had no effect on the ease of separation of the Ge and graphite.

Either a tungsten rod or a tantalum rod of diameter 0.76 mm (0.030 in.) was placed in the cylindrical arrangement on one of the radii extending from the central graphite probe with its length parallel to the cylinder axis. The arrangement was lowered into the liquid Ge and maintained at about 1000°C for about 8 hr with and without an electric field. On cooling to room temperature, the graphite cylinder and rod could not be separated from the Ge. To examine the area of contact, it was necessary to fracture the ingot and cylinder. The material adhering tightly to the inner wall of the cylinder over the area of contact was examined by x-ray diffraction by obtaining powder patterns of specimens scraped from the inner wall. Ge was removed from the contact by etching with HF, HNO_3, and $Cu(NO_3)_2$ to disclose a layer on the area of contact. Powder patterns were obtained of material from these layers. The Ge-layer-C contact was checked for rectification with area contacts.

With the tungsten rod, the etching revealed a bluish-black layer on the area of contact. A powder pattern of material from this layer showed, in addition to graphite lines, lines which belong to a hexagonal structure, $a = 2.905$Å, $c = 2.839$Å. Westgren and Phragmen (1) found that WC is hexagonal with $a = 2.907$Å, $c = 2.836$Å (calculated from values in kX). Subtraction of these lines and the Ge and graphite lines from the boundary region pattern obtained before etching left 8 lines, 6 of which belong to a hexagonal structure, $a = 3.00$Å, $c = 4.73$Å. Westgren and Phragmen found that W_2C is hexagonal with $a = 2.992$Å, $c = 4.722$Å. This evidence indicates that a layer containing WC and W_2C is formed at the germanium-graphite interface. That the W_2C and not the WC is dissolved by the etchant agrees with a table of solubilities given by Brewer, *et al.* (2).

With the Ta rod, the layer exposed by etching away the Ge has a reddish-brown color. The powder pattern of the reddish-brown material contains a strong pattern, which agrees with that calculated for a NaCl type structure, $a_o = 4.456$Å, in addition to graphite and weak Ge and unknown lines. TaC is cubic (3), $a_o = 4.454$Å.

The Ge-tungsten carbide-C contact gave rectification ratios of better than 200 to 1. The Ge-TaC-C contact gave no measurable rectification. The formation of the carbides must result from the metal dissolving in the Ge, diffusing through the liquid, and reacting with the carbon on coming into contact with it. Qualitative observation of the thickness of the carbide layer indicated that the diffusion or reaction occurred much faster in the presence of an electric field, suggesting that this procedure might be useful for the purification of Ge.

Manuscript received June 15, 1959. This work was supported by a Signal Corps contract.

Any discussion of this paper will appear in a Discussion Section to be published in the June 1960 JOURNAL.

REFERENCES

1. A. Westgren and G. Phragmen, *Zs. f. Anorg. Chemie*, **156**, 27 (1926).
2. L. Brewer, et al., Thermodynamic and Physical Properties of Carbides, in L. L. Quill, Vol. IV-19B of Nuclear Energy Series, p. 40, McGraw-Hill Book Company, Inc., New York (1950).
3. R. W. G. Wyckoff, "Crystal Structures," Vol. I, Interscience Publishers, Inc., New York (1951).

[1] Present address: Monsanto Chemical Company, Dayton, Ohio.

Monographs of The Electrochemical Society

ECS Series

The following are books developed and sponsored by The Electrochemical Society and published by John Wiley & Sons, Inc., 440 Fourth Ave. New York 16, N. Y. Members of The Electrochemical Society can receive a 33 1/3% discount by ordering volumes from Society Headquarters, 1860 Broadway, New York 23, N. Y. Book and invoice will be mailed by John Wiley & Sons. Nonmembers (including subscribers) should order direct from Wiley.

Corrosion Handbook. Edited by Herbert H. Uhlig. Published 1948, 1188 pages, **$16.00**

Modern Electroplating. Edited by Allen G. Gray. Published 1953, 563 pages, **$8.50**

Abstracts of the Literature on Semiconducting and Luminescent Materials and Their Applications. Compiled by Battelle Memorial Institute.

Vol. I, 1953 Issue—published 1955, 169 pages, **$5.00** (soft cover)

Vol. II, 1954 Issue—published 1955, 200 pages, **$5.00** (soft cover)

Vol. III, 1955 Issue—Edited by E. Paskell; published 1957, 322 pages, **$10.00** (hard cover)

Vol. IV, 1956 Issue—Edited by E. Paskell; published 1959, 456 pages, **$12.00** (hard cover)

Electrochemistry in Biology and Medicine. Edited by Theodore Shedlovsky. Published 1955, 369 pages, **$11.50**

Vapor Plating (The Formation of Metallic and Refractory Coatings by Vapor Deposition), by C. F. Powell, I. E. Campbell, and B. W. Gonser. Published 1955, 158 pages, **$5.50**

High-Temperature Technology (Materials, Methods, and Measurements). Edited by I. E. Campbell. Published 1956, 526 pages, **$15.00**

Stress Corrosion Cracking and Embrittlement. Edited by W. D. Robertson. Published 1956, 202 pages, **$7.50**

Arcs in Inert Atmospheres and Vacuum. Edited by W. E. Kuhn. Published 1956, 188 pages, **$7.50**
(Papers Presented at the Symposium on Arcs in Inert Atmospheres and Vacuum of the Electrothermics and Metallurgy Division of The Electrochemical Society, April 30 and May 1, 1956, San Francisco, Calif.)

Technology of Columbium (Niobium). Edited by B. W. Gonser and E. M. Sherwood. Published 1958, 120 pages, **$7.00**
(Papers Presented at the Symposium on Columbium—Niobium of the Electrothermics and Metallurgy Division of The Electrochemical Society, May 15 and 16, 1958, Washington, D. C.)

The Structure of Electrolytic Solutions. Edited by Walter J. Hamer. Published 1959, 441 pages, **$18.50**
(Based on a Symposium held in Washington, D. C., in May 1957, sponsored by The Electrochemical Society, New York, and The National Science Foundation, Washington, D. C.)

Vacuum Metallurgy

Vacuum Metallurgy, third printing, 1958. Edited by J. M. Blocher, Jr.; 216 pages; **$5.00,** less a 20% discount to ECS members only. Available from Electrochemical Society Headquarters, 1860 Broadway, New York 23, N. Y.

(Papers Presented at the Vacuum Metallurgy Symposium of the Electrothermics and Metallurgy Division of The Electrochemical Society held in Boston, Mass., October 6 and 7, 1954)

Current Affairs

Science Film Program Under Way at Bell Telephone Laboratories

Six new audio-visual aids to science education have been produced by Bell Telephone Laboratories, and they are now being made available without charge for use in college science and engineering courses. They were prepared by Bell Labs. scientists and engineers, recognized experts in their fields, as their contribution to the furthering of science education.

The films are designed either to fit within the content of a specific college course, or to provide a broad view of a particular technological field that cuts across several diffrent college courses. The following titles have been released.

1. Crystals—An Introduction.—Motion picture: 16 mm; color; sound; 25 min. This classroom film is designed primarily to provide an introduction to crystallography for students of electrical engineering. It also is appropriate for some courses in physics, chemistry, and metallurgy. The film introduces the subject of crystals by demonstrating the orderly arrangement of atoms in the crystalline state and the relation of this arrangement to the physical properties of the substances. It was prepared in close cooperation with Dr. Elizabeth A. Wood, a past president of the American Crystallographic Association.

2. Brattain on Semiconductor Physics.—Motion picture: 16 mm; black and white; sound; 30 min. Walter H. Brattain, Nobel Laureate in Physics, gives an introductory college-level lecture on the physics of semiconductors. He demonstrates thermal emf, photo emf, and rectification; and introduces a simple mathematical model which describes the observed properties of semiconductors. The history and impact of semiconductor phenomena, and new semiconductor phenomena are also briefly treated. Dr. Brattain shared the Nobel Prize in 1956 for his co-invention of the transistor.

3. Submarine Cable System Development.—Motion picture: 16 mm; sound; color; 18 min. An informational film describing the work of mechanical engineers in designing and developing underwater communication systems. The film was prepared under the technical supervision of Dr. N. H. Upthegrove.

4. Zone Melting.—Filmstrip: color; 133 frames; narration on two 33 1/3 rpm records with universal groove; 45 min. Describes the new method of ultrapurifying solids and controlling the distribution of impurities in solids. Prepared by William G. Pfann, the inventor of Zone Melting. Four parts, which can be shown separately or consecutively: I. Introduction to Zone Melting, Purification by Crystallization; II. Zone Refining Theory; III. Zone Refining Techniques, Floating Zone Refining, Continuous Zone Refining; IV. Zone Leveling, Temperature Gradient Zone Melting, Zone Remelting, Solar Zone Refining, Zone Melting Applications.

5. The Formation of Ferromagnetic Domains.—Filmstrip: color; 132 frames; narration on two 33 1/3 rpm records with universal groove; 45 min. Discusses the physical principles of domain formation with particular emphasis on the energies involved in the process. Techniques used in observing domains are described and domain patterns which conform to theory are shown. The filmstrip was prepared under the supervision of H. J. Williams, who has made outstanding contributions to the field of ferromagnetic domains over many years.

6. The Science of Sound.—Record album: two 33 1/3 rpm microgroove recordings; 90 min. Demonstrates 19 different acoustic phenomena with narration written by Bell Labs. scientists.

The three motion pictures, two filmstrips, and record album are part of a comprehensive Aid to Science Education Program which Bell Labs. initiated several years ago. They were produced following a survey of engineering colleges, conducted by Bell Labs., to determine the need for advanced-level science and engineering films. The response

Brief Communications

The JOURNAL accepts short technical reports having unusual importance or timely interest, where speed of publication is a consideration. The communication may summarize results of important research justifying announcement before such time as a more detailed manuscript can be published. Consideration also will be given to reports of significant unfinished research which the author cannot pursue further, but the results of which are of potential use to others. Comments on papers already published in the JOURNAL should be reserved for the Discussion Section published biannually.

Submit communications in triplicate, typewritten double-spaced, to the Editor, Journal of The Electrochemical Society, 1860 Broadway, New York 23, N. Y.

of educators was enthusiastic. With their advice, a Science Film Production Unit was formed at Bell Labs. for the primary purpose of making films that college instructors could use to complement their regular lectures in science and engineering.

In all cases, a Bell Labs. scientist who is a well-known authority in his scientific area acts as consultant during the production of the films. The films are also screened by other scientific experts to double-check technical accuracy before release. For each production, educators in appropriate fields are consulted to ensure proper educational values.

The audio-visual aids contain no advertising material, and are loaned without charge to professional groups as well as to educational institutions through local Bell Telephone Co. offices.

Division News

E & M Round Table on Methods of Reducing Iron Ores, Spring 1960

The Electrothermics and Metallurgy Division of the Society proposes to hold a round-table conference on the timely subject "Methods of Reducing Iron Ores" at the Spring 1960 Meeting of the Society to be held in Chicago, May 1-5. The purpose of the conference is to compare the various nonelectric methods of reducing typical iron ores with one another, and with electric smelting methods.

The conference will consist of:

1. A number of formal papers, each one by a specialist in one particular type of reduction
2. A general discussion of the subject.

R. R. Rogers, Mines Branch, Dept. of Mines & Technical Surveys, 552 Booth St., Ottawa, Ont., Canada, would be glad to receive suggestions as to the types of iron ore to be discussed, the types of reduction which should be covered in the formal papers, and specialists who would be qualified to discuss these particular types of reduction.

E & M Symposium on High-Purity Vanadium, Spring 1960

Papers on the subject "High-Purity Vanadium—Its Preparation, Properties, and Alloys" are being solicited by the Electrothermics and Metallurgy Division of the Society for a symposium, under the Co-Chairmanship of D. J. Hansen and M. Schussler of Union Carbide Metals Co., at the Spring Meeting of the Society in Chicago, May 1-5, 1960.

Topics on which contributions will be welcomed include:

- Resources of Vanadium Minerals—Domestic and Foreign
- Mining and Beneficiation of Vanadium Minerals
- Techniques for Reduction to High-Purity Metal
- Consolidation and Fabrication Techniques
- Properties of Alloys Based on High-Purity Vanadium
- Applications for Ductile Vanadium and Its Alloys.

Availability of ductile vanadium has stimulated exploratory work on its properties and potential uses in many laboratories. If enough of this information is presented at the symposium to warrant separate publication, the Division will sponsor preparation of a booklet containing the papers and discussion.

Titles, authors' names, and abstracts in triplicate (*not exceeding 75 words*) must be received at Society Headquarters, 1860 Broadway, New York 23, N. Y., *by January 4, 1960*. Abstracts should bear the notation "For Vanadium Symposium, Spring 1960," and the name of the author who will present the paper should be underlined. Complete manuscripts, ready for publication in all details, must be given to the Symposium Chairman immediately following presentation.

E & M Symposium on Rhenium, Spring 1960

The Electrothermics and Metallurgy Division is inviting papers on various aspects of rhenium technology to be combined into a symposium for the Spring Meeting in Chicago, May 1-5, 1960. Bruce W. Gonser of Battelle Memorial Institute is Chairman of this symposium.

Although emphasis may be given to the extractive and physical metallurgy of rhenium, a broader coverage is planned. In particular, papers are desired that cover recent investigations on properties, alloys, and development of applications.

Rhenium is relatively expensive, but in recent years excellent sources of supply have been developed which are far in excess of current consumption. Some excellent and unique properties indicate that more rhenium could be used advantageously if it were better known.

Titles, authors' names, and abstracts in triplicate (*not exceeding 75 words*) must be received at Society Headquarters, 1860 Broadway, New York 23, N. Y., *by January 4, 1960*. Abstracts should bear the notation "For Rhenium Symposium, Spring 1960," and the name of the author who will present the paper should be underlined. Complete manuscripts, ready for publication in all details, must be given to the Symposium Chairman immediately following presentation.

Personals

Hugh S. Cooper, founder of the Beryllium Corp., also the Kemet Co. (Division of Union Carbide Corp.), and Cooper Metallurgical Associates, has resigned from the latter corporation to pursue independent research in the fields of chemistry, metallurgy, and, in particular, fused salt electrolysis.

W. Stanley Herbert has been appointed associate director of research at the Carl F. Norberg Research Center of the Electric Storage Battery Co. at Yardley, Pa. Dr. Herbert formerly was technical director of the Ray-O-Vac Co. which became a division of the Electric Storage Battery Co. in November 1957. He is a member of the Executive Committee of the Battery Division of The Electrochemical Society, and is well known for his development of small alkaline "crown" cells.

Sheldon Matlow, Eugene L. Ralph, and Nathan Yagol, all of Hoffman Electronics Corp., have transferred from Evanston, Ill., to the El Monte, Calif., facility of the corporation, Semiconductor Division. Dr. Matlow was promoted from unit supervisor to manager of techniques research section, and Mr. Ralph was promoted from senior engineer to unit supervisor of solar methods engineering. Mr. Yagol continues as senior engineer.

Notice to Members
Re Voting Ballot

By now you have received your official voting ballot from Society Headquarters. If you have not already done so, please return the ballot *by December 15* so that your vote can be included in the final election count.

News Items

Conference of Electric Furnace Committee, Metallurgical Society

A busy program of ten technical meetings has been prepared for the 17th Annual Conference of the Electric Furnace Committee, Iron and Steel Division of The Metallurgical Society. The sessions will be held December 2-4, 1959, in the Cleveland Hotel, Cleveland, Ohio.

The Metallurgical Society is a constituent organization of the American Institute of Mining, Metallurgical, and Petroleum Engineers.

The opening technical session, the morning of December 2, will have "Consumable Electrode Melting" as its main theme. There will be three meetings that afternoon: "Ingot Technical Session-Refractories"; "Castings Technical Session-Quality Control of Electric Furnace Melting"; "Special Arc Technical Session on Raw Materials and Special Alloys Beneficiation of Low-Grade Domestic Chrome Ores."

On December 3, the morning program will be an Ingot Technical Session on "Construction and Tool Steels"; a Castings Technical Session on "Degassing of Steels for Foundry Melting Practice"; Special Arc Technical Session on "Manufacture of Calcium Carbide and Refractories."

The afternoon themes on December 3 will include an Ingot Technical Session on "Stainless Steels"; a Castings Technical Session on "Pouring, Refractories, Gadgets and Tricks"; a Special Arc Technical Session on "Electrode Penetration and Automatic Furnace Regulation."

Foote Mineral to Expand Electrolytic Manganese Facilities

Foote Mineral Co. has announced plans to expand its electrolytic manganese facilities by January 1, 1960 and said it has awarded contracts for new construction at the larger of its two Knoxville, Tenn., plants. The expansion, which will increase the plant's capacity by 30%, is the first step of a major program necessitated by the growing demand for electrolytic manganese in stainless and mild steels.

The new construction will incorporate process improvements which have resulted from an intensive research study begun shortly after Foote and Electromanganese merged in 1956. The increase in production levels is expected to come

(Continued on page 292C)

ECS Membership Statistics

The following three tables give breakdown of membership as of Oct. 1, 1959. The Secretary's Office feels that a regular accounting of membership will be very stimulating to membership committee activities. In Table I it should be noted that the totals appearing in the right-hand column are *not* the sums of the figures in that line since members belong to more than one Division and, also, because Sustaining Members are not assigned to Divisions. But the totals listed are the total membership in each Section. In Table I, Sustaining Members have been credited to the various Sections.

Table I. *ECS Membership by Sections and Divisions*

Section	Division: Battery	Corrosion	Electric Insulation	Electrodeposition	Electronics	Electro-Organic	Electrothermics & Met.	Industrial Electrolytic	Theoretical Electrochem.	No Division	Total as of 1/1/59	Total as of 10/1/59	Net Change
Boston	18	28	6	37	71	8	27	14	29	6	151	162	+11
Chicago	15	31	4	41	27	9	14	10	26	15	132	132	0
Cleveland	49	30	2	53	40	8	30	33	36	13	198	194	− 4
Columbus, Ohio	2	14	0	14	9	2	26	2	8	4	49	56	+ 7
Detroit	12	19	4	52	10	6	8	6	22	18	91	94	+ 3
India	8	7	2	19	8	6	8	10	15	3	35	35	0
Indianapolis	13	9	6	12	13	5	8	3	7	2	39	46	+ 7
Midland	9	15	0	5	2	3	7	14	11	1	43	42	− 1
Mohawk-Hudson	4	15	14	7	15	1	9	1	19	5	54	66	+12
New York	91	111	31	146	161	35	74	70	106	41	517	558	+41
Niagara Falls	13	25	1	25	11	6	77	67	29	18	183	176	− 7
Ontario-Quebec	9	24	1	15	8	2	39	30	12	14	82	92	+10
Pacific Northwest	6	9	0	9	3	1	10	11	10	10	44	43	− 1
Philadelphia	30	28	4	36	77	9	26	20	47	31	185	203	+18
Pittsburgh	2	46	4	26	29	7	42	17	35	10	133	132	− 1
San Francisco	9	13	1	19	22	4	16	20	20	4	71	75	+ 4
S. Calif.-Nevada	19	26	3	33	47	5	25	17	34	10	105	132	+27
Washington-Baltimore	37	39	7	37	24	3	11	10	33	6	129	135	+ 6
U.S. Non-Section	68	91	14	91	95	44	65	82	124	30	408	442	+34
Foreign Non-Section	47	65	10	67	39	33	42	61	79	89	262	281	+19
Total as of Jan. 1, 1959	441	638	103	723	621	190	549	486	656	329	2911		
Total as of Oct. 1, 1959	461	645	114	744	711	197	564	498	702	330		3096	
Net Change	+20	+7	+11	+21	+90	+7	+15	+12	+46	+1			

Table II. *ECS Membership by Grade*

	Total as of 1/1/59	Total as of 10/1/59	Net Change
Active	2538	2681	+143
Faraday (Active)	30	32	+ 2
Deutsche Bunsen Gesellschaft (Active)	15	17	+ 2
Delinquent	70	94	+ 24
Active Representative Patron Members	10	10	0
Active Representative Sustaining Members	99	110	+ 11
Total Active Members	2762	2944	+182
Life	17	17	0
Emeritus	49	49	0
Associate	31	27	− 4
Student	46	52	+ 6
Honorary	6	7	+ 1
Total	2911	3096	+185

The figures pertaining to Patron and Sustaining Member Representatives, and Faraday and Deutsche Bunsen Gesellschaft members subscribing to the JOURNAL, have been added to reflect reclassifications and changes in membership status.

Table III. *ECS Patron and Sustaining Membership*

	Total as of 1/1/59	Total as of 10/1/59	Net Change
Patron Member Companies	5	5	0
Sustaining Member Companies	148	158	+ 10

Looking Back at the Philadelphia Meeting

Row 1—President Sherlock Swann presenting R. M. Burns' Certificate of Honorary Membership to H. H. Uhlig who received it in Dr. Burns' absence; President Swann presenting Certificates of Honorary Membership to G. W. Heise and to F. C. Mathers. **Row 2**—Mr. and Mrs. E. G. Enck (General Chairman Philadelphia Meeting and Chairman Ladies' Program, respectively) and Ruth G. Sterns; Lottie Fink and H. S. Lukens; F. L. LaQue (Society Vice-President-Elect) and A. J. deBethune. **Row 3**—A. C. Haskell and Dr. and Mrs. E. M. Sherwood; I. E. Campbell (Secretary-Elect); President Swann presenting Certificate of Appreciation to H. B. Linford. **Row 4**—L. E. Vaaler and H. R. Cherry; J. G. Miller (Philadelphia Committee-Entertainment) and M. B. Diggin; C. W. Clapper. **Row 5**—A. E. Middleton, R. A. Schaefer, and Norman Hackerman; H. Tropper, T. J. Lewis, T. D. Callinan, R. Guizonnier, M. J. Morant, K. A. Macfadyen, and L. J. Frisco; J. G. Miller and J. H. Westbrook.

Row 1—Ralph Roberts, J. E. B. Randles, and H. C. Mandell, Jr. (Philadelphia Committee-Publicity); Dr. and Mrs. T. D. Callinan; Abner Brenner. **Row 2**—H. F. Church, T. Salomon, E. H. Reynolds, and H. Basseches; Dr. and Mrs. G. M. Butler, dancing; Dr. and Mrs. R. M. Hunter and Dr. and Mrs. H. J. Read. **Row 3**—C. W. Faust with daughter and Mrs. Faust, and Dr. and Mrs. H. R. Neumark; **standing**—E. B. Yeager, Ralph Roberts, B. E. Conway, K. J. Vetter, Manfred Breiter, and R. A. Marcus, **seated**—J. E. B. Randles, J. Llopis, Paul Delahay, Juro Horiuto, C. W. Tobias, Roger Parsons, Sigmund Schuldiner, and L. Gierst; Dr. and Mrs. W. M. McNabb, dancing.

The sign in the foreground reads "Gross Weight Limit 5 Tons, Maximum Speed 15 Miles Per Hour."

June 1960 Discussion Section

A Discussion Section, covering papers published in the July—December 1959 JOURNALS, is scheduled for publication in the June 1960 issue. Any discussion which did not reach the Editor in time for inclusion in the December 1959 Discussion Section will be included in the June 1960 issue.

Those who plan to contribute remarks for this Discussion Section should submit their comments or questions in triplicate to the Managing Editor of the JOURNAL, 1860 Broadway, New York 23, N. Y., *not later than March 1, 1960.* All discussion will be forwarded to the author(s) for reply before being printed in the JOURNAL.

(Continued from page 289C)
both from new deposition cell capacity and from higher efficiencies throughout the plant.

Symposium on Molecular Fluorescence and Phosphorescence

The Subcommittee on Fluorescence Spectroscopy sponsored by A.S.T.M. Committee E-13 is planning to hold a one-day symposium on molecular fluorescence and phosphorescence during the next Pittsburgh Conference on Analytical Chemistry and Applied Spectroscopy, which will be held during the first week of March 1960.

Papers, 10 to 20 minutes in length, will be on the theory or application of fluorescence or phosphorescence and on instrumentation in this field.

Program Chairman is Dr. Joseph W. Goldzieher, Southwest Foundation for Research and Education, P. O. Box 2296, San Antonio, Texas.

Burgess Enters Nickel Cadmium Field

The Burgess Battery Co., Division of Servel, Inc., recently announced that it will manufacture and market sealed nickel-cadmium batteries.

Battery cells will be available in six sizes from 0.4 inch to 2 inches in diameter as well as penlight (AA) and standard flashlight (D) size. For higher voltages, multicell batteries are made by connecting cells in series by means of a silver wax which is said to form a rugged permanent contact.

Detailed technical data, including statistical charts for estimating service life, recharging circuit diagrams, and discharge characteristics, are available from Dept. CD-500, Burgess Battery Co., Division of Servel, Inc., Freeport, Ill.

Sylvania Expands Manufacturing Operations

Sylvania Electric Products Inc. recently announced plans to expand production of molybdenum, tungsten, and other refractory metals.

At the headquarters of Sylvania's Chemical and Metallurgical Division in Towanda, Pa., a custom-built 16-ton isostatic press has been installed to produce ingots up to 4 feet long and 10 inches in diameter. Production of molybdenum ingots 4 feet long and 4½ inches in diameter has already begun. These ingots weigh approximately 275 pounds. Until recently, commercially available tungsten and molybdenum ingots have weighed less than 100 pounds.

Sylvania also has arranged to purchase a 25,000-square-foot plant at Manchester, N. H., for the manufacture of transistors, it was announced by Dr. William J. Pietenpol, vice-president and general manager of the company's Semiconductor Division.

Within the next few months, new production machinery and testing equipment designed and built at division headquarters at Woburn, Mass., will be installed in the facility. Manufacturing operations are scheduled to begin early in 1960.

The new plant, situated on a 10-acre site, will employ between 800 and 1000 persons.

Journal of ECS Microfilmed

The Electrochemical Society announces that an agreement has been entered into with University Microfilms, Inc., Ann Arbor, Mich., for the microfilming of all volumes of the TRANSACTIONS and JOURNAL of the Society.

This consists of 15 reels and covers Vol. 1-104 (1902-1957), and positive microfilm copies of all these volumes sell for $375.00. When reels are sold separately for any of these volumes, the price is $25.00 each.

Subsequent volumes of the JOURNAL will be on separate reels. Vol. 105 (1958) is now available for $3.10.

One of the most pressing problems faced by libraries is that of providing adequate space for their publications. Microfilm editions are one solution to this problem.

Inquiries concerning purchase should be addressed to University Microfilms, Inc., 313 N. First St., Ann Arbor, Mich.

News from Union Carbide Corporation

Formation of Consumer Products Co. Announced

Union Carbide Corp. has formed a new operating division to expand its consumer products business, it was announced in September.

The new division will be known as Union Carbide Consumer Products Co. Initially, it will market the corporation's Prestone and Eveready brand products, which have been handled by National Carbon Co., division of Union Carbide. These products include batteries, antifreeze, automotive specialty products, and garden chemicals. National Carbon Co. will continue to manufacture and market electrodes, arc lighting carbons, brushes for electric motors, and other carbon and graphite specialties.

It is felt that specialization in these diverse areas heretofore combined in National Carbon Co. can add to the corporation's effectiveness and help in providing better products and services to both industrial and consumer product customers.

Adger S. Johnson, formerly president of National Carbon Co., has been elected a vice-president of Union Carbide Corp. and will supervise the consumer product activities of the corporation. Arthur C. Bryan has been appointed president of the Union Carbide Consumer Products Co., and William H. Feathers president of National Carbon Co.

Construction of Research Institute Building to Commence

Construction will commence on the building to house the Union Carbide Research Institute, a special research activity of Union Carbide Corp., it was announced recently by Morse G. Dial, chairman of the board and chief executive officer. The building will be located at Union Carbide's Westchester County, 280-acre property at Eastview, near Tarrytown, N. Y. It will be completed and ready for occupancy the latter part of 1960. On the same site, a technical service laboratory, which will be used by Union Carbide Chemicals Co., is nearing completion.

Union Carbide Research Institute was formed in 1956 in order to complement and extend the scope of the basic research being carried on in

1960 Bound Volume

Members and subscribers who wish to receive bound copies of Vol. 107 (for 1960) can receive the volume for the low, prepublication price of $6.00 if their orders are received at Society Headquarters, 1860 Broadway, New York 23, N. Y., by *December 1, 1959*. After that date, members will be charged $12.00, and nonmembers, including subscribers, $18.00, subject to prior acceptance.

Bound volumes are *not* offered independently of JOURNAL subscription.

the corporation's research laboratories.

Programs already under way or in the planning stage include such areas of study as solid-state physics, the theory of metal bonds, and the structure of plastics. A substantial program of biochemical research is also included. A specific example of the projects to be undertaken is one which the Institute just recently initiated that will emphasize theoretical and experimental studies on the fundamental physical and chemical principles affecting high-temperature materials.

Union Carbide to Produce High-Purity Tungsten Raw Material

Plans for the expansion of the company's tungsten refining plant in Bishop, Calif., were announced by Union Carbide Nuclear Co., division of Union Carbide Corp. The new unit will produce a high-purity tungsten raw material, ammonium paratungstate, at the mine site.

The unique process represents an extension of the refining stage already in operation at the Bishop facilities. It is the first direct method for preparing ammonium paratungstate of this high purity from scheelite ore sources. The final product contains less than 0.003% each of molybdenum and silicon.

The new plant addition will be capable of producing large commercial quantities of tungsten as high purity ammonium paratungstate in addition to scheelite concentrate (calcium tungstate) manufacture. Scheduled completion of this expansion has been set for December 1959.

Atomic Energy Contract Extended Four Years by Commission

The Atomic Energy Commission has extended until June 30, 1964, a cost-plus-fixed-fee contract with Union Carbide Corp. for operation of four major Commission facilities, S. R. Sapirie, manager of the Commission's Oak Ridge operations, announced recently.

Union Carbide Nuclear Co., division of Union Carbide Corp., operates two large production plants and a research and development laboratory in Oak Ridge. Tenn., and the gaseous diffusion plant at Paducah, Ky. The present contract for operation of these facilities was to expire June 30, 1960, but was extended for four years.

Union Carbide contributed to the research and planning for the original gaseous diffusion plant at Oak Ridge and has operated it since January 1945. Union Carbide assumed operations of the Y-12 plant at Oak Ridge in 1947 and operation of the Oak Ridge National Laboratory in 1948. In 1951, Union Carbide was selected as the operating contractor for the new gaseous diffusion plant at Paducah, Ky.

Book Review

Proceedings of the Ninth Meeting of the International Committee of Electrochemical Thermodynamics and Kinetics—C.I.T.C.E. (Paris, 1957). Published by Butterworths, London, and Butterworth and Co. (Canada) Ltd., Toronto, 1959. 489 pages; $24.00.

This handsome volume presents, after a lapse of two years, the account of the Ninth Meeting of C.I.T.C.E. (Paris, 1957). Fifty-three papers and abstracts, about equally divided between French, German, and English, cover the topics: 1. potential-pH diagrams, 2. fundamentals, 3. experimental methods, 4. batteries, 5. corrosion, 6. kinetics, 7. semiconductors, 8. electroanalytical chemistry, and 9. program of work. Of 97 authors, four represented the U.S.A., five the U.S.S.R., seven the Commonwealth, and the balance Western and Central Europe.

In Part 1, Pourbaix and coworkers continue their valuable collection of potential-pH diagrams with As, Sb, Bi, Tc, Re, Nb(Cb), Ta, Zr, B, Al, Cl; Maronny and Valensi summarize the standard thermodynamic properties of sulfide and polysulfide ion; Bernard reviews the use of polarography in thermodynamics; Vincent's abstract, suggesting that a correlation exists between pH, rH, and ρ (resistivity) of body fluids and the occurrence of major pathological disorders (tuberculosis, cancer, etc.), based on the study of more than 300 French patients, only serves to whet the reader's appetite for more information.

In Part 2, Van Rysselberghe brings C.I.T.C.E.'s formal system of definitions up to date, and suggests *electrode tension* as a synonym for electrode potential (with the Stockholm sign). In Part 3, Fischer summarizes the status of experimental methods; Vincent describes his micro-pH-rH-ρ-cell; and Chauvin, *et al.*, their high temperature cell; Gerischer discusses potentiostats for fast reactions; Fischer, *et al.*, inhibitors and H overpotential; Lewartowicz, polarization measurements; Ibl, *et al.*, and Tomassi, powder electrodes; Breyer, the tensammetric method; Brouillet, *et al.*, very high overpotentials; and Bluet, *et al.*, electrolyte permittivity.

In part 4, Brenet, *et al.*, review major battery problems; Winkler discusses gassing in Ni-Cd batteries; Trädgardh, the potential of Ni electrodes in alkali batteries; Kabanov, the double layer properties of Pb-storage cells. In Part 5, Schwabe reviews the passivity of Ni and Co.

Part 6 presents papers on electrode kinetics by Wynne-Jones; Gerischer (Ag); Rius, *et al.*, (persulfates and chlorites); Chauvin, *et al.*, (Hf and Zr); Frumkin (O^{18} and anodic mechanisms); Gorbunova (crystalline deposits); Kolotyrkin (anion adsorption and H overpotential); and Bonnemay and Lapluye (Pt). Part 7 presents papers on semiconductors by Billig; Busch, *et al.*, (InSb); François (Ge); Holmes (Ge and Si); Llopis, *et al.*, (sulfuration of metal surfaces); Epelboin and Froment (Ge and Si). Part 8 gives addresses by Hoar and Kolthoff to the joint Colloquium on Modern Electrochemical Methods in Analytical Chemistry, and Gauguin's detailed abstract of this Colloquium.

The format and typography are up to the excellent standards of preceding volumes. While most authors use the Stockholm sign for electrode potentials consistently, Bernard's paper unfortunately mixes up indiscriminately data in both the Latimer and Stockholm sign conventions, without any distinction or warning to the reader! Ten papers are available only as abstracts, and one paper only by title. These regrettable omissions seem a necessary consequence of the attempt to put out the proceedings of a large scientific meeting under the covers of one single book within a reasonable lapse of time. This difficulty is being overcome by the appearance this year of the new journal, *Electrochimica Acta*, so that the present volume concludes the series of the Proceedings of C.I.T.C.E. The volume

Notice to Members and Subscribers
(Re Changes of Address)

To insure receipt of each issue of the JOURNAL, please be sure to give us your old address, as well as your new one, when you move. Our records are filed by states and cities, not by individual names. The Post Office does not forward magazines.

does contain a wealth of excellent, well-presented material that should find its place on the shelves of every serious worker in our science. T. P. Hoar's brief presidential addresses provide delightful reading, particularly his closing admonition: "Unless a verbal presentation is acute, brief and clear, it leads to misunderstandings, besides wasting time and energy. May I therefore suggest a revolutionary slogan for future meetings—the ABC of verbal presentation—Acuité, Brièveté et Clarté."

André J. deBéthune

Announcements from Publishers

"The Sequestration of Metals." Edited by Robert Smith. Published by the MacMillan Co., New York City, 1959. vii + 256 pages; $8.50.

This is a general discussion of sequestering agents and uses, aimed at practical chemists who are interested in a tool without any great interest in the theory. The simplest explanation of coordination has been used which is adequate to the understanding of the theory. There are 70 pages of elementary theory, about 50 pages on properties of sequestering agents, and 110 pages of application of which 8 pages are on the use of EDTA in metal finishing. The references are through 1956.

"Organic Sequestering Agents." Edited by Stanley Chaberek and Arthur E. Martell. Published by John Wiley & Sons, Inc., New York City, 1959. xv + 616 pages; $25.00.

The aim of this book is to present a straightforward and up-to-date explanation of the basic principles of chelation as well as a summary of applications. The emphasis, even in the section of application, is on explanation and mechanism. For example, there are 40 pages devoted to experimental methods of determining formulas of metal chelates and 25 pages on methods of determining chelate formation constants. The book is well illustrated with much use of structural formulas. References are through 1957.

"U.S.S.R. Patents and Inventions" (English translation of "Biulleten'izobretenii"). Executive Editor, I.V. Makarov; Editorial Board, V.N. Bakastov, A. I. Dorkin, I. V. Makarov, O. A. Koskvin, and I. I. Rafalkov. Available from Pergamon Press, New York, London, Paris, Los Angeles, or from any reputable subscription agent. Number of pages per annum, 2000. Annual subscription price, $100.00.

The U.S.S.R. Government is permitting for the first time since 1940 the export abroad of copies of its patent specifications and applications. This Russian "Bulletin" is published 24 times a year and gives exhaustive information on some 10,000 patents granted annually. It also includes descriptions of inventions from previous years, the earlier publication of which was prohibited. Pergamon Press, in collaboration with the Pergamon Institute, has decided to publish a monthly cover-to-cover translation of the "Biulleten'izobretenii," to be known as "U.S.S.R. Patents and Inventions."

Subscriptions to specialized sections are accepted, i.e., Chemistry and Chemical Engineering, $40.00; Electrical and Mechanical Engineering, $40.00. Copies of Russian patents can be supplied on request at the price of $1.00 each. Translations of patents can be supplied at $5.00 per patent.

"Russian Patents Gazette." Editors, M. M. Barash and P. L. B. Oxley. Published by Technical Information Co., Chancery Lane, London, W.C. 2, England.

This is a semimonthly publication containing English language abstracts of all new Russian patents and invention certificates arranged under 91 class headings. Issues available are January 1959 onward. The first January issue was published in June 1959. Subsequent issues will be published rapidly to bring the "Gazette" up to date.

Subscription rates are: 1. "Russian Patents Gazette" (Comprehensive), $120.00; 2. General, Mechanical, and Electrical Section only, $80.00; 3. Chemistry and Chemical Engineering Section only, $80.00; airmail, $15.00 extra. Copies of Russian patents are supplied at $1.20 each ($2.00 airmail). Translations of Russian patent specifications are available to subscribers at $6.00 each, higher for exceptionally long specifications.

Correction

Dr. A. N. Frumkin, 1959 Palladium Medalist of the Society, has informed us that he is 63 years of age, not 65 as indicated in the write-up which appeared on page 244C of the September JOURNAL.

Notice to Subscribers

Your subscription to the JOURNAL of The Electrochemical Society will expire on *December 31, 1959*. Avoid missing any issue. Send us your remittance now in the amount of $18.00 for your 1960 subscription. (Subscribers located outside the United States must add $1.00 to the subscription price for postage, and payment must be made by Money Order or New York draft, not local check.) An expiration notice has been mailed to all subscribers.

A bound volume of the 1960 JOURNALS can be obtained at the prepublication price of $6.00 by adding this amount to your remittance. However, no orders will be accepted at this rate after *December 1, 1959*, when the price will be increased to $18.00 subject to prior acceptance. Bound volumes are *not* offered independently of your JOURNAL subscription.

Soviet Science Briefs

The following items are brief reviews of translated articles and abstracts on Soviet Bloc progress in science and technology appearing in "Scientific Information Report" (SIR) and "Information on Soviet Bloc International Geophysical Cooperation" (IGYex), two periodicals published by the Office of Technical Services, U. S. Dept. of Commerce, Washington 25, D. C.

Feasibility of operating fuel cells on gasoline has been demonstrated by Russian researchers. Their experimental solid-electrolyte cells, although short-lived, developed a current of 1.0 to 1.5 amp at a potential of 0.5 to 0.7 v. The cells are said to work best at temperatures from 700° to 750°. The electrolyte was prepared by high-temperature mixing of sodium carbonate, sodium silicate, cerium dioxide, and tungsten trioxide. (SIR-22).

Electrochemical desalting of sea water is reported to cut time and cost of providing ships with fresh

water. Membranes or diaphragms of ion-exchange resins separate brine from water. Principal parts are of "viniplast, polychlorovinyl plastic, and chemically resistant rubber." The apparatus, which is said to have proved its worth on a Russian ship, may be used in trains, industry, and agriculture, according to the periodical "Promyshlenno-Ekonomicheskaya Gazeta." (SIR-20).

New Products

Semiconductor Intermetallic Compounds

Those currently doing research in solid state materials for thermoelectric, infrared, and electronic applications will welcome the report that Ohio Semiconductors, Inc., of Columbus, Ohio, is now producing commercially a wide range of intermetallic semiconductor compounds.

The following materials, some in single crystal form and others in polycrystalline form, can be obtained on immediate or short-term delivery: InSb; InAs; GaAs; GaSb; AlSb; Bi_2Te_3; Bi_2Se_3; PbTe; CdTe; InP; GaP; Ag_2Te; Ag_2Se; Ag_2S; In(P,As); (In,Ga)Sb; (In,Ga)As; Pb; Bi; Te; In; Sb. Other materials are available on request.

For further information, including specifications and performance features of all materials and devices available, write direct to Ohio Semiconductors, Inc., 1035 West Third Ave., Columbus 8, Ohio.

Rechargeable Silver-Zinc Batteries

A new line of silver-zinc secondary (rechargeable) batteries for missiles and spacecraft have extremely high energy-to-weight ratios compared to ordinary batteries. The silver-zinc cells range in size and output from the Type SC-04 miniature cell of 0.5 amp-hr capacity which weighs only 0.05 lb and has an output of up to 10 amp, to the Type SC-450, a single cell with a weight of 9.7 lb and an output of 450 amp-hr. All cells are rated with a terminal voltage of 1.4 v under load.

For further information about the SC line of rechargeable silver-zinc batteries, contact Cook Batteries, a subsidiary of Telecomputing Corp., 3850 Olive St., Denver 7, Colo.

Silver-Zinc Missile Battery

A new automatically activated silver-zinc primary battery, the 20xPA50, has been developed for the missile field by Yardney Electric Corp., manufacturers of Silvercel and Silcad batteries.

This new Yardney Silvercel primary is capable of 31.0 whr/lb and 1.7 whr/cu in. It can be activated and readied to meet specification voltages within 3 sec, and can be discharged at numerous rates—ranging from rates even less than the 50-amp rate (at 37 v for 90 min) to the 350-amp rate (at 28 v for 11 min).

Weighing only 72 lb, it has a volume of 1290 cu in., exclusive of external mountings. Its shelf life, in the dry condition, is approximately 5 yr; in the activated condition, 8 hr.

For further information, contact Yardney Electric Corp., 40-50 Leonard St., New York, N. Y.

Low-Cost UHF Insulating Material Has Outstanding Temperature Stability

"Enrad II," an improved form of irradiated polyolefin developed by Enflo Corp., exhibits mechanical and electrical properties that far surpass most polyolefins such as the well-known polyethylene.

Dielectric strength of Enrad II is on the order of 1000, almost twice that of linear polyethylene. This, and an unusually low dissipation factor of 0.0005, makes the material well suited for ultrahigh-frequency applications. It is currently in use as a microwave strip line material. Other applications include electrical insulators, tube sockets, connectors, wire insulation, and other uses where low losses and long life are essential. In addition, Enrad II's unequaled bond strength makes it particularly useful as a copper-clad laminate for printed circuits.

Enrad II retains excellent form stability to beyond 300°C. It will not melt at any temperature, and it remains hard and tough with little or no cold-flow at low temperatures. Thanks to new methods of irradiating and processing, Enrad II can be molded in both simple and complex shapes with complete uniformity of properties. The material is currently available as a powder or as bars, rods, and sheets for ready machining.

Samples of Enrad II and a report comparing the typical properties of Enrad II with linear polyethylene are available on request from the Enflo Corp., Fellowship Rd. and Route 73, Maple Shade, N. J.

Cormet A, Porous Nickel

A pressed and sintered porous nickel, capable of operating at temperatures to 575°F, is being produced in large and intricate shapes by Corning Glass Works, Corning, N. Y.

Called Cormet A, the material is fabricated by a new Corning process into sheets 12 x 30 in., as well as cylinders 2 ft in length, with 12-in. diameters. Large sizes are made

Manuscripts and Abstracts for Spring 1960 Meeting

Papers are now being solicited for the Spring Meeting of the Society, to be held at the Lasalle Hotel in Chicago, Ill., May 1, 2, 3, 4, and 5, 1960. Technical sessions probably will be scheduled on Electric Insulation (including a Symposium on "Electrolytic Capacitors"), Electronics (including Luminescence and Semiconductors), Electrothermics and Metallurgy (including a symposium on "High-Purity Vanadium" and a round table on "Methods of Reducing Iron Ores"), Industrial Electrolytics, and Theoretical Electrochemistry.

To be considered for this meeting, triplicate copies of abstracts (*not exceeding 75 words in length*) must be received at Society Headquarters, 1860 Broadway, New York 23, N. Y., *not later than January 4, 1960. Please indicate on abstract for which Division's symposium the paper is to be scheduled, and underline the name of the author who will present the paper.* Complete manuscripts should be sent in triplicate to the Managing Editor of the JOURNAL at the same address.

• • •

The Fall 1960 Meeting will be held in Houston, Texas, October 9, 10, 11, 12, and 13, 1960, at the Shamrock Hotel. Sessions will be announced in a later issue.

possible by a new hydrostatic pressing process.

The material can be used as a noncontacting conveyor when processing extrasensitive materials such as camera and x-ray film, gelatinized paper, adhesive materials, plastics, and products that have high surface sensitivity at elevated temperatures.

Products ride on a thin cushion of air forced through the pores of the material.

Cormet A is used by the glass industry as a noncontacting chute for molten glass. Chute marks and wrinkles are eliminated by carrying the molten glass on a cushion of air from the furnace to the mold.

Cormet A can be made in sheet, piping, and elbowed or straight chutes. Unusual shapes, not possible by conventional pressing, also can be made by the new manufacturing process. Holes, projections, and indentations can be produced without additional finishing.

The process permits more uniform porosity of the nickel, according to Corning. Pore diameter of the material can be tailored to specifications between the limits of 1 to 45 μ.

Depending on porosity, yield strengths will go up to 10,000 psi. Maximum thickness of available pieces is 1 in., although thicker pieces can be made, the company stated. Fine orifice holes (0.012 in.) for burner plates can be drilled through as much as 5/8-in. thickness, using conventional metalworking machinery.

Potted Battery Power Packs with Shock Resistance up to 2000 g's

Development of potted battery power packs with proven shock resistance up to 2000 g's has been announced by the Alkaline Battery Division of Gulton Industries, Inc., Metuchen, N. J.

Designed for use in satellites, missiles, rockets, and telemetry applications, the CG, "Power Packs" can be fabricated into configurations that are seldom possible with standard round or square batteries. Using any number of cells, the "Power Packs" can be custom formed to fill often considered "dead" space, providing any voltage and current capacity required.

In addition to true hermetic sealing and high shock resistance, the new "Power Packs," because of perfect restriction, also greatly increase the electrical capacity of the battery cells through compression.

Developed originally for a contractor to the AEC to fulfill an extremely high-g application, the new designs employ all sizes of the Gulton VO nickel-cadmium button cell battery series, including 80, 180, 250, 500, 800, and 1750 MAH cells, each of which has a nominal rating of 1.2 volts.

Literature from Industry

Silicon Readout Photocells for Computer, Data Handling Systems—Silicon photovoltaic readout matrices feature extremely fast response time in the order of 10 μsec. Developed by International Rectifier Corp., the self-generating devices convert light energy directly into electricity, with no need for external power supplies. Typical current generated is 300 μa for 0.01 sq in. of active cell area at 1000 ft-c illumination. For more detailed data, request Bulletin SR-277 from International Rectifier Corp., El Segundo, Calif.

Since 1861
AMES has been making these
SILVER SALTS
to YOUR specifications

Silver Nitrate
Silver Cyanide
Silver Chloride
Silver Sulfate
Monovalent Silver Oxide
Divalent Silver Oxide

And now for your Battery
Silver Flour
and
for powder metallurgy
Nodular Silver

M. AMES CHEMICAL WORKS, INC.
17-19 Rogers Street
Glen Falls, New York
Phone 2-4394

STORAGE BATTERY ENGINEERS

Nationally Known Manufacturer
of
Industrial Type Storage Batteries
needs

ENGINEERING and PRODUCTION PERSONNEL with ten or more years' experience in the production of lead acid storage batteries of the motive power type.

College graduates preferred—Age 35 to 55. Salary Open. Send complete resume to:

Technical Employment Supervisor
THOMAS A. EDISON INDUSTRIES
McGRAW-EDISON COMPANY
West Orange, New Jersey

All replies held strictly confidential.

"Industrial Nickel Plating"—In a new booklet, the International Nickel Co. presents informative data and descriptive material on many aspects of this major industrial process, and describes properties of the coating, fabrication possibilities, and both general and specific applications. In addition, the booklet features extensive corrosion data taken from actual plant tests. "Industrial Nickel Plating" is available without charge through the Readers Service Section of the International Nickel Co., Inc., 67 Wall St., New York 5, N. Y.

Corrosion Chart—An unusually detailed calculator, showing preferred materials for 247 different types of corrosives, has been made available by Hoke, Inc., manufacturer of small fluid control products. These handy calculators cover the degree of preference for handling corrosives with aluminum, brass, carbon steel, inconel, Kel-F, monel, nickel, nitril rubber, polyethylene, polyvinyl chloride, 304 stainless steel, 316 stainless steel, 430 stainless steel, Teflon, titanium, and other materials.

The chart is intended only as a guide to the selection of materials of construction, based on "substantial," "moderate," "questionable," or "inadequate" resistance to the chemical in question at atmospheric pressure and temperature. Also included on the jacket of the slide-rule type calculator are a listing and illustrations of some of Hoke's fluid control products designed for handling corrosive fluids. These include valves, stainless steel sample cylinders, and pressure regulators.

Copies of the Hoke Corrosion Chart are available on request from Hoke, Inc., 155 Piermont Rd., Cresskill, N. J.

Arc Furnace Transformers—Bulletin GEA-6236A, 24 pages, gives descriptive and technical data on transformers for electric arc furnaces for steel, ferroalloy, nonferrous metal, and chemical industries. It includes tables of performance, electrical characteristics, dimensions, weights, and estimating prices for units ranging from 750 to 35,000 kva, with input voltages from 2.4 to 34.4 kv. General Electric Co., Schenectady 5, N. Y.

Cryogenerators—A new folder entitled "Norelco Cryogenerators—For Gas Liquefaction Systems" is available gratis. Engineering information is given on four models: 3000 Btu/hr, 12,000 Btu/hr, 30,000 Btu/hr, and 170,000 Btu/hr, all at 320 degrees below zero Fahrenheit. Cryogenics Division, North American Philips Co., Inc. 100 Stevens Ave., Mount Vernon, N. Y.

Lead Acid Battery Technology Handbook—Industrial storage battery users and maintenance men will be interested in a new 36-page handbook of technical instructions and engineering data on the care of motive power storage batteries. Prepared by the Industrial Division of Gould-National Batteries, Inc., the illustrated booklet, "Instructions and Maintenance Data" (GB-1896), covers all phases of battery theory, operation, and maintenance. Copies of Bulletin GB-1896 can be obtained from Gould-National Batteries, Inc., Trenton 7, N. J.

Reference Summary of Metal Finishing Literature—A pocket-size reference summary of metal finishing literature produced by MacDermid Inc., Waterbury, Conn., manufacturer of metal cleaning, plating, and finishing chemicals, is now available on request. MacDermid technical data sheets give metal finishers valuable where-to-use information, make-up, operating instructions, analysis, and control for a wide variety of cleaners, copper-plating processes, dry acid salts, Macromate coatings, and many other specialties. This summary folder lists data sheets by number, trade name, and use.

Organic Chemist for Semiconductor Research PSI

PACIFIC SEMICONDUCTORS, INC., a subsidiary of Thompson Ramo Wooldridge Inc., offers an unusual opportunity to an organic chemist of outstanding talent.

The man we are seeking to fill this important post should hold an advanced degree and have a background and interest in polymer science, thin films and organic coatings.

He will investigate synthesis of the organo-silicon and organo-metallic polymers and correlations of molecular structure with electrical properties. He should further possess a consuming scientific curiosity and ranging technical interest which will lead him to probe deeply the problems in his specific area of work while deriving stimulation from contingent technical fields.

You may write in confidence to Larry Long,
Technical Staff Placement,

PSI

Pacific Semiconductors, Inc.

10451 WEST JEFFERSON BOULEVARD, CULVER CITY, CALIFORNIA

Advertiser's Index

American Brass Company 286C
M. Ames Chemical Works, Inc. 296C
Bell Telephone Laboratories, Inc. 281C
E. I. du Pont de Nemours & Company (Inc.) 280C
The Eagle-Picher Company 285C
Thomas A. Edison Industries 296C
Enthone, Incorporated ..... Cover 4
Great Lakes Carbon Corp., Electrode Division ..... Cover 2
Pacific Semiconductors, Inc. 297C
Sylvania Electric Products Inc. 283C

The Electrochemical Society

Patron Members

Aluminum Co. of Canada, Ltd.,
Montreal, Que., Canada
International Nickel Co., Inc.,
New York, N. Y.
Olin Mathieson Chemical Corp.,
Niagara Falls, N. Y.
Industrial Chemicals Div., Research
and Development Dept.
Union Carbide Corp.
Divisions:
Union Carbide Metals Co.,
New York, N. Y.
National Carbon Co., New York, N. Y.
Westinghouse Electric Corp., Pittsburgh, Pa.

Sustaining Members

Air Reduction Co., Inc.,
New York, N. Y.
Ajax Electro Metallurgical Corp.,
Philadelphia, Pa.
Allen-Bradley Co., Milwaukee, Wis.
Allied Chemical & Dye Corp.
General Chemical Div., Morristown, N. J.
Solvay Process Div., Syracuse, N. Y.
(3 memberships)
Allied Research Products, Inc.,
Detroit, Mich.
Alloy Steel Products Co., Inc., Linden, N. J.
Aluminum Co. of America,
New Kensington, Pa.
American Machine & Foundry Co.,
Raleigh, N. C.
American Metal Climax, Inc.,
New York, N. Y.
American Potash & Chemical Corp.,
Los Angeles, Calif. (2 memberships)
American Zinc Co. of Illinois,
East St. Louis, Ill.
American Zinc, Lead & Smelting Co.,
St. Louis, Mo.
American Zinc Oxide Co., Columbus, Ohio
M. Ames Chemical Works, Inc.,
Glens Falls, N. Y.
Auto City Plating Company Foundation,
Detroit, Mich.
Basic Inc., Maple Grove, Ohio
Bell Telephone Laboratories, Inc.,
New York, N. Y. (2 memberships)
Bethlehem Steel Co., Bethlehem, Pa.
(2 memberships)
Boeing Airplane Co., Seattle, Wash.
Burgess Battery Co., Freeport, Ill.
(4 memberships)
C & D Batteries, Inc., Conshohocken, Pa.
Canadian Industries Ltd., Montreal, Que.,
Canada
Carborundum Co., Niagara Falls, N. Y.
Catalyst Research Corp., Baltimore, Md.
Chrysler Corp., Detroit, Mich.
Ciba Pharmaceutical Products, Inc., Summit,
N. J.
Columbian Carbon Co., New York, N. Y.
Columbia-Southern Chemical Corp.,
Pittsburgh, Pa.
Consolidated Mining & Smelting Co. of
Canada, Ltd., Trail, B. C., Canada
(2 memberships)
Continental Can Co., Inc., Chicago, Ill.
Cooper Metallurgical Associates, Cleveland,
Ohio
Corning Glass Works, Corning, N. Y.
Crane Co., Chicago, Ill.
Diamond Alkali Co., Painesville, Ohio
(2 memberships)
Dow Chemical Co., Midland, Mich.
Wilbur B. Driver Co., Newark, N. J.
(2 memberships)
E. I. du Pont de Nemours & Co., Inc.,
Wilmington, Del.
Eagle-Picher Co., Chemical Div., Joplin, Mo.
Eastman Kodak Co., Rochester, N. Y.
Electric Auto-Lite Co., Toledo, Ohio
Electric Storage Battery Co.,
Philadelphia, Pa.
Englehard Industries, Inc., Newark, N. J.
(2 memberships)
The Eppley Laboratory, Inc., Newport, R. I.
(2 memberships)
Erie Resistor Corp., Erie, Pa.
Exmet Corp., Tuckahoe, N.Y.
Fairchild Semiconductor Corp., Palo Alto,
Calif.
Federal Telecommunication Laboratories,
Nutley, N. J.
Food Machinery & Chemical Corp.
Becco Chemical Div., Buffalo, N. Y.
Westvaco Chlor-Alkali Div., South
Charleston, W. Va.
Foote Mineral Co., Paoli, Pa.
Ford Motor Co., Dearborn, Mich.
General Electric Co., Schenectady, N. Y.
Chemistry & Chemical Engineering
Component, General Engineering
Laboratory
Chemistry Research Dept.
General Physics Research Dept.
Metallurgy & Ceramics Research Dept.
General Instrument Corp., Newark, N. J.

(Sustaining Members cont'd)

General Motors Corp.
Brown-Lipe-Chapin Div., Syracuse, N. Y. (2 memberships)
Guide Lamp Div., Anderson, Ind.
Research Laboratories Div., Detroit, Mich.
General Transistor Corp., Jamaica, N. Y.
Gillette Safety Razor Co., Boston, Mass.
Gould-National Batteries, Inc., Depew, N. Y.
Grace Electronic Chemicals, Inc., Baltimore, Md.
Great Lakes Carbon Corp., New York, N. Y.
Hanson-Van Winkle-Munning Co., Matawan, N. J. (3 memberships)
Harshaw Chemical Co., Cleveland, Ohio (2 memberships)
Hercules Powder Co., Wilmington, Del.
Hill Cross Co., Inc., New York, N. Y.
Hoffman Electronics Corp., Evanston, Ill.
Hooker Chemical Corp., Niagara Falls, N. Y. (3 memberships)
Houdaille Industries, Inc., Detroit, Mich.
Hughes Aircraft Co., Culver City, Calif.
International Business Machines Corp., Poughkeepsie, N. Y.
International Minerals & Chemical Corp., Chicago, Ill.
Jones & Laughlin Steel Corp., Pittsburgh, Pa.
K. W. Battery Co., Skokie, Ill.
Kaiser Aluminum & Chemical Corp.
Chemical Research Dept., Permanente, Calif.
Div. of Metallurgical Research, Spokane, Wash.
Kennecott Copper Corp., New York, N. Y.
Keokuk Electro-Metals Co., Keokuk, Iowa
Libbey-Owens-Ford Glass Co., Toledo, Ohio
P. R. Mallory & Co., Indianapolis, Ind.
McGean Chemical Co., Cleveland, Ohio
Merck & Co., Inc., Rahway, N. J.
Metal & Thermit Corp., Detroit, Mich.
Minnesota Mining & Manufacturing Co., St. Paul, Minn.
Monsanto Chemical Co., St. Louis, Mo.
Motorola, Inc., Chicago, Ill.
National Cash Register Co., Dayton, Ohio
National Lead Co., New York, N. Y.
National Research Corp., Cambridge, Mass.
National Steel Corp., Weirton, W. Va.
New York Air Brake Co., Vacuum Equipment Div., Camden, N. J.
Northern Electric Co., Montreal, Que., Canada
Norton Co., Worcester, Mass.
Olin Mathieson Chemical Corp., Niagara Falls, N. Y.
High Energy Fuels Organization (2 memberships)
Pennsalt Chemicals Corp., Philadelphia, Pa.
Phelps Dodge Refining Corp., Maspeth, N. Y.
Philco Corp., Philadelphia, Pa.
Philips Laboratories, Inc., Irvington-on-Hudson, N. Y.
Pittsburgh Metallurgical Co., Inc., Niagara Falls, N. Y.
Poor & Co., Promat Div., Waukegan, Ill.
Potash Co. of America, Carlsbad, N. Mex.
Radio Corp. of America, Harrison, N. J.
Ray-O-Vac Co., Madison, Wis.
Raytheon Manufacturing Co., Waltham, Mass.
Reynolds Metals Co., Richmond, Va. (2 memberships)
Rheem Semiconductor Corp., Mountain View, Calif.
Schering Corporation, Bloomfield, N. J.
Shawinigan Chemicals Ltd., Montreal, Que., Canada
Speer Carbon Co.
International Graphite & Electrode Div., St. Marys, Pa. (2 memberships)
Sprague Electric Co., North Adams, Mass.
Stackpole Carbon Co., St. Marys, Pa.
Stauffer Chemical Co., New York, N. Y.
Sumner Chemical Co., Div. of Miles Laboratories, Inc., Elkhart, Ind.
Sylvania Electric Products Inc., Bayside, N. Y. (2 memberships)
Tennessee Products & Chemical Corp., Nashville, Tenn.
Texas Instruments, Inc., Dallas, Texas
Metals & Controls Div., Attleboro, Mass.
Three Point Four Corp., Yonkers, N. Y.
Titanium Metals Corp. of America, Henderson, Nev.
Tung-Sol Electric Inc., Newark, N. J.
Udylite Corp., Detroit, Mich. (4 memberships)
Universal-Cyclops Steel Corp., Bridgeville, Pa.
Upjohn Co., Kalamazoo, Mich.
Victor Chemical Works, Chicago, Ill.
Western Electric Co., Inc., Chicago, Ill.
Wyandotte Chemicals Corp., Wyandotte, Mich.
Yardney Electric Corp., New York, N. Y.

These Enstrip Metal Strippers work between shifts!

Nickel plated scissors on left were immersed overnight in an Enstrip A solution and left without supervision. Next morning (see right) they were down to bare steel ready for replating.

How would you like to dump your rejected plated parts into a stripping solution and "forget" them? Next morning, there they are, completely stripped and ready for replating! That's what Enstrip S and Enstrip A can do for you. These patented products of Enthonics research are alkaline solutions that dissolve nickel, copper, brass, silver, zinc and cadmium plate without attacking steel basis metals. Even when parts remain in the bath for hours after completion of stripping, the base metal remains as bright and shiny as it was prior to original plating.

Enstrip S and Enstrip A solutions operate at room temperature. No temperature, voltage or current to control. No electrical contacts to keep tight. Never any need to "rescue" the work upon completion of stripping. If you want rapid stripping, Enstrip S and Enstrip A solutions, operated at elevated temperatures, will dissolve .0015" of nickel or .0030" of copper per hour!

Write for the handy Enstrip Selection Chart which gives complete information about these new Enstrips, along with Enstrip 165 S (to dissolve nickel from copper and brass); Enstrip T-L (to dissolve soft solder, tin, and lead from steel and copper base alloys); Enstrip L-88 (to anodically remove copper, nickel, and chromium from zinc base die castings in a single operation), and many others. Ethone Incorporated, 442 Elm Street, New Haven, Connecticut.

ASARCO

ANOTHER PRODUCT OF *Enthonics* RESEARCH

ENTHONE

A Subsidiary of American Smelting and Refining Company